SENSOR ARRAY PROCESSING IN DIFFICULT AND NON-IDEALISTIC CONDITIONS

Vom Fachbereich Elektrotechnik und Informationstechnik
der Technischen Universität Darmstadt
zur Erlangung des akademischen Grades eines
Doktor-Ingenieurs (Dr.-Ing.)
genehmigte Dissertation

von

Pouyan Parvazi, M.Sc.
Geboren am 21. März 1975 in Tehran, Iran.

Referent:	Prof. Dr.-Ing. Marius Pesavento
Korreferent:	Prof. Dr.-Ing. Christoph F. Mecklenbräuker
Tag der Einreichung:	8. Dezember, 2011
Tag der mündlichen Prüfung:	18. Januar, 2012

D17
Darmstädter Dissertation
2012

To my parents,

Minoo Mobassery *and* ***Ebrahim Parvazi****,*

for their unbounded and unconditional love.

Acknowledgments

I would like to express my deepest gratitude to:

Alex Gershman

who made all this possible. May he rest in peace.

Marius Pesavento

who is my supervisor, my colleague, and my friend; all in one. For his patience and for his invaluable advices.

Christoph Mecklenbräuker

for his time and support.

Marlis Gorecki

for all her kindness and help.

Adrian, Ahmed, Christian, Imran, Michael, Nils, Nima, and Philipp

and all my colleagues and friends in NTS group for all their support and help, and for all the discussions and laughs.

and ...

Shadi

my love and my joy.

Zusammenfassung

Die vielfältigen Anwendungen der Sensorgruppensignalverarbeitung und ihre spezifischen Herausforderungen in der Praxis bilden die Motivation für die vorliegende Arbeit. Schwierigkeiten, die unter nicht-idealen Bedingungen auftreten und in dieser Arbeit betrachtet werden sind: eine begrenzte Anzahl von verfügbaren Schnappschüssen oder eine niedrige Signalleistung, eine ungenaue Kenntnis der Sensorgruppenanordnung und das Fehlen bestimmter zeitlicher oder raumlicher Abtastwerte. Diese Bedingungen werden bei der Schätzung der folgenden Parameter berücksichtigt: die Einfallsrichtung (DOA) der Signale auf die Sensorgruppe, die Array-Mannigfaltigkeit, und die Frequenz und die Dämpfungsfaktoren der Harmonischen des Signals.

Um praktische Gegebenheiten wie die begrenzte Anzahl von Schnappschüssen oder eine geringen Signalleistung zu bewältigen wird zunächst eine Methode eingeführt, die auf der Idee einer Schätzer-Bank und der Detektion und Korrektur fehlerhafter Schätzwerte basiert. Das vorgeschlagene Verfahren verbessert die Güte der DOA-Schätzung signifikant in Szenarien, in denen einige der Quellen eng beieinander liegen.

Dann werden Unbestimmtheiten bezüglich der relativen Lage der Sensorgruppen betrachtet. Der Fokus dieses Teils der Untersuchung liegt auf der Richtungsschätzung sowie auf der Sensorgruppenkalibrierung bei teilkalibrierten Sensorgruppen. Drei verschiedene Typen teilkalibrierter Sensorgruppen werden untersucht: die allgemeinste Form einer teilkalibrierten Sensorgruppe, die Anordnung eines teilweise kalibrierten Arrays bestehend aus mehreren identischen Untergruppen und Anordnung einer Sensorgruppe bestehend aus paarweise kalibrierten Sensoren. Die hochauflösenden Verfahren zur blinden Sensorgruppenkalibrierung und simultanen Richtungsschätzung, die für jede dieser Sensorgruppenanordnung vorgeschlagen werden, weisen eine erheblich verbesserte Schätzgenauigkeit

auf als Methoden, die dem bisherigen Stand der Technik entsprechen.

Schließlich wird das Fehlen bestimmter Abtastwerte bzw. Sensordaten bei der Schätzung der Frequenz- und Dämpfungsparameter einer Superposition von mehreren Harmonischen betrachtet. Dieses Problem kann als Verallgemeinerung des zuvor betrachteten Richtungschätzproblems mittels Sensorgruppen betrachtet werden. Es werden suchfreie und doch hochauflösende Verfahren zur eindeutigen Schätzung der Signalparameter vorgestellt, die sich durch exzellente Schätzgenauigkeit auszeichnen.

Abstract

The variety of sensor array processing applications and their practical concerns are the motivations behind the present thesis. The uncertainties in the non-ideal conditions considered in this thesis are: the limited number of available snapshots or low signal power, uncertainties in the sensor array geometry, and the nonavailability of specific temporal or spatial samples. These conditions are taken into account in the estimation process of the following parameters: the direction-of-arrival (DOA) of the signals impinging on the array, the array manifold, and the frequencies and the damping factors of the signal harmonics.

First, to deal with the practical situations of a limited number of snapshots or a low signal power, a method is introduced based on the estimator bank approach combined with detection and cure of erroneous estimates. The proposed technique significantly improves the DOA estimation performance in the scenarios where some sources are closely-spaced.

Next, uncertainties in the array sensor locations are considered. The focus of this part of the study lies on the blind calibration and joint DOA estimation in partly-calibrated arrays. Three types of partly-calibrated array geometries are investigated: the arbitrary partly-calibrated array, the partly-calibrated array composed of multiple identical subarrays, and the pairwise-calibrated array. The novel high-resolution DOA and array manifold estimation techniques proposed for each of these array types demonstrate superior DOA estimation performance in comparison with the state-of-the-art methods.

Lastly, the nonavailability of specific samples in the harmonic retrieval problem, i.e., the problem of estimating the frequencies and the damping factors of a harmonic mixture, is considered. The harmonic retrieval problem can be regarded as the generalization of the DOA estimation problem. In the case of incomplete samples, search-free yet high-resolution techniques are proposed which demonstrate excellent harmonic estimation performance.

Table of Contents

List of Figures

List of Tables

Acronyms

APCA	arbitrary partly-calibrated array
AR	auto-regressive
CDF	cumulative distribution function
CRB	Cramer-Rao bound
DOA	direction-of-arrival
EB	estimator bank
ESPRIT	estimation of signal parameters via rotational invariance technique
FB	forward/backward averaging
FOV	field-of-view
GESPRIT	generalized ESPRIT
GLRT	generalized likelihood ratio test
HR	harmonic retrieval
IAA	iterative adaptive approach
I&C	identification and cure
LMPT	locally most powerful test
LR	likelihood ratio
LS	least squares
LSE	least squares error
LTE	long-term evolution
MA	moving-average

MAPES	missing data amplitude and phase estimation
MDF	multidimensional folding
MI	multiple invariance
MIAA	missing data iterative adaptive approach
MI-MUSIC	multiple invariance MUSIC
ML	maximum likelihood
MLSE	minimum least squares error
MODE	method of DOA estimation
MP	matrix polynomial
MUSIC	multiple signal classification
NRMSE	normalized root-mean-square error
NMR	nuclear magnetic resonance
PCA	partly-calibrated array
PCAMIS	partly-calibrated array composed of multiple identical subarrays
PDF	probability density function
PWCA	pairwise-calibrated array
QA	quality assessment
RARE	rank-reduction method
RMSE	root-mean-square error
SNR	signal-to-noise ratio
ULA	uniform linear array
UCA	uniform circular array
UMPT	uniformly most powerful test
WLS	weighted least squares
WMI	weighted multiple invariance
WMUSIC	weighted-MUSIC

Notation

$[\cdot]_{(m)}$	the m-th entry of a vector
$[\cdot]_{(m,l)}$	the entry in the m-th row and the l-th column of a matrix
$(\cdot)^*$	conjugate of a complex variable
$(\cdot)^T$	Transpose of a matrix
$(\cdot)^H$	Hermitian of a matrix
$(\cdot)^\dagger$	Moore-Penrose pseudo-inverse of a matrix
$\lvert\cdot\rvert$	absolute value of a complex variable
$\lVert\cdot\rVert$	Frobenius norm of a matrix
$\measuredangle(\cdot)$	phase of a complex variable
$\mathcal{D}\{\cdot\}$	operator replacing the off-diagonal entries of a square matrix by zeros and constraining the diagonal entries to unit magnitude
$\mathcal{CN}$	complex normal distribution
$\mathcal{CW}$	complex Wishart distribution
$\det\{\cdot\}$	determinant of a matrix
$\mathrm{diag}\{\cdot\}$	main diagonal of a matrix or a diagonal matrix with the inside vector as the main diagonal
$\mathrm{diag}_+\{\cdot\}$	a diagonal matrix constructed from the positive diagonal entries of another matrix while replacing the non-positive diagonal and all the off-diagonal entries with zeros
$\mathrm{E}\{\cdot\}$	statistical expectation
$\mathrm{Im}\{\cdot\}$	imaginary part of the entries of a complex matrix

$\mathcal{L}^{(l)}\{\cdot\}$	the l-th largest eigenvalue of a matrix
$\mathcal{L}_{\min}\{\cdot\}$	the minimum eigenvalue of a matrix
$\mathcal{N}\{\cdot\}$	null-space of a matrix
$\mathcal{O}$	order of complexity
$\mathcal{R}\{\cdot\}$	range-space of a matrix
$\text{rank}\{\cdot\}$	column-rank of a matrix
$\text{Re}\{\cdot\}$	real part of the entries of a complex matrix
$\text{Res}(f, g)$	resultant of two polynomials f and g
$\text{tr}\{\cdot\}$	trace of a matrix
$\mathcal{V}_{\min}\{\cdot\}$	minor eigenvector of a matrix
$\mathbf{a}$	array manifold vector
$\mathbf{A}$	array manifold matrix
$\mathcal{B}$	the set of random estimators
$\mathbf{C}$	matrix depending on the masking indicators v and the parametric generator μ in the WMI method
$\mathbf{e}_m$	the m-th column of an identity matrix
$\mathbf{E}_{m,l}$	a matrix containing a one in the (m, l) entry and zeros elsewhere
$\mathbf{G}(\mu)$	MP containing signal subspace matrix which drops rank when its variable is equal to the true harmonics
H_0	null hypothesis
H_1	alternative hypothesis
$\mathbf{h}$	rows of the signal generator matrix in the HR method
$\mathbf{I}$	identity matrix
J_r	number of Monte-Carlo runs
$\mathbf{K}_{\text{R}}$	the block diagonal matrix containing the known part of the manifold vectors in RARE method
K	number of the subarrays
L	number of the signals
M	number of array sensors or number of samples in HR problem

$\bar{M}$	number of available samples
M_0	the maximum utilized shift in the HR method
M_k	number of sensors in the k-th subarray
$\mathbf{M}(\mu)$	MP containing signal generator matrix which drops rank when its variable is equal to the true harmonics
$\mathbf{n}$	noise vector
N	number of snapshots
N_g	number of search grid points in a search-based method
$\mathbf{P}$	mixing matrix
Q	estimator bank size or number of random estimators
$r_{s,l}$	the l-th source power
$\hat{r}_{s,l}$	estimated l-th source power
$\hat{\mathbf{r}}_s$	estimated source power vector
$\mathbf{R}$	received signal covariance matrix
$\hat{\mathbf{R}}$	sample received signal covariance matrix
$\tilde{\mathbf{R}}$	reconstructed received signal covariance matrix
$\mathbf{R}_{\mathrm{s}}$	signal covariance matrix
$\mathbf{s}$	signal vector
t	time index
$\mathcal{T}$	set of estimates from all the random estimators in an estimator bank
$\mathbf{U}_{\mathrm{N}}$	noise subspace matrix
$\mathbf{U}_{\mathrm{S}}$	signal subspace matrix
$\mathbf{V}$	diagonal matrix consisting of binary masking indicators in HR
v	binary masking indicator in HR
$\bar{v}$	available sample positions
$\mathbf{w}$	weight vector
$\mathbf{W}$	weight matrix
$[x_m \ y_m]^T$	location of the m-th sensor in the xy plane
$\mathbf{z}$	received signal vector

$\mathbf{z}_a$	available received signal vector
$[\alpha_k \ \beta_k]^T$	the k-th displacement vector
γ_0	quality assessment value
$\delta_{i,k}$	Kronecker delta function (equal to one if $i = k$ and zero otherwise)
ε	step size in FOV scanning
$\boldsymbol{\eta}_k$	the k-th displacement vector
θ_l	DOA of the l-th signal
$\boldsymbol{\theta}$	DOA vector
$\hat{\boldsymbol{\theta}}$	DOA estimate vector
κ	assigned threshold value
λ	signal wavelength
λ_m	received signal covariance matrix eigenvalue
$\boldsymbol{\Lambda}_{\mathrm{N}}$	noise eigenvalue matrix
$\boldsymbol{\Lambda}_{\mathrm{S}}$	signal eigenvalue matrix
$\boldsymbol{\mu}$	unknown signal-dependent parameters
$\boldsymbol{\Pi}$	projector matrix
$\boldsymbol{\Pi}^{\perp}$	orthogonal projector matrix
$\boldsymbol{\rho}$	estimated parameter set $\boldsymbol{\rho} = \{\hat{\boldsymbol{\theta}}, \hat{\mathbf{r}}_s, \hat{\sigma^2}\}$
σ^2	noise power
$\hat{\sigma^2}$	estimated noise power
$\boldsymbol{\Phi}$	displacement-phase matrix
φ	roots in root-MUSIC method
$\boldsymbol{\Psi}$	unknown array geometry-dependent parameter matrix
ω	frequency harmonic in the MIAA
$\boldsymbol{\omega}$	vector containing the real and the imaginary parts of the true harmonics
$\boldsymbol{\Omega}$	matrix containing the derivatives of signal generator vectors with respect to each generator

Chapter 1

Introduction

Sensor array signal processing is a well-established yet still active research area of interest in signal processing. The objective of sensor array processing is the estimation of the signal parameters generated by some emitters (sources) making use of snapshots of the received signals at the output of the sensors located at different points. These parameters consist of (but are not limited to) the number of sources, the signal powers, the signal waveforms, the signal polarizations, the source velocities, the signal frequencies, the distances of the sources from the array in both the near-field and the far-field cases, and the direction-of-arrival (DOA), i.e., the azimuth and the elevation angles of the signals. Estimating the array parameters such as the spatial signature or the array manifold through sources at known or unknown locations, i.e., array calibration, is yet another crucial problem, e.g., for DOA estimation, in the array processing.

Parameter estimation in array processing plays a significant role in many diverse applications. In radar, the phased antenna arrays are used both in active (as transmitters) and in passive (as receivers) modes for estimating parameters such as velocity, range, and DOA of the target objects. In sonar, the sensor arrays are used for similar purposes as in radar with the major difference that acoustic waves are used in water instead of electromagnetic waves in the atmosphere. Hence, the type of the sensors (hydrophones in the case of sonar, antennas in the case of radar) and the array design become different. Another application for antenna arrays is radio astronomy where the passive sparse array aperture covers large areas and the array is used to record images of a certain region of the sky and to estimate the

characteristics of astronomical objects such as pulsars and galaxies. In wireless communications, the smart antenna arrays, i.e., adaptive arrays, are used in multi-user communication environment for applications such as beamforming in both active and passive modes, and estimating the propagation delays in a multiuser asynchronous environment. In seismology, arrays of geophones are used, e.g., to acquire information about the earth layers for oil exploration, or to study earthquakes. Array processing has also found its way into medical applications such as brain activity localization and tomography, as well as into industrial applications such as automatic monitoring, fault detection, and localization.

The variety of the applications and their particular requirements are the motivations behind the present thesis. Our focus lies on the process of the estimation of the signal parameters (signal DOAs or signal frequencies and damping factors) and of the estimation of array manifold. In this thesis, difficult and non-ideal conditions and uncertainties are considered in the sensor array processing. By difficult conditions we are referring specifically to limited number of available snapshots and low power signals which make the estimation of the signal DOAs difficult. Robust estimators for the sparse sensor arrays is another subject of the present thesis. In the sparse sensor array model where the array is composed of several subarrays, uncertainties in the time synchronization between subarrays, the fading for different subarrays, and inter-subarray displacements may lead to a severe performance degradation of conventional DOA estimators. Therefore, robust estimation techniques able to properly estimate the signal parameters despite those uncertainties are of practical importance. Uncertainties like corrupt samples are considered for the case of signal frequency (and its damping factor) estimation in the harmonic retrieval problem.

The following ideas and techniques are presented in this thesis to overcome such difficult and non-ideal conditions:

In practical situations where the number of snapshots is limited or the SNR is low, the DOA estimation performance of subspace-based methods degrades substantially [29], [95]. To mitigate such performance degradations, several methods have been proposed in [2], [7], [17], [35], [46], [52], [73]. In Chapter 4, a method is introduced based on the concepts of "estimator bank" [17] and of the detection and cure of erroneous estimates, i.e., outliers

[1], [2]. For the purpose of outlier detection and cure, hypothesis testing is used. Two ways for computing the test statistics are presented. The proposed techniques based on the estimator bank approach, as we shall see, significantly improve the DOA estimation performance in the scenarios where the number of snapshots is small, the signal powers are low, and the sources are closely-spaced. Moreover, two methods to combine the sets of estimates obtained from the estimator bank are proposed. The following publications report the results of this chapter:

- P. Parvazi, A. B. Gershman, Y. I. Abramovich, "Detecting outliers in the estimator bank-based direction finding techniques using the likelihood ratio quality assessment," *International Conference on Acoustics, Speech, and Signal Processing (ICASSP'07)*, Honolulu, USA, vol. 2, pp. 1065-1068, Apr. 2007.

- P. Parvazi, A. B. Gershman, and Y. I. Abramovich, "Improving the threshold performance of the estimator bank direction finding techniques using outlier identification and cure", *IEEE International Symposium on Wireless Pervasive Computing (ISWPC'08)*, Santorini, Greece, pp. 270 - 273, May 2008.

Uncertainties in the array manifold, particularly in the sensor array geometry of large aperture arrays, are considered in Chapter 5. Due to the sensitivity of subspace-based methods to such uncertainties and errors [14], [81], [90], either calibration techniques [43], [50], [51], [55], [63], [72], [79], [103] are used to obtain the complete array manifold model before estimating the DOAs, or the DOAs are estimated directly utilizing only the available information about the array model [16], [77], [80], [92]. The focus of Chapter 5 lies on joint DOA and array manifold estimation, i.e., blind calibration, in partly-calibrated arrays (PCAs). Three PCA models with proper applicability are studied: arbitrary partly-calibrated arrays (APCAs), partly-calibrated arrays composed of multiple identical subarrays (PCAMISs), and pairwise-calibrated arrays (PWCAs). The APCA and the PCAMIS models can be applied to many cases of large sparse arrays (described in more detail in Chapter 5), e.g., where the subarrays are not stationary. The PWCA model can have applications in the upcoming long-term evolution (LTE) wireless networks, where the handsets contain a pair

of antennas instead of just a single antenna. The common contribution of the different techniques introduced in this chapter is the exploitation of the estimate of the unknown or uncertain part of the array manifold and its known structure in the DOA estimation algorithms. The novel high-resolution DOA and array manifold estimation techniques proposed for each of these types of arrays demonstrate superior performance in comparison with the state-of-the-art methods. The results of this chapter have been presented in the following publications:

- P. Parvazi and A. B. Gershman, "Direction-of-arrival and spatial signature estimation in antenna arrays with pairwise sensor calibration," *IEEE International Conference on Acoustics, Speech, and Signal Processing (ICASSP'10)*, Dallas, TX, USA, pp. 2618-2621, Mar. 2010.

- P. Parvazi, M. Pesavento, and A. B. Gershman, "Direction-of-arrival estimation and array calibration for partly-calibrated arrays," *IEEE International Conference on Acoustics, Speech, and Signal Processing (ICASSP'11)*, Prague, Czech Republic, pp. 2552-2555, May 2011.

- P. Parvazi and M. Pesavento, "A new direction-of-arrival estimation and calibration method for arrays composed of multiple identical subarrays," *IEEE International Workshop on Signal Processing Advances in Wireless Communications (SPAWC'11)*, San Francisco, CA, USA, pp. 166-170, June 2011.

The nonavailability of some sensors in array processing applications and of some data (also referred to as samples) in the generic model of harmonic retrieval (HR) problem is considered in Chapter 6. In the harmonic retrieval model, which is the generalization of the model introduced in sensor array processing applications, the frequencies and the damping factors of a superposition of signals have to be estimated. The harmonic retrieval problem has been studied extensively for various applications [8], [12], [22], [34], [36], [37], [38], [39], [40], [42], [64], [70], [75], [89], [91], [97], [107], [110]. There are techniques for estimating the desired parameters using a search-free scheme [22], [34], [42], [64], [91], [97], [110] where

all the samples are available, and there are techniques, which consider the incomplete or missing sample case [12], [40], [89], [107]. However, the search-free methods to deal with the incomplete samples for the generic harmonic retrieval problem have not been studied. To this end, in Chapter 6, the search-free weighted multiple invariance (WMI) method [69] in the complete sample case is presented. In this case, scenario-dependent conditions are derived under which unique harmonics can be obtained. For the incomplete sample case, such conditions do not exist, hence, the proposed algorithm has to be modified and new techniques are required. One way is to select the best estimates from all the obtained estimates. Another way is to obtain the estimates directly making use of the intersection of polynomials with common factors. These fast, i.e., search-free, yet high-resolution proposed techniques, as can be seen from the simulations, can overcome the non-uniqueness issue and display efficient performance. The following publications report the results of this chapter:

- P. Parvazi, M. Pesavento, and A. B. Gershman, "Exploiting multiple shift-invariances in harmonic retrieval: the incomplete data case," *IEEE Workshop on Statistical Signal Processing (SSP'11)*, Nice, France, pp. 729-732, June 2011.

- P. Parvazi, M. Pesavento, and A. B. Gershman, "Rooting-based harmonic retrieval using multiple shift-invariances: the complete and the incomplete sample cases," *IEEE Trans. Signal Processing*, 2011, accepted.

The present thesis is organized as following:

In Chapter 2, the signal model and the subspace separation technique which is common to all the proposed methods in this thesis are introduced. In Chapter 3, the state-of-the-art and existing estimation techniques which are going to be compared with the proposed methods are described. In Chapter 4, a method to improve the DOA estimation performance for fully-calibrated arrays in the cases of low SNR and small number of snapshots is proposed. In this chapter, after describing the "estimator bank" idea, the hypothesis testing concept to detect and also to cure the erroneous estimates is introduced. Then, methods to combine these two concepts to obtain an improved performance, as shown by the simulations at the end of this chapter, are proposed. In Chapter 5, novel methods for high-resolution DOA

estimation and array calibration for three types of PCAs are presented. These methods display superior performance compared to the existing methods as demonstrated by the simulations at the end of this chapter. In Chapter 6, new search-free algorithms for the complete and the incomplete sample cases of the harmonic retrieval problem are proposed. Chapter 7 concludes the thesis, and some future works and extensions of the problems studied in this thesis are also suggested for further research.

Chapter 2

Signal Model

Consider an array with M identical omni-directional sensors as displayed in Fig. 2.1. The location of each sensor m (for $m = 1, \ldots, M$) is denoted by $[x_m, y_m]^T$ in the Cartesian coordinate system. Depending on the scenario, the array geometry can be partitioned into smaller subarrays with completely known or partly known geometry. Assume that there are L ($< M$) far-field point sources emitting narrow-band signals whose baseband model at time index t is denoted by $\mathbf{s}(t)$. We also assume that N observations or snapshots are available, i.e., $t = 1, 2, \ldots, N$. Throughout the text, we have the following assumptions for the sources:

Assumption 1: The number of sources L is known or can be estimated using the well-known methods presented in [26], [101], [102].

Assumption 2: The sources are uncorrelated.

The noise in the m-th sensor for $m = 1, 2, \ldots, M$, is modeled as independently identically distributed (i.i.d.) zero-mean complex white Gaussian additive noise, i.e.,

$$n_m(t) \sim \mathcal{CN}(0, \sigma^2). \tag{2.1}$$

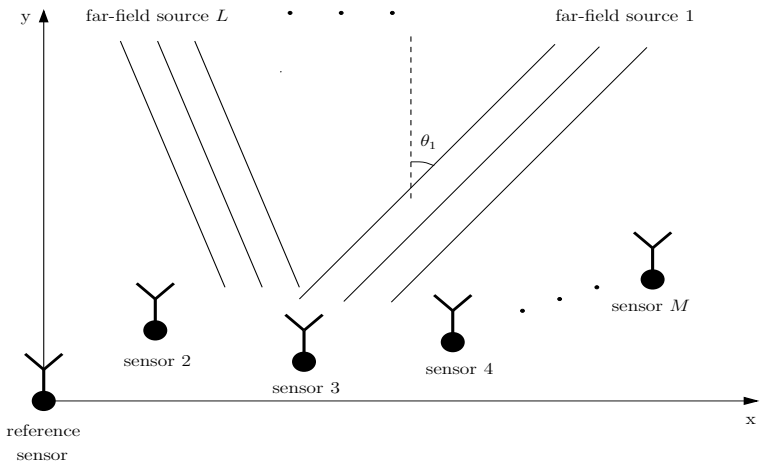

Figure 2.1: Sensor array model

The noise vector $\mathbf{n}(t)$ is defined as

$$\mathbf{n}(t) \triangleq [n_1(t), n_2(t), \ldots, n_M(t)]^T \tag{2.2}$$

and it is assumed to have the following statistical properties:

Assumption 3: The noise is both spatially and temporally white

$$\mathrm{E}\{\mathbf{n}(t_1)\mathbf{n}^H(t_2)\} = \begin{cases} \sigma^2\mathbf{I}, & t_1 = t_2 \\ \mathbf{0}, & t_1 \neq t_2 \end{cases} \tag{2.3}$$

and

$$\mathrm{E}\{\mathbf{n}(t_1)\mathbf{n}^T(t_2)\} = \mathbf{0}. \tag{2.4}$$

The t-th snapshot of the array observation vector (also referred to as array output signal) in the presence of the sensor noise $\mathbf{n}(t)$ is given by

$$\mathbf{z}(t) = \sum_{l=1}^{L} \mathbf{a}(\boldsymbol{\mu}_l, \boldsymbol{\Psi}) s_l(t) + \mathbf{n}(t) \tag{2.5}$$

$$= \mathbf{A}(\boldsymbol{\mu}, \boldsymbol{\Psi})\mathbf{s}(t) + \mathbf{n}(t) \tag{2.6}$$

where

$$\mathbf{s}(t) = [s_1(t), s_2(t), \ldots, s_L(t)]^T \tag{2.7}$$

is the signal waveform vector which is assumed to be stochastic. The $M \times L$ matrix $\mathbf{A}(\boldsymbol{\mu}, \boldsymbol{\Psi})$ can be partitioned into L vectors, each corresponding to a particular source such that

$$\mathbf{A}(\boldsymbol{\mu}, \boldsymbol{\Psi}) \triangleq [\mathbf{a}(\mu_1, \boldsymbol{\Psi}), \mathbf{a}(\mu_2, \boldsymbol{\Psi}), \cdots, \mathbf{a}(\mu_L, \boldsymbol{\Psi})]\,. \tag{2.8}$$

In the sensor array processing application, the matrix $\mathbf{A}(\boldsymbol{\mu}, \boldsymbol{\Psi})$ denotes the array manifold matrix representing the directional characteristics of the array output. In a more general model which we encounter in harmonic retrieval applications, the matrix $\mathbf{A}(\boldsymbol{\mu},\boldsymbol{\Psi})$ denotes the signal generator matrix. This case will be discussed briefly later in this section and in more details in Chapter 6. To achieve the minimum requirement for the uniqueness of the DOA estimates, we take into account the following important assumption:

Assumption 4: The matrix $\mathbf{A}(\boldsymbol{\mu}, \boldsymbol{\Psi})$ is of full-rank, i.e., $\text{rank}\{\mathbf{A}(\boldsymbol{\mu}, \boldsymbol{\Psi})\} = L$.

As it can be seen, the matrix $\mathbf{A}(\boldsymbol{\mu}, \boldsymbol{\Psi})$ depends on two sets of unknown parameters. The signal-dependent parameters contained in vector $\boldsymbol{\mu}$ express the received signal parameters which are the subjects of the estimation process such as the signal DOAs, frequencies or damped factors depending on the application. The second set of parameters in $\mathbf{A}(\boldsymbol{\mu}, \boldsymbol{\Psi})$, namely $\boldsymbol{\Psi}$, denotes the source signal-independent unknowns. In the array processing applications the matrix $\boldsymbol{\Psi}$ represents, for instance, the array geometry-dependent matrix. This matrix, depending on the scenario, can contain the unknown displacement vectors between the subarrays in the array or the unknown geometry of subarrays in the array. The matrix $\boldsymbol{\Psi}$ can also represent other model errors such as channel mismatches or synchronization errors. In the harmonic retrieval model, this matrix represents the unusable samples or sensors.

The scenarios that we are going to discuss can be summarized as:

Scenario I: DOA estimation in fully-calibrated arrays

In this scenario the information about the arbitrary array geometry is completely known, therefore $\boldsymbol{\Psi}$ is an empty vector, and $\boldsymbol{\mu} = \boldsymbol{\theta}$ where

$$\boldsymbol{\theta} \triangleq [\theta_1, \theta_2, \ldots, \theta_L]^T \tag{2.9}$$

is the DOA vector.

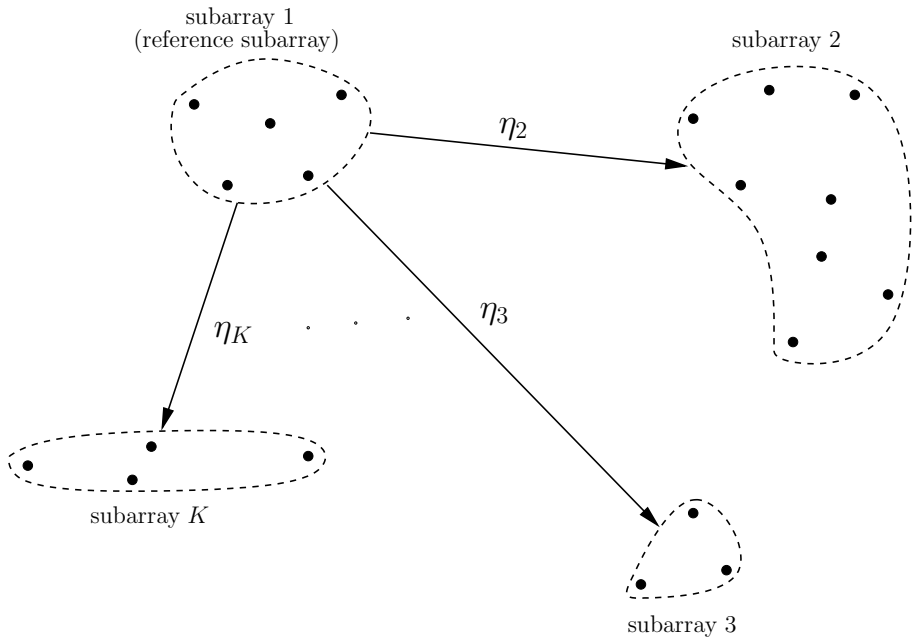

Figure 2.2: Scenario II (APCA geometry): arbitrary known subarrays with arbitrary unknown displacements

Scenario II: DOA estimation/calibration in arbitrary partly-calibrated arrays

An arbitrary partly-calibrated array (APCA) which consists of K arbitrary known subarrays is considered in this scenario as shown in Fig. 2.2. The displacement vectors between these subarrays are assumed to be unknown. Therefore $\boldsymbol{\mu} = \boldsymbol{\theta}$ defined in (2.9) and $\boldsymbol{\Psi} = [\boldsymbol{\eta}_2, \boldsymbol{\eta}_3, \ldots, \boldsymbol{\eta}_K]$ where $\boldsymbol{\eta}_k$ for $k = 2, \ldots, K$ is the k-th displacement vector between the first subarray (also called the reference subarray) and the k-th subarray. By this definition the first displacement vector is $\boldsymbol{\eta}_1 = 0$ and, therefore, known and is not considered.

Scenario III: DOA estimation/calibration in partly-calibrated arrays composed of multiple identical subarrays

Partly-calibrated arrays with multiple identical subarrays (PCAMIS) marks a special case of APCA of Scenario II where all subarrays have identical geometry and

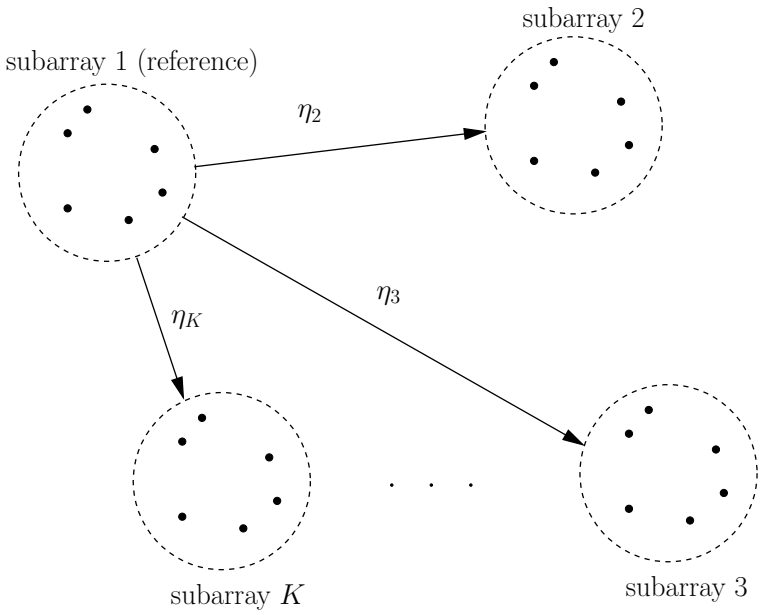

Figure 2.3: Scenario III (PCAMIS geometry): identical arbitrary known/unknown subarrays with arbitrary unknown/known displacements

identically oriented as shown in Fig. 2.3. Here, without loss of generality, we assume that the displacement vectors are known. Therefore $\boldsymbol{\mu} = \boldsymbol{\theta}$ defined in (2.9) and $\boldsymbol{\Psi}$ corresponds to the subarray geometry.

Scenario IV: DOA estimation/calibration in pairwise-calibrated array

A pairwise-calibrated array (PWCA) is defined as an array consisting of two different M_1-sensor subarrays with unknown geometry and known displacement vectors between the pairs of sensors each in one of the subarrays as shown in Fig. 2.4. This scenario can also be regarded as a special case of APCA of Scenario II where each subarray is composed of only two sensors as shown in Fig. 2.5. Therefore, $\boldsymbol{\mu} = \boldsymbol{\theta}$ defined in (2.9) and $\boldsymbol{\Psi}$ is corresponding to the first subarray geometry.

Scenario V: Harmonic retrieval problem in the incomplete sample case

The harmonic retrieval problem is the generalization of the DOA estimation problem and the array output model for fully-calibrated uniform linear arrays (see Fig. 2.6) boils down to the model of the present scenario. In harmonic retrieval problem the

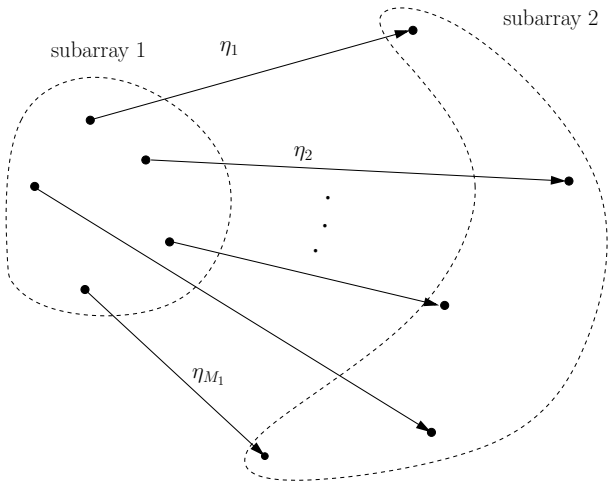

Figure 2.4: Scenario VI (PWCA geometry): two arbitrary unknown subarrays with arbitrary known displacements between sensor pairs

frequencies and damping factors of a discrete harmonic mixture from one or multiple observations (or samples) taken, e.g., along time, frequency or space have to be estimated. In the model of (2.6), in this case, the vector $\boldsymbol{\mu}$ expresses the harmonics together with their possible damping factor $\boldsymbol{\mu} = [\mu_1, \mu_2, \ldots, \mu_L]^T$ where $\mu_l \in \mathbb{C}$, $|\mu_l| \leq 1$ for $l = 1, \ldots, L$, then

$$\mathbf{A}(\boldsymbol{\mu}) = \begin{bmatrix} 1 & 1 & \cdots & 1 \\ \mu_1 & \mu_2 & \cdots & \mu_L \\ \mu_1^2 & \mu_2^2 & \cdots & \mu_L^2 \\ \vdots & \vdots & \cdots & \vdots \\ \mu_1^{M-1} & \mu_2^{M-1} & \cdots & \mu_L^{M-1} \end{bmatrix}. \tag{2.10}$$

In Section 6.2, we consider the case where some samples in this scenario may be unavailable, due to their uncertainty or their being affected by too much noise. Therefore, the matrix $\boldsymbol{\Psi}$ demonstrates these unavailable or missing samples whose locations are assumed to be known. The location of these missing samples (or sensors in the array processing context) is defined by an $M \times M$ diagonal matrix $\mathbf{V}$. Then, the matrix $\mathbf{A}$ in this case (see Section 6.2 for more details) can be shown to be $\mathbf{A}(\boldsymbol{\mu}, \boldsymbol{\Psi}) = \mathbf{V}\mathbf{A}(\boldsymbol{\mu})$. In the case where all the samples are available we have $\mathbf{V} = \mathbf{I}$.

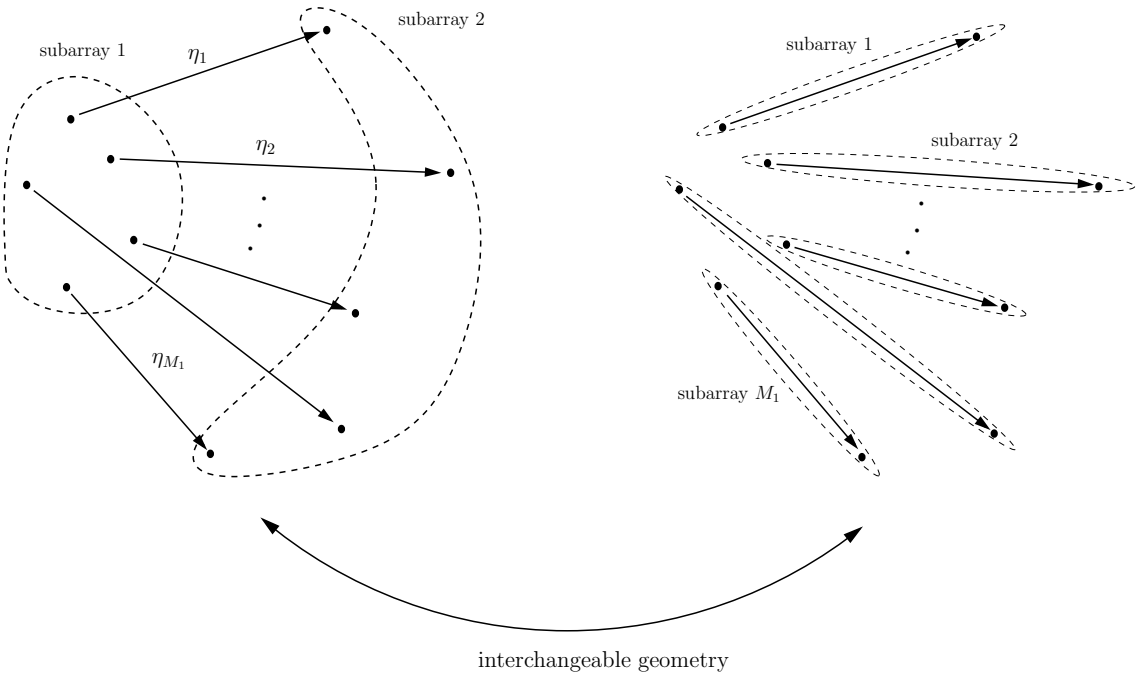

Figure 2.5: PWCA geometry and its relation to APCA geometry

In DOA estimation under Scenarios I-IV, we assume that sensors are located in the xy plane with the position of the m-th sensor denoted by $[x_m, y_m]^T$. Without loss of generality, we assume that the first sensor is located in the origin (hence $x_1 = y_1 = 0$). The array manifold matrix can be described as [33], [96], [98]

$$\begin{aligned}\mathbf{A}(\boldsymbol{\theta}) &= [\mathbf{a}(\theta_1), \mathbf{a}(\theta_2), \cdots, \mathbf{a}(\theta_L)] \\ &= \begin{bmatrix} 1 & 1 & \cdots & 1 \\ e^{-j(2\pi/\lambda)(x_2 \sin\theta_1 + y_2 \cos\theta_1)} & e^{-j(2\pi/\lambda)(x_2 \sin\theta_2 + y_2 \cos\theta_2)} & \cdots & e^{-j(2\pi/\lambda)(x_2 \sin\theta_L + y_2 \cos\theta_L)} \\ e^{-j(2\pi/\lambda)(x_3 \sin\theta_1 + y_3 \cos\theta_1)} & e^{-j(2\pi/\lambda)(x_3 \sin\theta_2 + y_3 \cos\theta_2)} & \cdots & e^{-j(2\pi/\lambda)(x_3 \sin\theta_L + y_3 \cos\theta_L)} \\ \vdots & \vdots & \cdots & \vdots \\ e^{-j(2\pi/\lambda)(x_M \sin\theta_1 + y_M \cos\theta_1)} & e^{-j(2\pi/\lambda)(x_M \sin\theta_2 + y_M \cos\theta_2)} & \cdots & e^{-j(2\pi/\lambda)(x_M \sin\theta_L + y_M \cos\theta_L)} \end{bmatrix}\end{aligned} \tag{2.11}$$

where the array manifold vector $\mathbf{a}(\theta_l)$ for the l-th source is given by

$$\mathbf{a}(\theta_l) = \begin{bmatrix} 1 \\ e^{-j(2\pi/\lambda)(x_2 \sin\theta_l + y_2 \cos\theta_l)} \\ e^{-j(2\pi/\lambda)(x_3 \sin\theta_l + y_3 \cos\theta_l)} \\ \cdots \\ e^{-j(2\pi/\lambda)(x_M \sin\theta_l + y_M \cos\theta_l)} \end{bmatrix} \tag{2.12}$$

for $l = 1, \ldots, L$ and λ is the signal wavelength assumed to be equal for all the signals.

A particular and popular array geometry is the uniform linear array (ULA) where all the array sensors lie on one axis, say x-axis, and the distance between the adjacent sensors d is identical for any two adjacent sensor (see Fig. 2.6). In general, the distance between the adjacent sensors is chosen as within half the signal wavelength $d = \lambda/2$ to avoid ambiguity in the estimates [33], [71]. The array manifold matrix for the ULAs can be written as

$$\begin{aligned} \mathbf{A}(\boldsymbol{\theta}) &= [\mathbf{a}(\theta_1), \mathbf{a}(\theta_2), \cdots, \mathbf{a}(\theta_L)] \\ &= \begin{bmatrix} 1 & 1 & \cdots & 1 \\ e^{-j(2\pi d/\lambda)\sin\theta_1} & e^{-j(2\pi d/\lambda)\sin\theta_2} & \ldots & e^{-j(2\pi d/\lambda)\sin\theta_L} \\ e^{-j2(2\pi d/\lambda)\sin\theta_1} & e^{-j2(2\pi d/\lambda)\sin\theta_2} & \ldots & e^{-j2(2\pi d/\lambda)\sin\theta_L} \\ \vdots & \vdots & \cdots & \vdots \\ e^{-j(M-1)(2\pi d/\lambda)\sin\theta_1} & e^{-j(M-1)(2\pi d/\lambda)\sin\theta_2} & \ldots & e^{-j(M-1)(2\pi d/\lambda)\sin\theta_L} \end{bmatrix} \end{aligned} \tag{2.13}$$

where

$$\mathbf{a}(\theta_l) = \begin{bmatrix} 1 \\ e^{-j(2\pi d/\lambda)\sin\theta_l} \\ e^{-j2(2\pi d/\lambda)\sin\theta_l} \\ \cdots \\ e^{-j(M-1)(2\pi d/\lambda)\sin\theta_l} \end{bmatrix} \tag{2.14}$$

for $l = 1, \ldots, L$. As it can be observed the obtained array manifold matrix for the ULAs exhibits the Vandermonde structure [21]. The popularity of the ULAs is due this structural feature which has been exploited to develop search-free, low computational complexity DOA estimation algorithms [7], [11], [19], [77], [88].

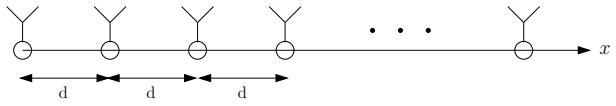

Figure 2.6: Uniform linear array (ULA) model

The covariance matrix of the array output signal for all the five scenarios is defined as

$$\begin{aligned}\mathbf{R} &\triangleq \mathrm{E}\{\mathbf{z}(t)\mathbf{z}^H(t)\} \\ &= \mathbf{A}(\boldsymbol{\mu},\boldsymbol{\Psi})\mathrm{E}\{\mathbf{s}(t)\mathbf{s}^H(t)\}\mathbf{A}^H(\boldsymbol{\mu},\boldsymbol{\Psi}) + \mathrm{E}\{\mathbf{n}(t)\mathbf{n}^H(t)\} \\ &= \mathbf{A}(\boldsymbol{\mu},\boldsymbol{\Psi})\mathbf{R}_{\mathrm{s}}\mathbf{A}^H(\boldsymbol{\mu},\boldsymbol{\Psi}) + \sigma^2\mathbf{I} \qquad (2.15)\end{aligned}$$

in which it is assumed that the noise and the signals are independent and have zero-mean. Moreover, in (2.15), we define the $L \times L$ signal covariance matrix as

$$\mathbf{R}_{\mathrm{s}} \triangleq \mathrm{E}\{\mathbf{s}(t)\mathbf{s}^H(t)\} \qquad (2.16)$$

where besides Assumption 2, the following assumption is also taken into account:

Assumption 5: The matrix $\mathbf{R}_{\mathrm{s}}$ is of full-rank, i.e., $\mathrm{rank}\{\mathbf{R}_{\mathrm{S}}\} = L$.

The diagonal entries of $\mathbf{R}_{\mathrm{s}}$ indicate the power of the signals and are denoted by positive parameters $r_{s,1}, r_{s,2}, \ldots, r_{s,L}$. From Assumptions 4 and 5, we can write

$$\mathbf{R}_{\mathrm{s}} = \mathrm{diag}\{r_{s,1}, r_{s,2}, \ldots, r_{s,L}\}. \qquad (2.17)$$

Therefore, since from Assumption 4 the $M \times L$ array manifold matrix $\mathbf{A}(\boldsymbol{\mu},\boldsymbol{\Psi})$ is of full-column rank, the $M \times M$ matrix $\mathbf{A}(\boldsymbol{\mu},\boldsymbol{\Psi})\mathbf{R}_{\mathrm{s}}\mathbf{A}^H(\boldsymbol{\mu},\boldsymbol{\Psi})$ is of rank L ($< M$), and, therefore, rank-deficient. This low-rank property can be exploited in the presence of the sensor noise to identify two complementary subspaces, i.e., the signal- and the noise subspace, respectively. These two subspaces are at the foundation of subspace-based estimation methods. From (2.15) it can be observed that $\mathbf{R}$ has $M - L$ eigenvalues equal to the noise power σ^2 and L eigenvalues greater than σ^2. In other words, if we define λ_m as the m-th largest eigenvalue

of $\mathbf{R}$ then

$$\lambda_1 \geq \lambda_2 \geq \cdots \geq \lambda_L > \lambda_{L+1} = \cdots = \lambda_M = \sigma^2. \tag{2.18}$$

Hence the L largest eigenvalues of $\mathbf{R}$ are called signal eigenvalues and the $M - L$ smallest eigenvalues are called noise eigenvalues. After performing the eigen-decomposition on the array output covariance matrix $\mathbf{R}$ we obtain

$$\begin{aligned} \mathbf{R} &= \sum_{m=1}^{M} \lambda_m \mathbf{u}_m \mathbf{u}_m^H \\ &= \mathbf{U}_\mathrm{S} \mathbf{\Lambda}_\mathrm{S} \mathbf{U}_\mathrm{S}^H + \mathbf{U}_\mathrm{N} \mathbf{\Lambda}_\mathrm{N} \mathbf{U}_\mathrm{N}^H \\ &= \mathbf{U}_\mathrm{S} \mathbf{\Lambda}_\mathrm{S} \mathbf{U}_\mathrm{S}^H + \sigma^2 \mathbf{U}_\mathrm{N} \mathbf{U}_\mathrm{N}^H \end{aligned} \tag{2.19}$$

where $\mathbf{\Lambda}_\mathrm{S}$ and $\mathbf{\Lambda}_\mathrm{N}$ denote, respectively, the $L \times L$ and the $(M - L) \times (M - L)$ diagonal matrices containing the signal and the noise eigenvalues, i.e.,

$$\mathbf{\Lambda}_\mathrm{S} = \mathrm{diag}\{\lambda_1, \lambda_2, \ldots, \lambda_L\} \tag{2.20}$$

$$\mathbf{\Lambda}_\mathrm{N} = \sigma^2 \mathbf{I}. \tag{2.21}$$

Moreover, the $M \times L$ signal- and the $M \times (M - L)$ noise eigenvector matrices $\mathbf{U}_\mathrm{S}$ and $\mathbf{U}_\mathrm{N}$, respectively, contain the eigenvectors corresponding to the signal and to the noise eigenvalues. We will refer to the matrices $\mathbf{U}_\mathrm{S}$ and $\mathbf{U}_\mathrm{N}$ as signal subspace matrix and noise subspace matrix, respectively, for the reasons that become apparent later on.

It is well-known [77] that considering Assumptions 4 and 5, both the array manifold matrix and the signal-eigenvector matrix span the same subspace, i.e.,

$$\mathcal{R}\{\mathbf{U}_\mathrm{S}\} = \mathcal{R}\{\mathbf{A}\} \tag{2.22}$$

where $\mathcal{R}\{\cdot\}$ denotes the range-space of a matrix and the dependency of $\mathbf{A}(\boldsymbol{\mu}, \mathbf{\Psi})$ on $\boldsymbol{\mu}$ and $\mathbf{\Psi}$ is dropped for the sake of notational brevity. In other words, there exists an $L \times L$ full-rank matrix $\mathbf{P}$, the so-called mixing matrix, such that

$$\mathbf{A} = \mathbf{U}_\mathrm{S} \mathbf{P}. \tag{2.23}$$

Similarly, since $\mathbf{P}$ is nonsingular, hence invertible, we can also write

$$\begin{aligned} \mathbf{U}_{\mathrm{S}} &= \mathbf{A}\mathbf{P}^{-1} \\ &= \mathbf{A}\mathbf{P}' \end{aligned} \tag{2.24}$$

where for the simplicity in the notations in the later sections we define

$$\mathbf{P}' \triangleq \mathbf{P}^{-1}. \tag{2.25}$$

The true array covariance matrix is generally unknown in practice, therefore, its finite sample estimate

$$\hat{\mathbf{R}} = \frac{1}{N}\sum_{t=1}^{N} \mathbf{z}(t)\mathbf{z}^{H}(t), \tag{2.26}$$

which is the ML estimate of the $\mathbf{R}$ in (2.15) in the case of Gaussian noise, is used. The following assumption is required so that the rank of the obtained sample covariance matrix $\hat{\mathbf{R}}$ (in the presence of the noise) becomes equal to M.

Assumption 6: The number of snapshots is larger than the number of sensors, i.e., $N \geq M$.

This assumption is a necessary condition for the subsequent construction of the signal and noise subspaces for the subspace-based methods which are discussed in following chapters. It is worth mentioning that for the ULAs, in the case of low-rank sample covariance matrix, e.g., when the sources are fully-correlated, there are forward-backward averaging (FB) and spatial smoothing techniques [41], [82] to artificially increase the number of snapshots to obtain sample covariance matrix of higher rank.

Let $\hat{\lambda}_m$, for $m = 1, \ldots, M$, denotes the m-th largest eigenvalue of the sample covariance matrix $\hat{\mathbf{R}}$ in (2.26) such that

$$\hat{\lambda}_1 \geq \hat{\lambda}_2 \geq \cdots \geq \hat{\lambda}_L \geq \hat{\lambda}_{L+1} \geq \cdots \geq \hat{\lambda}_M. \tag{2.27}$$

Similar to the true covariance matrix $\mathbf{R}$, the eigenvalues can be partitioned into the signal eigenvalues containing the L largest eigenvalues, i.e., $\hat{\lambda}_1, \ldots, \hat{\lambda}_L$, and the noise eigenvalues

consisting of the $M - L$ smallest eigenvalues, i.e., $\hat{\lambda}_{L+1}, \ldots, \hat{\lambda}_M$. Similarly, the eigen-decomposition of the sample covariance matrix $\hat{\mathbf{R}}$ can be written as

$$\begin{aligned} \hat{\mathbf{R}} &= \sum_{m=1}^{M} \hat{\lambda}_m \hat{\mathbf{u}}_m \hat{\mathbf{u}}_m^H \\ &= \hat{\mathbf{U}}_{\mathrm{S}} \hat{\mathbf{\Lambda}}_{\mathrm{S}} \hat{\mathbf{U}}_{\mathrm{S}}^H + \hat{\mathbf{U}}_{\mathrm{N}} \hat{\mathbf{\Lambda}}_{\mathrm{N}} \hat{\mathbf{U}}_{\mathrm{N}}^H \end{aligned} \tag{2.28}$$

where $\hat{\mathbf{\Lambda}}_{\mathrm{S}}$ and $\hat{\mathbf{\Lambda}}_{\mathrm{N}}$ denote, respectively, the $L \times L$ and the $(M - L) \times (M - L)$ diagonal matrices containing the signal and the noise eigenvalues, i.e.,

$$\hat{\mathbf{\Lambda}}_{\mathrm{S}} = \mathrm{diag}\{\hat{\lambda}_1, \hat{\lambda}_2, \ldots, \hat{\lambda}_L\} \tag{2.29}$$

$$\hat{\mathbf{\Lambda}}_{\mathrm{N}} = \mathrm{diag}\{\hat{\lambda}_{L+1}, \hat{\lambda}_{L+2}, \ldots, \hat{\lambda}_M\}. \tag{2.30}$$

The matrices $\hat{\mathbf{U}}_{\mathrm{S}}$ and $\hat{\mathbf{U}}_{\mathrm{N}}$ are, respectively, the estimates of the $M \times L$ signal- and the $M \times (M - L)$ noise eigenvector matrices containing of the eigenvectors corresponding to the signal and to the noise eigenvalues.

Chapter 3

Previous Works and the State-of-the-Art

3.1 Introduction

In this chapter, we introduce some existing state-of-the-art DOA estimation and HR methods. In the following chapters we compare the estimation performance of our proposed methods to the performance of the methods described in the present chapter. First, we present the well-known multiple signal classification (MUSIC) method [78] and we discuss its drawbacks. Then, the weighted-MUSIC method, which is the generalization of the MUSIC method, and the root-MUSIC method [7] are introduced. The MUSIC method and its variants are only applicable to fully-calibrated arrays. For partly-calibrated arrays (PCAs), we present other DOA estimation techniques such as the rank-reduction (RARE) method [66], [68], [80], the multiple invariance MUSIC (MI-MUSIC) method [92], the estimation of signal parameters via rotational invariance techniques (ESPRIT) [77], and the generalized ESPRIT (GESPRIT) method [16], [96]. At the end, for the harmonic retrieval problem in the incomplete sample case (discussed in Chapter 6), we introduce the latest method of the missing data iterative adaptive approach (MIAA) [89]. We remark that the DOA

estimation methods can also be applied to estimate the signal harmonics.

3.2 Multiple Signal Classification (MUSIC) and Its Variants

3.2.1 MUSIC

It can be shown [78] that each column of the manifold matrix in (2.11) must be orthogonal to the noise subspace matrix $\mathbf{U}_{\mathrm{N}}$ obtained from (2.19), hence

$$\mathbf{U}_{\mathrm{N}}^{H}\mathbf{a}(\theta_l) = \mathbf{0} \tag{3.1}$$

for $\theta_l = \theta_1, \ldots, \theta_L$ or equivalently

$$\mathbf{a}^{H}(\theta_l)\mathbf{U}_{\mathrm{N}}\mathbf{U}_{\mathrm{N}}^{H}\mathbf{a}(\theta_l) = 0 \tag{3.2}$$

where $\mathbf{a}(\theta_l)$ is defined in (2.12). This is the core idea of the MUSIC estimation method. In practice, in order to estimate the DOAs, the estimate of the noise subspace matrix $\hat{\mathbf{U}}_{\mathrm{N}}$ obtained from the sample covariance matrix $\hat{\mathbf{R}}$ in (2.28) must be used. Therefore, the following "spectral" function is proposed in [78]

$$\begin{aligned} f_{\mathrm{MUSIC}}(\theta) &= \frac{1}{\|\hat{\mathbf{U}}_{\mathrm{N}}^{H}\mathbf{a}(\theta)\|^2} \\ &= \frac{1}{\mathbf{a}^{H}(\theta)\hat{\mathbf{U}}_{\mathrm{N}}\hat{\mathbf{U}}_{\mathrm{N}}^{H}\mathbf{a}(\theta)}. \end{aligned} \tag{3.3}$$

The estimated DOAs $\hat{\theta}_1, \ldots, \hat{\theta}_L$ are then obtained as the angles θ corresponding to the L largest maxima of $f_{\mathrm{MUSIC}}(\theta)$ in (3.3). The denominator of the MUSIC function in (3.3) can be interpreted as the measure of the projection of the array manifold vector onto the noise subspace $\hat{\mathbf{U}}_{\mathrm{N}}$ which ideally for the true DOAs is zero. Then, the estimated DOAs are the ones that minimize this projection. To find the DOAs, a scan over the entire field-of-view (FOV) is required and the function $f_{\mathrm{MUSIC}}(\theta)$ in (3.3) needs to be evaluated for each θ.

The accuracy of the estimates obtained from the MUSIC spectral function in (3.3) depends on many factors such as:

- the step size ε with which the FOV is being scanned

- SNR
- the number of snapshots N
- the accuracy of the available array manifold vectors $\mathbf{a}(\theta)$, itself dependent on factors such as the precision of the array and sensor calibration or the exact sensor locations

Some explanation regarding these factors are in order. In order to evaluate the MUSIC function in (3.3), a limited number of scanning points should be selected, hence, a step size should be defined. If the step size is chosen small, then not only the estimation accuracy will increase but also the computational cost of the method. Therefore, some compromise must be made to have a reasonable step size (not too small) and at the same time a reasonable estimation accuracy. The effects of the value of SNR and the number of snapshots on DOA estimation of the MUSIC method will be examined in more detail later in Chapter 4. Moreover, to reduce the negative effects of these factors on the DOA estimation performance, some methods which are capable of identifying the erroneous estimates will be presented in Chapter 4. The MUSIC algorithm is known to be very sensitive to uncertainties and errors in the array manifold vectors [14], [81], [90]. This makes the exact calibration of the sensor array crucial for DOA estimation. The calibration issue in the arrays, especially large sparse arrays will be addressed in Chapter 5 and some novel techniques to simultaneously estimate the DOAs and to calibrate the sensor array will also be proposed.

3.2.2 Weighted-MUSIC

As it can be observed, in the MUSIC spectral function of (3.3), all the noise eigenvectors are treated equally. The MUSIC method can be extended to include a specific weighting matrix for controlling the effect of each noise eigenvector on the estimates. A proper choice of the weighting matrix will be particularly useful to improve the performance of the estimators in difficult situations such as low number of snapshots and low SNR to overcome some of the shortcomings of the MUSIC method [74], [98]. Toward this end, the following spectrum

function is defined to take into account the different effects of the noise eigenvectors

$$f_{\text{WMUSIC}}(\theta) = \frac{1}{\mathbf{a}^H(\theta)\hat{\mathbf{U}}_{\text{N}}\mathbf{W}\hat{\mathbf{U}}_{\text{N}}^H\mathbf{a}(\theta)}. \tag{3.4}$$

It is clear that the conventional MUSIC function in (3.3) is a special case of the weighted-MUSIC function in (3.4) with $\mathbf{W} = \mathbf{I}$. It should be remarked that the weighted-MUSIC function in (3.4) plays an important role in constructing the "estimator bank" in Section 4.2.

A useful choice of the weighting matrix is

$$\mathbf{W} = \hat{\mathbf{U}}_{\text{N}}^H\mathbf{e}_1\mathbf{e}_1^T\hat{\mathbf{U}}_{\text{N}} \tag{3.5}$$

where $\mathbf{e}_1$ is the first column of the $M \times M$ identity matrix. The choice of $\mathbf{W}$ in (3.5) coincides with the well-known Min-Norm method [31], [32], [74]. In the Min-Norm method, a non-zero vector with minimum norm in the noise subspace, i.e., a linear combination of the noise eigenvectors, is obtained. Then, the orthogonality of this minimum length vector and the array manifold vector is measured similar to the one used for the MUSIC method in (3.3) for the angles in the FOV. The Min-Norm method is known to yield an improved resolution capability of distinguishing two close sources, as compared to the MUSIC method in the ULAs [98].

3.2.3 Root-MUSIC

The root-MUSIC DOA estimation method [7] exploits the Vandermonde structure of the array manifold vector in the ULAs in (2.14) to estimate the DOAs through a search-free algorithm based on polynomial rooting. Defining

$$\varphi \triangleq e^{-j(2\pi d/\lambda)\sin\theta}, \tag{3.6}$$

the parametric array manifold vector $\mathbf{a}(\theta)$ becomes

$$\mathbf{a}(\varphi) = \left[1, \varphi, \varphi^2, \cdots, \varphi^{M-1}\right]^T. \tag{3.7}$$

Furthermore, it is simple to show that

$$\mathbf{a}^H(\varphi) = \mathbf{a}^T(1/\varphi). \tag{3.8}$$

Then, the MUSIC criterion in (3.2) transforms into

$$\mathbf{a}^T(1/\varphi_l)\mathbf{U}_\mathrm{N}\mathbf{U}_\mathrm{N}^H\mathbf{a}(\varphi_l) = 0 \tag{3.9}$$

where

$$\varphi_l = e^{-j(2\pi d/\lambda)\sin\theta_l} \tag{3.10}$$

for $l = 1, \ldots, L$. Let us define

$$f_{\mathrm{r-ideal}}(\varphi) \triangleq \mathbf{a}^T(1/\varphi)\mathbf{U}_\mathrm{N}\mathbf{U}_\mathrm{N}^H\mathbf{a}(\varphi). \tag{3.11}$$

From (3.8), it can be seen that if φ is a root of the polynomial in (3.11), then its conjugate reciprocate $1/\varphi^*$ is also a root. Therefore, from (3.9), the polynomial in (3.11), which is of degree $2M-2$, has $2M-2$ roots with $M-1$ roots on/inside the unit-circle and their $M-1$ conjugate reciprocate pairs on/outside the unit-circle. In practice, the estimate of the noise subspace matrix, i.e., $\hat{\mathbf{U}}_\mathrm{N}$ in (2.28), from the sample covariance matrix $\hat{\mathbf{R}}$ in (2.26) is used and the following polynomial is obtained

$$f_{\mathrm{root-MUSIC}}(\varphi) = \mathbf{a}^T(1/\varphi)\hat{\mathbf{U}}_\mathrm{N}\hat{\mathbf{U}}_\mathrm{N}^H\mathbf{a}(\varphi). \tag{3.12}$$

To estimate the DOAs, the L complex roots of $f_{\mathrm{root-MUSIC}}(\varphi)$, namely $\hat{\varphi}_1, \ldots, \hat{\varphi}_L$, closest to the unit-circle and inside it should be selected and the estimated DOAs can be computed for $l = 1, \ldots, L$ from

$$\hat{\theta}_l = \sin^{-1}\left\{\frac{-\lambda}{2\pi d}\measuredangle(\hat{\varphi}_l)\right\} \tag{3.13}$$

where $\measuredangle(\cdot)$ denotes the phase of a complex variable. It has been demonstrated [85], [86] that both MUSIC and root-MUSIC have the same asymptotic performances. From (3.13), one can observe that the estimated DOA $\hat{\theta}_l$ (for $l = 1, \ldots, L$) depends only on the phase of the root $\hat{\varphi}_l$ of the root-MUSIC polynomial in (3.12) and not on the magnitude of $\hat{\varphi}_l$. Hence, any changes in the magnitude has no effect on the estimated DOAs and the root-MUSIC method

is robust to the radial errors of the estimated roots [98]. Because of this property, the root-MUSIC method enjoys superior performance in comparison to the MUSIC method in low SNR and low number of snapshots, although the root-MUSIC method is only applicable to the ULAs and also to the uniform circular arrays (UCAs) [45], and not to any arbitrary array geometry (unlike the MUSIC method). However, there are methods, such as array interpolation [15] and beamspace methods [109], in which the array manifold of an arbitrary array geometry can be approximately transformed into the array manifold of a virtual ULA so that the root-MUSIC method can be implemented.

3.3 Rank-Reduction (RARE) Method

The RARE technique has been developed in [66], [68], and [80] for the case of sensor arrays consisting of K fully-calibrated subarrays (with the total number of sensors equal to M) without any calibration information in-between subarrays (see Fig. 2.2). This case corresponds to Scenario II or APCA model of Section 5.2. For this class of arrays, the columns of the array manifold matrix can be described as

$$\mathbf{a}(\theta_l, \mathbf{\Psi}) = \mathbf{K}_{\mathrm{R}}(\theta_l)\boldsymbol{\phi}_{\mathrm{R}}(\theta_l, \mathbf{\Psi}) \tag{3.14}$$

where the $M \times K$ matrix $\mathbf{K}_{\mathrm{R}}(\theta_l)$ is defined as

$$\mathbf{K}_{\mathrm{R}}(\theta_l) \triangleq \begin{bmatrix} \mathbf{a}_1(\theta_l) & \mathbf{0} & \cdots & \mathbf{0} \\ \mathbf{0} & \mathbf{a}_2(\theta_l) & \cdots & \mathbf{0} \\ \vdots & \vdots & \ddots & \vdots \\ \mathbf{0} & \mathbf{0} & \cdots & \mathbf{a}_K(\theta_l) \end{bmatrix} \tag{3.15}$$

for $\theta_l = \theta_1, \ldots, \theta_L$, $\mathbf{a}_k(\theta_l)$ for $k = 1, \ldots, K$ is the l-th column of the manifold matrix for the k-th subarray such that the first sensor of that subarray is considered as the reference sensor of the corresponding subarray. The $K \times 1$ vector $\boldsymbol{\phi}_{\mathrm{R}}(\theta_l, \mathbf{\Psi})$ contains the phase information resulting from the uncalibrated or unknown part of the array such as intersubarray displacement vectors $\boldsymbol{\eta}_k = [\alpha_k, \beta_k]^T$ for $k = 2, \ldots, K$ such that

$$\boldsymbol{\phi}_{\mathrm{R}}(\theta_l, \mathbf{\Psi}) = [1, \phi_2(\theta), \ldots, \phi_K(\theta)]^T \tag{3.16}$$

where

$$\phi_k(\theta_l) \triangleq e^{-j(2\pi/\lambda)(\alpha_k \sin\theta_l + \beta_k \cos\theta_l)} \tag{3.17}$$

for $k = 2, \ldots, K$ and $l = 1, \ldots, L$.

Note that, $\mathbf{K}_{\mathrm{R}}(\theta)$ depends only on the DOAs and the known or calibrated part of the array. The MUSIC criterion in Section 3.2.1, which exploits the property of the orthogonality of the noise subspace matrix and the array manifold matrix (3.2), can then be used

$$\begin{aligned} \mathbf{a}^H(\theta_l, \boldsymbol{\Psi})\mathbf{U}_{\mathrm{N}}\mathbf{U}_{\mathrm{N}}^H\mathbf{a}(\theta_l, \boldsymbol{\Psi}) &= \\ \boldsymbol{\phi}_{\mathrm{R}}^H(\theta_l, \boldsymbol{\Psi})\mathbf{K}_{\mathrm{R}}^H(\theta_l)\mathbf{U}_{\mathrm{N}}\mathbf{U}_{\mathrm{N}}^H\mathbf{K}_{\mathrm{R}}(\theta_l)\boldsymbol{\phi}_{\mathrm{R}}(\theta_l, \boldsymbol{\Psi}) &= \\ \boldsymbol{\phi}_{\mathrm{R}}^H(\theta_l, \boldsymbol{\Psi})\mathbf{F}_{\mathrm{RARE}}(\theta_l)\boldsymbol{\phi}_{\mathrm{R}}(\theta_l, \boldsymbol{\Psi}) &= 0 \end{aligned} \tag{3.18}$$

where

$$\mathbf{F}_{\mathrm{RARE}}(\theta_l) \triangleq \mathbf{K}_{\mathrm{R}}^H(\theta_l)\mathbf{U}_{\mathrm{N}}\mathbf{U}_{\mathrm{N}}^H\mathbf{K}_{\mathrm{R}}(\theta_l). \tag{3.19}$$

The idea in the RARE algorithm is based on the observation that if $K \leq M - L$, then $\mathrm{rank}\{\mathbf{U}_{\mathrm{N}}\} \geq K$. In this case, equation (3.18) holds true only when the $K \times K$ matrix $\mathbf{F}_{\mathrm{RARE}}(\theta_l)$ drops rank, i.e., when $\mathrm{rank}\{\mathbf{F}_{\mathrm{RARE}}(\theta_l)\} < K$. In the finite sample case, however, the $K \times K$ matrix $\hat{\mathbf{F}}_{\mathrm{RARE}}(\theta)$

$$\hat{\mathbf{F}}_{\mathrm{RARE}}(\theta) \triangleq \mathbf{K}_{\mathrm{R}}^H(\theta)\hat{\mathbf{U}}_{\mathrm{N}}\hat{\mathbf{U}}_{\mathrm{N}}^H\mathbf{K}_{\mathrm{R}}(\theta) \tag{3.20}$$

is used instead. Then, in order to estimate the DOAs, the L maxima of the following function in the entire FOV must be found

$$f_{\mathrm{RARE}}(\theta) = \frac{1}{|\det\{\hat{\mathbf{F}}_{\mathrm{RARE}}(\theta)\}|}. \tag{3.21}$$

It should be remarked that the spectral-RARE function can be expressed in other ways as well, e.g., by using the minimum eigenvalue of $\hat{\mathbf{F}}_{\mathrm{RARE}}(\theta)$ in (3.21) instead of its determinant which yields approximately the same DOA estimation performance [80]. For specific array geometries, where the PCA is composed of identically oriented uniform subarrays, a search-free RARE algorithm, known as root-RARE, can be applied [66].

3.4 Multiple Invariance MUSIC (MI-MUSIC)

In [92], several DOA estimation techniques for arrays composed of multiple identical subarrays (possibly with overlapping sensors) have been developed which corresponds to Scenario IV, i.e., PCAMIS geometry, in Section 5.3 (see Fig. 2.3). However, some of those methods are only applicable to a specific PCAMIS structures, for which search-free implementations exist. Since those very special array structures are not considered in this thesis, we only present here the method, namely MI-MUSIC, which is a search-based method and can be applied to the considered more general subarray model. In [92], using a subspace-fitting method [100] and assuming as in our model in Section 5.3 that there are no overlapping sensors between the subarrays, the authors in [92] developed a MUSIC function (3.2) such that

$$f_{\text{MI-MUSIC1}}(\theta, \boldsymbol{\Psi}) = \big(\boldsymbol{\Phi}_{\text{MI-MUSIC}}(\theta) \otimes \mathbf{a}_1(\theta, \boldsymbol{\Psi})\big)^H \boldsymbol{\Pi}^{\perp}_{\hat{\mathbf{E}}_{\text{s}}} \big(\boldsymbol{\Phi}_{\text{MI-MUSIC}}(\theta) \otimes \mathbf{a}_1(\theta, \boldsymbol{\Psi})\big) \quad (3.22)$$

where

$$\boldsymbol{\Phi}_{\text{MI-MUSIC}}(\theta) \triangleq \text{diag}\{\phi_2(\theta), \ldots, \phi_K(\theta)\}, \quad (3.23)$$

$\phi_k(\theta)$ is defined in (3.17), and

$$\boldsymbol{\Pi}^{\perp}_{\hat{\mathbf{E}}_{\text{s}}} = \mathbf{I} - \hat{\mathbf{E}}_{\text{s}}(\hat{\mathbf{E}}_{\text{s}}^H \hat{\mathbf{E}}_{\text{s}})^{-1} \hat{\mathbf{E}}_{\text{s}}^H. \quad (3.24)$$

Therefore, considering the unit-norm constraint of the manifold vectors, the DOAs can be shown to be estimated from the L minima of

$$f_{\text{MI-MUSIC2}}(\theta) = \mathcal{L}_{\min}\{(\boldsymbol{\Phi}_{\text{MI-MUSIC}}(\theta) \otimes \mathbf{I})^H \boldsymbol{\Pi}^{\perp}_{\hat{\mathbf{E}}_{\text{s}}} (\boldsymbol{\Phi}_{\text{MI-MUSIC}}(\theta) \otimes \mathbf{I})\}. \quad (3.25)$$

3.5 Estimation of Signal Parameters via Rotational Invariance Techniques (ESPRIT)

The ESPRIT technique is a search-free DOA estimation method applicable to arrays composed of two identical, possibly unknown, subarrays composed of M_1 sensors with known

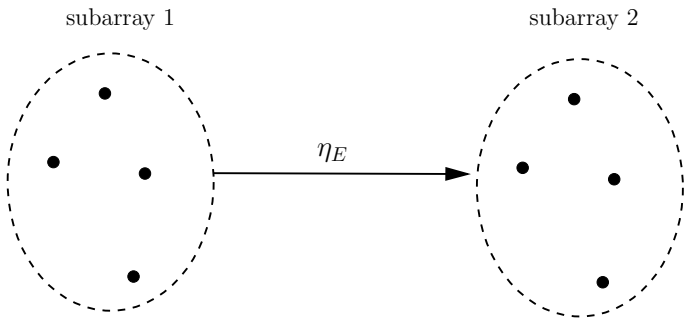

Figure 3.1: ESPRIT geometry: two arbitrary subarrays with known intersubarray displacement vector

intersubarray displacement in the direction of x-axis η_E as shown in Fig. 3.1. The array geometry in ESPRIT technique can be regarded as either a special case of Scenario III in Fig. 2.3, where all the displacements are identical, or a special case of Scenario IV in Fig. 2.4 where the number of subarrays are limited to two subarrays.

Let us partition the signal eigenvector matrix $\mathbf{U}_{\mathrm{S}}$ such that

$$\mathbf{U}_{\mathrm{S}} = \begin{bmatrix} \mathbf{U}_{\mathrm{S},1} \\ \mathbf{U}_{\mathrm{S},2} \end{bmatrix}. \tag{3.26}$$

Following the reasoning in [77], it can be said that the rank of the $M_1 \times 2L$ matrix

$$\mathbf{U}_{\mathrm{S},1,2} \triangleq [\mathbf{U}_{\mathrm{S},1}, \mathbf{U}_{\mathrm{S},2}] \tag{3.27}$$

is L and that both $\mathbf{U}_{\mathrm{S},1}$ and $\mathbf{U}_{\mathrm{S},2}$ span the same subspace spanned by the manifold matrix of the first subarray. Hence, there exists a $2L \times L$ matrix

$$\mathbf{F}_{\mathrm{N}} = \begin{bmatrix} \mathbf{F}_{\mathrm{N},1} \\ \mathbf{F}_{\mathrm{N},2} \end{bmatrix} \tag{3.28}$$

which spans the null-space of $\mathbf{U}_{\mathrm{S},1,2}$, i.e., $\mathbf{U}_{\mathrm{S},1,2}\mathbf{F}_{\mathrm{N}} = \mathbf{0}$. It is shown in [77] that the eigenvalues of the matrix $-\mathbf{F}_{\mathrm{N},1}\mathbf{F}_{\mathrm{N},2}^{-1}$ contain the information about the DOAs such that

$$\hat{\theta}_l = \sin^{-1}\left\{\frac{-\lambda}{2\pi\eta_E}\measuredangle(\mathcal{L}^{(l)}\{-\mathbf{F}_{\mathrm{N},1}\mathbf{F}_{\mathrm{N},2}^{-1}\})\right\} \tag{3.29}$$

where $\mathcal{L}^{(l)}\{\cdot\}$ denotes the l-th eigenvalue of a matrix for $l = 1, \ldots, L$.

The ESPRIT algorithm can also be used as a search-free algorithm in the fully-calibrated ULAs where the distance between two adjacent sensors is d. Let us define the two matrices $\overline{\mathbf{A}}$ and $\underline{\mathbf{A}}$ as the array manifold matrix with the first and the last row removed, respectively. Then, by defining $\overline{\mathbf{U}}_{\mathrm{S}}$ and $\underline{\mathbf{U}}_{\mathrm{S}}$ as the signal eigenvector matrix $\mathbf{U}_{\mathrm{S}}$ with the first and the last row removed, respectively, it can be shown that the signal DOAs can be estimated from the eigenvalues of the matrix $\overline{\mathbf{U}}_{\mathrm{S}}^{\dagger}\underline{\mathbf{U}}_{\mathrm{S}}$ such that

$$\hat{\theta}_l = \sin^{-1}\left\{\frac{-\lambda}{2\pi d}\measuredangle(\mathcal{L}^{(l)}\{\overline{\mathbf{U}}_{\mathrm{S}}^{\dagger}\underline{\mathbf{U}}_{\mathrm{S}}\})\right\} \tag{3.30}$$

for $l = 1, \ldots, L$.

3.6 Generalized ESPRIT (GESPRIT)

The generalized ESPRIT approach of [16] has been originally formulated for the array model composed of two M_1-sensor subarrays with pairwise sensor calibration such that the displacement vectors $\tilde{\boldsymbol{\eta}}_m = [x_m - x_{m+M_1}, y_m - y_{m+M_1}]^T$ for $m = 1, \ldots, M_1$ between the m-th sensor in the first subarray and its corresponding sensor, i.e., the $(m + M_1)$-th sensor in the second subarray, is known. This corresponds to Scenario III, i.e., PWCA geometry (see Fig. 2.4). The array geometry and the signal model are discussed in detail in Section 5.4.

It is shown in [16] that if $L \leq M_1$, then for any $M_1 \times L$ full-rank matrix $\mathbf{W}$, the matrix $\mathbf{W}^H\Big(\mathbf{U}_{\mathrm{S},2} - \boldsymbol{\Phi}_{\mathrm{p}}(\theta)\mathbf{U}_{\mathrm{S},1}\Big)$ drops rank where $\mathbf{U}_{\mathrm{S},1}$ and $\mathbf{U}_{\mathrm{S},2}$ are defined in (3.26) and the $M_1 \times M_1$ diagonal matrix $\boldsymbol{\Phi}_{\mathrm{p}}(\theta)$ contains the displacement-phase information between the sensor pairs and the M_1 diagonal entries are defined as

$$[\boldsymbol{\Phi}_{\mathrm{p}}(\theta)]_{(m,m)} \triangleq e^{-j\left((x_m - x_{m+M_1})\sin\theta + (y_m - y_{m+M_1})\cos\theta\right)} \tag{3.31}$$

for $m = 1, \ldots, M_1$. In [16], $\mathbf{W} = \mathbf{U}_{\mathrm{S},1}$ has been chosen. This choice leads to the following generalized ESPRIT spectrum [16]

$$f_{\mathrm{GES1}}(\theta) = \frac{1}{|\det\{\hat{\mathbf{U}}_{\mathrm{S},1}^H\hat{\mathbf{U}}_{\mathrm{S},2} - \hat{\mathbf{U}}_{\mathrm{S},1}^H\boldsymbol{\Phi}(\theta)\hat{\mathbf{U}}_{\mathrm{S},1}\}|} \tag{3.32}$$

where the signal DOAs are estimated from the L highest peaks of (3.32).

Another meaningful choice of $\mathbf{W}$ is $\mathbf{W} = \mathbf{U}_{\mathrm{S},2} - \mathbf{\Phi}_{\mathrm{p}}(\theta)\mathbf{U}_{\mathrm{S},1}$ [96]. Then, the GESPRIT spectral function becomes

$$f_{\mathrm{GES2}}(\theta) = \frac{1}{|\det\{\big(\mathbf{U}_{\mathrm{S},2} - \mathbf{\Phi}(\theta)\mathbf{U}_{\mathrm{S},1}\big)^H(\mathbf{U}_{\mathrm{S},2} - \mathbf{\Phi}(\theta)\mathbf{U}_{\mathrm{S},1}\big)\}|}. \tag{3.33}$$

The function in (3.33) is the one that we use for simulation comparisons in Section 5.5.

3.7 The Missing Data Iterative Adaptive Approach (MIAA)

In this section, we briefly introduce the latest method in HR problem for the incomplete sample case [89]. The missing data iterative adaptive approach (MIAA) can be applied to the missing samples at arbitrary positions of a uniform sampling grid. This method has been originally proposed to recover the missing samples (or data) based on the iterative adaptive approach (IAA) [107]. However, the search-based method of MIAA can also estimate the signal frequencies, therefore, it can be used in the undamped harmonic cases. However, at the cost of two-dimensional exhaustive search, it can also be applied to the damped harmonic cases. This method uses a single snapshot and as it is shown in Section 6.7, in order to resolve multiple sources with closely-separated generators, it requires large sample size. The MIAA can be modified so that it can also perform for the case where multiple snapshots are available similar to the IAA in [107]. Here, we present the modified algorithm of the MIAA for multiple snapshots without going into the details (for more details see [89] and [107]). Since it is irrelevant to the topic in this thesis, the sample recovery part of the MIAA is not mentioned.

Suppose that the number of search grid points in the frequency domain is N_g where the frequency parameter is defined as

$$\omega_g \triangleq 2\pi g/N_g \tag{3.34}$$

for $g = 1, \ldots, N_g$. Let $\bar{M}$ be the total number of available samples, $\mathbf{z}_a(n)$ denotes the vector containing the available samples in the presence of noise in the n-th snapshot for

Modified MIAA for Multiple Snapshots

Step 1: Set $\mathbf{R}_a = \mathbf{I}$.

Step 2: Compute the complex-valued amplitude for each frequency in the grid such that

$$\hat{s}(\omega_g, n) = \frac{\mathbf{h}_a^H(\omega_g)\mathbf{R}_a^{-1}\mathbf{z}_a(n)}{\mathbf{h}_a^H(\omega_g)\mathbf{R}_a^{-1}\mathbf{h}_a(\omega_g)} \tag{3.36}$$

for all the points in the search grid, i.e., for $g = 1, \ldots, N_g$ and for all the snapshots, i.e., for $n = 1, \ldots, N$.

Step 3: Calculate the average signal power over all the snapshots at each point on the grid

$$\hat{r}(\omega_g) = \frac{1}{N}\sum_{n=1}^{N} |\hat{s}(\omega_g, n)|^2. \tag{3.37}$$

Step 4: Obtain the covariance matrix for the available samples

$$\mathbf{R}_a = \sum_{g=1}^{N_g} \hat{r}(\omega_g)\mathbf{h}_a(\omega_g)\mathbf{h}_a^H(\omega_g). \tag{3.38}$$

Step 5: Start from Step 2 until convergence of $\sum_{g=1}^{N_g} \hat{r}(\omega_g)$.

Step 6: Estimate the frequencies $\hat{\omega}_1, \ldots, \hat{\omega}_L$ from the L maxima of $\hat{r}(\omega)$ for $\omega = \omega_1, \ldots, \omega_{N_g}$ and, consequently, μ_l for $l = 1, \ldots, L$ from

$$\hat{\mu}_l = e^{j\hat{\omega}_l}. \tag{3.39}$$

Table 3.1: Modified MIAA for multiple snapshots

$n = 1, \ldots, N$, and $\bar{v}_1, \bar{v}_2, \ldots, \bar{v}_{\bar{M}}$ be the positions where the samples are available. Defining

$$\mathbf{h}_a(\omega_g) \triangleq \begin{bmatrix} e^{j\omega_g \bar{v}_1} \\ e^{j\omega_g \bar{v}_2} \\ \vdots \\ e^{j\omega_g \bar{v}_{\bar{M}}} \end{bmatrix}, \tag{3.35}$$

the algorithm can be described as shown in Table 3.1.

Chapter 4

Threshold Performance Improvement in Fully-Calibrated Arrays

4.1 Introduction

Sensor array processing is a rather mature field of research and many techniques have been developed to fulfill the DOA estimation task. The stochastic maximum likelihood (ML) method is known to provide the best DOA estimation performance [9] in both asymptotic and non-asymptotic regions; an ideal property which its counterpart, deterministic ML, obviously lacks [86]. Nevertheless, this family of techniques are seldom applicable since the ML method contains a nonlinear optimization problem, hence a multi-dimensional search with often prohibitively high computational cost is required. The same drawback is of main concern in other similar techniques such as weighted subspace fitting method (WSF) [54]. Several papers, e.g. [11], [88] and [108], address this issue and have made attempts to lower the computational cost of stochastic ML by exploiting the array manifold structure in order to reap, although not entirely, its excellent performance property.

Another family of DOA estimation techniques is the eigen-structure-based methods also known as subspace-based methods which originated from early works as [70] and [78]. These methods are optimal for single source scenarios yet suboptimal in the case of multiple sources [108] in comparison with the stochastic ML and became widely popular mainly

because of their reduced computational complexity. MUSIC method (Subsection 3.2.1) [78] and Min-Norm method (Subsection 3.2.2) [31] utilize one dimensional search. Root-MUSIC method (Subsection 3.2.3) [7], and other subspace-based methods like ESPRIT (Section 3.5) [77] benefit from a search-free algorithm and use either rooting a polynomial or eigen-decomposition of a matrix to directly estimate the DOAs. In the case of moderate to high SNRs or adequately large number of snapshots, the performance of subspace-based techniques is close to the best achievable estimation error variance (a.k.a. Cramer-Rao lower bound or CRB for short).

However, it is a well-known fact that in the case of low SNRs or alternatively small number of snapshots, the performance becomes severely deteriorated as the SNR/number of snapshots goes below a certain level (referred to as performance threshold hereafter). This phenomena is referred to as the performance threshold effect. In other words, below a certain threshold of SNR/snapshots, the sources cannot be resolved by the estimator and severely erroneous estimates which are referred to as "outliers" are generated [3], [94]. Here, we define the resolution of an estimator as the estimator's ability to distinguish between two closely-spaced sources. The DOA estimation performance degradation is demonstrated in the performance figures (e.g., Fig. 4.5) by the distance of the estimation performance curve from the CRB in the low SNR or small number of snapshot regions. The performance threshold is strongly dependent on the scenario, i.e., the source parameters such as location and power, and the array parameters such as sensor locations and aperture size. The threshold effect is not limited to subspace-based methods; the optimal ML method suffers from a similar performance breakdown, too. However, the ML performance breakdown occurs in much lower SNR or smaller number of snapshot regions than in the MUSIC method [2], [29], [108].

To mitigate the degrading performance threshold issue and to overcome the gap between the ML performance threshold and the MUSIC performance threshold, many researchers have analyzed the problem [24], [29], [46], [94], [95]. The breakdown in subspace-based techniques has been related to the subspace swap phenomenon. This phenomenon occurs when, due to low SNR or snapshot size effects, the estimates of the noise eigenvalues $\lambda_{L+1} =$

$\lambda_{L+2} = \ldots = \lambda_M = \sigma^2$ become larger than the estimates of the signal subspace eigenvalues $\lambda_1 \geq \lambda_2 \geq \ldots \geq \lambda_L$ [94]. In other words, the subspace swap happens when some of the estimated signal eigenvectors are wrongly interpreted as part of the noise subspace [24]. However, recently it was shown that the performance breakdown can be caused by "*intersubspace leakage (rather than full subspace swap) whereby a small portion of the true signal eigenvector resides in the sample noise subspace (and vice-versa)*"[29].

To overcome the gap between the ML performance threshold and the MUSIC performance threshold, several methods have been proposed in [7], [35], [52], [73] and more recently in [2], [17] and [46]. One simple way to deal with this problem in subspace-based methods (compared to the ML method) is to increase the number of snapshots. However, this slows the system response time and moreover, it is not possible in applications involving short-lived signals. Therefore, we propose to use the estimator bank idea [17] along with the outlier detection and cure [1] and [2] to overcome, to a great extent, the mentioned performance breakdown. The idea developed in [17], [19], and [20] is to use a set of different parallel DOA estimates to form the so-called *estimator bank* and to choose only the "successful" estimates and to drop the outlying ones. How to detect these "successful" estimates among the estimates available in the estimator bank, is itself a challenging problem. In [17] a criteria for whether or not the estimation is successful, was implemented by using preliminary information about the angular sectors which can be determined with the help of a simple beamforming technique. Unfortunately, in the practical cases, the information about source angular sectors is not always available or may be imprecise. Another method was proposed in [19] and [87] where the sets of DOA estimated resulting from multiple parallel estimators were substituted into the likelihood function and then the set of estimates with the highest value of this function were selected as the final DOA estimates. As a result of this more practical approach, the threshold effect is reduced.

In the present chapter, after introducing the estimator bank concept, we propose the sphericity test and the likelihood ratio quality assessment [1], [2] to be used in the estimator bank. The objective is not only to detect the outlying estimates in the estimator bank, but also to correct the outliers at the output of each estimator. Then, to achieve a superior

threshold performance, two ways to combine the "cured" estimates are proposed which according to the computer simulations demonstrate substantial improvement in the threshold performance (see also [56] and [57]).

It shall be noted that for the DOA estimation methods presented in this chapter the complete knowledge of the array manifold matrix is necessary. Hence, the array must be fully-calibrated, i.e., Scenario I, is considered in this chapter.

4.2 Estimator Bank-Based Direction Finding

The idea behind the estimator bank-based direction finding is to construct a bank of Q different parallel estimators in order to generate Q different sets of estimates and then pick the non-outlying ones among them [17], [20]. These estimators display approximately identical asymptotic and threshold performance but with different spectral functions. All functions use the same data snapshots or equivalently, the same sample covariance matrix $\hat{\mathbf{R}}$ defined in (2.26). Feeding the matrix $\hat{\mathbf{R}}$ to these estimators, the estimator bank

$$\mathcal{B} \triangleq \{f^{(1)}(\theta), f^{(2)}(\theta), \ldots, f^{(Q)}(\theta)\} \tag{4.1}$$

is formed where $f^{(q)}(\theta)$ for $q = 1, \cdots, Q$ is the q-th estimator function. The estimator function considered in this chapter is the weighted-MUSIC spectral function in (3.4) discussed in Subsection 3.2.2. Applying different weighting matrices to the weighted-MUSIC function in (3.4) enables us to generate as many estimators as desired. As it has already been mentioned in Section 3.2, in order to achieve acceptable accuracy in the estimation, the one-dimensional search over the entire field-of-view (FOV) needs to be carried out over a fine angular grid. For the weighted-MUSIC function used in this section, the computational cost of the search can be reduced using a rank-one weighting matrix [17]

$$\mathbf{W} = \mathbf{w}\mathbf{w}^H. \tag{4.2}$$

Therefore, the spectral function can be expressed as

$$f_{\mathbf{w}}(\theta) = \frac{1}{|\mathbf{a}^H(\theta)\hat{\mathbf{U}}_{\mathrm{N}}\mathbf{w}|^2} \tag{4.3}$$

where the estimated noise subspace matrix $\hat{\mathbf{U}}_{\mathrm{N}}$ can be obtained from (2.28) and the array manifold vector $\mathbf{a}(\theta)$ is defined in (2.12). To assign a different weighting vector $\mathbf{w}^{(q)}$ to each estimator for $q = 1, \cdots, Q$, the sequence of Q zero-mean statistically independent complex weighting vectors $\mathbf{w}^{(q)}$ can be successively drawn from the complex Gaussian random generator [20]

$$\mathbf{w}^{(q)} \sim \mathcal{CN}(\mathbf{0}, \mathbf{I}) \tag{4.4}$$

so that for $i, k = 1, \ldots, Q$

$$\mathrm{E}\{\mathbf{w}^{(i)}\mathbf{w}^{(k)^H}\} = \delta_{i,k} \tag{4.5}$$

$$\mathrm{E}\{\mathbf{w}^{(i)}\mathbf{w}^{(k)^T}\} = 0 \tag{4.6}$$

where $\delta_{i,k}$ is the delta function. In this way, an arbitrary number of estimators can be generated each having the following different spectral function

$$f_{\mathbf{w}}^{(q)}(\theta) = \frac{1}{|\mathbf{a}^H(\theta)\hat{\mathbf{U}}_{\mathrm{N}}\mathbf{w}^{(q)}|^2}. \tag{4.7}$$

Consequently, each estimator in the estimator bank $\mathcal{B}$

$$\mathcal{B} = \{f_{\mathbf{w}}^{(1)}(\theta), f_{\mathbf{w}}^{(2)}(\theta), \ldots, f_{\mathbf{w}}^{(Q)}(\theta)\} \tag{4.8}$$

is based on a different spectral function (4.7), therefore generates different DOA estimates. In other words, with a single sample covariance matrix, different estimates are produced. To exploit the additional information hidden in the different estimates, the estimators are put into an estimation competition in which the unsuccessful estimators, and their corresponding sets of estimates, will be ignored, and only the successful estimators, and their corresponding sets of estimates, are taken into consideration for computing the final set of estimates.

It is worth mentioning that a full-rank random weighting matrix $\mathbf{W}$, instead of a random weighting vector, can also be used in the estimator functions, similar to the function in (3.4), at the cost of the increase in the computational complexity. The estimator function in (4.7) with random weighting vector can be interpreted as a function which computes the

orthogonality of the array manifold vector (for each point in the FOV) and a single random vector in the noise subspace.

As it has already been discussed earlier, the strong degradation of the DOA estimation is mainly caused by increased number of the erroneous estimates called the outliers below the performance threshold. In the spectral function, these outliers are characterized either by spurious peaks which are higher than some of the peaks corresponding to the true DOAs, or by merging one true peak into another. The removal of the outliers helps to improve the performance. Therefore, an estimate is called successful when it contains no outlier and an estimator is called successful when it generates such successful set of estimates.

Many methods have been proposed to formulate the test to identify the outlying estimates. To this end, in [17], the pre-estimation of the angular sectors where the sources are located, using conventional beamforming DOA estimation methods (i.e., Bartlett beamformer) [33], has been proposed. The rejection/approval rule for the estimates in this method was based on the number of peaks in the aforementioned angular sectors. Unfortunately, preliminary estimates of the angular sectors are not always available in practice. Moreover, in the case when the sources have significantly different powers, these pre-estimated sectors might be erroneous.

Another well-known approach to identify the outliers in the estimates obtained from the estimator bank is to substitute each set of the DOA estimates from each estimator into the likelihood function [24]

$$f_{\mathrm{ML}}(\boldsymbol{\theta}) = \mathrm{tr}\{\boldsymbol{\Pi}_{\mathbf{A}(\boldsymbol{\theta})}\hat{\mathbf{R}}\} \tag{4.9}$$

where

$$\boldsymbol{\Pi}_{\mathbf{A}(\boldsymbol{\theta})} = \mathbf{A}(\boldsymbol{\theta})\big(\mathbf{A}^H(\boldsymbol{\theta})\mathbf{A}(\boldsymbol{\theta})\big)^{-1}\mathbf{A}^H(\boldsymbol{\theta}) \tag{4.10}$$

always picking the set of estimates that yields the highest value of the function $f_{ML}(\boldsymbol{\theta})$ in (4.9) [19], [87].

A new competitive approach to detect outlying estimates in estimator banks is presented in the next section. The proposed method offers significant advantages as compared to the existing outlier detection techniques. In particular, no preliminary estimates of the source

angular sectors are required as in the approach of [17]. Also, the proposed method provides improved threshold performance as compared to the approach presented in [87]. Moreover, in contrast to the method of [19] and [87], our approach also provides useful information about the reliability of the set of DOA estimates. In other words, it enables us to determine whether the generated set of DOA estimates itself is likely to contain an outlier or not.

It is possible to move even one step further and perform an identification and cure (I & C) procedure [2] for each sets of the DOA estimates as discussed in Section 4.4. Then the Q sets of the cured estimates are combined to obtain the final set of estimates as discussed in Section 4.5.

4.3 Detecting Outlying Estimates Using Hypothesis Testing

The detection of the outlying estimates is achieved through hypothesis testing and in particular the sphericity test. In this section, two hypothesis testing methods are proposed for the sphericity test. The first is the widely used generalized likelihood ratio test (GLRT) [1], [48]. The second method is the less known locally most powerful test (LMPT) [27], [48]. Both of the proposed approaches, when applied to the DOA estimates, are based on the computation of, e.g., likelihood ratio, for the estimates obtained from weighted-MUSIC method using the sphericity test. The main concept of the outlier detection method is, first of all, to estimate the signal DOAs and the source and the noise powers, called the estimated parameter set, and then to compare an artificially reconstructed covariance matrix $\tilde{\mathbf{R}}$ to the sample covariance matrix $\hat{\mathbf{R}}$ in (2.26). The estimated parameter set is defined as

$$\boldsymbol{\rho} \triangleq \{\hat{\boldsymbol{\theta}}, \hat{\mathbf{r}}_s, \hat{\sigma^2}\} \tag{4.11}$$

where

$$\hat{\mathbf{r}}_s \triangleq [\hat{r}_{s,1}, \hat{r}_{s,2}, \ldots, \hat{r}_{s,L}] \tag{4.12}$$

is the signal power estimate vector, $\hat{r}_{s,l}$ denotes the estimated power of the l-th source,

$$\hat{\boldsymbol{\theta}} \triangleq \left[\hat{\theta}_1, \hat{\theta}_2, \ldots, \hat{\theta}_L\right]^T \tag{4.13}$$

is the estimated DOA vector, and $\hat{\sigma^2}$ is the noise power estimate.

The reconstructed covariance matrix $\tilde{\mathbf{R}}$, as will be explained in the following, is obtained from the preliminary estimated parameter set $\boldsymbol{\rho}$ in (4.11) and the known array manifold in (2.11). To calculate $\tilde{\mathbf{R}}$, the estimated DOA vector $\hat{\boldsymbol{\theta}}$ in (4.13) obtained in the standard manner is the starting point. From $\hat{\boldsymbol{\theta}}$, the estimate of the array manifold matrix $\mathbf{A}(\hat{\boldsymbol{\theta}})$ defined as

$$\mathbf{A}(\hat{\boldsymbol{\theta}}) = [\mathbf{a}(\hat{\theta}_1), \mathbf{a}(\hat{\theta}_2), \cdots, \mathbf{a}(\hat{\theta}_L)] \tag{4.14}$$

can be computed. Then the noise power is estimated by averaging over the noise eigenvalues [53]

$$\hat{\sigma^2} = \frac{1}{(M-L)} \sum_{l=L+1}^{M} \hat{\lambda}_l. \tag{4.15}$$

Finally, the source covariance matrix is obtained from [53]

$$\hat{\mathbf{R}}_{\mathrm{s}} = \mathrm{diag}_{+}\{\mathbf{A}^{\dagger}(\hat{\boldsymbol{\theta}})(\hat{\mathbf{R}} - \hat{\sigma^2}\mathbf{I})\mathbf{A}^{\dagger H}(\hat{\boldsymbol{\theta}})\} \tag{4.16}$$

where $(\cdot)^{\dagger}$ denotes the Moore-Penrose pseudo-inverse defined for a tall full column-rank matrix $\mathbf{X}$ as

$$\mathbf{X}^{\dagger} \triangleq \left(\mathbf{X}^H\mathbf{X}\right)^{-1}\mathbf{X}^H \tag{4.17}$$

and $\mathrm{diag}_{+}\{\cdot\}$ transforms a square matrix to a diagonal matrix by keeping its positive diagonal entries and replacing the non-positive diagonal entries and all the off-diagonal entries with zeros. This transformation is done so that according to Assumption 2 (in Chapter 2) and (2.17), the estimated signal covariance matrix $\hat{\mathbf{R}}_{\mathrm{s}}$ becomes a positive diagonal matrix, and hence, can expressed as

$$\hat{\mathbf{R}}_{\mathrm{s}} = \mathrm{diag}\{\hat{r}_{s,1}, \hat{r}_{s,2}, \ldots, \hat{r}_{s,L}\}. \tag{4.18}$$

Having estimated these parameters, $\tilde{\mathbf{R}}$ can be computed from

$$\tilde{\mathbf{R}} = \mathbf{A}(\hat{\boldsymbol{\theta}})\hat{\mathbf{R}}_{\mathrm{s}}\mathbf{A}^H(\hat{\boldsymbol{\theta}}) + \hat{\sigma^2}\mathbf{I}. \tag{4.19}$$

In order to define an abstract measure for the closeness of the reconstructed covariance matrix $\tilde{\mathbf{R}}$ and the observed sample covariance matrix $\hat{\mathbf{R}}$, a test hypothesis will be set up.

Applying the sphericity test [1], [48] with the following hypotheses

$$H_0: \quad \mathrm{E}\{\tilde{\mathbf{R}}^{-1/2}\hat{\mathbf{R}}\tilde{\mathbf{R}}^{-1/2}\} = c\mathbf{I} \qquad \text{against} \tag{4.20}$$

$$H_1: \quad \mathrm{E}\{\tilde{\mathbf{R}}^{-1/2}\hat{\mathbf{R}}\tilde{\mathbf{R}}^{-1/2}\} \neq c\mathbf{I} \tag{4.21}$$

for $c \geq 0$, we can attain test procedures to distinguish the proper and the outlying estimates. Two methods for testing these hypotheses are explained in the following.

4.3.1 The Generalized Likelihood Ratio Test (GLRT)

The likelihood ratio (LR) for the hypotheses (4.20) and (4.21) is given by [1], [48]

$$\gamma(\tilde{\mathbf{R}}) = \left(\frac{\det\{\tilde{\mathbf{B}}\}}{\left[\frac{1}{M}\mathrm{tr}\{\tilde{\mathbf{B}}\}\right]^M} \right)^N \triangleq \gamma_0^N(\tilde{\mathbf{R}}) \tag{4.22}$$

where

$$\tilde{\mathbf{B}} \triangleq \tilde{\mathbf{R}}^{-1/2}\hat{\mathbf{R}}\tilde{\mathbf{R}}^{-1/2}. \tag{4.23}$$

Therefore, the value $\gamma_0(\tilde{\mathbf{R}})$

$$\gamma_0(\tilde{\mathbf{R}}) = \frac{\det\{\tilde{\mathbf{B}}\}}{\left[\frac{1}{M}\mathrm{tr}\{\tilde{\mathbf{B}}\}\right]^M} \tag{4.24}$$

indicates the closeness of the reconstructed covariance matrix $\tilde{\mathbf{R}}$ and the sample covariance matrix $\hat{\mathbf{R}}$, and can be interpreted as the amount of reliability, i.e., the assessment of the quality, of a set of DOA estimates. Moreover, it takes a value between zero and one, i.e.,

$$0 < \gamma_0(\tilde{\mathbf{R}}) \leq 1. \tag{4.25}$$

The closer the value of $\gamma_0(\tilde{\mathbf{R}})$ is to one, the more reliable the DOA estimates are. In [1] and [2], it has been pointed out that the values of $\gamma_0(\tilde{\mathbf{R}})$ corresponding to non-outlying DOA estimates is bounded from below by $\gamma_0(\mathbf{R})$, i.e., the value of $\gamma_0(\mathbf{R})$ taken at the true covariance matrix $\mathbf{R}$ such that

$$\gamma_0(\mathbf{R}) = \frac{\det\{\mathbf{B}\}}{\left[\frac{1}{M}\mathrm{tr}\{\mathbf{B}\}\right]^M} \tag{4.26}$$

where

$$\mathbf{B} \triangleq \mathbf{R}^{-1/2}\hat{\mathbf{R}}\mathbf{R}^{-1/2}. \tag{4.27}$$

Taking this into account, an assessment of the LR optimization efficiency for any set of estimates can be performed by a direct comparison of LRs

$$\gamma_0(\tilde{\mathbf{R}}) \geq \gamma_0(\mathbf{R}). \tag{4.28}$$

However, in practical cases, the true covariance matrix $\mathbf{R}$ is not available, so the value of the lower bound $\gamma_0(\mathbf{R})$ is not known. Therefore, the statistical characteristics of $\gamma_0(\mathbf{R})$, which as shown in [1] is not scenario-dependent and only depends on the number of sensors in the array M and the number of snapshots N, can be used. The matrix $\mathbf{B}$ defined in (4.27) is a random matrix corresponding to a central complex Wishart distribution $\mathcal{CW}(N, M; \mathbf{I})$ [1], [48] where $N \geq M$ (Assumption 6). Using this property, the exact probability density function (PDF) for $\gamma_0(\mathbf{R})$, shown as $p\big(\gamma_0(\mathbf{R})\big)$, and its associated moments can be calculated [1]. Let us define P_κ as any desired threshold for probability of incorrect identification. P_κ is, in fact, the type-I error (false alarm) probability, i.e., the probability of that the proper set of estimates is classified wrongly as non-optimal and treated as containing at least one outlier. We can define P_κ as

$$P_\kappa \triangleq P\big(\gamma_0(\mathbf{R}) \leq \kappa\big) = \int_0^\kappa p\big(\gamma_0(\mathbf{R})\big)\, d\gamma_0 \tag{4.29}$$

where $P(\cdot)$ stands for the cumulative distribution function (CDF) and κ is the threshold value. In this way, by assigning a confidence interval and then computing the decision threshold value κ, the latter can be used instead of $\gamma_0(\mathbf{R})$ in (4.28). Thus, we have the following likelihood ratio-based quality assessment test that amounts to checking whether or not the inequality

$$\gamma_0(\tilde{\mathbf{R}}) \geq \kappa \tag{4.30}$$

is satisfied for $\tilde{\mathbf{R}}$. If the inequality is not satisfied for a given set of DOA estimates, then these estimates are classified as estimates containing at least one outlier or outlying estimates. Otherwise they are labeled as "proper" set of estimates.

4.3.2 The Locally Most Powerful Test (LMPT)

In this subsection, we present an alternative test to identify the outlying estimates. In this context it is important to note that the "power" of a certain test is defined [13] as its probability of rejecting the null hypothesis H_0 as a function of the parameter to be decided on. Note also that for a certain test, the power function computed for all values belonging to the subset of H_0 is normally required to be less than a given level called the level of significance. A uniformly most powerful test (UMPT) is then defined as a test procedure that maximizes the power function simultaneously for every value belonging to the subset of alternative hypothesis H_1 for a given level of significance. It is known that for hypotheses testing problems, UMPT can only exist if the alternative hypothesis H_1 is one-sided [13]. In our case, the alternative hypothesis H_1 is two-sided, i.e., it can be located on both sides of the critical value $c\mathbf{I}$ in (4.21). Therefore, there is no UMPT in this case. The locally most powerful test has the optimal property of being the locally best, or the locally most powerful invariant test [27], [48]. In other words, for every $\xi \geq 0$ close to c in (4.21) and for every other invariant test, there is a neighbourhood of $\xi\mathbf{I}$ such that the power of the optimal test is no less than the power of any other test. The test statistics of an optimal test with the previously mentioned hypotheses of (4.20) and (4.21) is [27]

$$\gamma_{\text{LMPT}}(\tilde{\mathbf{R}}) = \frac{\mathcal{L}^{(1)}\{\tilde{\mathbf{B}}\}^2 + \mathcal{L}^{(2)}\{\tilde{\mathbf{B}}\}^2 + \cdots + \mathcal{L}^{(M)}\{\tilde{\mathbf{B}}\}^2}{\left(\mathcal{L}^{(1)}\{\tilde{\mathbf{B}}\} + \mathcal{L}^{(2)}\{\tilde{\mathbf{B}}\} + \cdots + \mathcal{L}^{(M)}\{\tilde{\mathbf{B}}\}\right)^2} \tag{4.31}$$

where $\mathcal{L}^{(m)}\{\tilde{\mathbf{B}}\}$ for $m = 1, \ldots, M$ is the eigenvalue of the matrix $\tilde{\mathbf{B}}$ defined in (4.23). Interestingly, the test statistics for the GLRT in (4.24) can also be interpreted as the ratio of geometric mean of the eigenvalues $\mathcal{L}^{(1)}\{\tilde{\mathbf{B}}\}, \mathcal{L}^{(2)}\{\tilde{\mathbf{B}}\}, \cdots, \mathcal{L}^{(M)}\{\tilde{\mathbf{B}}\}$ to their arithmetic mean. From (4.31) the following inequality can be easily verified

$$\gamma_{\text{LMPT}}(\tilde{\mathbf{R}}) \geq \frac{1}{M}. \tag{4.32}$$

The test rejects the null hypothesis H_0, i.e., considers the estimates as containing at least one outlier, when $\gamma_{\text{LMPT}}(\tilde{\mathbf{R}})$ is greater than a certain threshold. So far, no closed form solution for the PDF of $\gamma_{\text{LMPT}}(\tilde{\mathbf{R}})$, except for a very simple case, is derived and only its

statistical moments are known [28]. Therefore, unlike the GLRT where the threshold value is computed using the PDF of $\gamma_0(\mathbf{R})$, the threshold value for the LMPT can only be obtained by Monte-Carlo runs, as in Section 4.6. The inequality (4.32) indicates that the closer the value lies to $1/M$, the higher is the confidence in the estimates. We observe that both sides of (4.32) are equal if the eigenvalues are all equal.

4.4 Outlier Identification and Cure (I&C)

Based on the method of assessing the quality of the estimate set described in the previous section, in this section, we present a technique to identify and to correct the possible outlier DOA estimate in the outlying estimates [2]. It is important to note that the identification and cure (I&C) procedure is introduced below in the context of the GLRT. However a similar technique can also be applied to the LMPT with only slight modifications as will be explained later.

Suppose that a particular set of estimates under consideration fails the quality assessment test of (4.30). Then, there must be at least one outlier among the estimates that need to be identified and, if possible, to be cured. The first step consists of identifying the possible outlier or outliers in the set of estimates. To achieve this goal, one source, say the l-th source for $l = 1, \ldots, L$, will be removed (considering Assumption 2 in Chapter 2) from the second order statistics model in the following way

$$\tilde{\mathbf{R}}_{(-l)} \triangleq \tilde{\mathbf{R}} - \hat{r}_{s,l}\mathbf{a}(\hat{\theta}_l)\mathbf{a}^H(\hat{\theta}_l) \tag{4.33}$$

where $\hat{r}_{s,l}$ is the estimated power of the l-th source from (4.18) and $\mathbf{a}(\hat{\theta}_l)$ is the manifold vector of the corresponding source. The covariance matrix in (4.33) is computed for each of the L sources. Thus L recovered covariance matrices $\{\tilde{\mathbf{R}}_{(-l)}\}_{l=1}^{L}$ are obtained in each of which one of the L sources is excluded. Then, for each of these matrices, the quality assessment value $\gamma_0(\tilde{\mathbf{R}}_{(-l)})$ is computed

$$\gamma_0(\tilde{\mathbf{R}}_{(-l)}) = \frac{\det\{\tilde{\mathbf{R}}_{(-l)}^{-1}\hat{\mathbf{R}}\}}{\left[\frac{1}{M}\mathrm{tr}\{\tilde{\mathbf{R}}_{(-l)}^{-1}\hat{\mathbf{R}}\}\right]^M}. \tag{4.34}$$

In the case that a DOA estimate corresponding to a true DOA has been removed in (4.33) a considerable degradation in $\gamma_0(\tilde{\mathbf{R}}_{(-l)})$, as compared to $\gamma_0(\tilde{\mathbf{R}})$, can be expected. However, removing an outlier from the set of estimates should have little effect on $\gamma_0(\tilde{\mathbf{R}}_{(-l)})$ in (4.34). Therefore, the outlying estimate $\hat{\theta}_{\text{out}}$ is, most likely, the estimate whose exclusion results in a reconstructed covariance matrix closest to the sample covariance matrix, i.e. the maximum of $\gamma_0(\tilde{\mathbf{R}}_{(-l)})$ over $l = 1, ..., L$. In other words,

$$\hat{\theta}_{\text{out}} = \hat{\theta}_{l_o} \tag{4.35}$$

where

$$l_o = \arg \max_l \left\{ \gamma_0(\tilde{\mathbf{R}}_{(-l)}) \right\}_{l=1}^{L}. \tag{4.36}$$

The next logical step after identifying the probable outlier is to replace the removed outlier estimate with a possibly correct one. Assume $\tilde{\mathbf{R}}_{(-l_o)}$ to be the estimated covariance matrix with one outlier removed, i.e., the one with the maximum LR value, and $\hat{\boldsymbol{\theta}}_{(-l_o)}$ to be the vector containing $L-1$ estimates when $\hat{\theta}_{l_o}$ is removed from $\hat{\boldsymbol{\theta}}$ in (4.13). To find a better estimate, a new parametric source will be added to the model and the following function is introduced

$$\tilde{\mathbf{R}}_{\text{new}}(\theta) \triangleq \tilde{\mathbf{R}}_{(-l_o)} + \hat{r}_s(\theta)\mathbf{a}(\theta)\mathbf{a}^H(\theta) \tag{4.37}$$

where $\hat{r}_s(\theta)$ is the signal power estimate of the additional parametric source using (4.16) and (4.18), and $\mathbf{a}(\theta)$ is the parametric array manifold vector. To estimate the proper source, it is sufficient to find the angles θ which maximizes the quality value of (4.37), i.e.,

$$\hat{\theta}_{\text{new}} = \arg \max_\theta \gamma_0\Big(\tilde{\mathbf{R}}_{\text{new}}(\theta)\Big). \tag{4.38}$$

That is to say, the entire grid of the FOV is searched to find an angle which together with $\hat{\boldsymbol{\theta}}_{(-l_o)}$ results in the closest covariance matrix to the sample version. Next, defining

$$\hat{\boldsymbol{\theta}}_{\text{new}} = \{\hat{\boldsymbol{\theta}}_{(-l_o)}, \hat{\theta}_{\text{new}}\} \tag{4.39}$$

the new LR quality assessment value $\gamma_0\Big(\tilde{\mathbf{R}}(\hat{\boldsymbol{\theta}}_{\text{new}})\Big)$ which has already been computed in (4.38) is required for the test. In the case that this value passes the test, the set of estimates

$\hat{\boldsymbol{\theta}}_{\text{new}}$ in (4.39) will be considered as the cured set of estimates. Otherwise, it will be regarded as the set of estimates containing outlier and the identification and cure process will be repeated. This process will be stopped when either the cured version passed the test or the number of iterations reaches a pre-determined value. The repetition of outlier correction procedure, referred to as refinement [2], [84] indeed generates more accurate estimates in each iteration. It may also happen that at some points the accuracy and the quality value remain unchanged, at which point the iteration will stop.

As indicated above the I&C method can also be applied to the LMPT by simply changing the "max" functions, in (4.35) and (4.38), to "min" and computing the quality assessment value according to (4.31) instead of (4.24).

4.5 Combination of the Cured Sets of Estimates

Despite the substantial efficiency of the I&C method in identifying and correcting the outliers, this method has the following limitations. The first problem appears in choosing the quality assessment threshold. Picking a conservative threshold (low for the GLRT and high for the LMPT) results in a low probability of false alarm (or type-I error), i.e. in a low probability of marking proper sets of estimates as outlying ones. However, in this case also a large number of truly outlying sets of estimates are considered as proper. This will lead to a degradation in the threshold performance whose improvement is the primary goal. On the other hand, choosing a more restrictive threshold value yields few proper sets of estimates and in the extreme case no proper sets of estimates at all. The second problem displayed itself in the so-called limit of the I&C method. Even a cured set of DOA estimates, especially in the weighted-MUSIC method used in the estimator bank, with an acceptable quality assessment value may, in fact, contains an outlier. Although it rarely happens in the relatively moderate SNRs. This phenomena [1] (see Section 4.6 for an example) causes undesirable errors in the performance. Because of the mentioned shortcomings, we develop new ways of extracting the final set of estimates from the cured outputs of the estimator bank.

A reasonable method to extract the final set of estimates is to pick those cured sets of estimates which pass the test, and the final set of estimates is obtained by averaging over them. If no such set of estimates exists in the output of the estimator bank, the one with the best quality value (the largest in the GLRT and the smallest in the LMPT) will be considered as the final set of estimate. It is essential to re-state that due to the limited number of refinement iterations and also the probable inherent deficiency of the sampled data, it happens quite frequently in restrictive threshold values, that an I&C procedure ends in the sets of estimate with an unacceptable quality value according to the threshold value κ in (4.30). Unfortunately applying this method to the estimator bank approach, as it will be shown later, may result either in a degradation in threshold performance and/or a substantial loss of performance in the asymptotic regions.

The proposed methods of combining the sets of estimates are based on the assumption that many of these sets in the estimator bank will be cured appropriately after the I&C procedure. In other words, these sets of estimates form a cluster around the true DOA vector, whereas the inappropriately cured sets of estimates will be scattered. This assumption is valid except in extreme cases, i.e., very closely-located sources, very low SNRs and/or very small number of snapshots. Therefore by exploiting this fact, it is expectable to achieve a better threshold performance as well as better asymptotic performance (for higher LR quality values) than the averaging over the proper sets of estimates combining method. The main idea is to detect the "cluster" of estimates and to average the sets of estimates of the cluster to obtain further improved final set of estimates.

Suppose that all of the cured estimates of the estimator bank are points in the L-dimensional space. The dimension is equal to the number of sources (for an illuminating example of this algorithm see Section 4.6). In order to detect the mentioned cluster two simple algorithms are proposed:

4.5.1 Method Based on Cluster Finding

Assume that the set $\mathcal{T}$ consists of Q parallel cured DOA estimate vectors

$$\mathcal{T} \triangleq \{\hat{\boldsymbol{\theta}}_{I\&C}^{(1)}, \hat{\boldsymbol{\theta}}_{I\&C}^{(2)}, \ldots, \hat{\boldsymbol{\theta}}_{I\&C}^{(Q)}\}. \tag{4.40}$$

The sets of estimates in $\mathcal{T}$ can be displayed as points in the L-dimensional DOA space. By placing a random initial point in this space, we plan to guide this point to the cluster. The process is done in two stages. First we find step-by-step, with as much accuracy as possible, the center of the cluster considering all the points. Second, to cancel the effect of non-cluster points, we average over the points inside a certain sphere with the estimated center and a pre-determined radius. In order to search for the cluster in the first stage, the decisive factor is the number of the points closely lying in an area, not their distance from the initial point. Therefore, we define at step (or iteration) i a normalized "attraction" vector for each point

$$\mathbf{f}_{(i)}^{(q)} = \frac{\hat{\boldsymbol{\theta}}_{I\&C}^{(q)} - \hat{\boldsymbol{\theta}}_{(i)}}{\|\hat{\boldsymbol{\theta}}_{I\&C}^{(q)} - \hat{\boldsymbol{\theta}}_{(i)}\|} \tag{4.41}$$

where $\hat{\boldsymbol{\theta}}_{I\&C}^{(q)}$ is the q-th cured set of estimate relating to the q-th estimator for $q = 1, \ldots, Q$ and $\hat{\boldsymbol{\theta}}_i$ is the estimate of the center of cluster in step i. The sum of the Q vectors in (4.41)

$$\mathbf{f}_{(i)} = \sum_{q=1}^{Q} \mathbf{f}_{(i)}^{(q)} \tag{4.42}$$

affects the course of the initial seeking point and leads the point to the cluster. We update the point at each step until we reach a pre-defined precision. The update process is as follows

$$\hat{\boldsymbol{\theta}}_{(i)} = \hat{\boldsymbol{\theta}}_{(i-1)} + \zeta \mathbf{f}_{(i-1)} \tag{4.43}$$

where ζ is the step size coefficient. The process will stop if the norm of the difference between two consecutive points, say $\hat{\boldsymbol{\theta}}_{(i_0)}$ and $\hat{\boldsymbol{\theta}}_{(i_0-1)}$, falls below a predefined value ϵ

$$\|\hat{\boldsymbol{\theta}}_{(i_0)} - \hat{\boldsymbol{\theta}}_{(i_0-1)}\| \leq \epsilon. \tag{4.44}$$

We can show that, in the general case (not necessarily the sets of DOA estimates) that if there exists one major cluster, the final optimum point (at the i_0-th iteration) is very

close to the center of the cluster. We assume that the number of points Q is very large. The points can be divided into two groups: the Q_1 points that belongs to a large number of closely-placed points and the Q_2 points that are scattered randomly all over the space and $Q = Q_1 + Q_2$. Let us define the center of the cluster as the average point of the cluster-points. Then, the value of $\sum_{q_1=1}^{Q_1} \mathbf{f}_c^{(q_1)}$, where $\mathbf{f}_c^{(q_1)}$ is the normalized "attraction" vector (4.41) in the center of the cluster, is equal to zero, since the optimum point is the center of the cluster. For the remaining Q_2 points, the value $\sum_{q_2=1}^{Q_2} \mathbf{f}_c^{(q_2)}$ must be equal to zero, since these points are randomly located in every direction and their "attraction" vector is direction-dependent rather than distant-dependent, hence, these vectors cancel each other. Consequently, for the ideal case, the optimum point, where the sum of all the normalized vectors is zero or sufficiently small, is the center of the cluster, i.e.,

$$\sum_{q=1}^{Q} \mathbf{f}_c^{(q)} = \sum_{q_1=1}^{Q_1} \mathbf{f}_c^{(q_1)} + \sum_{q_2=1}^{Q_2} \mathbf{f}_c^{(q_2)} = 0. \tag{4.45}$$

As for the case when the number of points is not large, the final point of the algorithm, where $\sum_{q=1}^{Q} \mathbf{f}^{(q)} \simeq 0$, will be close to the center of the cluster.

After determining $\hat{\boldsymbol{\theta}}_{(i_0)}$ with adequate precision, in the second stage of the proposed method an average will be calculated over the estimate points which lie inside a sphere with pre-defined radius (depends on the required resolution precision) and center of $\hat{\boldsymbol{\theta}}_{(i_0)}$. In this way, the probable outlying estimates will be removed from the final computation of the set of estimates.

4.5.2 Method Based on Deadzone-Linear Function

The second method is built upon the common convex problem of penalty function approximation [10] utilizing the "deadzone-linear" function

$$f_{\mathrm{DZ}}(u) = \begin{cases} 0 & , \quad \mid u \mid \leq r_d \\ \mid u \mid - r_d & , \quad \mid u \mid > r_d \end{cases} \tag{4.46}$$

as the penalty function. This function can be used to obtain the final set of estimates from the sets of the DOA estimates. The optimum point is defined as the point that minimizes

Algorithm EBQA (for the GLRT)

Step 1: Compute $\hat{\mathbf{R}}$ from (2.26) and consequently $\hat{\mathbf{U}}_{\mathrm{S}}$ and $\hat{\mathbf{U}}_{\mathrm{N}}$ from (2.28).

Step 2: Generate Q random vectors $\mathbf{w}^{(1)}, \ldots, \mathbf{w}^{(Q)}$ to form Q estimators from (4.7).

Step 3: For each estimator $q = 1, 2, \ldots, Q$ compute the set of estimates $\hat{\boldsymbol{\theta}}^{(q)}$ and its associated LR $\gamma_0(\tilde{\mathbf{R}}^{(q)})$ from (4.24).

Step 4: Average over the estimates with $\gamma_0^{(q)} \leq \kappa$ with κ acquired from (4.29) to obtain the final set of estimate. If $\gamma_0^{(q)} \geq \kappa$ for all q then the final set of estimate is the one with the largest QA value.

Table 4.1: Algorithm EBQA (for the GLRT)

the sum of the penalized-distances to the sets of the DOA estimates $\hat{\boldsymbol{\theta}}^{(q)}$ for $q = 1, \ldots, Q$. The problem can be expressed as

$$\hat{\boldsymbol{\theta}}_{\mathrm{opt}} = \arg \min_{\hat{\boldsymbol{\theta}}} \sum_{q=1}^{Q} f_{\mathrm{DZ}}(\|\hat{\boldsymbol{\theta}} - \hat{\boldsymbol{\theta}}^{(q)}\|) \tag{4.47}$$

where the minimization is taken over the L-dimensional parameter $\hat{\boldsymbol{\theta}}$. The defined penalty function $f_{\mathrm{DZ}}(u)$ considers no penalty for points in the vicinity of the optimum point, i.e., inside a sphere with the optimum point as its center and the radius r_d, however, the function linearly penalizes the points outside the circle. Therefore, the optimum point must lie near the closely-located points, i.e., near to the "cluster" we are looking for. It should be stated that this method is more costly in terms of computational complexity than the simple cluster finding method since a convex optimization problem has to solved to combine the proper sets of estimates. Therefore, this method is regarded as a benchmark for the cluster finding method.

We will see in the next section that applying the idea explained above to the computation of the final set of estimates of an estimator bank results in a much better threshold performance than that of the averaging over the proper sets of estimates.

In Tables 4.1 and 4.2, we provide a brief summary of our proposed algorithms whose simulation results will be shown in the next section.

Algorithm EBIC (for the GLRT)

Step 1: Compute $\hat{\mathbf{R}}$ from (2.26) and consequently $\hat{\mathbf{U}}_{\mathrm{S}}$ and $\hat{\mathbf{U}}_{\mathrm{N}}$ from (2.28).

Step 2: Generate Q random vectors $\mathbf{w}^{(1)}, \ldots, \mathbf{w}^{(Q)}$ to form Q estimators from (4.7).

Step 3: For each estimator $q = 1, 2, \ldots, Q$ compute the set of estimates $\hat{\boldsymbol{\theta}}^{(q)}$ and its associated LR $\gamma_0(\tilde{\mathbf{R}}^{(q)})$ from (4.24).

Step 4: If $\gamma_0^{(q)} \leq \kappa$ for κ obtained from (4.29) then perform the I&C procedure from Subsection 4.4.

Step 5: Combine the obtained estimates based on either of the methods presented in Subsection 4.5 to obtain the final set of DOA estimate.

Table 4.2: Algorithm EBIC (for the GLRT)

Similar algorithms can be presented for the LMPT. It should be mentioned that even if only the sets of estimates with QA value larger than threshold value κ are used for averaging without the I&C procedure (i.e., Algorithm EBQA in Table 4.1), then the significant performance improvement can be observed as we will see from simulations. Therefore, the difference between the two algorithms EBQA and EBIC is that there exists an additional step in Algorithm EBIC where the estimates containing outliers are passing through the I&C procedure. Hence, the EBIC algorithm is more costly in terms of computational complexity. Fig. 4.1 displays the block diagram illustrating the estimation steps in Algorithm EBIC.

4.6 Simulations

In this section, extensive simulation examples concerning all of the previously proposed methods are displayed. For the simulations we consider a ULA consisting of 10 identical omni-directional sensors spaced half a wavelength apart and three sources with equal power located at 12°, 27° and 31° with respect to the array broadside direction. The number of snapshots N through all the simulations is 100 unless otherwise specified.

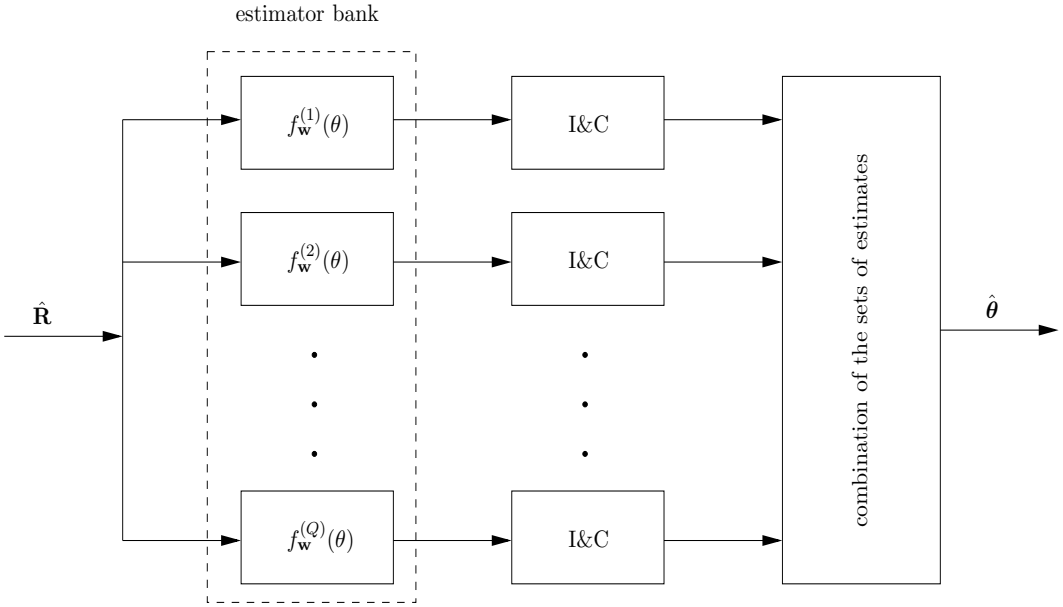

Figure 4.1: Illustration of estimator bank method combined with outlier I&C.

The following list provides the notation that is used to refer to the various methods implemented in the simulations:

Spectral MUSIC denotes the MUSIC method discussed in Subsection 3.2.1.

EBML denotes the estimator bank method with the ML choice of the final set of estimates.

EBQA-I denotes the estimator bank method with averaging over the proper sets of estimates counting all the runs and maximum LR value estimates as the final set of estimates when no successful estimator exits.

EBQA-II denotes the estimator bank method with averaging over the proper sets of estimates counting only the runs with at least one successful estimator.

single estimator+I&C denotes the conventional spectral MUSIC followed by I&C.

EBIC+AvP denotes the estimator bank method with I&C and averaging over the successful sets of estimates.

EBIC+ClF denotes the estimator bank method with I&C and cluster finding method of Section 4.5 to obtain the final set of estimate.

EBIC+DZ denotes the estimator bank method with I&C and the optimization with the deadzone penalty function ($r_d = 0.2$) of Section 4.5 to obtain the final set of estimate.

In Figs. 4.2, 4.3, and 4.4, we display the representative relationship between estimation error characterized by the root-mean-square error (RMSE) and the GLRT and also the LMPT quality assessment value, for the same scenario but for different SNR values. At each run the signal DOAs are estimated from a conventional MUSIC estimator, then according to the procedure described in Section 4.3, the reconstructed covariance matrix $\tilde{\mathbf{R}}$ is computed and from that, the GLRT quality assessment value $\gamma_0(\tilde{\mathbf{R}})$ is obtained. The upper parts of Figs. 4.2 and 4.3 show histograms (in percentage) of these values in 2000 runs, and the lower diagrams demonstrate the distributions of RMSE of the DOA estimates versus their LR value. In our simulations the threshold value κ was obtained from Monte-Carlo simulations. This is in contrast to [56] where the threshold value was calculated by an approximation. As an example, for $P_\kappa = 0.95$ a GLRT threshold value κ of approximately 0.66 was obtained from (4.30) and similarly the threshold value corresponding to $P_\kappa = 0.05$ is approximately 0.48. It should be emphasized again that this value is scenario-independent, i.e., it only depends on the number of sensors M and the number of snapshots N. By selecting a higher GLRT threshold κ, i.e., higher P_κ, a proper set of estimates can be falsely classified, with a considerable probability, as containing outlier. On the other hand, by setting a lower GLRT threshold κ, i.e., lower P_κ, the situation will be reversed, i.e., we avoid, as much as possible, to accept an outlying set as the proper one, as can be clearly observed from Fig. 4.2. Fig. 4.4 displays the histogram of $\gamma_{LMPT}(\tilde{\mathbf{R}})$ and the distribution of RMSE of the DOA estimates versus $\gamma_{LMPT}(\tilde{\mathbf{R}})$ similar to those shown in Fig. 4.3.

In Fig. 4.5, we assume an estimator bank consisting of 20 estimators ($Q = 20$). These estimators utilize the weighted-MUSIC method with random weight vectors (4.3) to estimate the DOAs. We apply both of the quality assessment algorithms to test whether the set of estimates contains an outlier or not. In certain simulation runs, as it has been observed,

it may happen that there exists not a single successful estimator in the bank. In this case, no further improvement can be done. However, the proposed algorithm can at least provide an indicator that the sets of estimates are all unsuccessful. In such cases, we can either ignore that run (which will be unfair to other methods but logical) or pick the estimates of the estimator with the largest LR value as our final estimates in that run, although we know that the proposed estimates are likely to be faulty. Fig. 4.5 displays the performance of various methods for the aforementioned scenario in comparison with the stochastic CRB. It can be seen that the proposed method of removing the outlying estimates in the estimator bank approach provides substantially lower SNR performance-threshold compared to conventional MUSIC and the earlier estimator bank approach (EBML).

Fig. 4.6 displays RMSE of methods EBQA-I , EBQA-II and spectral MUSIC for different snapshot numbers for $Q = 20$ with $P_\kappa = 0.5$ and the GLRT method. Here, we can also observe the performance improvement of the proposed methods.

Fig. 4.7 demonstrates the same curves (with $P_\kappa = 0.5$) but for the LMPT and Fig. 4.8 illustrates the comparison of the two quality assessment methods considering the case of accepting the probable outlying estimates with the best value as the final estimates when no "proper" sets of estimate is available. It can be observed that both methods have approximately the same threshold performance although that of the LMPT seems to be slightly better.

Fig. 4.9 displays the effect of the outlier I&C procedure on the estimates generated from the conventional weighted-MUSIC method for different values of decision thresholds κ. The scenario is the same as used in previous simulations. The upper part displays the distribution of the DOAs root-mean-square error (RMSE), in degrees, for an estimator bank containing 5000 sets of spectral weighted-MUSIC estimates with SNR $= -3$dB. The I&C algorithm applied to these estimates for three different cases of κ: $P_\kappa = 0.95$ a rather high decision threshold value, $P_\kappa = 0.5$ a relatively low decision threshold value, and $P_\kappa = 0.05$ a very low decision threshold value. Our earlier assumption (see Section 4.5) that, except for some extreme cases, most of the cured sets of estimates which are correctly classified as proper, will be gathered around the true signal DOAs is confirmed in these

three cases. These figures also verify the phenomenon that it may happen that even a cured set of estimates with acceptable GLRT quality value can be, in fact, an outlying set of estimates and therefore cause huge errors in the performance. A representative Monte-Carlo simulation of random weighted-MUSIC method indicates that in this scenario after I&C procedure with SNR $= -3$dB for $P_\kappa = 0.05$ approximately 60 percent, for $P_\kappa = 0.5$ approximately 45 percent, and for $P_\kappa = 0.95$ approximately 29 percent of the cured sets of estimates have RMSE$\geq 2^\circ$ while the CRB is approximately 0.97°. For example, from Fig. 4.9 it can be observed that for $P_\kappa = 0.05$ approximately 40 percent of the sets of estimates with acceptable error are close to each other forming a "cluster", the other 60 percent with unacceptable errors, although greater in number, are scattered in the 3-dimensional parameter space.

Different update-stages of the cluster finding approach appear in Figs. 4.10 and 4.11. We have selected a 2-dimensional space, which is easier to be displayed. The data points in Fig. 4.10 consists of some randomly chosen points in the entire space and a cluster of points randomly distributed around the origin. Using the proposed method ($\epsilon = 0.001$ and $\zeta = 0.2$), the algorithm quickly reaches its estimated point [-0.489 -0.259], that ideally should be the origin. Then, the average is calculated over the data points inside the circle with radius equal to 2 to nullify the effect of the irrelevant points. The averaging, which is also the solution to the least-mean-square-error problem for the desired points, results in the even further improved estimates [0.082,0.046] which is closer to the origin. The optimization approach using deadzone-linear penalty function ($r_d = 0.2$) for the same data provides us with the estimate [0.6353,-0.0998]. Fig. 4.11 shows the same procedure with the simulated output estimates obtained from an estimator bank as the data points. Since the DOA space is two-dimensional, we have chosen two sources located at 10° and 15° with the same array configuration previously mentioned in our example. Here again the starting point is random. The final point in both of the proposed methods results in a more accurate estimate with RMSE of approximately 0.45 degree where as the final estimate in averaging-over-the-proper-estimates method gives us a poor estimate with RMSE of approximately 3.96 degree.

The last series of figures exhibit the simulation results for DOA estimation performance of the scenario mentioned earlier ($L = 3$) with sources located at 12°, 27° and 31° for various methods in a bank of estimators with the dimension of 20 ($Q = 20$). Figs. 4.12 and 4.13 display the RMSE-versus-SNR comparison for different threshold values $P_\kappa = 0.95$ and $P_\kappa = 0.5$, respectively, using the I&C procedure with the GLRT and Figs. 4.14 shows the same but using the LMPT. Figs. 4.15 and 4.16 demonstrate the effect of the number of snapshots on the DOA estimation RMSE for the methods utilizing the I&C procedure with the GLRT. We can observe from these figures and also from Fig. 4.12 that the combining method of averaging over the proper sets of estimates fails to perform in the threshold region when P_κ is decreased to 0.5 while the cluster finding method maintains its excellent performance. This is due to the fact that by reducing P_κ the number of outlying estimates regarded as proper sets of estimates increases in the pre-I&C procedure and they never undergo the I&C procedure and this deteriorates the averaging method. It should be remarked that although the cluster finding method and the method using deadzone penalty function both exhibit a significant robustness against P_κ, yet for very low values of P_κ the performance of these methods may also degrade. We remark that by assigning a lower value to P_κ the computational cost associated with the I&C procedure for the estimator bank decreases substantially since the number of the sets of estimates that require the mentioned I&C procedure will decrease. As we can see from Figs. 4.12-4.16, the cluster finding method, as well as the costly method using deadzone penalty function, for combining the proper sets of estimates offer superior performance. Not only it results in a considerably better threshold performance but also it has none of the obvious discrepancies of the other combining method (i.e., averaging over the proper sets of estimates after I&C). Both the proposed combining methods seem to have approximately the same performance. They also remain close to CRB in the asymptotic regions.

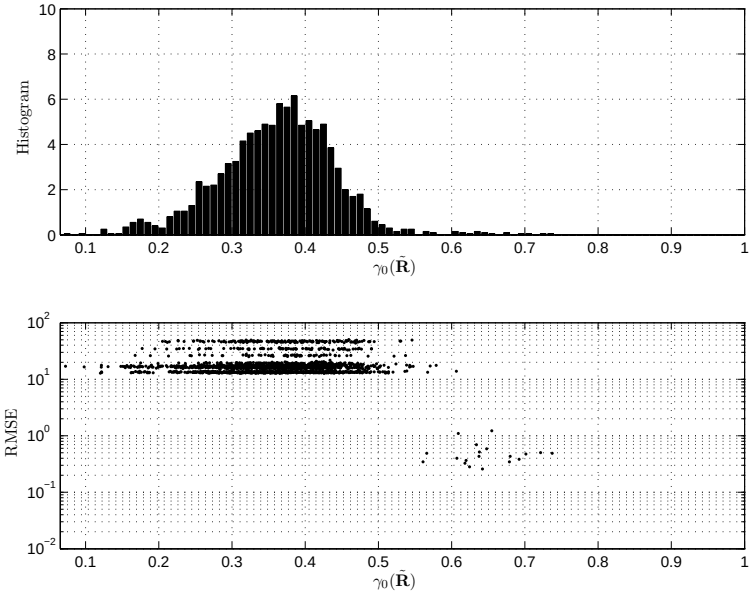

Figure 4.2: Histogram of $\gamma_0(\tilde{\mathbf{R}})$ and the scatter plot of the RMSEs of the MUSIC-generated DOA estimates versus $\gamma_0(\tilde{\mathbf{R}})$ for SNR = 0dB.

4.7 Chapter Summary

We have introduced the idea of estimator bank and new applications of the quality assessment methods for evaluating the sets of estimates in the estimator bank for fully-calibrated arrays. These methods are based on hypothesis testing, namely sphericity test, and two approaches of the GLRT and of the LMPT have been presented. To choose the successful sets of estimates, a quality-assessment threshold is required to decide which sets of estimates to keep and which to reject and if possible to cure the sets of estimates using the I&C procedure. We discussed and illustrated from numerical simulations, the effect of choosing different QA thresholds on the performance of the proposed method. We have also presented methods to combine efficiently the proper or cured sets of estimates of the estimator bank. Our simulation results demonstrate significant improvement both in reducing the performance threshold and in achieving even closer RMSEs to the CRB.

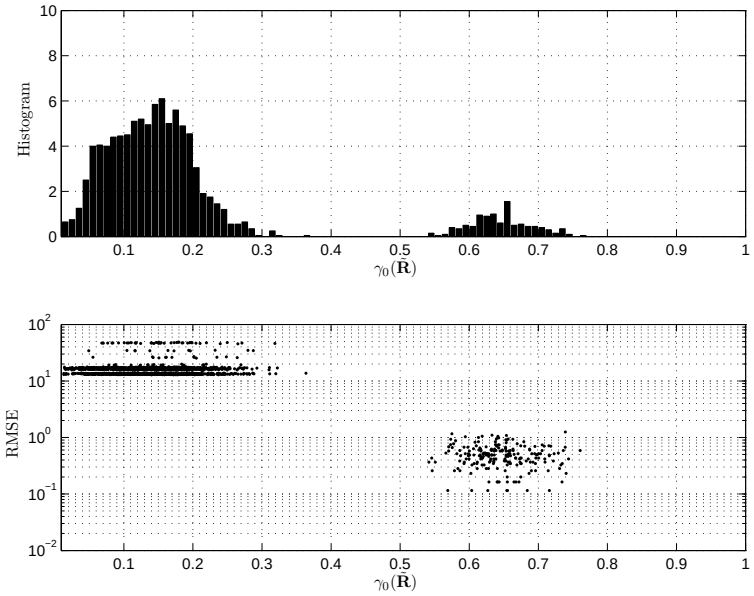

Figure 4.3: Histogram of $\gamma_0(\tilde{\mathbf{R}})$ and the scatter plot of the RMSEs of the MUSIC-generated DOA estimates versus $\gamma_0(\tilde{\mathbf{R}})$ for SNR = 3dB.

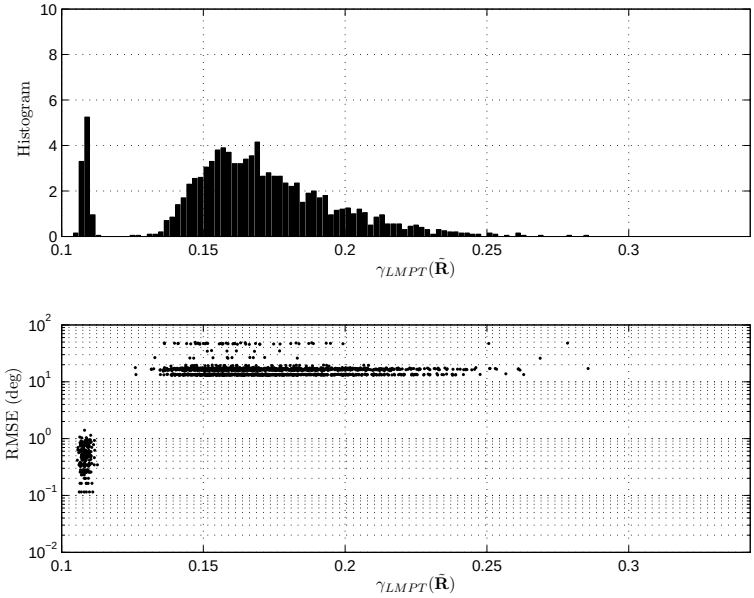

Figure 4.4: Histogram of $\gamma_{LMPT}(\tilde{\mathbf{R}})$ and the scatter plot of the RMSEs of the MUSIC-generated DOA estimates versus $\gamma_{LMPT}(\tilde{\mathbf{R}})$ for SNR = 3dB.

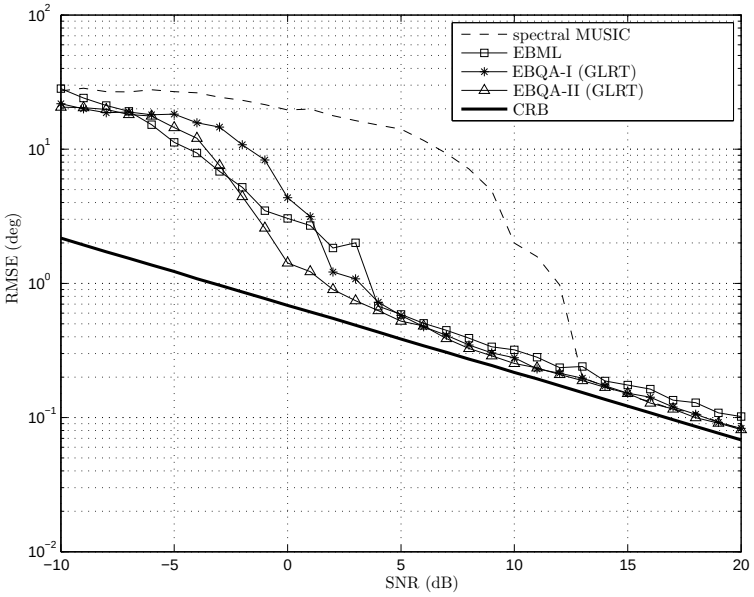

Figure 4.5: RMSE versus SNR for the GLRT quality assessment method and $P_\kappa = 0.5$

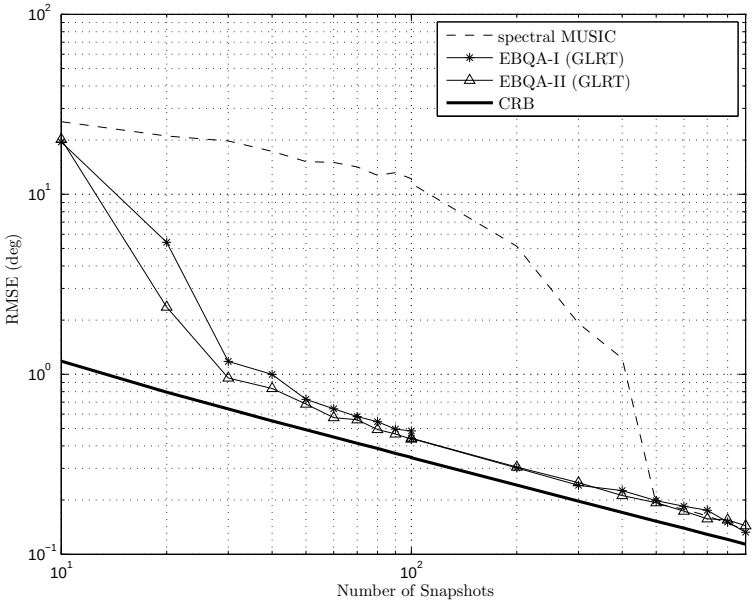

Figure 4.6: RMSE versus sample number for the GLRT quality assessment method and $P_\kappa = 0.5$, SNR= 6dB

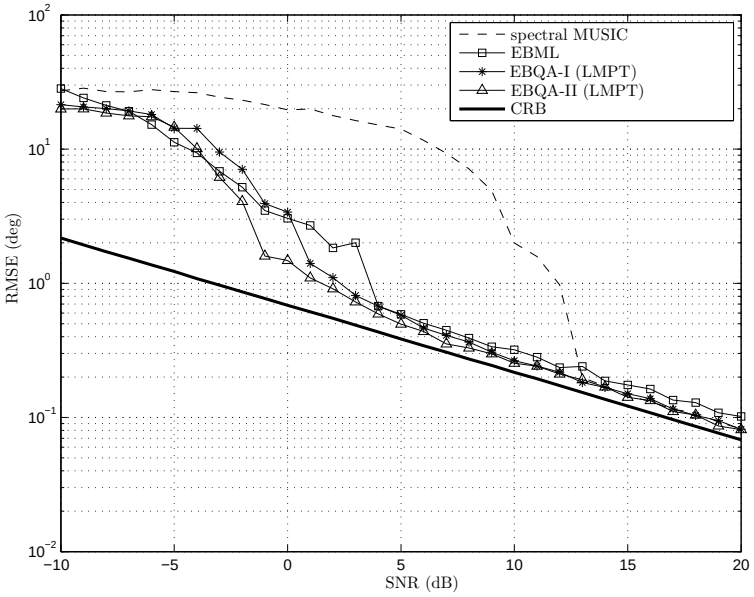

Figure 4.7: RMSE versus SNR for the LMPT quality assessment method and $P_\kappa = 0.5$

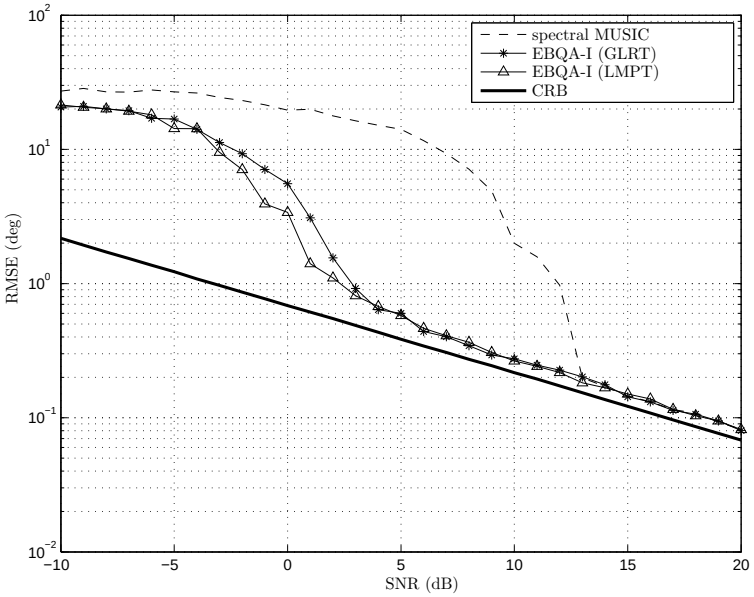

Figure 4.8: RMSE versus SNR: comparing the GLRT and the LMPT (with detected outliers)

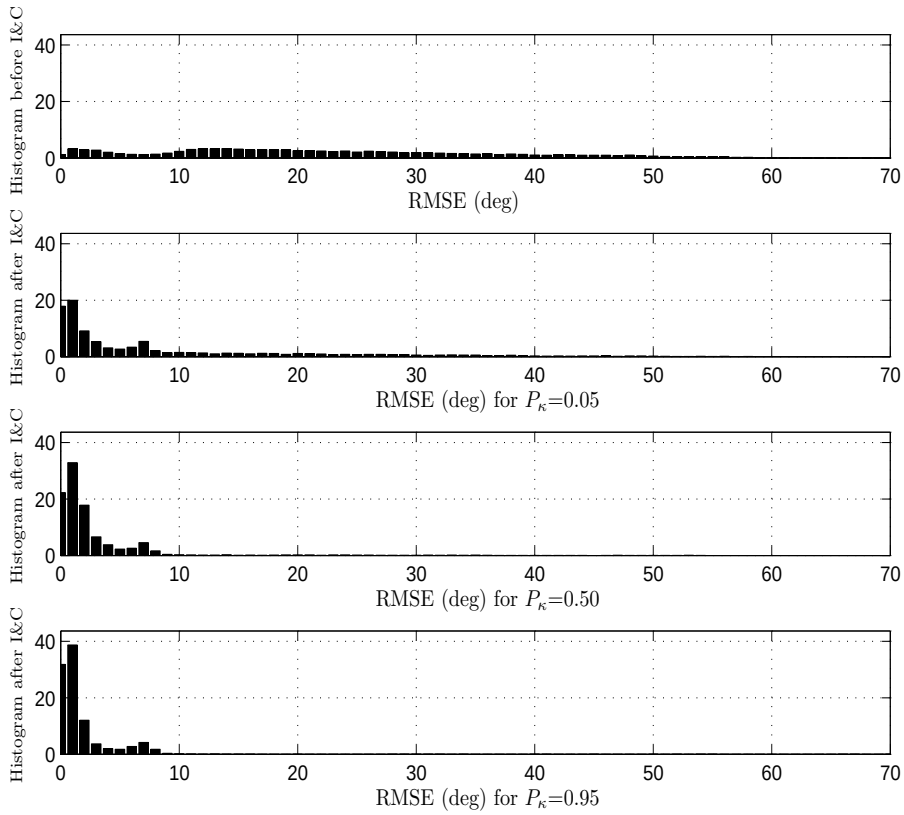

Figure 4.9: Distribution of RMSEs before and after the I&C for different threshold values

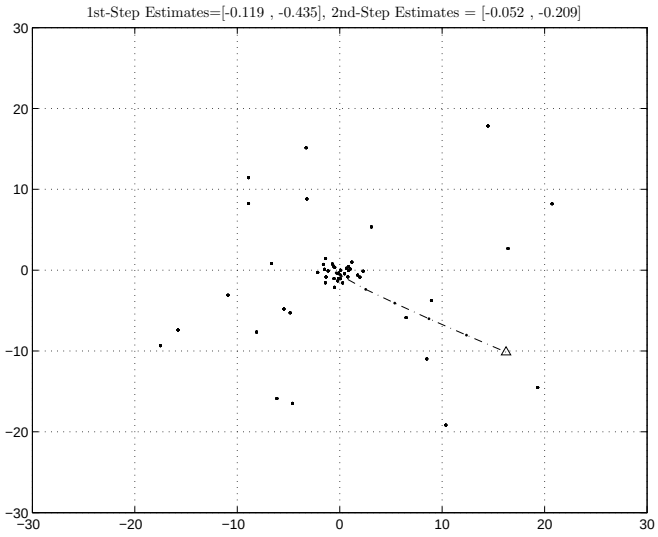

Figure 4.10: Illustration of the cluster finding method with random data points

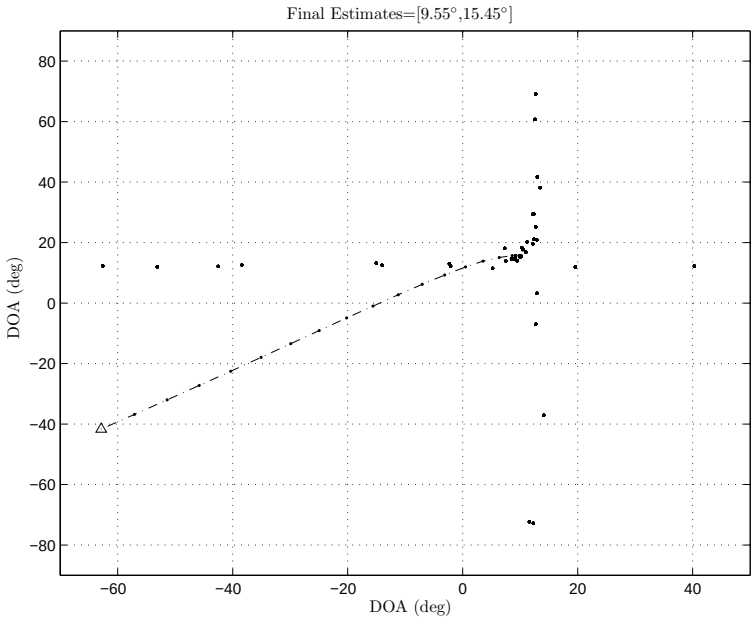

Figure 4.11: Illustration of the cluster finding method with simulated DOA estimates from estimator bank at SNR= -7dB data points

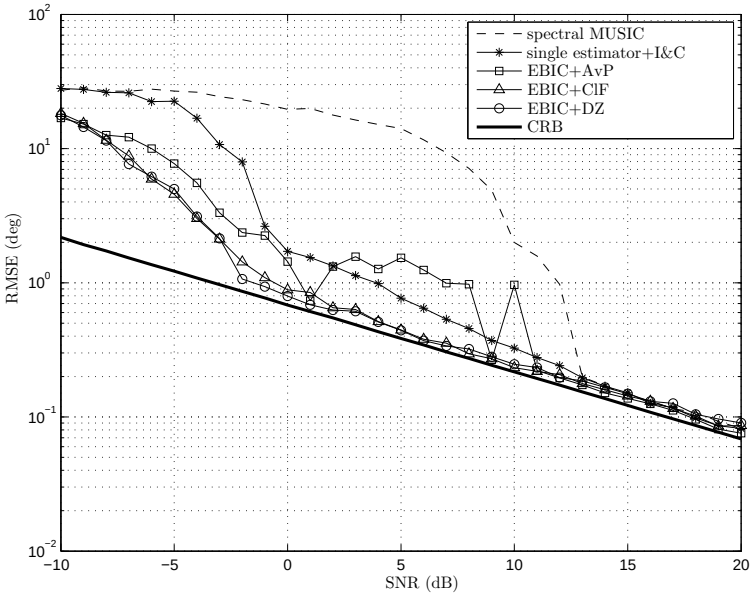

Figure 4.12: RMSE vs. SNR for $P_\kappa = 0.5$ and the GLRT method

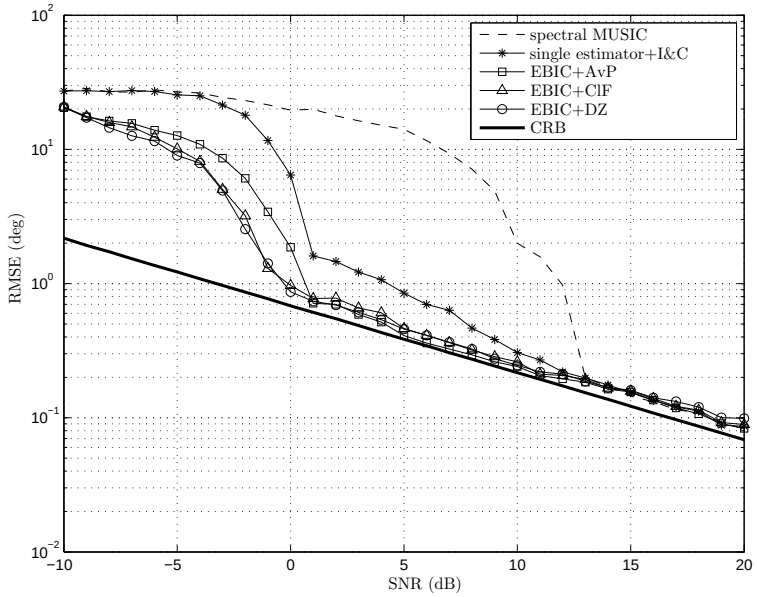

Figure 4.13: RMSE vs. SNR for $P_\kappa = 0.95$ and the GLRT method

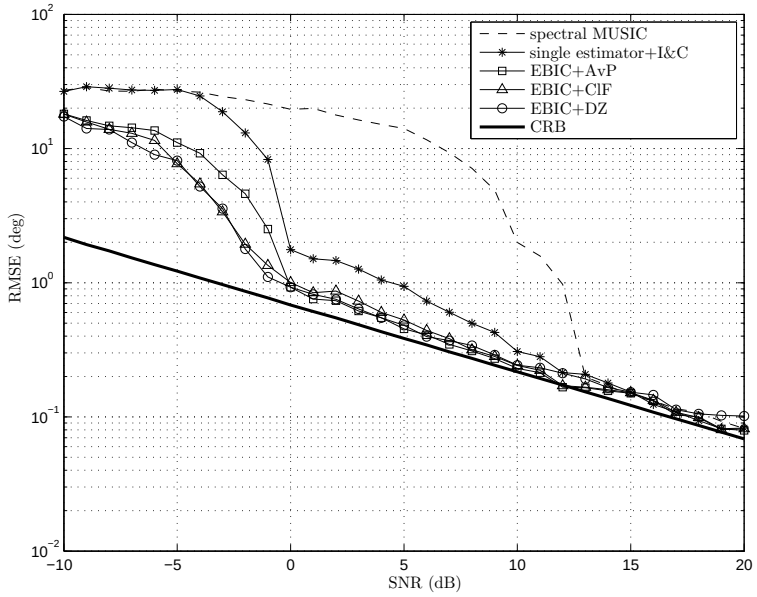

Figure 4.14: RMSE vs. SNR for $P_\kappa = 0.95$ and the LMPT method

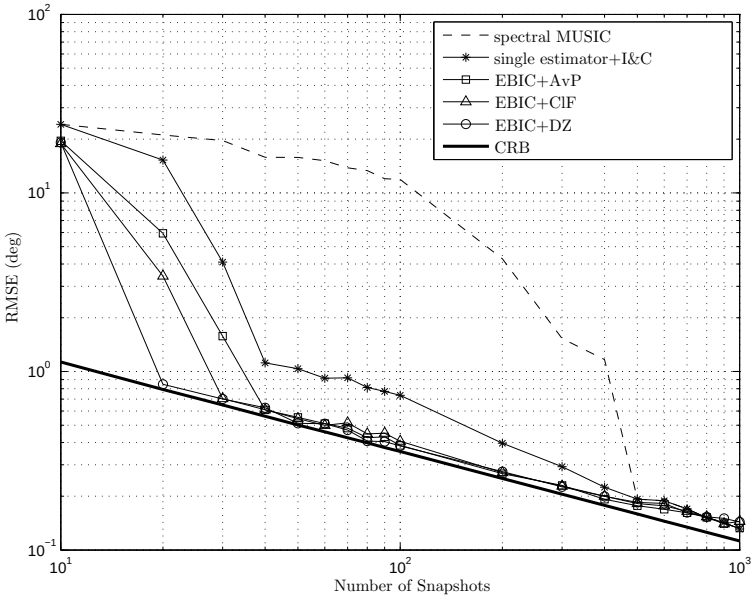

Figure 4.15: DOA estimation RMSEs versus number of snapshots for $P_\kappa = 0.95$ and the GLRT method

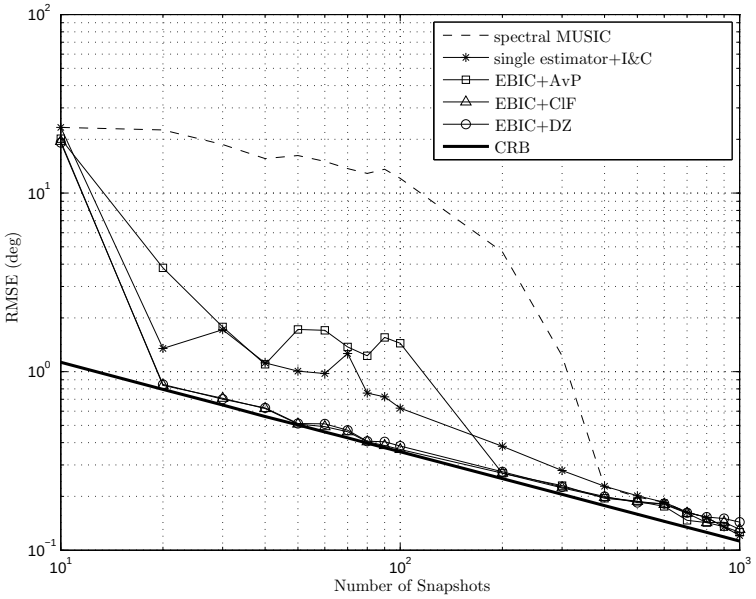

Figure 4.16: DOA estimation RMSEs versus number of snapshots for $P_\kappa = 0.5$ and the GLRT method

Chapter 5

Joint DOA Estimation and Array Manifold Calibration in Partly-Calibrated Arrays

5.1 Introduction

Sensor arrays with large aperture size are favorable due to their ability to estimate signal DOAs more accurately. However, large sensor arrays are costly. Moreover, array manifold errors in such arrays can occur due to various factors such as: unknown mutual coupling between sensors, unknown channel mismatches between subarrays, sensor gain and phase uncertainties, uncertainties in sensor locations, near-field scattering of sources and multipath propagation, and time synchronization issue between the subarrays. Particularly, controlling and determining the location of each sensor in the large (probably moving) arrays is a difficult task. Traditional subspace-based DOA estimation methods, like MUSIC [78] and the so-called method of DOA estimation (MODE) [88], are known to be sensitive to modeling errors, especially those resulting from uncertainties in the sensor locations [14], [81], [90] and require an accurate array calibration. This is in contrast to the classical DOA estimation methods, e.g., beamforming techniques such as Bartlett beamformer method and Capon method [33] which are more robust to the array geometry perturbations. Conventional methods for array calibration are usually applied offline and require the knowledge of reference sources [43], [51], [93], [104]. However, these methods are generally not applicable

in the case of time-varying sensor arrays or in large arrays with remote sensors.

The calibration methods can be categorized into two groups: calibration techniques using known sources and self-calibration methods. The methods in the first group take advantage of known sources which are usually disjoint in time or frequency. The methods described in [43], [50], [51], [55], [79] and references therein, deal with array calibration using sources at known locations. On the other hand, self-calibration or auto/blind calibration methods use sources at unknown locations. These methods are more complex than the methods in the first category since it is required to estimate a larger number of parameters. Most of the self-calibration methods, e.g., [63], [72], [103], make use of iterative algorithms based on subspace-fitting techniques or the maximum likelihood method and they need prior array information, e.g., an accurate initial point or the nominal sensor locations assuming small perturbations, to accomplish their objectives. The conditions on the number of known and unknown signals for the observability of the array geometry and the sensor locations are investigated in [44] and [76]. The existing calibration methods either require additional information like known sources or require complex, iterative methods as well as nominal, initial information about array geometry. Therefore, in order to avoid such calibration issues and to facilitate the calibration of the array manifold, the idea of sparse sensor arrays [4], [66], [77], [80], [91], [92] is proposed in this chapter. In sparse sensor arrays, the array while keeping its large aperture, is partitioned into several smaller subarrays where the aperture of each subarray is small compared to the aperture of the entire array, therefore, it is much easier to calibrate the subarrays instead of the entire array. We call the sparse arrays, partly-calibrated arrays (PCAs) because these types of arrays are assumed to be composed of multiple subarrays with intersubarray displacements and either the subarrays or the displacements are unknown.

Many DOA estimation methods applicable to PCAs are restricted by the fact that they are developed for specific array geometries. These methods can be categorized into closed-form search-free methods and search-based methods whose objective function needs to be evaluated over a fine grid to find the largest peaks. In [77] (see Section 3.5), the popular search-free ESPRIT method, has been introduced for PCAs composed of two identical

subarrays of known or unknown geometry and known displacement between the subarrays as displayed in Fig. 3.1. Another search-free method for PCAs composed of identically oriented uniform subarrays with unknown subarray displacements has been proposed in [66]. In [92] methods based on rooting a polynomial similar to the root-MUSIC method [7] and MODE [88] are proposed for the PCAMIS model shown in Fig. 2.3 but with the displacement vectors all along the same direction. Search-based methods, in contrast, are applicable to more general classes of array configurations at the expense of increased computational complexity. In [80], the root-RARE approach of [66] has been extended to arbitrary PCAs shown in Fig. 2.2 (see Section 3.3). Sensor arrays composed of identical subarrays with different known subarray displacements, shown in Fig. 2.3, have been considered in [92] (see Section 3.4). A rank-reduction method for PWCAs, shown in Fig. 2.4, is developed in [16] (see also Section 3.6).

In the present chapter, several new joint DOA estimation and calibration methods for various types of PCAs are introduced. First, in Section 5.2 the general case of the arbitrary PCA is considered and several techniques are presented to improve the DOA estimation performance (see also [59]). Second, in Section 5.3 a particular case of PCAs is considered where all the subarrays are identical and two new methods are proposed (see also [62]). Then in the Section 5.4, another special PCA geometry is investigated with two uncalibrated subarrays and known displacements between the sensor pairs, one in each subarray (see also [58]). In terms of computational complexity, the new methods are comparable to their competing methods in [16], [80], and [92]. The novelty of the proposed methods lies in taking advantage of two often neglected yet important points: incorporating the estimation of the unknown part of the array geometry into the DOA estimation process and using the information about the structure of the mentioned unknown parts. This explains the DOA estimation performance superiority of the proposed methods to that of the competing methods presented briefly in Sections 3.3, 3.4, and 3.6.

5.2 Arbitrary Partly-Calibrated Array (APCA)

In this section, the general model for PCA is taken into account where the array is composed of multiple arbitrary subarrays with arbitrary displacement vectors between them as shown in Fig. 2.2. We assume that the each subarray is fully-calibrated but the displacement vectors are unknown. The DOA estimation and self-calibration approach introduced in this section use the idea of separating the unknown array geometry-dependent part of the manifold matrix from the unknown signal-dependent part, i.e., the signal DOAs $\boldsymbol{\theta}$. However, unlike in the competing methods, this unknown array geometry-dependent part is taken into account in our proposed DOA estimation procedure. Furthermore, the structure of the unknown array geometry-dependent part of the array manifold is exploited fully using two different techniques in the proposed DOA estimation process in Section 5.2.2. Afterwards, a multivariate function from the combination of subspace mismatch functions between subarrays is obtained from which the DOAs can be estimated from minimizing it using, for instance, the alternating projection method [108] described briefly in Section 5.2.3 and in Table 5.1. The computational complexity of this algorithm can be further reduced by transforming the function into a single variable function and using weighting coefficients in combining the mismatch functions. We propose two methods in Section 5.2.4 which use random weighting coefficients and select the best set of them to obtain the DOAs. The simulation results displayed in Section 5.5 show far better performance in comparison with the existing methods.

5.2.1 Signal Model for APCA

Consider an array with M sensors composed of K different subarrays, each containing M_k omni-directional sensors so that

$$M = \sum_{k=1}^{K} M_k. \tag{5.1}$$

Assume, as before, the signals originate from L uncorrelated narrow-band sources, located in the far-field at the DOAs $\boldsymbol{\theta} = [\theta_1, \ldots, \theta_L]^T$. We choose the first subarray as the reference

and we assume that the subarray displacement vectors between the first subarray and the k-th subarray, denoted by $\boldsymbol{\eta}_k = [\alpha_k, \beta_k]^T$ for $k = 2, \ldots, K$, are unknown. More accurately, the vector $\boldsymbol{\eta}_k$ is defined as the displacement vector between the first sensor, i.e., the reference sensor, in the first subarray and the first sensor, i.e., the reference sensor, in the k-th subarray. Let us assume that the m_k-th sensor for $m_k = 1, \ldots, M_k$ in the k-th subarray for $k = 1, \ldots, K$ is the m-th sensor in the whole M-sensor array such that equation (5.1) holds. Then, the location of the m-th sensor, i.e., the m_k-th sensor of the k-th subarray, can be expressed as

$$x_m = \alpha_k + \tilde{x}_{m_k} \tag{5.2}$$

$$y_m = \beta_k + \tilde{y}_{m_k} \tag{5.3}$$

for $m_k = 1, \ldots, M_k$ and $k = 1, \ldots, K$ where $\tilde{x}_{m_k}$ and $\tilde{y}_{m_k}$ are the coordinates of m-th sensor inside its associated subarray and relative to the reference sensor of the same subarray. Choosing the first sensor of the first subarray as the reference sensor, we obviously have $\alpha_1 = 0$ and $\beta_1 = 0$, hence,

$$\boldsymbol{\eta}_1 = \mathbf{0}. \tag{5.4}$$

We assume that each subarray is perfectly calibrated, i.e., the array manifold matrix for each subarray is known. The output of the sensor array at the times $t = 1, \ldots, N$ can then be modeled as in (2.6), i.e., $\mathbf{z}(t) = \mathbf{A}(\boldsymbol{\theta}, \boldsymbol{\Psi})\mathbf{s}(t) + \mathbf{n}(t)$, where

$$\boldsymbol{\Psi} \triangleq [\boldsymbol{\eta}_2, \ldots, \boldsymbol{\eta}_K] \tag{5.5}$$

is the $2 \times (K-1)$ matrix containing all the unknown displacements, $\mathbf{s}(t)$ is the signal waveform vector defined in (2.7), $\mathbf{n}(t)$ is the noise vector defined in (2.2) with all its statistical properties described in Assumption 3 in Chapter 2, and $\mathbf{A}(\boldsymbol{\theta}, \boldsymbol{\Psi})$ is the $M \times L$ array manifold matrix of the array that depends on the unknown DOA vector $\boldsymbol{\theta}$ and the unknown $K-1$ displacement vectors $\boldsymbol{\eta}_2, \ldots, \boldsymbol{\eta}_K$. Note that the matrix $\boldsymbol{\Psi}$, besides demonstrating the unknown displacement vectors, can represent any other type of uncertainties mentioned in Section 5.1, be it the channel mismatch between the subarrays, imperfect subarray synchronization in time or signal fading [80].

Using equation (2.11), the (m,l) entry of the array manifold matrix, which corresponds to the m_k-th sensor in the M_k-th subarray and the l-th source can be written as

$$\begin{aligned}[\mathbf{A}(\boldsymbol{\theta},\boldsymbol{\Psi})]_{(m,l)} &= e^{-j(2\pi/\lambda)(x_m\sin\theta_l+y_m\cos\theta_l)} \\ &= e^{-j(2\pi/\lambda)(\alpha_k\sin\theta_l+\beta_k\cos\theta_l)}e^{-j(2\pi/\lambda)(\tilde{x}_{m_k}\sin\theta_l+\tilde{y}_{m_k}\cos\theta_l)}. \end{aligned} \tag{5.6}$$

Defining

$$\phi_{k,l} \triangleq e^{-j(2\pi/\lambda)(\alpha_k\sin\theta_l+\beta_k\cos\theta_l)}, \tag{5.7}$$

equation (5.6) then becomes

$$[\mathbf{A}(\boldsymbol{\theta},\boldsymbol{\Psi})]_{(m,l)} = \phi_{k,l}\,[\mathbf{A}_k(\boldsymbol{\theta},\boldsymbol{\Psi})]_{(m_k,l)} \tag{5.8}$$

where $\mathbf{A}_k(\boldsymbol{\theta})$ is the known $M_k \times L$ manifold matrix of the k-th subarray. Hence, the array manifold matrix $\mathbf{A}(\boldsymbol{\theta},\boldsymbol{\Psi})$ can be partitioned into K blocks

$$\mathbf{A}(\boldsymbol{\theta},\boldsymbol{\Psi}) = \begin{bmatrix} \mathbf{A}_1(\boldsymbol{\theta}) \\ \mathbf{A}_2(\boldsymbol{\theta})\boldsymbol{\Phi}_2(\boldsymbol{\theta},\boldsymbol{\eta}_2) \\ \vdots \\ \mathbf{A}_K(\boldsymbol{\theta})\boldsymbol{\Phi}_K(\boldsymbol{\theta},\boldsymbol{\eta}_K) \end{bmatrix} \tag{5.9}$$

where

$$\boldsymbol{\Phi}_k(\boldsymbol{\theta},\boldsymbol{\eta}_k) = \mathrm{diag}\{\phi_{k,1},\phi_{k,2},\ldots,\phi_{k,L}\} \tag{5.10}$$

is the diagonal displacement-phase matrix that contains the unknown phase rotations due to the subarray displacements. Note that based on (5.4), (5.7), and (5.10) we have $\boldsymbol{\Phi}_1 = \mathbf{I}$.

The array covariance matrix $\mathbf{R}$ and its eigen-decomposition are defined in (2.15) and (2.19), respectively, in Chapter 2. Due to the unavailability of $\mathbf{R}$ in practice, its estimate $\hat{\mathbf{R}}$ is used from (2.26). The $M \times L$ matrix of the estimate of the signal subspace matrix $\hat{\mathbf{U}}_{\mathrm{S}}$ and the $(M-L)\times L$ matrix of the estimate of the noise subspace matrix $\hat{\mathbf{U}}_{\mathrm{N}}$ are obtained from the eigen-decomposition of $\hat{\mathbf{R}}$ in (2.28) explained in Chapter 2. Similar to the partitioning of the array manifold matrix in (5.9), the signal subspace matrix $\mathbf{U}_{\mathrm{S}}$ can be partitioned

into submatrices as

$$\mathbf{U}_{\mathrm{S}} = \begin{bmatrix} \mathbf{U}_{\mathrm{S},1} \\ \mathbf{U}_{\mathrm{S},2} \\ \vdots \\ \mathbf{U}_{\mathrm{S},K} \end{bmatrix} \tag{5.11}$$

where $\mathbf{U}_{\mathrm{S},k}$ is the submatrix of $\mathbf{U}_{\mathrm{S}}$ corresponding to the k-th subarray.

From the covariance model in (2.15) and (2.19), and as defined in (2.23), there exists an $L \times L$ full-rank matrix $\mathbf{P}$ such that $\mathbf{A}(\boldsymbol{\theta}, \boldsymbol{\Psi}) = \mathbf{U}_{\mathrm{S}}\mathbf{P}$. Then, from (5.9) and (5.11), we have

$$\mathbf{A}_1(\boldsymbol{\theta}) = \mathbf{U}_{\mathrm{S},1}\mathbf{P} \tag{5.12}$$

$$\mathbf{A}_k(\boldsymbol{\theta})\boldsymbol{\Phi}_k(\boldsymbol{\theta}, \boldsymbol{\eta}_k) = \mathbf{U}_{\mathrm{S},k}\mathbf{P} \tag{5.13}$$

for $k = 2, \ldots, K$. Assuming that $L \leq M_1$, the mixing matrix $\mathbf{P}$ can be estimated in the LS sense from (5.12) such that

$$\hat{\mathbf{P}}_{\mathrm{LS}} = \mathbf{U}_{\mathrm{S},1}^{\dagger}\mathbf{A}_1(\boldsymbol{\theta}). \tag{5.14}$$

Replacing $\mathbf{P}$ in (5.13) by its estimate $\hat{\mathbf{P}}_{\mathrm{LS}}$ in (5.14) yields

$$\mathbf{U}_{\mathrm{S},k}\mathbf{U}_{\mathrm{S},1}^{\dagger}\mathbf{A}_1(\boldsymbol{\theta}) = \mathbf{A}_k(\boldsymbol{\theta})\boldsymbol{\Phi}_k(\boldsymbol{\theta}, \boldsymbol{\eta}_k) \tag{5.15}$$

for $k = 2, \ldots, K$.

In order to estimate the DOAs and to calibrate the array, from (5.15) a subspace matching approach is proposed which consists of minimizing the following normalized mismatch functions, for $k = 2, \ldots, K$, over $\boldsymbol{\theta}$ and $\boldsymbol{\eta}_k$

$$g_k(\boldsymbol{\theta}, \boldsymbol{\eta}_k) = \frac{\|\mathbf{U}_{\mathrm{S},k}\mathbf{U}_{\mathrm{S},1}^{\dagger}\mathbf{A}_1(\boldsymbol{\theta}) - \mathbf{A}_k(\boldsymbol{\theta})\boldsymbol{\Phi}_k(\boldsymbol{\theta}, \boldsymbol{\eta}_k)\|^2}{\|\mathbf{U}_{\mathrm{S},k}\mathbf{U}_{\mathrm{S},1}^{\dagger}\mathbf{A}_1(\boldsymbol{\theta})\|^2}. \tag{5.16}$$

From (5.12) and (5.13) it can be seen that the subspace spanned by the k-th subarray, for $k = 2, \ldots, K$, can be related to the subspace spanned by the first subarray through the matrices $\boldsymbol{\Phi}_k(\boldsymbol{\theta}, \boldsymbol{\eta}_k)$, $\mathbf{U}_{\mathrm{S},1}$, and $\mathbf{U}_{\mathrm{S},k}$. Hence, the function $g_k(\boldsymbol{\theta}, \boldsymbol{\eta}_k)$ in (5.16) can be regarded as the subspace mismatch between the two subspaces spanned by the k-th subarray and by the first subarray. The mismatch function in (5.16) is normalized to provide fairness to all the mismatch errors from all the subarrays. Taking all the subarrays into account, the

problem can be formulated into the summation of all the mismatch error functions $g_k(\boldsymbol{\theta}, \boldsymbol{\eta}_k)$ so that we obtain

$$\begin{aligned} h(\boldsymbol{\theta}, \boldsymbol{\eta}_2, \ldots, \boldsymbol{\eta}_K) &= \sum_{k=2}^{K} g_k(\boldsymbol{\theta}, \boldsymbol{\eta}_k) \\ &= \sum_{k=2}^{K} \frac{\|\mathbf{U}_{\mathrm{S},k}\mathbf{U}_{\mathrm{S},1}^{\dagger}\mathbf{A}_1(\boldsymbol{\theta}) - \mathbf{A}_k(\boldsymbol{\theta})\boldsymbol{\Phi}_k(\boldsymbol{\theta}, \boldsymbol{\eta}_k)\|^2}{\|\mathbf{U}_{\mathrm{S},k}\mathbf{U}_{\mathrm{S},1}^{\dagger}\mathbf{A}_1(\boldsymbol{\theta})\|^2} \end{aligned} \tag{5.17}$$

which must be minimized over $\boldsymbol{\theta}, \boldsymbol{\eta}_2, \ldots, \boldsymbol{\eta}_K$ to obtain the DOAs.

We remark that for a particular k the function $g_k(\boldsymbol{\theta}, \boldsymbol{\eta}_k)$ in (5.16) depends only on a single subarray displacement vector $\boldsymbol{\eta}_k$. Therefore, we can minimize (5.16) with respect to $\boldsymbol{\Phi}_k$. Two methods to estimate the displacement-phase matrix $\boldsymbol{\Phi}_k(\boldsymbol{\theta}, \boldsymbol{\eta}_k)$ are introduced in the next subsection.

5.2.2 Methods for Estimating the Displacement-Phase Matrix

Least Squares (LS) Estimation Method of $\boldsymbol{\Phi}_k(\boldsymbol{\theta})$

The displacement-phase matrix $\boldsymbol{\Phi}_k(\boldsymbol{\theta}, \boldsymbol{\eta}_k)$ can be estimated from minimization of $g_k(\boldsymbol{\theta}, \boldsymbol{\eta}_k)$ in (5.16) with respect to $\boldsymbol{\Phi}_k(\boldsymbol{\theta}, \boldsymbol{\eta}_k)$ while the variables in $\boldsymbol{\theta}$ are considered constant. Therefore, assuming $L \leq M_k$ it can be seen that

$$\hat{\boldsymbol{\Phi}}_k(\boldsymbol{\theta}) = \mathbf{A}_k^{\dagger}(\boldsymbol{\theta})\mathbf{U}_{\mathrm{S},k}\mathbf{U}_{\mathrm{S},1}^{\dagger}\mathbf{A}_1(\boldsymbol{\theta}). \tag{5.18}$$

Note that from equation (5.10) the matrix $\boldsymbol{\Phi}_k(\boldsymbol{\theta})$ is diagonal with all the diagonal entries of $\boldsymbol{\Phi}_k$ having unit magnitude, i.e.,

$$|\phi_{k,l}| = 1; \quad l = 1, \ldots, L. \tag{5.19}$$

Therefore, we can enforce this specific structure of $\boldsymbol{\Phi}_k(\boldsymbol{\theta})$ in (5.10) and correspondingly modify the estimate in (5.18) as

$$\hat{\hat{\boldsymbol{\Phi}}}_k(\boldsymbol{\theta}) = \mathcal{D}\{\hat{\boldsymbol{\Phi}}_k(\boldsymbol{\theta})\} \tag{5.20}$$

where $\mathcal{D}\{\cdot\}$ denotes the operator that replaces the off-diagonal entries of a square matrix by zeros and constraints the diagonal entries to unit magnitude, that is for any matrix $\mathbf{X}$

$$\mathcal{D}\{\mathbf{X}\} \triangleq \mathrm{diag}\{e^{-j\measuredangle\{[\mathbf{X}]_{(1,1)}\}}, e^{-j\measuredangle\{[\mathbf{X}]_{(2,2)}\}}, \ldots, e^{-j\measuredangle\{[\mathbf{X}]_{(L,L)}\}}\}. \tag{5.21}$$

Direct Estimation Method of $\boldsymbol{\Phi}_k(\boldsymbol{\theta})$

In this method we try to find a diagonal matrix that minimizes $g_k(\boldsymbol{\theta}, \boldsymbol{\eta}_k)$ instead of forcing the diagonal property onto the matrix that minimizes $g_k(\boldsymbol{\theta}, \boldsymbol{\eta}_k)$. After finding this desired matrix for each $\boldsymbol{\theta}$, we can project the entries of the matrix on the unit-circle to obtain the final estimate. Defining the matrix $\mathbf{G}_{\mathrm{D}}(\boldsymbol{\theta})$ as

$$\mathbf{G}_{\mathrm{D}}(\boldsymbol{\theta}) \triangleq \mathbf{U}_{\mathrm{S},k}\mathbf{U}_{\mathrm{S},1}^{\dagger}\mathbf{A}_1(\boldsymbol{\theta}) \tag{5.22}$$

and assuming that

$$\hat{\boldsymbol{\Phi}}_k(\boldsymbol{\theta}) = \mathrm{diag}\{\hat{\phi}_{k,1}, \hat{\phi}_{k,2}, \ldots, \hat{\phi}_{k,L}\}, \tag{5.23}$$

we can estimate the diagonal entries from (5.16) such that

$$\hat{\phi}_{k,l} = \frac{1}{M_k}\sum_{k'=1}^{M_k}\frac{[\mathbf{A}_k(\boldsymbol{\theta})]_{(k',l)}}{[\mathbf{G}_{\mathrm{D}}(\boldsymbol{\theta})]_{(k',l)}} \tag{5.24}$$

for $l = 1, \ldots, L$. The entries of the displacement-phase matrix all exhibit the unit magnitude property (5.19). Therefore the final estimation of the matrix becomes

$$\hat{\hat{\boldsymbol{\Phi}}}_k(\boldsymbol{\theta}) = \mathrm{diag}\{\hat{\hat{\phi}}_{k,1}, \hat{\hat{\phi}}_{k,2}, \ldots, \hat{\hat{\phi}}_{k,L}\} \tag{5.25}$$

where for $l = 1, \ldots, L$ we define

$$\hat{\hat{\phi}}_{k,l} \triangleq e^{-j\measuredangle\{\hat{\phi}_{k,l}\}}. \tag{5.26}$$

5.2.3 DOA Estimation Using a Multivariate Function

Having estimated the displacement-phase matrix $\boldsymbol{\Phi}_k(\boldsymbol{\theta})$ from either of the two proposed methods of Subsection 5.2.2, we proceed to estimate the DOA vector $\boldsymbol{\theta}$. Substituting $\boldsymbol{\Phi}_k(\boldsymbol{\theta}, \boldsymbol{\eta}_k)$ in (5.16) with its estimate $\hat{\hat{\boldsymbol{\Phi}}}_k(\boldsymbol{\theta})$ either from (5.20) or from (5.25) into (5.17), the concentrated minimization problem becomes equivalent to the minimization of

$$h(\boldsymbol{\theta}) = \sum_{k=2}^{K}\frac{\|\mathbf{U}_{\mathrm{S},k}\mathbf{U}_{\mathrm{S},1}^{\dagger}\mathbf{A}_1(\boldsymbol{\theta}) - \mathbf{A}_k(\boldsymbol{\theta})\hat{\hat{\boldsymbol{\Phi}}}_k(\boldsymbol{\theta})\|^2}{\|\mathbf{U}_{\mathrm{S},k}\mathbf{U}_{\mathrm{S},1}^{\dagger}\mathbf{A}_1(\boldsymbol{\theta})\|^2}. \tag{5.27}$$

Equation (5.27) now only depends on the DOA parameters and can, for example, be solved iteratively using the alternating projection (AP) method of [108].

AP Algorithm for $h(\boldsymbol{\theta})$
Step 1 Compute the initial estimate $\boldsymbol{\theta}_{\text{in}}$.
Step 2 Set $l = 1$.
Step 3 Fix all variables of the vector $\boldsymbol{\theta}$ in $h(\boldsymbol{\theta})$ except for θ_l.
Step 4 Find θ_l that minimizes the function $h(\boldsymbol{\theta})$.
Step 5 Set $l = l + 1$ and go to Step 3 if $l \leq L$.
Step 6 Start over from Step 2 until convergence.

Table 5.1: AP Algorithm for $h(\boldsymbol{\theta})$

The AP approach can sequentially solve the problem (5.27) by optimizing the objective function with respect to a single variable at each iteration while fixing the others and then repeating similar procedure for the remaining variables until convergence. The AP method [108] for the minimization of the multivariate function $h(\boldsymbol{\theta})$ in (5.27) can be summarized as shown in Table 5.1.

There are two issues with this algorithm that should be highlighted. First, an acceptable initial estimate $\boldsymbol{\theta}_{\text{in}}$ is vital at the beginning of the above algorithm. Second, as it was stated in [108], the convergence of the AP method to a global optimum is not guaranteed and critically depends on the initial estimates. To overcome both of these problems, first we propose a method to obtain the initial estimates. Then, based on that, two methods are introduced. Both of these methods use a univariate function instead of the multivariate function proposed in (5.27) which requires costly multi-dimensional search for optimal estimation. Moreover, the proposed methods do not involve any iterations, hence, there is no concern about proper choice of initialization for convergence.

In order to obtain a sufficiently accurate initial DOA estimate, we propose to minimize the function in (5.27) assuming a single source, i.e., replacing the vector $\boldsymbol{\theta}$ with scalar parameter θ, and $\mathbf{A}_k$ with $\mathbf{a}_k$, where $\mathbf{a}_k$ is the known manifold vector of the k-th subarray. In this case, the minimization of the multivariate function of (5.27), which requires an L-dimensional search, is replaced by the minimization of the univariate version of (5.27),

i.e.,

$$\begin{aligned} h(\theta) &= \sum_{k=2}^{K} g_k(\theta) \\ &= \sum_{k=2}^{K} \frac{\|\mathbf{U}_{\mathrm{S},k}\mathbf{U}_{\mathrm{S},1}^{\dagger}\mathbf{a}_1(\theta) - \hat{\hat{\phi}}_k(\theta)\mathbf{a}_k(\theta)\|^2}{\|\mathbf{U}_{\mathrm{S},k}\mathbf{U}_{\mathrm{S},1}^{\dagger}\mathbf{a}_1(\theta)\|^2} \end{aligned} \tag{5.28}$$

where

$$g_k(\theta) = \frac{\|\mathbf{U}_{\mathrm{S},k}\mathbf{U}_{\mathrm{S},1}^{\dagger}\mathbf{a}_1(\theta) - \hat{\hat{\phi}}_k(\theta)\mathbf{a}_k(\theta)\|^2}{\|\mathbf{U}_{\mathrm{S},k}\mathbf{U}_{\mathrm{S},1}^{\dagger}\mathbf{a}_1(\theta)\|^2} \tag{5.29}$$

and

$$\hat{\hat{\phi}}_k(\theta) = \mathcal{D}\{\frac{1}{M_k}\mathbf{a}_k^H(\theta)\mathbf{U}_{\mathrm{S},k}\mathbf{U}_{\mathrm{S},1}^{\dagger}\mathbf{a}_1(\theta)\}, \tag{5.30}$$

which requires a one-dimensional search. The function in (5.28) has at least L minima since the array manifold vector corresponding to each of the L sources can minimize the function. Therefore, in practice, by searching in one-dimension, the L minima of (5.28) are obtained that can be used as the initial DOA estimates for the AP procedure described in Table 5.1. The proposed algorithm is summarized in Table 5.2.

In contrast to the conventional ESPRIT approach [77] and the methods of [16], [66] [80] and [92] which only take into account the known parts of the array, i.e., either the subarray displacements or the sensor placements within the subarray, and ignore the calibration information, our method exploits all the available calibration information about the array. In particular, the proposed method makes use of both the structure of the subarray manifold matrix $\mathbf{A}_k(\boldsymbol{\theta})$ in (5.9) and the subarray displacements in (5.10). Note that the proposed algorithm does not only provide estimates of the DOAs but also simultaneously estimates the displacement-phase matrices $\boldsymbol{\Phi}_2(\boldsymbol{\theta}), \ldots, \boldsymbol{\Phi}_K(\boldsymbol{\theta})$, which can be obtained from (5.20). In other words, the unknown part of the array manifold is blindly reconstructed using our approach.

It is worth mentioning that it is also possible to use the following penalty function

$$h_{\mathrm{D}}(\boldsymbol{\theta}) = \sum_{k=2}^{K} \|\hat{\boldsymbol{\Phi}}_k(\boldsymbol{\theta}) - \hat{\hat{\boldsymbol{\Phi}}}_k(\boldsymbol{\theta})\|^2 \tag{5.31}$$

Algorithm APCA-I

Step 1: Compute $\hat{\mathbf{R}}$ from (2.26) and after its eigen-decompostion obtain $\hat{\mathbf{U}}_{\mathrm{S}}$ and consequently all its submatrices $\hat{\mathbf{U}}_{\mathrm{S},1},\cdots,\hat{\mathbf{U}}_{\mathrm{S},K}$.

Step 2: Calculate $\boldsymbol{\theta}_{\mathrm{in}}$ from L peaks of $h(\theta)$ in (5.28) using $\hat{\hat{\phi}}_k(\theta)$ from (5.30) and applying $\hat{\mathbf{U}}_{\mathrm{S},1},\cdots,\hat{\mathbf{U}}_{\mathrm{S},K}$.

Step 3: Minimize $h(\boldsymbol{\theta})$ in (5.27) using $\hat{\mathbf{U}}_{\mathrm{S},1},\cdots,\hat{\mathbf{U}}_{\mathrm{S},K}$ and $\boldsymbol{\theta}_{\mathrm{in}}$ from Step 2 by applying the AP technique [108] described in Table 5.1. For each $\boldsymbol{\theta}$, calculate $\hat{\boldsymbol{\Phi}}_k(\boldsymbol{\theta})$ for $k = 2,\ldots,K$ either from (5.18) and modify it using $\hat{\hat{\boldsymbol{\Phi}}}_k(\boldsymbol{\theta}) = \mathcal{D}\{\hat{\boldsymbol{\Phi}}_l(\boldsymbol{\theta})\}$ in (5.20) and (5.21), or from (5.24) and (5.25).

Table 5.2: Algorithm APCA-I

for the minimization in Step 3 instead of (5.28) to obtain the DOA estimates. In fact, using (5.31) for DOA estimation can be interpreted as finding a vector $\boldsymbol{\theta}$ that makes the estimated displacement-phase matrix as close as possible in the Frobenius-norm sense, a diagonal matrix with all the entries on the unit-circle.

Interestingly, simulation results in Section 5.5 reveal that even using the initial estimates obtained from the L minima of (5.28) without the costly alternating projection procedure yields in many cases better DOA estimation threshold performance than the existing method [80] for the general partly-calibrated arrays. This motivates the introduction of a low complexity estimation scheme in the next section.

5.2.4 DOA Estimation Using a Univariate Function

The idea of the estimation technique proposed in this subsection is to modify the linear combination (5.28) of the mismatch functions (5.29) from the different subarrays. Instead of uniform weighting of the mismatch functions (5.29) in the function $h(\theta)$ in (5.27), we introduce weighting coefficients such that

$$h_{\mathbf{w}}(\theta) \triangleq \sum_{k=2}^{K} w_k g_k(\theta). \tag{5.32}$$

We define the weighting coefficient vector composed of $(K-1)$ weighting coefficients as

$$\mathbf{w} \triangleq [w_2, w_3, \ldots, w_K]^T . \tag{5.33}$$

It is clear that different choices of the vector $\mathbf{w}$ lead to different estimates. Therefore, in this section we propose two methods to benefit from the effect of the weighting coefficients on the estimates.

The LR Quality Assessment Method

In this subsection the quality assessment approach (see Section 4.3) to evaluate the estimates is presented. It was first introduced for fully-calibrated arrays in [1] and then in [56] (also presented in Chapter 4) it was successfully applied to improve the performance threshold of the DOA estimation. However, in the APCA model the array manifold matrix, which is an essential known element in the LR quality assessment procedure in (4.14), is not completely known. This difference demands some modification in the implementation of the LR quality assessment procedure in the present model. In Section 4.3, the weighted-MUSIC estimator bank combined with the LR procedure was used to select the best weights $\mathbf{w}$ among randomly chosen weights. A similar concept is used in the present subsection to select the best randomly chosen weights in (5.32).

Let us define

$$h_{\mathbf{w}}^{(q)}(\theta) = \sum_{k=2}^{K} w_k^{(q)} g_k(\theta) \tag{5.34}$$

where $w_k^{(q)}$ for $q = 1, \ldots, Q$ and $k = 1, \ldots, K$ are random weighting coefficients. The minimizers of each of the so-obtained one-dimensional weighted mismatch functions in (5.34), for $q = 1, \ldots, Q$, represent Q different DOA estimators. Each of the estimators generates the DOA estimate vector

$$\hat{\boldsymbol{\theta}}^{(q)} = \left[\hat{\theta}_1^{(q)}, \ldots, \hat{\theta}_L^{(q)}\right]^T . \tag{5.35}$$

In order to select the non-outlying estimates from the Q generated estimates, we propose to assign the LR quality assessment value discussed and implemented for fully-calibrated arrays in Section 4.3 ([1] and [56]), to each of sets of estimates. Then, to construct the final

set of estimates, the set of estimates corresponding to the largest LR value is selected. For the q-th estimator, the LR value $\gamma_0(\tilde{\mathbf{R}}^{(q)})$ is computed based on the hypothesis testing (4.20) and (4.21) of the observed sample covariance matrix $\hat{\mathbf{R}}$ and the reconstructed covariance matrix $\tilde{\mathbf{R}}^{(q)}$

$$\tilde{\mathbf{R}}^{(q)} = \hat{\mathbf{A}}(\hat{\boldsymbol{\theta}}^{(q)}, \hat{\boldsymbol{\Psi}}^{(q)})\, \hat{\mathbf{R}}_{\mathrm{s}}\, \hat{\mathbf{A}}^{H}(\hat{\boldsymbol{\theta}}^{(q)}, \hat{\boldsymbol{\Psi}}^{(q)}) + \hat{\sigma^2}\mathbf{I} \tag{5.36}$$

where $\hat{\mathbf{A}}(\hat{\boldsymbol{\theta}}^{(q)}, \hat{\boldsymbol{\Psi}}^{(q)})$ is the estimate of the array manifold matrix using $\hat{\boldsymbol{\theta}}^{(q)}$ and $\hat{\boldsymbol{\Psi}}^{(q)}$. The matrix $\hat{\mathbf{R}}_{\mathrm{s}}$ is the estimated source covariance matrix obtained similar to (4.16) from

$$\hat{\mathbf{R}}_{\mathrm{s}} = \mathrm{diag}_{+}\{\hat{\mathbf{A}}^{\dagger}(\hat{\boldsymbol{\theta}}^{(q)}, \hat{\boldsymbol{\Psi}}^{(q)}) \left[\hat{\mathbf{R}} - \hat{\sigma^2}\mathbf{I}\right] \hat{\mathbf{A}}^{\dagger H}(\hat{\boldsymbol{\theta}}^{(q)}, \hat{\boldsymbol{\Psi}}^{(q)})\} \tag{5.37}$$

and $\hat{\sigma^2}$ denotes the noise power estimated from (4.15). Then the LR quality assessment value for the q-th set of estimates can be calculated from

$$\gamma_0^{(q)} \triangleq \frac{\det\{\tilde{\mathbf{R}}^{(q)^{-1}}\hat{\mathbf{R}}\}}{\left[\frac{1}{M}\mathrm{tr}(\tilde{\mathbf{R}}^{(q)^{-1}}\hat{\mathbf{R}})\right]^{M}}. \tag{5.38}$$

We remark that in order to compute the reconstructed covariance matrix $\tilde{\mathbf{R}}^{(q)}$ in (5.36), the complete knowledge of the array manifold matrix is required. In the case of PCAs, this knowledge is only partly available a priori since the displacement vectors and consequently the displacement-phase matrices $\boldsymbol{\Phi}_2, \ldots, \boldsymbol{\Phi}_K$ are unknown. However, the entries of the displacement-phase matrices can be estimated using (5.30) during the DOA estimation process such that the complete required estimated array manifold matrix becomes

$$\hat{\mathbf{A}}(\hat{\boldsymbol{\theta}}^{(q)}, \hat{\boldsymbol{\Psi}}^{(q)}) = \begin{bmatrix} \mathbf{a}_1(\hat{\theta}_1) & \cdots & \mathbf{a}_1(\hat{\theta}_L) \\ \mathbf{a}_2(\hat{\theta}_1)\hat{\hat{\phi}}_2(\hat{\theta}_1) & \cdots & \mathbf{a}_2(\hat{\theta}_L)\hat{\hat{\phi}}_2(\hat{\theta}_L) \\ \vdots & \vdots & \vdots \\ \mathbf{a}_K(\hat{\theta}_1)\hat{\hat{\phi}}_K(\hat{\theta}_1) & \cdots & \mathbf{a}_K(\hat{\theta}_L)\hat{\hat{\phi}}_K(\hat{\theta}_L) \end{bmatrix}. \tag{5.39}$$

The proposed algorithm is summarized in Table 5.3.

Note, that the complete manifold matrix has already been estimated for each of set of the estimates $\hat{\boldsymbol{\theta}}^{(q)}$ in the Q estimators in Step 6. Having obtained the final set of DOA estimates, we can select its associated manifold matrix in Step 6 as the final set of estimate of the complete array manifold matrix.

Algorithm APCA-II

Step 1: Compute $\hat{\mathbf{R}}$ from (2.26) and after its eigen-decompostion from (2.28) obtain $\hat{\mathbf{U}}_{\mathrm{S}}$ and consequently all its submatrices $\hat{\mathbf{U}}_{\mathrm{S},1},\cdots,\hat{\mathbf{U}}_{\mathrm{S},K}$ from (5.11).

Step 2: Calculate $g_2(\theta),\ldots,g_K(\theta)$ from (5.29) and (5.30) for each subarray and for all the values of θ in the FOV.

Step 3: Generate Q random weight vectors $\mathbf{w}^{(1)},\mathbf{w}^{(2)}\ldots,\mathbf{w}^{(Q)}$.

Step 4: Compute $h_{\mathbf{w}}^{(1)}(\theta),h_{\mathbf{w}}^{(2)}(\theta),\ldots,h_{\mathbf{w}}^{(Q)}(\theta)$ from (5.34) using the generated weights $\mathbf{w}^{(1)},\mathbf{w}^{(2)},\ldots,\mathbf{w}^{(Q)}$ and the functions $g_2(\theta),\ldots,g_K(\theta)$.

Step 5: Estimate the DOAs $\hat{\boldsymbol{\theta}}^{(q)}$ for each of the Q estimators from the L minima of the function $h_{\mathbf{w}}^{(q)}(\theta)$.

Step 6: Estimate the array manifold matrix for each of the Q estimators based on $\hat{\boldsymbol{\theta}}^{(q)}$, from the modification of (5.30) and then from (5.39).

Step 7: Calculate $\gamma_0^{(q)}(\tilde{\mathbf{R}}^{(q)})$ from (5.38) for each of the estimated DOAs $\hat{\boldsymbol{\theta}}^{(q)}$.

Step 8: Select the set of the DOA estimates associated with the largest value of the LR quality value among the estimated DOA sets of the Q random estimators as the final estimated DOA set $\hat{\boldsymbol{\theta}}$.

Table 5.3: Algorithm APCA-II

We remark that in the minimization of (5.34) for different $q=1,\ldots,Q$ it is sufficient to evaluate each of the normalized mismatch functions $g_k(\theta)$, for different values of θ in the FOV, only once, regardless of the number of estimators Q. Then, the linear combinations in (5.34) can easily be computed even when the number of estimators Q is large. Therefore, the number of estimators Q has moderate effect on the computational complexity of the proposed algorithm.

The Minimum Least Squares Error (MLSE) Method

In this subsection, we develop a suboptimal procedure for selecting the weighting coefficients that does not involve the costly computation of the LR values in (5.38). This approach is

based on finding the weighting coefficients which yields the minimum least squares error of the sum of the mismatch functions in (5.29) among the randomly generated coefficients. In contrast to the previous technique in Subsection 5.2.4 for the estimation of each of the DOAs in $\boldsymbol{\theta}$, as we shall see later, a different set of coefficients might be the "best" one. The proposed method is based on the consideration that there might be no single set of coefficients which yields the uniformly best estimation performance for all the DOAs $\theta_1, \theta_2, \ldots, \theta_L$.

The problem of finding proper weighting coefficients for $h_{\mathbf{w}}(\theta)$ in (5.34) to estimate the DOAs can be formulated as finding L weight vectors $\mathbf{w}$ that minimize the L minima of $h_{\mathbf{w}}(\theta)$. To prevent the trivial solution of $\mathbf{w} = \mathbf{0}$, the norm of the weighting coefficient vector $\mathbf{w}$ is restricted such that

$$\|\mathbf{w}\| = 1. \tag{5.40}$$

This problem is highly non-linear and non-convex with respect to the parameter θ and is generally difficult to solve. Therefore, we propose a suboptimal method to estimate DOAs and their corresponding $\mathbf{w}$. We suggest to generate a number of random weighting coefficients similar to forming Q random estimators $h_{\mathbf{w}}^{(q)}(\theta)$ from (5.34) in the previous section. The weight vectors $\mathbf{w}^{(q)}$, for $q = 1, \ldots, Q$, are drawn randomly from a Q-dimensional hypersphere to satisfy the constraint in (5.40). Here, we propose using a computationally simple method to select the estimates. Let us assume that for each $\mathbf{w}^{(q)}$, for $q = 1, \ldots, Q$, the DOA estimates $\hat{\theta}_1^{(q)}, \hat{\theta}_2^{(q)}, \ldots, \hat{\theta}_L^{(q)}$ are obtained after sorting out, along with their mismatch error functions $h_{\mathbf{w}}^{(q)}(\hat{\theta}_1), h_{\mathbf{w}}^{(q)}(\hat{\theta}_2), \ldots, h_{\mathbf{w}}^{(q)}(\hat{\theta}_L)$ defined in (5.34), respectively. Then, for each of the L sources from the whole set of estimates defined as

$$\hat{\boldsymbol{\theta}}_l \triangleq \left[\hat{\theta}_l^{(1)}, \hat{\theta}_l^{(2)}, \ldots, \hat{\theta}_l^{(Q)}\right]^T, \tag{5.41}$$

for $l = 1, \ldots, L$, the one that yields the minimum mismatch error, say $h_{\mathbf{w}}^{(q_l)}(\hat{\theta}_l^{(q_l)})$, is selected and its associated DOA estimate is considered as the final estimate $\hat{\theta}_l^{(q_l)}$ for the l-th source. It should be noted that the superscript "(q_l)", for $l = 1, \ldots, L$, has a value from the set $\{1, \ldots, Q\}$ but can be different depending on l, hence referred to as q_l, since it corresponds to the estimator that yields the minimum value of the mismatch error for the l-th source.

Algorithm APCA-III

Step 1: Compute $\hat{\mathbf{R}}$ from (2.26) and after its eigen-decompostion from (2.28) obtain $\hat{\mathbf{U}}_{\mathrm{S}}$ and consequently all its submatrices $\hat{\mathbf{U}}_{\mathrm{S},1},\cdots,\hat{\mathbf{U}}_{\mathrm{S},K}$ from (5.11).

Step 2: Calculate $g_2(\theta),\ldots,g_K(\theta)$ from 5.29) and (5.30) for each subarray and for all the values of θ in the FOV.

Step 3: Generate Q random weight vectors $\mathbf{w}^{(1)},\mathbf{w}^{(2)},\ldots,\mathbf{w}^{(Q)}$ such that $\|\mathbf{w}^{(q)}\|=1$ for $q=1,\ldots,Q$.

Step 4: Compute $h_{\mathbf{w}}^{(1)}(\theta),h_{\mathbf{w}}^{(2)}(\theta),\ldots,h_{\mathbf{w}}^{(Q)}(\theta)$ from (5.34) using the generated weights $\mathbf{w}^{(1)},\mathbf{w}^{(2)},\ldots,\mathbf{w}^{(Q)}$ and the error functions $g_2(\theta),\ldots,g_K(\theta)$.

Step 5: Estimate the DOAs $\hat{\theta}_1^{(q)},\hat{\theta}_2^{(q)},\ldots,\hat{\theta}_L^{(q)}$ for each of the Q estimators from the L minima of $h_{\mathbf{w}}^{(q)}(\theta)$.

Step 6: For $l=1,\ldots,L$ find the estimate $\hat{\theta}_l$ with the minimum value of the mismatch error function (5.34) from $\hat{\boldsymbol{\theta}}_l \triangleq \left[\hat{\theta}_l^{(1)},\hat{\theta}_l^{(2)},\ldots,\hat{\theta}_l^{(Q)}\right]^T$.

Table 5.4: Algorithm APCA-III

At the end, the final estimate is constructed from the same procedure for all the L sources so that

$$\hat{\boldsymbol{\theta}} = \left[\hat{\theta}_1^{(q_1)},\hat{\theta}_2^{(q_2)},\ldots,\hat{\theta}_L^{(q_L)}\right]^T. \tag{5.42}$$

The proposed algorithm is summarized in Table 5.4.

Comparing Algorithm APCA-II and Algorithm APCA-III, the latter algorithm offers lower computational complexity since there is no need for additional calculation of the LR value. Moreover, Algorithm APCA-III, as shown in the simulations, slightly outperforms Algorithm APCA-II. The reason is that in Algorithm APCA-II, the estimate of the array manifold is used in calculating the LR value $\gamma_0^{(q)}(\tilde{\mathbf{R}}^{(q)})$ and this, in the threshold regions, generally results in a very low LR values even for acceptable DOA estimates and therefore, distinguishing the proper estimates and the outlying ones becomes difficult.

5.3 Partly-Calibrated Array Composed of Multiple Identical Subarrays (PCAMIS)

In this section, a special scenario for the general PCA model, shown in Fig. 2.3, is studied where all the subarrays are identical. This model is in accordance with Scenario III described in Chapter 2. Generally, the algorithms presented in this section can be applied to both the cases where the subarrays are unknown and the displacements are known or vice versa. The idea behind the proposed algorithms is similar to the one explained in Section 5.2 in this sense that the unknown array geometry-dependent part and its structure is exploited in the estimation of the DOAs. We propose different new techniques, each with its own advantages mostly in terms of computational complexity, to estimate the DOAs and the unknown array-geometry dependent part be it the subarray manifold or the displacement-phase matrix. The simulated performance of the proposed algorithms shows improvement compared to the competing methods.

5.3.1 Signal Model for PCAMIS

Consider a sensor array of M identical sensors, as depicted in Fig. 2.3, that contains K non-overlapping identical subarrays of M_1 sensors each, such that $M = KM_1$. The k-th displacement vector $\boldsymbol{\eta}_k = [\alpha_k, \beta_k]^T$ between the first and the k-th subarray, for $k = 1, \ldots, K$, is assumed to be arbitrary yet exactly known, and there is no information available about the geometry of the identical subarrays. The unknown $2\times(K-1)$ array geometry-dependent matrix in this model is defined as the sensor locations of the first subarray

$$\boldsymbol{\Psi} \triangleq \left[\begin{pmatrix} x_2 \\ y_2 \end{pmatrix}, \begin{pmatrix} x_3 \\ y_3 \end{pmatrix}, \ \ldots \ , \begin{pmatrix} x_{M_1} \\ y_{M_1} \end{pmatrix} \right]. \tag{5.43}$$

It can be considered that this model is a generalization of the model in ESPRIT [77]. It is clear that if there are only two subarrays, then the array model reduces to the well-known shift invariant sensor arrays that are exploited in the ESPRIT algorithm. We remark, that this type of PCA geometry can be modeled from two slightly different perspectives,

which can be interchangeably used. The PCA geometry presented in this subsection can be regarded as an array with known subarrays and unknown displacement vectors as, e.g., in [16] ,[58] and [66]. Alternatively, it can also be viewed as an array composed of unknown subarrays, yet with known displacement vectors between the subarrays as, e.g., in [77] and [92]. In the present text, we adopt the latter point-of-view on the array model to estimate the DOAs and their corresponding array manifold vectors.

Let us assume that all sensors in the array are omni-directional with equal gain, and the signals from L ($\leq M_1$) uncorrelated narrow-band far-field sources impinge on the array from the unknown DOAs. The t-th snapshot of the $M \times 1$ received signal vector $\mathbf{z}(t)$ can be written as in (2.6) where

$$\mathbf{A}(\boldsymbol{\theta}, \boldsymbol{\Psi}) \triangleq [\mathbf{a}(\theta_1, \boldsymbol{\Psi})\ \mathbf{a}(\theta_2, \boldsymbol{\Psi})\ \cdots\ \mathbf{a}(\theta_L, \boldsymbol{\Psi})] = \begin{bmatrix} \mathbf{A}_1(\boldsymbol{\theta}, \boldsymbol{\Psi}) \\ \mathbf{A}_2(\boldsymbol{\theta}, \boldsymbol{\Psi}) \\ \vdots \\ \mathbf{A}_K(\boldsymbol{\theta}, \boldsymbol{\Psi}) \end{bmatrix} \tag{5.44}$$

is the $M \times L$ array manifold matrix defined in (2.11) with $\mathbf{a}(\theta_l, \boldsymbol{\Psi})$ as its l-th column defined in (2.12) and the $M_1 \times L$ submatrix $\mathbf{A}_k(\boldsymbol{\theta})$ defined as the k-th subarray manifold matrix

$$\mathbf{A}_k(\boldsymbol{\theta}, \boldsymbol{\Psi}) \triangleq [\mathbf{a}_k(\theta_1, \boldsymbol{\Psi})\ \mathbf{a}_k(\theta_2, \boldsymbol{\Psi})\ \cdots\ \mathbf{a}_k(\theta_L, \boldsymbol{\Psi})]\,. \tag{5.45}$$

Taking into account the displacement vectors, we write

$$\mathbf{A}_k(\boldsymbol{\theta}, \boldsymbol{\Psi}) = \mathbf{A}_1(\boldsymbol{\theta}, \boldsymbol{\Psi})\boldsymbol{\Phi}_k(\boldsymbol{\theta}) \tag{5.46}$$

where the $L \times L$ diagonal matrix $\boldsymbol{\Phi}_k(\boldsymbol{\theta})$ represents the displacement-phase matrix and can be expressed as

$$\boldsymbol{\Phi}_k(\boldsymbol{\theta}) \triangleq \mathrm{diag}\{\phi_{k,1}, \phi_{k,2}, \ldots, \phi_{k,L}\} \tag{5.47}$$

where

$$\phi_{k,l} \triangleq e^{-j(2\pi/\lambda)(\alpha_k \sin\theta_l + \beta_k \cos\theta_l)}. \tag{5.48}$$

It should be emphasized that in this scenario the displacement vectors are perfectly known, and thus $\boldsymbol{\Phi}_k(\boldsymbol{\theta})$ only depends on the unknown DOAs. The array manifold matrix of the

first subarray $\mathbf{A}_1(\boldsymbol{\theta}, \boldsymbol{\Psi})$ is, however, unknown and depends on the unknown array geometry-dependent parameters as well.

We can partition the matrix $\mathbf{U}_{\mathrm{S}}$ similar to $\mathbf{A}(\boldsymbol{\theta}, \boldsymbol{\Psi})$ in (5.44) as in (5.11) where $\mathbf{U}_{\mathrm{S},k}$, for $k = 1, \ldots, K$, is in this scenario the $M_1 \times L$ submatrix of $\mathbf{U}_{\mathrm{S}}$ that corresponds to the k-th subarray. Correspondingly, $\hat{\mathbf{U}}_{\mathrm{S},1}, \hat{\mathbf{U}}_{\mathrm{S},2}, \ldots, \hat{\mathbf{U}}_{\mathrm{S},K}$ are defined as the sample counterparts of $\mathbf{U}_{\mathrm{S},1}, \mathbf{U}_{\mathrm{S},2}, \ldots, \mathbf{U}_{\mathrm{S},K}$, respectively.

The signal subspace matrix and the array manifold matrix span the same subspace and are related to each other through the $L \times L$ full-rank mixing matrix $\mathbf{P}$ in (2.23). The matrix $\mathbf{P}$ can be represented by its columns such that

$$\mathbf{P} = [\mathbf{p}(\theta_1), \mathbf{p}(\theta_2), \cdots, \mathbf{p}(\theta_L)]\,. \tag{5.49}$$

Notice that the l-th column of $\mathbf{P}$ corresponds to the l-th signal only. The notation in (5.49) in which the dependency of the columns of $\mathbf{P}$ on the true DOAs is explicitly expressed turns out to be helpful later on when we describe our DOA estimation algorithm. From (2.23) and (5.11), we can construct $K - 1$ pairs of equations such that

$$\begin{aligned} \mathbf{A}_1(\boldsymbol{\theta}, \boldsymbol{\Psi}) &= \mathbf{U}_{\mathrm{S},1}\mathbf{P} \\ \mathbf{A}_k(\boldsymbol{\theta}, \boldsymbol{\Psi}) &= \mathbf{U}_{\mathrm{S},k}\mathbf{P} \end{aligned} \tag{5.50}$$

for $k = 2, \ldots, K$. Let us define the parametric displacement-phase function for each of the $K - 1$ displacements as

$$\phi_k(\theta) \triangleq e^{-j(2\pi/\lambda)(\alpha_k \sin\theta + \beta_k \cos\theta)} \tag{5.51}$$

for $k = 2, \ldots, K$.

In order to estimate the DOAs, we propose a method that first estimates the array manifold vector $\mathbf{a}_1(\theta)$ for each angle in the FOV from which the DOAs can then be estimated. From here, two paths can be followed to estimate $\mathbf{a}_1(\theta, \boldsymbol{\Psi})$. One way is to estimate first the vector $\mathbf{p}(\theta)$ to then obtain $\mathbf{a}_1(\theta, \boldsymbol{\Psi})$, and the other is to directly estimate $\mathbf{a}_1(\theta, \boldsymbol{\Psi})$ without any intermediate step.

5.3.2 Indirect Estimation of the Manifold Vector

Similar to [16] and [67], we write

$$\big(\mathbf{U}_{\mathrm{S},k} - \phi_k(\theta)\mathbf{U}_{\mathrm{S},1}\big)\mathbf{p}(\theta) = \mathbf{a}_k(\theta, \mathbf{\Psi}) - \phi_k(\theta)\mathbf{a}_1(\theta, \mathbf{\Psi}). \tag{5.52}$$

It can be observed from (5.50) and (5.51) that for the true DOAs $\theta_1, \ldots, \theta_L$, the right-hand side of (5.52) becomes equal to zero. In other words, $\mathbf{p}(\theta_l)$ lies in the null-space of the matrix $\mathbf{U}_{\mathrm{S},k} - \phi_k(\theta_l)\mathbf{U}_{\mathrm{S},1}$, that is

$$\mathcal{R}\{\mathbf{p}(\theta_l)\} = \mathcal{N}\{\mathbf{U}_{\mathrm{S},k} - \phi_k(\theta_l)\mathbf{U}_{\mathrm{S},1}\} \tag{5.53}$$

where $\mathcal{R}\{\cdot\}$ and $\mathcal{N}\{\cdot\}$ denote the range-space and the null-space of a matrix, respectively.

Let us define the $(M - M_1) \times L$ matrix $\mathbf{D}(\theta)$ such that

$$\mathbf{D}(\theta) \triangleq \begin{bmatrix} \mathbf{U}_{\mathrm{S},2} - \phi_2(\theta)\mathbf{U}_{\mathrm{S},1} \\ \mathbf{U}_{\mathrm{S},3} - \phi_3(\theta)\mathbf{U}_{\mathrm{S},1} \\ \vdots \\ \mathbf{U}_{\mathrm{S},K} - \phi_K(\theta)\mathbf{U}_{\mathrm{S},1} \end{bmatrix} \tag{5.54}$$

then, for $\theta = \theta_1, \ldots, \theta_L$, the columns of $\mathbf{P}$, i.e., $\mathbf{p}(\theta_1), \ldots, \mathbf{p}(\theta_L)$, are the eigenvectors associated with the zero eigenvalues of the matrix $\mathbf{D}^H(\theta)\mathbf{D}(\theta)$. In other words, for the true DOAs the columns of the mixing matrix $\mathbf{P}$ in (5.49) are the L minor eigenvectors of $\mathbf{D}^H(\theta)\mathbf{D}(\theta)$. Hence, for the true DOAs

$$\mathbf{p}(\theta) = \mathcal{V}_{\min}\{\mathbf{D}^H(\theta)\mathbf{D}(\theta)\} \tag{5.55}$$

where $\mathcal{V}_{\min}\{\cdot\}$ denotes the eigenvector corresponding to the smallest eigenvalue, i.e., the minor eigenvector.

Interestingly, it was shown in [67], that the RARE criteria in [66] and [80] corresponds to a search for angles θ for which the matrix $\mathbf{D}^H(\theta)\mathbf{D}(\theta)$ becomes singular. However, unlike in the RARE method, we propose to make use of the structure of the unknown manifold vectors to enhance the DOA estimation accuracy. From (5.50) and (5.55), we can express the manifold vectors as

$$\begin{aligned} \mathbf{a}_k(\theta_l, \mathbf{\Psi}) &= \mathbf{U}_{\mathrm{S},1}\mathbf{p}(\theta_l)\phi_k(\theta_l) \\ &= \mathbf{a}_1(\theta_l, \mathbf{\Psi})\phi_k(\theta_l) \end{aligned} \tag{5.56}$$

where

$$\mathbf{a}_1(\theta_l, \mathbf{\Psi}) = \mathbf{U}_{\mathrm{S},1}\mathbf{p}(\theta_l). \tag{5.57}$$

Inserting the manifold vectors (5.56) and (5.57) into the MUSIC criterion [78] we obtain for the true DOAs

$$\begin{aligned} f_{\mathrm{PCAMIS}}(\theta) &\triangleq \mathbf{a}^H(\theta, \mathbf{\Psi})\mathbf{U}_{\mathrm{N}}\mathbf{U}_{\mathrm{N}}^H\mathbf{a}(\theta, \mathbf{\Psi}) \\ &= \sum_{k=1}^{K} \mathbf{a}_k^H(\theta_l, \mathbf{\Psi})\mathbf{U}_{\mathrm{N},k}\mathbf{U}_{\mathrm{N},k}^H\mathbf{a}_k(\theta_l, \mathbf{\Psi}) \\ &= \sum_{k=1}^{K} \phi_k^*(\theta)\mathbf{a}_1^H(\theta_l, \mathbf{\Psi})\mathbf{U}_{\mathrm{N},k}\mathbf{U}_{\mathrm{N},k}^H\mathbf{a}_1(\theta_l, \mathbf{\Psi})\phi_k(\theta) \\ &= \sum_{k=1}^{K} \phi_k^*(\theta)\mathbf{p}^H(\theta)\mathbf{U}_{\mathrm{S},1}^H\mathbf{U}_{\mathrm{N},k}\mathbf{U}_{\mathrm{N},k}^H\mathbf{U}_{\mathrm{S},1}\mathbf{p}(\theta)\phi_k(\theta) \\ &= 0 \end{aligned} \tag{5.58}$$

where the $M_1 \times (M - L)$ matrix $\mathbf{U}_{\mathrm{N},k}$ for $k = 1, \ldots, K$ is the k-th submatrix of the noise subspace matrix $\mathbf{U}_{\mathrm{N}}$ partitioned as

$$\mathbf{U}_{\mathrm{N}} = \begin{bmatrix} \mathbf{U}_{\mathrm{N},1} \\ \mathbf{U}_{\mathrm{N},2} \\ \vdots \\ \mathbf{U}_{\mathrm{N},K} \end{bmatrix}. \tag{5.59}$$

Moreover, we assume $\phi_1(\theta) = 1$ to be consistent with the definition of $\phi_k(\theta)$ in (5.51).

It is important to notice that there is a scaling ambiguity in the eigenvector $\mathbf{p}(\theta)$ in (5.55) which has no effect on the function value of (5.58) computed at the true DOAs in (5.58). However, we need to prevent the function in (5.58) to become zero for values of θ other than the true DOAs as this would lead to ambiguities in the solution of (5.58). In the array signal model in Section 5.3.1 we assumed that for the special case of omni-directional identical sensors, all the entries of the true vector $\mathbf{a}_1(\theta)$, and subsequently $\mathbf{a}_k(\theta)$, lie on the unit circle in the complex plane. Therefore, to avoid the ambiguities we suggest taking advantage of the nominal structure of the manifold vector in (5.44) and imposing this structure to $\mathbf{a}(\theta)$ for all the angles θ in the function (5.58). To this end, the following

two-step structure-imposing operation on $\mathbf{a}(\theta)$ is proposed: First, to remove any negative effects of the scaling ambiguity of $\mathbf{p}(\theta)$ on the small values of $f_{\text{PCAMIS}}(\theta)$, we can normalize the entries of $\mathbf{a}_1(\theta)$ or equivalently $\mathbf{U}_{\text{S},1}\mathbf{p}(\theta)$ in (5.58) to its entry with minimum absolute value. Second, we can project all the entries of $\mathbf{a}_1(\theta)$ onto the unit circle by normalizing each entry to its own absolute value. We should note that this structure-imposing operation has no effect on the function for the true DOAs, since in the ideal case of the true DOAs, the structure is implicitly present in the array manifold vector.

In the finite sample case, our proposed algorithm for estimating the DOAs can be summarized as shown in Table 5.5.

5.3.3 Direct Estimation of the Manifold Vector

From (5.50) and for $k = 2, \ldots, K$ it follows that

$$\mathbf{U}_{\text{S},1}\mathbf{U}_{\text{S},k}^{\dagger}\mathbf{A}_k(\boldsymbol{\theta}, \boldsymbol{\Psi}) = \mathbf{A}_1(\boldsymbol{\theta}, \boldsymbol{\Psi}). \tag{5.65}$$

Using (5.50) and the relation between the first and the k-th subarrays

$$\mathbf{a}_k(\theta) = \phi_k(\theta)\mathbf{a}_1(\theta, \boldsymbol{\Psi}) \tag{5.66}$$

for $\theta = \theta_1, \ldots, \theta_L$, we can write

$$\phi_k(\theta_l)\mathbf{U}_{\text{S},1}\mathbf{U}_{\text{S},k}^{\dagger}\mathbf{a}_1(\theta, \boldsymbol{\Psi}) = \mathbf{a}_1(\theta, \boldsymbol{\Psi}). \tag{5.67}$$

Therefore, the array manifold vectors of the first subarray $\mathbf{a}_1(\theta, \boldsymbol{\Psi})$ for $\theta = \theta_1, \ldots, \theta_L$ can be estimated by solving the following equations

$$\left(\mathbf{I} - \phi_k(\theta)\mathbf{U}_{\text{S},1}\mathbf{U}_{\text{S},k}^{\dagger}\right)\mathbf{a}_1(\theta, \boldsymbol{\Psi}) = \mathbf{0} \tag{5.68}$$

for $k = 2, \ldots, K$, subject to the constraint

$$\|\mathbf{a}_1(\theta, \boldsymbol{\Psi})\| = \text{const.} \tag{5.69}$$

Algorithm PCAMIS-I

Step 1: Estimate the signal- and noise subspace matrices $\hat{\mathbf{U}}_{\mathrm{S}}$ and $\hat{\mathbf{U}}_{\mathrm{N}}$, respectively, from $\hat{\mathbf{R}}$ in (2.26).

Step 2: Define

$$\hat{\mathbf{D}}(\theta) \triangleq \begin{bmatrix} \hat{\mathbf{U}}_{\mathrm{S},2} - \phi_2(\theta)\hat{\mathbf{U}}_{\mathrm{S},1} \\ \hat{\mathbf{U}}_{\mathrm{S},3} - \phi_3(\theta)\hat{\mathbf{U}}_{\mathrm{S},1} \\ \vdots \\ \hat{\mathbf{U}}_{\mathrm{S},K} - \phi_K(\theta)\hat{\mathbf{U}}_{\mathrm{S},1} \end{bmatrix}. \tag{5.60}$$

Step 3: Compute the minor eigenvector

$$\hat{\mathbf{p}}(\theta) = \mathcal{V}_{\min}\{\hat{\mathbf{D}}^H(\theta)\hat{\mathbf{D}}(\theta)\} \tag{5.61}$$

for all θ in the search-grid of the FOV.

Step 4: Estimate the manifold vector $\mathbf{a}(\theta)$ for each θ in the FOV from

$$\hat{\mathbf{a}}_1(\theta) = \hat{\mathbf{U}}_{\mathrm{S},1}\hat{\mathbf{p}}(\theta) \tag{5.62}$$

and normalize the entries of $\hat{\mathbf{a}}_1(\theta)$ to the entry with minimum absolute value.

Step 5: In the case of omni-directional sensors, project the entries of $\hat{\mathbf{a}}_1(\theta)$ in (5.62) onto the unit circle to obtain an improved estimate of the manifold vector $\hat{\hat{\mathbf{a}}}_1(\theta)$, i.e.,

$$[\hat{\hat{\mathbf{a}}}_1(\theta)]_{(m)} = \frac{[\hat{\mathbf{a}}_1(\theta)]_{(m)}}{|[\hat{\mathbf{a}}_1(\theta)]_{(m)}|} \tag{5.63}$$

for $m = 1, \ldots, M_1$.

Step 6: Estimate the DOAs from the L peaks of the following function

$$f_{\mathrm{PCAMIS1}}(\theta) = \frac{1}{\sum_{k=1}^{K} \phi_k^*(\theta)\hat{\hat{\mathbf{a}}}_1^H(\theta)\hat{\mathbf{U}}_{\mathrm{N},k}\hat{\mathbf{U}}_{\mathrm{N},k}^H\hat{\hat{\mathbf{a}}}_1(\theta)\phi_k(\theta)}. \tag{5.64}$$

Table 5.5: Algorithm PCAMIS-I

The latter constraint is required to avoid the trivial solution $\mathbf{a}_1 = \mathbf{0}$. Let us define the $(M - M_1) \times M_1$ matrix $\mathbf{D}_{\mathrm{I}}(\theta)$ such that

$$\mathbf{D}_{\mathrm{I}}(\theta) \triangleq \begin{bmatrix} \mathbf{I} - \phi_k(\theta)\mathbf{U}_{\mathrm{S},1}\mathbf{U}_{\mathrm{S},2}^{\dagger} \\ \mathbf{I} - \phi_k(\theta)\mathbf{U}_{\mathrm{S},1}\mathbf{U}_{\mathrm{S},3}^{\dagger} \\ \vdots \\ \mathbf{I} - \phi_k(\theta)\mathbf{U}_{\mathrm{S},1}\mathbf{U}_{\mathrm{S},K}^{\dagger} \end{bmatrix}. \tag{5.70}$$

Therefore, it is clear that for the true DOAs, $\mathbf{a}_1(\theta)$ is a nonzero vector that lies in the null-space of the matrix $\mathbf{D}_{\mathrm{I}}(\theta)$. In other words,

$$\mathbf{a}_1(\theta, \mathbf{\Psi}) = \mathcal{V}_{\min}\{\mathbf{D}_{\mathrm{I}}^H(\theta)\mathbf{D}_{\mathrm{I}}(\theta)\}. \tag{5.71}$$

The first entry of the array manifold vector is assumed to be equal to one, since the first sensor is considered as the reference sensor. Hence, in practice, all the entries of the estimated manifold vector should be normalized to the first entry. As a further refinement in the practical case, and in the case of omni-directional sensors, the estimated manifold vector $\mathbf{a}_1(\theta)$ can be forced to be placed on the unit-circle by normalizing each entry of the estimated vector to its absolute value. This structure-imposing, which is important to obtain unique estimates, consequently improves the DOA estimation performance significantly. In order to estimate the DOAs, a similar procedure should be performed as in Section 5.3.2, i.e., the estimated manifold vector can be used in the MUSIC spectrum function. The overall procedure is similar to the scheme proposed in Section 5.3.2 with the important difference that instead of estimating $\mathbf{p}(\theta)$ in Step 3 of PCAMIS-II, the manifold vector $\mathbf{a}_1(\theta)$ is obtained directly. The proposed algorithm is summarized in Table 5.6.

As a by-product of the proposed approaches, i.e., Algorithms PCAMIS-I and PCAMIS-II, the manifold vectors can be estimated as $\left\{\hat{\hat{\mathbf{a}}}(\hat{\theta}_l)\right\}_{l=1}^{L}$. As it can be observed, these techniques also allow the estimation of the manifold vector of the uncalibrated parts of the array, i.e., the vectors $\mathbf{a}_1(\theta)$. Therefore, the proposed algorithms provide the calibration information for the unknown subarrays simultaneously along with the estimates of the DOAs.

Algorithm PCAMIS-II

Step 1: Estimate the signal- and noise subspace matrices $\hat{\mathbf{U}}_{\mathrm{S}}$ and $\hat{\mathbf{U}}_{\mathrm{N}}$, respectively, from $\hat{\mathbf{R}}$ in (2.26).

Step 2: Define

$$\hat{\mathbf{D}}_{\mathrm{I}}(\theta) \triangleq \begin{bmatrix} \mathbf{I} - \phi_k(\theta)\hat{\mathbf{U}}_{\mathrm{S},1}\hat{\mathbf{U}}_{\mathrm{S},k}^{\dagger} \\ \mathbf{I} - \phi_k(\theta)\hat{\mathbf{U}}_{\mathrm{S},1}\hat{\mathbf{U}}_{\mathrm{S},k}^{\dagger} \\ \vdots \\ \mathbf{I} - \phi_k(\theta)\hat{\mathbf{U}}_{\mathrm{S},1}\hat{\mathbf{U}}_{\mathrm{S},k}^{\dagger} \end{bmatrix}. \tag{5.72}$$

Step 3: Compute the minor eigenvector

$$\hat{\mathbf{a}}_1(\theta) = \mathcal{V}_{\min}\{\hat{\mathbf{D}}_{\mathrm{I}}^H(\theta)\hat{\mathbf{D}}_{\mathrm{I}}(\theta)\} \tag{5.73}$$

for all θ in the search-grid of the FOV and normalize the entries of $\hat{\mathbf{a}}_1(\theta)$ to its first entry.

Step 4: In the case of omni-directional sensors, project the entries of $\hat{\mathbf{a}}_1(\theta)$ in (5.62) onto the unit circle to obtain an improved estimate of the manifold vector $\hat{\hat{\mathbf{a}}}_1(\theta)$, i.e.,

$$[\hat{\hat{\mathbf{a}}}_1(\theta)]_{(m)} = \frac{[\hat{\mathbf{a}}_1(\theta)]_{(m)}}{|[\hat{\mathbf{a}}_1(\theta)]_{(m)}|} \tag{5.74}$$

for $m = 1, \ldots, M_1$.

Step 5: Estimate the DOAs from the L peaks of the following function

$$f_{\mathrm{PCAMIS2}}(\theta) = \frac{1}{\sum_{k=1}^{K} \phi_k^*(\theta)\hat{\hat{\mathbf{a}}}_1^H(\theta)\hat{\mathbf{U}}_{\mathrm{N},k}\hat{\mathbf{U}}_{\mathrm{N},k}^H\hat{\hat{\mathbf{a}}}_1(\theta)\phi_k(\theta)}. \tag{5.75}$$

Table 5.6: Algorithm PCAMIS-II

It should be mentioned that Algorithm PCAMIS-I avoids the possible inaccuracies in computing the pseudo-inverse of the matrices $\hat{\mathbf{U}}_{\mathrm{S},2},\ldots,\hat{\mathbf{U}}_{\mathrm{S},K}$ which occurred in Algorithm PCAMIS-II. Although in Algorithm PCAMIS-II when $L \leq M_1$ (which is assumed in the model described in Subsection 5.3.1) we have more degrees of freedom than in Algorithm PCAMIS-I. This is due to the fact that in the former method the $M_1 \times 1$ manifold vector $\mathbf{a}(\theta)$ instead of the $L \times 1$ vector of $\mathbf{p}(\theta)$ must be estimated. Hence, we observe that Algorithm PCAMIS-II performs slightly better than Algorithm PCAMIS-I in Section 5.5.

We should also remark that apart from the last step in our algorithm, which has no computational burden, the methods presented in [92] and [80] and our proposed algorithms of PCAMIS-I and PCAMIS-II, all require to perform eigen-decomposition in their spectral functions for each point in the FOV. Therefore, the complexity of the proposed algorithm is comparable to both of the existing methods.

5.3.4 Convex Optimization Approach for Estimating the Manifold Vector

In this subsection, we cast the problem of estimating the manifold vector at each θ into a convex optimization problem. In this approach, the computationally costly optimization problem has to be repeated at each θ in the FOV to estimate $\mathbf{a}_1(\theta)$ optimally. Since the associated computational cost is very high in this case, the obtained solutions can be used as a benchmark to evaluate the performance of the simpler methods of Algorithms PCAMIS-I and PCAMIS-II and of the competing methods.

To estimate the mixing vector corresponding to a source at DOA θ denoted by $\mathbf{p}(\theta)$ and the manifold vector of the first subarray $\mathbf{a}_1(\theta)$, taking into account the structure of the nominal manifold vectors $\mathbf{a}_1(\theta)$, we can write the following optimization problem:

$$\begin{aligned} &\min_{\mathbf{p}(\theta)} \ \|\hat{\mathbf{D}}(\theta)\mathbf{p}(\theta)\|^2 \\ &\text{s.t.} \ \min_{\mathbf{a}_1(\theta)} \|\hat{\mathbf{U}}_{\mathrm{S},1}\mathbf{p}(\theta) - \mathbf{a}_1(\theta)\| \\ &\qquad |[\mathbf{a}_1(\theta)]_{(m)}| = 1; \ m = 1,\ldots,M_1 \end{aligned} \tag{5.76}$$

where $\hat{\mathbf{D}}(\theta)$ is defined in (5.60). The inner minimization of the above problem represents a minimization over all vectors with complex entries of unit magnitude. It should be noted

that the vector $\mathbf{a}_1(\theta)$ in the above problem may no longer belong to the actual array manifold. The dependency of $\mathbf{a}_1$ to θ is, however, shown to emphasize that the minimization of the above problem must be performed for each angle θ in the FOV and $\mathbf{a}_1$ has to be estimated at each angle θ. From the first constraint, we obtain $\hat{\mathbf{p}}(\theta)$ as the least-squares solution of the minimization of $\|\hat{\mathbf{U}}_{\mathrm{S},1}\mathbf{p}(\theta) - \mathbf{a}_1(\theta)\|$ such that

$$\hat{\mathbf{p}}(\theta) = \hat{\mathbf{U}}_{\mathrm{S},1}^{\dagger}\mathbf{a}_1(\theta). \tag{5.77}$$

Hence, by replacing $\mathbf{p}(\theta)$ with $\hat{\mathbf{p}}(\theta)$ from (5.77) in (5.76) we can rewrite the problem as

$$\begin{aligned} \min_{\mathbf{a}_1(\theta)} \quad & \|\hat{\mathbf{D}}_2(\theta)\mathbf{a}_1(\theta)\|^2 \\ \text{s.t.} \quad & |[\mathbf{a}_1(\theta)]_{(m)}| = 1;\ m = 1, \ldots, M_1 \end{aligned} \tag{5.78}$$

where $\hat{\mathbf{D}}_2(\theta) \triangleq \hat{\mathbf{D}}(\theta)\hat{\mathbf{U}}_{\mathrm{S},1}^{\dagger}$ is an $(M - M_1) \times L$ matrix. It is clear that for the true DOAs the problem in (5.78) yields the true manifold vectors and an objective value of zero is attained. In the case that θ is not equal to the true DOAs then it is fairly unlikely that an objective function value close to zero will be obtained.

The problem in (5.78) for each θ in the FOV can be transformed into

$$\begin{aligned} \min_{\tilde{\mathbf{A}}_1(\theta)} \quad & \mathrm{tr}\{\tilde{\mathbf{A}}_1(\theta)\mathbf{D}_n(\theta)\} \\ \text{s.t.} \quad & [\tilde{\mathbf{A}}_1(\theta)]_{(m,m)} = 1; \quad \text{for} \ \ m = 1, \ldots, M_1 \\ & \mathrm{rank}\{\tilde{\mathbf{A}}_1(\theta)\} = 1 \end{aligned} \tag{5.79}$$

where $\tilde{\mathbf{A}}_1(\theta) \triangleq \mathbf{a}_1(\theta)\ \mathbf{a}_1^H(\theta)$ and $\mathbf{D}_n(\theta) \triangleq \mathbf{D}_2^H(\theta)\mathbf{D}_2(\theta)$. Notice that the matrix $\tilde{\mathbf{A}}_1(\theta)$ is a rank-one matrix. In order to convert the optimization problem into a convex one, this condition of $\mathrm{rank}\{\tilde{\mathbf{A}}_1(\theta)\} = 1$ is relaxed to $\tilde{\mathbf{A}}_1(\theta) \succeq 0$. Therefore, the problem in (5.79) is transformed into a semi-definite relaxation problem of

$$\begin{aligned} \min_{\tilde{\mathbf{A}}_1(\theta)} \quad & \mathrm{tr}\{\tilde{\mathbf{A}}_1(\theta)\mathbf{D}_n(\theta)\} \\ \text{s.t.} \quad & [\tilde{\mathbf{A}}_1(\theta)]_{(m,m)} = 1; \quad \text{for} \ \ m = 1, \ldots, M_1 \\ & \tilde{\mathbf{A}}_1(\theta) \succeq 0. \end{aligned} \tag{5.80}$$

The optimization problem in (5.80) can be easily solved using interior point methods. Let $\tilde{\mathbf{A}}_1(\theta)$ be the solution to the above convex optimization problem. Given $\tilde{\mathbf{A}}_1(\theta)$ for each angle θ on the search-grid, we can obtain the estimated manifold vector $\tilde{\mathbf{a}}_1(\theta)$ in two ways: either by using one of the randomization techniques in [83] or by simply computing the principle eigenvector of the matrix $\tilde{\mathbf{A}}_1(\theta)$. Then we can directly apply $\tilde{\mathbf{a}}_1(\theta)$ to the function in (5.64) in place of $\hat{\tilde{\mathbf{a}}}_1(\theta)$ in the last step of Algorithm PCAMIS-I to estimate the DOAs.

It should be noted that the approach described in this subsection is for the estimation of $\mathbf{a}_1(\theta)$ through estimation of $\mathbf{p}(\theta)$, yet it can be easily applied to the direct estimation $\mathbf{a}_1(\theta)$ by replacing the matrix $\hat{\mathbf{D}}_2(\theta)$ in (5.78) with the matrix $\hat{\mathbf{D}}_1(\theta)$ in (5.72) to directly obtain $\hat{\mathbf{a}}_1(\theta)$ directly.

We remark that all the above algorithms, in the case of non-omni-directional sensors with the known gain, can be slightly modified to include the sensor gain. In the Algorithms PCAMIS-I and PCAMIS-II, the entries of the normalized estimate of $\mathbf{a}(\theta)$, i.e., $\hat{\tilde{\mathbf{a}}}(\theta)$, must be multiplied by the known gain before using the spectral MUSIC function. In the convex optimization technique, the constraint must be equal to the known gain instead of one.

5.4 Pairwise-Calibrated Arrays (PWCA)

In this section, a DOA estimation method for the pairwise calibrated array model is considered which corresponds to Scenario IV and Fig. 2.4. The DOA estimation method for this type of arrays is also referred to as the generalized ESPRIT (GESPRIT) method in [16] since the array model can be viewed as yet another generalization of the ESPRIT array model of [77] (see Fig. 3.1). The other generalization of the model has been discussed in Section 5.3. To avoid any confusion, the array model introduced here is labeled as the PWCA while the GESPRIT method is only referred to the method proposed in [16] and [96]. As it is shown in Fig. 2.5, the PWCA geometry can also be transformed to the APCA geometry of Scenario II presented in Section 5.2. The approaches proposed in this section are related to the ones proposed in Section 5.3 in the sense that they exploit the unknown subarray geometry structure in the process of DOA estimation. However, in the methods

proposed in Section 5.3 the array structure was completely different from the array structure considered in the present section.

5.4.1 Signal Model for PWCA

The array model for PWCA, as depicted in Fig. 2.4, consists of M identical omni-directional sensors and involves two non-overlapping subarrays of M_1 sensors each such that $M = 2M_1$. Without loss of generality, the indices $1, \ldots, M_1$ are assigned to the sensors of the first subarray and $M_1 + 1, \ldots, M$ to the sensors of the second subarray, respectively.

Assume that the location of the m-th sensor is denoted by $[x_m, y_m]^T$ in the xy-plane. Let the m-th displacement vector for $m = 1, \ldots, M_1$ along the x- and y-axes

$$\tilde{\boldsymbol{\eta}}_m \triangleq [x_m - x_{m+M_1}, y_m - y_{m+M_1}]^T \tag{5.81}$$

be defined as the displacement vector between the m-th sensor of the first subarray and their corresponding sensor, i.e., the m-th sensor, in the second subarray. It is assumed that all the M_1 displacement vectors are exactly known. It can be clearly seen from Fig. 2.4 that this scenario is a generalization of the model introduced in the ESPRIT [77]. If all the displacement vectors are equal to each other, then the array model reduces to the ESPRIT array geometry of Fig. 3.1 where the two subarrays are identical with a single known vector characterizing their displacement but possibly unknown geometry of the subarrays.

The unknown array geometry-dependent matrix $\boldsymbol{\Psi}$ in this scenario is defined as in (5.43), i.e., it consists in the unknown geometry of the first subarray. Let us introduce the $M_1 \times M_1$ displacement-phase matrix $\boldsymbol{\Phi}_{\mathrm{p}}(\theta)$ as [16]

$$\boldsymbol{\Phi}_{\mathrm{p}}(\theta) \triangleq \mathrm{diag}\{e^{-j\phi_1(\theta)}, e^{-j\phi_2(\theta)}, \ldots, e^{-j\phi_{M_1}(\theta)}\} \tag{5.82}$$

where

$$\phi_m(\theta) = (x_m - x_{m+M_1}) \sin\theta + (y_m - y_{m+M_1}) \cos\theta \tag{5.83}$$

for $m = 1, \ldots, M_1$ are the phase differences between the m-th sensor pair corresponding to the direction θ. The matrix $\boldsymbol{\Phi}_{\mathrm{p}}(\theta)$ contains the displacement-phase information between the sensor pairs, unlike its counterpart in Sections 5.2 and 5.3 where it contains the

displacement-phase information between the subarrays. Hence, for the sake of notational clarity, we add the subscript "p". Using this notation, the $M \times L$ array manifold matrix $\mathbf{A}(\boldsymbol{\theta}, \boldsymbol{\Psi})$ in the considered case of pairwise calibrated sensors can be expressed as [16]

$$\mathbf{A}(\boldsymbol{\theta}, \boldsymbol{\Psi}) = \begin{bmatrix} \mathbf{A}_1(\boldsymbol{\theta}, \boldsymbol{\Psi}) \\ \mathbf{A}_2(\boldsymbol{\theta}, \boldsymbol{\Psi}) \end{bmatrix} \tag{5.84}$$

where

$$\mathbf{A}_1(\boldsymbol{\theta}, \boldsymbol{\Psi}) \triangleq [\mathbf{a}_1(\theta_1, \boldsymbol{\Psi}), \mathbf{a}_1(\theta_2, \boldsymbol{\Psi}), \ldots, \mathbf{a}_1(\theta_L, \boldsymbol{\Psi})], \tag{5.85}$$

$$\mathbf{A}_2(\boldsymbol{\theta}, \boldsymbol{\Psi}) \triangleq [\boldsymbol{\Phi}_{\mathrm{p}}(\theta_1)\mathbf{a}_1(\theta_1, \boldsymbol{\Psi}), \boldsymbol{\Phi}_{\mathrm{p}}(\theta_2)\mathbf{a}_1(\theta_2, \boldsymbol{\Psi}), \ldots, \boldsymbol{\Phi}_{\mathrm{p}}(\theta_L)\mathbf{a}_1(\theta_L, \boldsymbol{\Psi})] \tag{5.86}$$

are, respectively, the $M_1 \times L$ manifold matrices of the first and second subarray, and $\mathbf{a}_1(\theta, \boldsymbol{\Psi})$ and $\mathbf{a}_2(\theta, \boldsymbol{\Psi})$ are the manifold vectors of the first and the second subarray, respectively and $\mathbf{a}_1(\theta, \boldsymbol{\Psi})$ is the $M \times 1$ the first subarray manifold vector which satisfies the property

$$\|\mathbf{a}_1(\theta, \boldsymbol{\Psi})\|^2 = M. \tag{5.87}$$

The same property also holds for $\mathbf{a}_2(\theta, \boldsymbol{\Psi})$.

5.4.2 DOA Estimation Method for PWCA

Similar to $\mathbf{A}(\boldsymbol{\theta}, \boldsymbol{\Psi})$ in (5.84), the matrix $\mathbf{U}_{\mathrm{S}}$ can be expressed as

$$\mathbf{U}_{\mathrm{S}} = \begin{bmatrix} \mathbf{U}_{\mathrm{S},1} \\ \mathbf{U}_{\mathrm{S},2} \end{bmatrix} \tag{5.88}$$

where $\mathbf{U}_{\mathrm{S},1}$ and $\mathbf{U}_{\mathrm{S},2}$ are submatrices of $\mathbf{U}_{\mathrm{S}}$ that correspond to the first and second subarrays, respectively. Similar to the APCA model in Section 5.2 and from (2.24) and (5.88) we have

$$\mathbf{U}_{\mathrm{S},1} = \mathbf{A}_1(\boldsymbol{\theta}, \boldsymbol{\Psi})\mathbf{P}' \tag{5.89}$$

$$\mathbf{U}_{\mathrm{S},2} = \mathbf{A}_2(\boldsymbol{\theta}, \boldsymbol{\Psi})\mathbf{P}'. \tag{5.90}$$

We can follow two approaches from here as we did in Section 5.3 for the estimation of the array manifold vector. For the sake of brevity only the approach for the direct estimation

of the array manifold vector is presented in this subsection. The other method can be developed in a similar way as in Section 5.3.2 and is not discussed here.

From (5.90), we have

$$\mathbf{U}_{\mathrm{S},1}\mathbf{U}_{\mathrm{S},2}^{\dagger}\mathbf{A}_2(\boldsymbol{\theta},\boldsymbol{\Psi}) = \mathbf{A}_1(\boldsymbol{\theta},\boldsymbol{\Psi}). \tag{5.91}$$

Then, using (5.91) and the relation between $\mathbf{a}_1(\theta_l,\boldsymbol{\Psi})$ and $\mathbf{a}_2(\theta_l,\boldsymbol{\Psi})$ in (5.86) for $l = 1,\ldots,L$, i.e.,

$$\mathbf{a}_2(\theta_l,\boldsymbol{\Psi}) = \boldsymbol{\Phi}_{\mathrm{p}}(\theta_l)\mathbf{a}_1(\theta_l,\boldsymbol{\Psi}), \tag{5.92}$$

we have

$$\mathbf{U}_{\mathrm{S},1}\mathbf{U}_{\mathrm{S},2}^{\dagger}\boldsymbol{\Phi}_{\mathrm{p}}(\theta_l)\mathbf{a}_1(\theta_l,\boldsymbol{\Psi}) = \mathbf{a}_1(\theta_l,\boldsymbol{\Psi}). \tag{5.93}$$

Therefore, the manifold vectors $\{\mathbf{a}_1(\theta_l,\boldsymbol{\Psi})\}_{l=1}^{L}$ can be estimated by solving

$$\Big(\mathbf{I} - \mathbf{U}_{\mathrm{S},1}\mathbf{U}_{\mathrm{S},2}^{\dagger}\boldsymbol{\Phi}_{\mathrm{p}}(\theta,\boldsymbol{\Psi})\Big)\mathbf{a}_1(\theta,\boldsymbol{\Psi}) = \mathbf{0} \tag{5.94}$$

subject to the constraint

$$\|\mathbf{a}_1(\theta,\boldsymbol{\Psi})\| = \text{const.} \tag{5.95}$$

The latter constraint is required to avoid the trivial solution $\mathbf{a}_1(\theta,\boldsymbol{\Psi}) = \mathbf{0}$. Let

$$\mathbf{D}_{\mathrm{p}}(\theta) \triangleq \mathbf{I} - \mathbf{U}_{\mathrm{S},1}\mathbf{U}_{\mathrm{S},2}^{\dagger}\boldsymbol{\Phi}(\theta), \tag{5.96}$$

then it can be seen that the manifold vectors $\mathbf{a}_1(\theta,\boldsymbol{\Psi})$ can be estimated from eigenvectors associated with the zero eigenvalues of $\mathbf{D}_{\mathrm{p}}^{H}(\theta)\mathbf{D}_{\mathrm{p}}(\theta)$, i.e., for the true DOAs the manifold vectors are the L minor eigenvectors of $\mathbf{D}_{\mathrm{p}}^{H}(\theta)\mathbf{D}_{\mathrm{p}}(\theta)$. Hence, for the true DOAs

$$\hat{\mathbf{a}}_1(\theta) = \mathcal{V}_{\min}\{\mathbf{D}_{\mathrm{p}}^{H}(\theta)\mathbf{D}_{\mathrm{p}}(\theta)\} \tag{5.97}$$

where $\hat{\mathbf{a}}_1(\theta)$ is the estimate of the manifold vector. The MUSIC spectral function becomes zero for the manifold vectors of the true DOAs $\theta_1,\ldots,\theta_L$ similar to their counterparts in PCAMIS in Section 5.3. Moreover, notice that for the omni-directional sensors, the absolute value of each entry of the manifold vector is equal to one. These properties can be exploited in the practical case to estimate the DOAs. Hence, the algorithm shown in Table 5.7 is proposed.

Algorithm PWCA

Step 1: Compute $\hat{\mathbf{U}}_{\mathrm{S},1}$ and $\hat{\mathbf{U}}_{\mathrm{S},2}$ from the eigen-decomposition of $\hat{\mathbf{R}}$ according to (2.26), (2.28), and (5.88).

Step 2: For all θ in the search-grid of the FOV define

$$\hat{\mathbf{D}}_{\mathrm{p}}(\theta) \triangleq \mathbf{I} - \hat{\mathbf{U}}_{\mathrm{S},1}\hat{\mathbf{U}}_{\mathrm{S},2}^{\dagger}\mathbf{\Phi}_{\mathrm{p}}(\theta). \tag{5.98}$$

and compute $\hat{\mathbf{a}}_1(\theta)$ from

$$\hat{\mathbf{a}}_1(\theta) = \mathcal{V}_{\min}\{\hat{\mathbf{D}}_{\mathrm{p}}^{H}(\theta)\hat{\mathbf{D}}_{\mathrm{p}}(\theta)\} \tag{5.99}$$

and normalize the obtained vector entries to its first entry.

Step 3: In the case of omni-directional sensors normalize each entry to its absolute value

$$[\hat{\hat{\mathbf{a}}}_1(\theta)]_{(m)} = \frac{[\hat{\mathbf{a}}_1(\theta)]_{(m)}}{|[\hat{\mathbf{a}}_1(\theta)]_{(m)}|}. \tag{5.100}$$

Step 4: Compute the refined estimates of $\mathbf{a}_2(\theta)$ and $\mathbf{a}(\theta)$, respectively, as

$$\hat{\hat{\mathbf{a}}}_2(\theta) = \mathbf{\Phi}(\theta)\hat{\hat{\mathbf{a}}}_1(\theta) \tag{5.101}$$

$$\hat{\hat{\mathbf{a}}}(\theta) = \begin{bmatrix} \hat{\hat{\mathbf{a}}}_1(\theta) \\ \hat{\hat{\mathbf{a}}}_2(\theta) \end{bmatrix}. \tag{5.102}$$

Step 5: Find the estimates $\{\hat{\theta}_l\}_{l=1}^{L}$ of the signal DOAs from the L largest maxima of

$$f_{\mathrm{PWCA}}(\theta) = \frac{1}{\hat{\hat{\mathbf{a}}}^{H}(\theta)\hat{\mathbf{U}}_{\mathrm{N}}\hat{\mathbf{U}}_{\mathrm{N}}^{H}\hat{\hat{\mathbf{a}}}(\theta)}. \tag{5.103}$$

If necessary, also estimate the source manifold vectors as $\left\{\hat{\hat{\mathbf{a}}}(\hat{\theta}_l)\right\}_{l=1}^{L}$.

Table 5.7: Algorithm PWCA

It is worth noting that like other proposed algorithms in this chapter, the proposed algorithm is able to estimate both the signal DOAs and manifold vectors or spatial signatures. The latter feature of all our proposed techniques in this chapter can be applied, e.g., to the receive and transmit beamforming problems.

Note that in the present array model the array manifold vector can be obtained from a convex optimization technique, similar to the method for PCAMIS introduced in Subsection 5.3.4, simply by using the matrix $\hat{\mathbf{D}}_{\mathrm{p}}(\theta)$ instead of $\hat{\mathbf{D}}_2(\theta)$ in (5.78).

5.5 Simulations

In this section, we demonstrate the performance of each of the proposed methods through simulations and compared their performance to the performance of the competing methods as well as to the CRB. It should be noted that the results of [80] can be directly used to compute the CRB corresponding to our partly-calibrated array signal model.

In the figures of this section, the following notation is used for different DOA estimation methods introduced in the present chapter and the competing methods of Sections 3.3, 3.4, and 3.6:

APCA-Ia denotes the technique for APCA (Scenario II) using the multivariate function in (5.27) and the AP algorithm [108] (presented in Table 5.1) with the estimation of the displacement-phase matrices $\{\boldsymbol{\Phi}_k\}_{k=1}^K$ from (5.20) and (5.21) (see Table 5.2).

APCA-Ib denotes the technique for APCA (Scenario II) using the multivariate function in (5.27) and the AP algorithm [108] (presented in Table 5.1) with the estimation of the displacement-phase matrices $\{\boldsymbol{\Phi}_k\}_{k=1}^K$ from (5.24) and (5.25) (see Table 5.2).

APCA-PD denotes the technique for APCA (Scenario II) using only the multivariate function $\mathbf{h}_{\mathrm{D}}(\boldsymbol{\theta})$ in (5.31) with the aid of the AP algorithm [108] (presented in Table 5.1).

APCA-II denotes the technique for APCA (Scenario II) using the univariate function in

(5.32), the random weights, and the LR quality assessment in Subsection 5.2.4 (see Table 5.3).

APCA-III denotes the technique for APCA (Scenario II) using the univariate function in (5.32), the random weights, and the MLSE approach in Subsection 5.2.4 (see Table 5.4).

PCAMIS-I denotes the method for PCAMIS (Scenario III) using the estimate of $\mathbf{p}(\theta)$ from (5.77) in Subsection 5.3.2 (see Table 5.5).

PCAMIS-II denotes the method for PCAMIS (Scenario III) directly using the estimate of $\mathbf{a}(\theta)$ from (5.77) in Subsection 5.3.3 (see Table 5.6).

PCAMIS-CVX denotes the method for PCAMIS (Scenario III) directly using the estimate of $\mathbf{a}(\theta)$ from the convex optimization problem of (5.80) in Subsection 5.3.4.

PWCA denotes the method for PWCA (Scenario IV) discussed in Section 5.4 (see Table 5.7).

RARE denotes the approach of [80] presented in Section 3.3.

MI-MUSIC denotes the approach of [92] presented in Section 3.4.

GESPRIT denotes the approach of [16] using (3.33) presented in Section 3.6.

Four different simulation setups with randomly-generated sensor locations in the subarrays as well as randomly-generated displacement vectors are taken into account:

Simulation Setup 1: A sensor array, consisting of 3 subarrays ($K = 3$) with 5, 4 and 2 sensors and unknown displacement vectors is assumed. The sensor locations are given by (0,0), (0.16λ,-0.85λ),(0.68λ,0.98λ), (-1.32λ,0.36λ), (-0.70λ,0.37λ), (-10.65λ,11.47λ), (-9.91λ,9.12λ),(-10.31λ,10.55λ), (-11.08λ,-10.58λ),(-4.06λ,-4.67λ), and (-5.01λ,-5.33λ) for the first, second, and third subarrays, respectively. We consider two equal-power plane-wave sources located at 11° and 15° relative to the y-axis. We chose $N = 100$ and the number of simulation runs equal to $J_r = 400$.

Simulation Setup 2: A sensor array, consisting of 3 subarrays ($K = 3$) with 6, 4 and 3 sensors with unknown displacement vectors is assumed. The sensor locations are given by (0,0), (-0.75λ,0.26λ), (-0.20λ,0.17λ), (0.75λ,-0.71λ), (0.78λ,-0.59λ), (0.73λ,0.74λ), (-9.79λ,-5.87λ), (-9.54λ,-6.64λ), (-10.21λ,-5.94λ), (-10.11λ,-6.11λ), (-13.00λ,1.73λ), (-14.59λ,1.23λ), and (-14.39λ,2.16λ) for the first, second, and third subarrays, respectively. The equal-power far-field sources are located at 10° and 12°. We choose $N = 100$ and the number of simulation runs equal to $J_r = 400$.

Simulation Setup 3: A sensor array with 4 identical subarrays of 4 sensors each, i.e., $M_1 = 4$, $K = 4$, with the locations of the first subarray at (0,0), (3.61λ,-15.95λ), (3.60λ,-5.34λ), and (-5.38λ,-7.34λ) is considered. The known displacement vectors are assumed to be (-0.53λ,-0.83λ), (0.71λ,-1.57λ), and (-1.85λ,-0.76λ). We choose $N = 50$ and $J_r = 400$ simulation runs have been used. The signals are emitted from two sources ($L = 2$) with equal powers, closely-spaced at 11° and 14°.

Simulation Setup 4: A PWCA composing of five sensor pairs, i.e., two subarrays containing five sensors each, is assumed. The first subarray sensor locations are at (0,0), (-7.75λ,1.96λ), (5.20λ,-9.82λ), (-7.45λ,4.28λ), and (9.15λ,-8.84λ). The displacement vectors are (-1.53λ,-0.72λ), (-1.59λ,1.39λ), (1.78λ,-2.39λ), (0.83λ,1.19λ), and (0.99λ, -1.48λ). Two equal-power far-field sources are located at 3° and 7°. The number of snapshots is equal to $N = 50$ and the number of simulation runs is $J_r = 400$.

First, Scenario II (APCA) for two different randomly-generated simulation setups is considered. The reason for this is the observation that the different algorithms behave differently (compared to each other) in each of these setups. At the beginning, Simulation Setup 1 is considered. In Fig. 5.1, the DOA estimation RMSEs of the proposed techniques and of their competing method RARE are displayed versus the SNR and compared to the corresponding stochastic CRB [49], [80]. For Algorithms APCA-II and APCA-III in Fig. 5.1, a number of $Q = 20$ random weight vectors is chosen. In order to demonstrate the effect of the choice of Q on the RMSE performance for two algorithms only Algorithm APCA-II is considered and the corresponding RMSE values of the DOA estimates are displayed in

Fig. 5.2 for $Q = 1, 10, 20, 50, 100$. Figs. 5.3 and 5.4 illustrate the percentage of runs in which the sources are successfully resolved versus the SNR for different methods with $Q = 20$ and also for the different values of Q, respectively. The sources are considered as resolved [17], [18], [98] when two estimated DOAs satisfy the condition

$$\sum_{l=1}^{2} |\hat{\theta}_l - \theta_l| < |\theta_1 - \theta_2|. \tag{5.104}$$

We can clearly observe from these figures that the computationally costly Algorithms APCA-Ia and APCA-Ib perform substantially better than RARE. This is due to the fact that in Algorithms APCA-Ia and APCA-Ib a multivariate function is used that takes advantage of the array manifold matrix for all the L sources together which is in contrast to the function used in the RARE method where the array manifold vector of only one source is considered. Interestingly, the non-iterative and computationally more attractive proposed single-source (with one-dimensional search) DOA estimation Algorithms APCA-II and APCA-III also outperform the RARE method even for $Q = 1$. The improvement in the performance can be attributed to the use of the structure of the unknown part of the array manifold matrix and the use of its estimate, i.e., simultaneous calibration, in the DOA estimation process. We can see that in Simulation Setup 1 Algorithm APCA-Ia outperforms Algorithm APCA-Ib threshold-wise, although the performance of the latter is closer to the CRB.

We remark that since Algorithm APCA-III does not require the additional step of computing the LR value, the weighting coefficients can be generated in greater numbers so that the chance of acquiring sets of coefficients which produce better estimates increases. Nevertheless, in order to maintain fairness, the number of random weight vectors for Algorithm APCA-II and for Algorithm APCA-III are set to be equal.

Figs. 5.5-5.8 exhibit similar performance curves but for Simulation Setup 2. Here, the improvements in the performance and the resolution percentage of the proposed algorithms as compared to the known methods is also apparent. We can see that Algorithm APCA-Ib performs slightly better than Algorithm APCA-Ia in this simulation setup. It can be

observed that Algorithm APCA-III outperforms Algorithm APCA-II for the same Q. Moreover, one can observe that Algorithm APCA-PD, although iterative and less costly than Algorithms APCA-I and APCA-Ib, performs well compared to the RARE method in this simulation setup.

It is interesting to note from Figs. 5.2, 5.4, 5.6, and 5.8, that for $Q \geq 20$ the single-source Algorithms APCA-II and APCA-III meet and in some simulation setups even outperform the iterative methods using the multivariate function of Section 5.2.3.

Next, we consider the PCAMIS case (Scenario III) and Simulation Setup 3. Since the PCAMIS model is a special case of APCA model, one of the single-source methods (which use one-dimensional search) for the APCA, namely Algorithm APCA-II, is also included in the simulations. To be fair in our comparison, we set $Q = 1$. Note that because of the relatively large size of the subarrays compared to the displacement vectors, we can view the above mentioned array setup in another perspective as the scenario of the known subarrays with the unknown displacements between them. Fig. 5.9 shows the RMSE of the DOA estimates obtained from the different methods versus the SNR. In this figure, the performance of the proposed method is compared to the MI-MUSIC technique discussed in [92] using the quadratic constraint, the RARE algorithm [80], and the corresponding CRB [80] as well as Algorithm APCA-III. As it can be observed from Fig. 5.9, our proposed method performs considerably better than the other techniques. In Fig. 5.10, the ability of the methods to resolve two closely-spaced sources for the methods under consideration is illustrated using the criteria in (5.104). It is shown that the proposed method is more powerful than the RARE method [80] and the MI-MUSIC method of [92] in distinguishing the sources in this simulation setup.

In Fig. 5.11, the estimation performance of the array manifold vector is compared for the different techniques. In specific, the performance of the Algorithms PCAMIS-I, PCAMIS-II, PCAMIS-CVX, the RARE method of [80], and the MI-MUSIC method of [92] are displayed versus the SNR. As a performance measure the normalized RMSE defined as

$$\text{NRMSE} = \sqrt{\frac{1}{J_r L} \sum_{i=1}^{J_r} \sum_{l=1}^{L} \frac{\|\tilde{\mathbf{a}}_1^{(i)}(\hat{\theta}_l^{(i)}) - \mathbf{a}_1(\theta_l)\|^2}{\|\mathbf{a}_1(\theta_l)\|^2}} \tag{5.105}$$

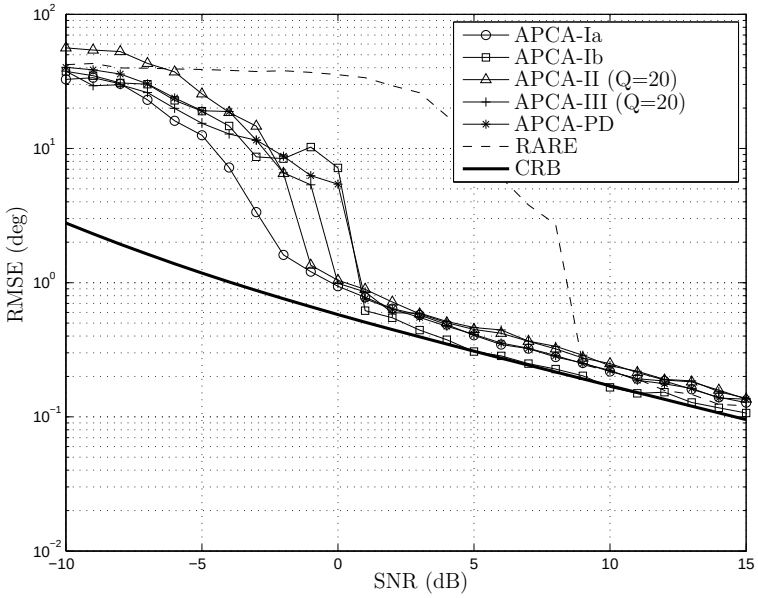

Figure 5.1: DOA estimation performance (RMSE) vs. SNR for Simulation Setup 1

has been used, where the superscript "(i)" denotes the estimate in the i-th simulation run. The estimated manifold vector is modified so that both the estimated and the true manifold vector have the same reference sensor. It can be clearly observed that in low SNR regions and for closely-spaced sources, the proposed methods estimate the manifold vector of the subarrays with higher accuracy than the competing methods.

Lastly, the PWCA case (Scenario IV) for Simulation Setup 4 is taken into account. Furthermore, as it is shown in Fig. 2.5, the PWCA geometry can be transformed to the APCA geometry. Hence, the algorithms proposed for the APCA geometry, e.g., Algorithm APCA-III, can also be applied and the results of the performance of Algorithm APCA-III are displayed. Fig. 5.12 shows the RMSE corresponding to the DOA estimates of the proposed algorithms tested versus the SNR. Fig. 5.13 displays the source resolution probability of the methods versus the SNR. It can be observed from these figures that the proposed Algorithm PWCA substantially outperforms the RARE and the GESPRIT algorithms in terms of threshold performance, and also slightly outperforms Algorithm APCA-III for $Q = 1$.

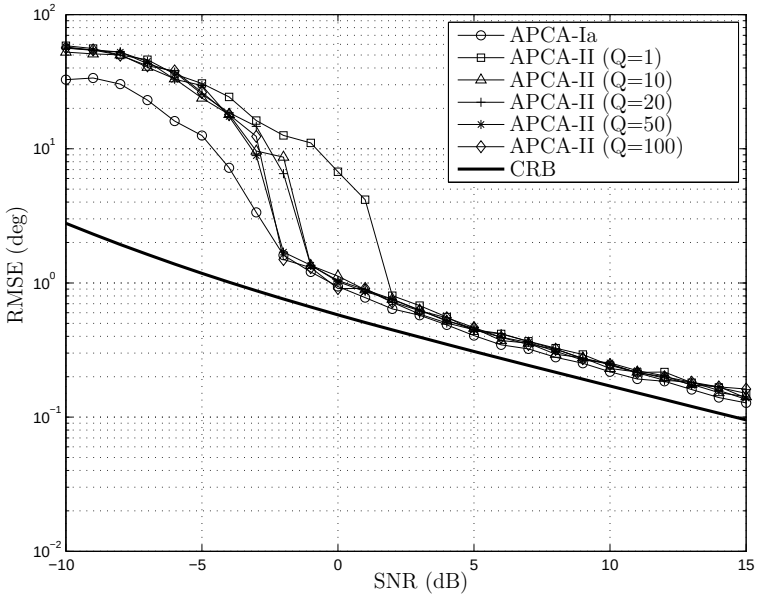

Figure 5.2: DOA estimation performance (RMSE) vs. SNR for Simulation Setup 1

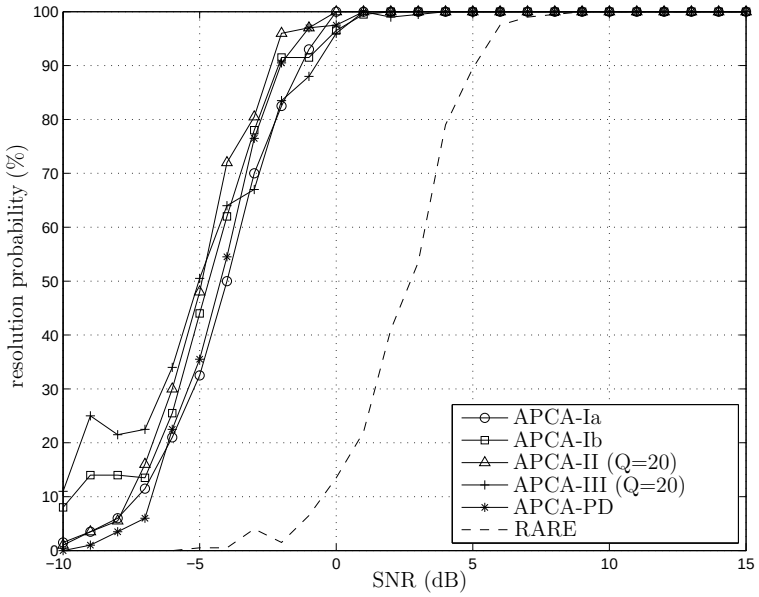

Figure 5.3: Resolution probability vs. SNR for Simulation Setup 1

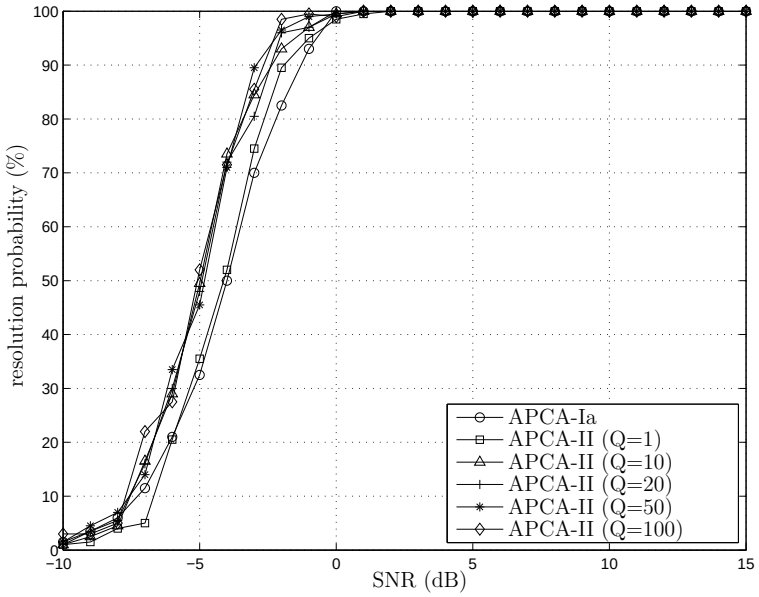

Figure 5.4: Resolution probability vs. SNR for Simulation Setup 1

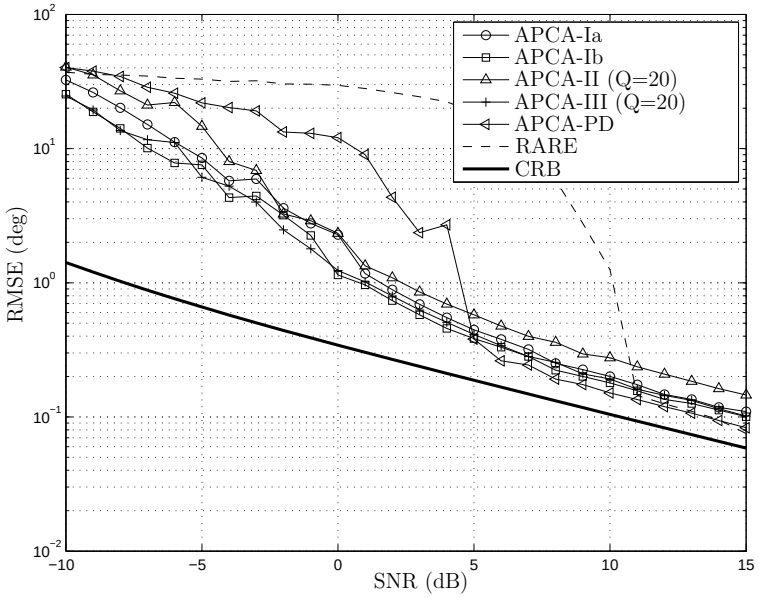

Figure 5.5: DOA estimation performance (RMSE) vs. SNR for Simulation Setup 2

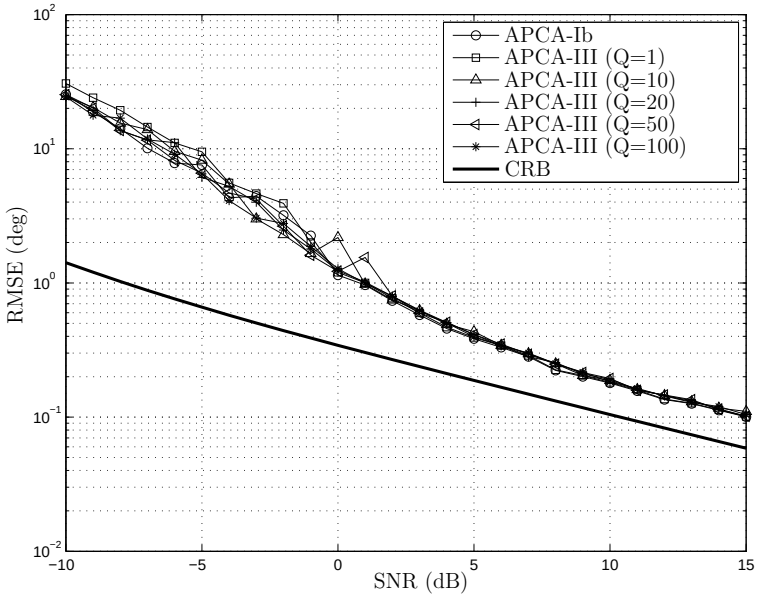

Figure 5.6: DOA estimation performance (RMSE) vs. SNR for Simulation Setup 2

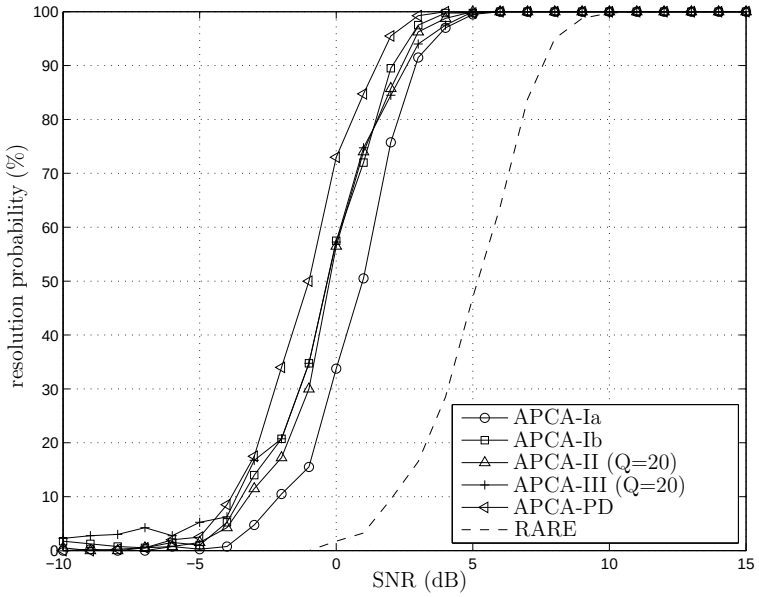

Figure 5.7: Resolution probability vs. SNR for Simulation Setup 2

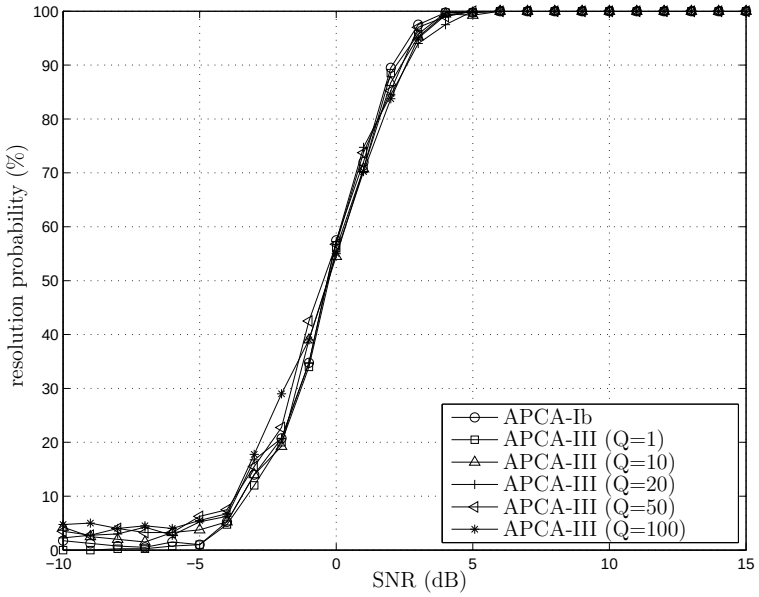

Figure 5.8: Resolution probability vs. SNR for Simulation Setup 2

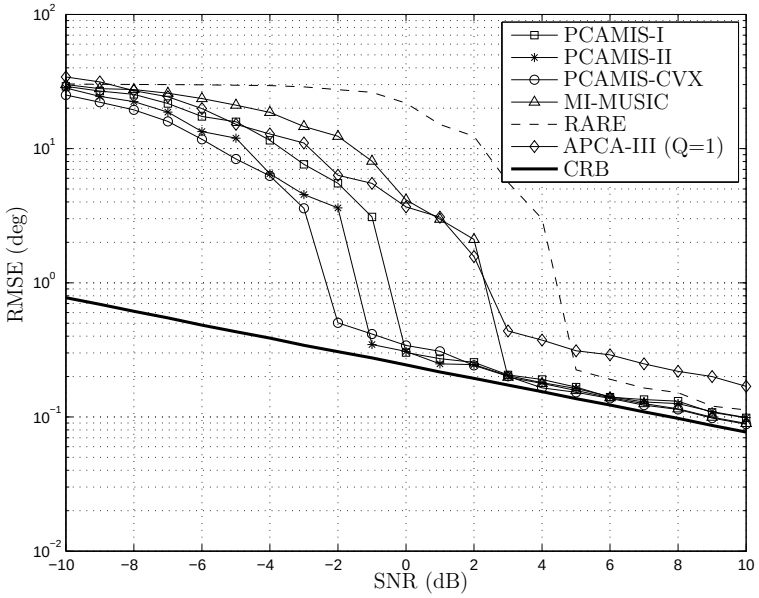

Figure 5.9: DOA estimation performance (RMSE) vs. SNR for Simulation Setup 3

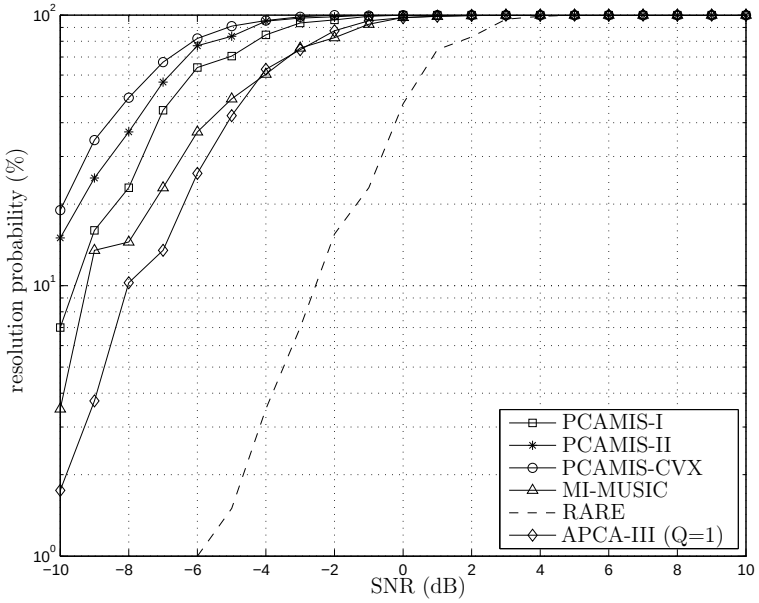

Figure 5.10: Resolution probability vs. SNR for Simulation Setup 3

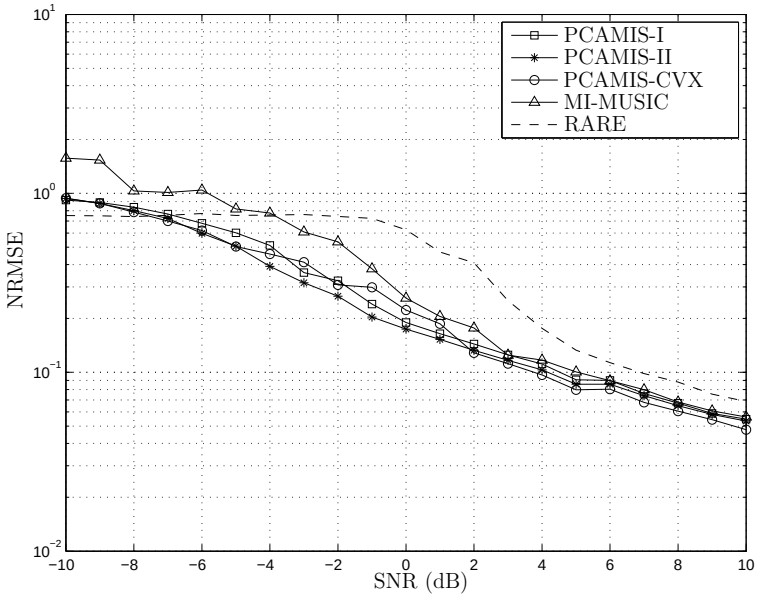

Figure 5.11: First subarray manifold estimation performance (RMSE) vs. SNR for Simulation Setup 3

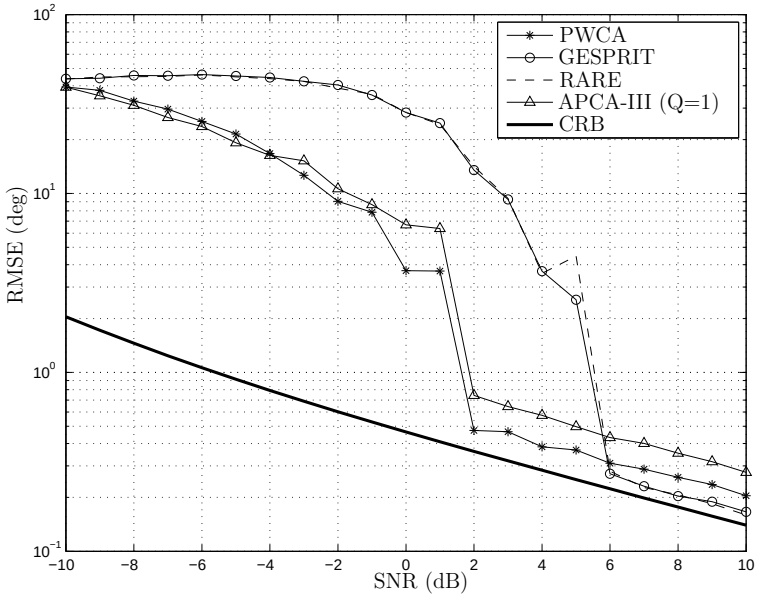

Figure 5.12: DOA estimation performance (RMSE) vs. SNR for Simulation Setup 4

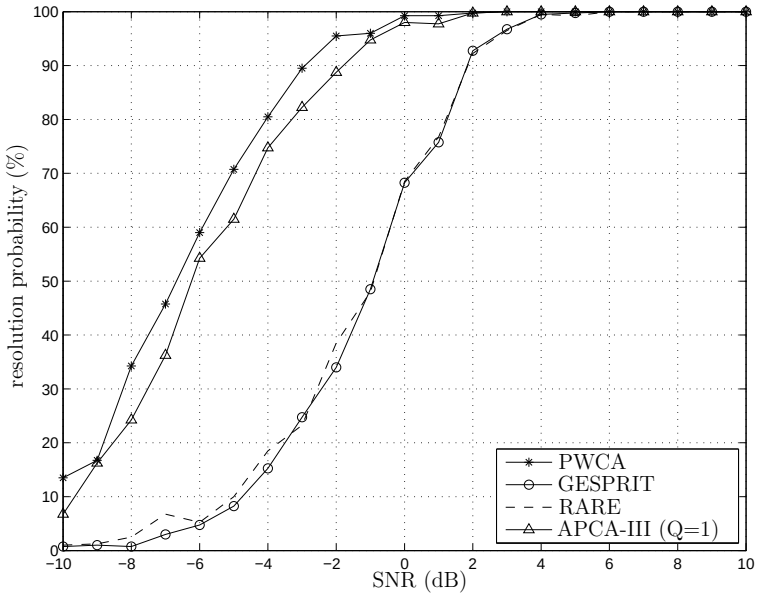

Figure 5.13: Resolution probability vs. SNR for Simulation Setup 4

5.6 Chapter Summary

Novel DOA estimation methods for various types of partly-calibrated array were proposed in this chapter. We considered sparse arrays composed of two or more subarrays where some parts of the array geometry, either the geometry of subarrays or the displacement vectors between them, are unknown. The common feature in all of the proposed techniques is the exploitation of the unknown array geometry-dependent part of the array manifold and its inherent structure while simultaneously estimating the DOAs. The simulations display significant performance improvement when compared to the existing competing methods. First, we considered the APCA (Scenario II) and introduced a new approach to jointly estimate the DOAs and to calibrate the array. To accomplish that, several techniques were proposed for this new approach including the estimator bank technique of Chapter 4 that was adapted for this problem. Then, the joint DOA estimation and calibration for the PCAMIS (Scenario III) was taken into account and an algorithm was devised which estimates the DOAs and the array manifold vectors simultaneously. Moreover, another method of manifold estimation was proposed by casting the problem as a constraint convex optimization problem involving relaxations. Here, the constraints were used to impose the structure of the known part of the partly-calibrated array manifold. This method, although still suboptimal and computationally costly, as the simulation have shown, is more accurate, and hence can be regarded as a benchmark. Lastly, the PWCA geometry (Scenario IV) was considered and methods similar, but not identical, to the methods for PCAMIS have been presented.

Chapter 6

Fast Algorithms For Harmonic Retrieval (HR) Problem

6.1 Introduction

In this chapter, the harmonic retrieval (HR) problem is considered. The HR problem of estimating the frequencies and damping factors of a discrete harmonic mixture from one or multiple observations taken, e.g., along time, frequency or space, is the underlying problem in various important estimation problems in signal processing and communications. The HR problem, specifically the undamped HR problem, can be regarded as the generalization of the DOA estimation problem (introduced in the previous chapters), e.g., for radar and sonar [77], [110]. Similarly, in parametric spectrum estimation [37], [39] and channel identification [47], [65], the estimation problem can be formulated as an undamped HR problem. In other applications like nuclear magnetic resonance (NMR) spectroscopy [8], [38], audio processing [99] and material damage monitoring [75], the estimation of damping factors along with the frequencies of the superimposed harmonics is required. In many engineering problems, in which the observed signals are modeled as auto-regressive (AR) or moving-average (MA) processes [36], HR is also applicable. The auto-correlation function of the

AR process, specifically, can be represented as a damped harmonic mixture, where the harmonics corresponding to the roots of the characteristic equation are associated with the AR parameters. The cross-correlation function associated with the MA processes also leads to the undamped HR problem from which the MA parameters can be estimated.

In the classical methods for the damped harmonic estimation, which can be considered as the generalization of the undamped HR, a full-search over the entire 2-D parameter space is required [36], [38], [70]. Pisarenko's method [70] was among the earliest works in subspace-based HR and many variations of this method have emerged afterwards. In [36] the state-space and the singular value decomposition approaches have been used for HR. In NMR spectroscopy [38], the classical MUSIC estimator of [78] (introduced in Subsection 3.2.1), originally developed for the undamped HR, was extended to the damped HR problem. The method presented in [38] requires an exhaustive search over its multi-dimensional spectral function in order to estimate the signal parameters, therefore, the associated computational complexity is rather high.

Search-free subspace-based methods for the undamped HR problem have gained considerable attention [22], [34], [42], [64], [91], [97], [110]. The ESPRIT algorithm [77] (see Section 3.5), originally developed for DOA estimation, and its extensions in [91] and [110] exploit specific shift-invariances inherent in the data model. These methods can straightforwardly be generalized to the damped HR case as well. Based on a generalization of the ESPRIT algorithm, a high resolution technique is presented in [5]. The advantage of this technique introduced in [5] is that the damping factors can also be estimated. Many of these search-free methods have been extended to the two- and multi-dimensional HR case for various applications [22], [34], [42], [64], [91], [97].

The subspace separation technique introduced in Chapter 2 for extracting the signal- and noise-subspaces from the sample covariance matrix defined in (2.26) is a common approach to subspace-based parameter estimation [91], [110]. This is only possible when multiple snapshots are available. If only a single snapshot is available, as is often encountered in, e.g., time-series analysis, then the rank of the estimated covariance matrix is not sufficient to span the signal subspace (see Assumption 6 in Chapter 2). In this case, as mentioned

before, in order to obtain an estimate of the covariance matrix with sufficient rank, forward-backward (FB) averaging [41] and smoothing techniques [34], [36], [97] can be applied. The multi-dimensional folding (MDF) algorithm was proposed in [42] and [47] for undamped HR in which the subspaces are estimated from a low-rank matrix. This low-rank matrix is constructed from the data samples directly rather than its second moments. The advantage of the MDF algorithm is that it yields the best trade-off between the subspace rank and aperture size, hence, maximizes the number of identifiable sources for a given number of observations.

There are applications where not all sensors or samples are available, as in the cases of impulsive noise or sensor failure. In such cases, the above methods for damped HR are not applicable or they can be applied only at the cost of a severe loss of information. This is due to the fact that these methods exploit the regular structure of the data model which in the missing sample case, becomes destroyed. Due to the loss of structure, it may then not even be possible to use all the available data samples. Several techniques for estimating the harmonic frequencies in the missing sample case have been introduced in recent years. The special case of the gapped data where only segments of data are available has been studied in [12] where a weighted least squares (WLS) technique has been proposed. In [40], the missing data amplitude and phase estimation (MAPES) method is introduced which estimates the signal frequencies using the expectation maximization algorithm iteratively. Based on the iterative adaptive approach (IAA) method of [107], the missing data IAA (MIAA) in [89] has been presented to estimate the missing data along with the harmonic frequencies. Although both the MIAA and the MAPES method are search-based methods, yet as claimed by their authors, the MIAA performs much faster than the MAPES method. While search-based techniques such as MIAA [89] (introduced briefly in Section 3.7) and rooting-based methods such as root-MUSIC [7] (described in Subsection 3.2.3) naturally extend to account for missing samples in the undamped HR, these methods represent a major problem in the damped HR case.

In this chapter, the weighted multiple invariance (WMI) approach first presented in [69] (see also [60] and [61]) is introduced. This algorithm is based on a linear combination

of the rank-reduction criteria obtained from different shift-invariances of the signal model. For the complete sample case, we derive conditions under which the damped harmonic parameters can be uniquely estimated from the roots of a matrix polynomial (MP). Then, the case of incomplete samples is investigated where it is proved that spurious roots that do not correspond to the true signal harmonics are generally obtained. New methods are proposed to overcome this ambiguity. First, the idea to select the best estimate according to some criteria (of which two are proposed in this thesis) is discussed. Then, a technique is developed based on polynomial intersection of two distinct polynomials in which the common factors corresponding to the true signal harmonics are directly extracted.

6.2 Signal Model for Harmonic Retrieval Problem

Assume that in the presence of additive noise the superposition of L complex exponentials is observed. The received signal at sample m can be written as [34]

$$z_m = \sum_{l=1}^{L} s_l \mu_l^{m-1} + n_m;\ m = 1, \ldots, M \tag{6.1}$$

where $\mu_l \in \mathbb{C}$ is the l-th signal generator which satisfies $|\mu_l| \leq 1$, s_l is the l-th complex random source amplitude, n_m is the complex white zero-mean Gaussian sensor noise with variance σ^2, and M is the number of samples. It should be remarked that the model in (6.1) represents a generic signal model in which, depending on the application, z_m may describe a time series at sample m, a spatial sample taken from the m-th sensor of a uniform linear array, or, more generally, a pre-processed data sample represented in a transformed domain, for instance, the m-th discrete Fourier coefficient. In this section, as in the previous chapters, Assumption 1 is considered, i.e., the number of signals L (also referred to as the modeling order in the HR problem) is supposed to be known or can be obtained, e.g., from techniques introduced in [6], [101], and [102].

Let us stack the samples in vectors (availability of all samples is assumed at the beginning of this section) and assume that N observation vectors (or snapshots) are available, then the signal model described in (2.6) is obtained, i.e., $\mathbf{z}(t) = \mathbf{A}(\boldsymbol{\mu})\mathbf{s}(t) + \mathbf{n}(t)$, where $\mathbf{s}(t)$

is the signal vector at snapshot index t defined in (2.7) and the $M \times L$ signal generator matrix, which is equivalent to the manifold matrix of (2.11) in the DOA estimation context, is defined as in (2.10) and can be represented such that

$$\begin{aligned} \mathbf{A}(\boldsymbol{\mu}) &\triangleq [\boldsymbol{\mu}_1, \boldsymbol{\mu}_2, \ldots, \boldsymbol{\mu}_L] \\ &\triangleq \left[\mathbf{h}_1^T, \mathbf{h}_2^T, \ldots, \mathbf{h}_M^T\right]^T \end{aligned} \tag{6.2}$$

where the $1 \times L$ row-vector $\mathbf{h}_m = \left[\mu_1^{m-1}, \mu_2^{m-1}, \ldots, \mu_L^{m-1}\right]$ denotes the m-th row of $\mathbf{A}(\boldsymbol{\mu})$ and the $M \times 1$ column-vector $\boldsymbol{\mu}_l \triangleq \left[1, \mu_l, \mu_l^2, \ldots, \mu_l^{M-1}\right]^T$ is the l-th column of $\mathbf{A}(\boldsymbol{\mu})$.

In the incomplete sample case where the observations are only available at specific sample locations, these samples are represented by the binary indicator v_m which takes the values

$$v_m = \begin{cases} 1, & \text{if the } m\text{-th sample is available;} \\ 0, & \text{otherwise.} \end{cases} \tag{6.3}$$

Then, the received signal model (6.1) in the incomplete sample case becomes

$$\begin{aligned} \tilde{\mathbf{z}}(t) &\triangleq \mathbf{V}\mathbf{z}(t) \\ &= \mathbf{V}\mathbf{A}(\boldsymbol{\mu})\mathbf{s}(t) + \mathbf{V}\mathbf{n}(t) \\ &= \tilde{\mathbf{A}}(\boldsymbol{\mu}, \mathbf{V})\mathbf{s}(t) + \tilde{\mathbf{n}}(t);\ t = 1, \ldots, N \end{aligned} \tag{6.4}$$

where

$$\mathbf{V} \triangleq \mathrm{diag}\{v_1, v_2, \ldots, v_M\} \tag{6.5}$$

is the diagonal matrix containing the binary entries defined in (6.3), and $\tilde{\mathbf{A}}(\boldsymbol{\mu}, \mathbf{V}) \triangleq \mathbf{V}\mathbf{A}(\boldsymbol{\mu})$, and $\tilde{\mathbf{n}}(t) \triangleq \mathbf{V}\mathbf{n}(t)$ denote the $M \times L$ signal generator matrix and the $M \times 1$ noise vector at snapshot t, respectively. Note that for notational convenience we represent the missing samples with zero entries at the respective positions using the diagonal matrix $\mathbf{V}$, rather than completely removing these entries from the data. Moreover, the dependency of $\mathbf{A}$ to $\boldsymbol{\mu}$ as well as that of $\tilde{\mathbf{A}}$ to $\boldsymbol{\mu}$ and $\mathbf{V}$ will be dropped hereafter. The dimensions and indices of the vectors and matrices in the incomplete sample case are thus equivalent to their corresponding counterparts in the complete sample case.

In this chapter, a subspace-based harmonic retrieval method is proposed where the subspace matrices are obtained from the eigen-decomposition of the sample covariance matrix (presented in Chapter 2). In literature, several subspace smoothing methods are available (see, e.g., [34], [36], [42] and [97]) in which the signal and noise subspaces are obtained from a single signal data snapshot, i.e., for $N = 1$.

The data covariance matrix is defined similar to (2.15) as

$$\begin{aligned} \mathbf{R} &\triangleq \mathrm{E}\{\tilde{\mathbf{z}}(t)\tilde{\mathbf{z}}^H(t)\} \\ &= \mathbf{V}\mathrm{E}\{\mathbf{z}(t)\mathbf{z}^H(t)\}\mathbf{V} \\ &= \mathbf{V}\mathbf{A}\mathbf{R}_s\mathbf{A}^H\mathbf{V} + \sigma^2\mathbf{V} \\ &= \tilde{\mathbf{A}}\mathbf{R}_s\tilde{\mathbf{A}}^H + \sigma^2\mathbf{V} \end{aligned} \tag{6.6}$$

where $\mathbf{R}_s$ is the signal covariance matrix defined in (2.16) and the properties $\mathbf{V}^H = \mathbf{V}$ and $\mathbf{V}\mathbf{V}^H = \mathbf{V}$ are taken into account. The signal- and the noise eigenvector matrices $\mathbf{U}_\mathrm{S}$ and $\mathbf{U}_\mathrm{N}$ and their sample counterparts $\hat{\mathbf{U}}_\mathrm{S}$ and $\hat{\mathbf{U}}_\mathrm{N}$ can be obtained from the eigen-decomposition of the data covariance matrix $\mathbf{R}$ and its sample estimate defined as

$$\hat{\mathbf{R}} = \frac{1}{N}\sum_{t=1}^{N}\tilde{\mathbf{z}}(t)\tilde{\mathbf{z}}^H(t) = \frac{1}{N}\sum_{t=1}^{N}\mathbf{V}\mathbf{z}(t)\mathbf{z}^H(t)\mathbf{V} \tag{6.7}$$

from (2.19) and (2.28), respectively.

6.3 The Weighted Multiple Invariance (WMI) Approach

For those v_k and v_{k+m} in (6.3) which are both equal to one, a shift-invariance property based on the Vandermonde structure of the signal generator matrix $\mathbf{A}$ defined in (6.2) can be established that relates the k-th row of $\mathbf{A}$, namely $\mathbf{h}_k$, with its respective $(k+m)$-th row, namely $\mathbf{h}_{k+m}$, as

$$\mathbf{h}_{k+m} = \mathbf{h}_k\mathbf{\Delta}^m \tag{6.8}$$

for $m = 1, \ldots, M-1$, where the diagonal shifting matrix is defined as

$$\mathbf{\Delta} \triangleq \mathrm{diag}\{\mu_1, \mu_2, \ldots, \mu_L\}. \tag{6.9}$$

In the classical ESPRIT algorithm [77], explained in Section 3.5, such invariance equations (6.8) are exploited for a particular m. Here, a similar idea as in [91] is followed where multiple shift-invariances are exploited simultaneously. We should note that, since the sampling grid is uniform, the shift-invariance equation (6.8) is valid for arbitrary integer shifts $m = 1, \ldots, M-1$. Therefore, it is meaningful to use the properties of all the shifts by constructing a linear combination of weighted invariance equations (6.8) for different shifts. Multiplying (6.8) with $\mathbf{h}_{k+m}^H$ from the left, and forming a linear combination with weighting coefficients $\{c_m\}_{m=1}^M$, ($c_m \in \mathbb{R}^+$), the following equation is obtained

$$\sum_{k=1}^{M-1} \sum_{m=1}^{M-k} c_m v_{k+m} v_k \left(\mathbf{h}_{k+m}^H \mathbf{h}_{k+m} - \mathbf{h}_{k+m}^H \mathbf{h}_k \mathbf{\Delta}^m \right) = \mathbf{0}_{L \times L}. \tag{6.10}$$

Availability of v_k and v_{k+m} in (6.13) indicates that in the incomplete sample case only shift-invariances for which both the samples k and $k+m$ are available can be used in (6.8). Multiplying from right both sides of equation (6.10) with $\mathbf{e}_l$, defined as the l-th column of an identity matrix, we have

$$\begin{aligned} \sum_{k=1}^{M-1} \sum_{m=1}^{M-k} c_m v_{k+m} v_k \left(\mathbf{h}_{k+m}^H \mathbf{h}_{k+m} - \mathbf{h}_{k+m}^H \mathbf{h}_k \mathbf{\Delta}^m \right) \mathbf{e}_l &= \\ \sum_{k=1}^{M-1} \sum_{m=1}^{M-k} c_m v_{k+m} v_k \left(\mathbf{h}_{k+m}^H \mathbf{h}_{k+m} - \mathbf{h}_{k+m}^H \mathbf{h}_k \mu_l^m \right) \mathbf{e}_l &= \mathbf{0}_{L \times 1} \end{aligned} \tag{6.11}$$

where the following property is used

$$\mathbf{\Delta}^m \mathbf{e}_l = \mu_l^m \mathbf{e}_l. \tag{6.12}$$

Thus, defining the MP

$$\begin{aligned} \mathbf{M}(\mu) &\triangleq \sum_{k=1}^{M-1} \sum_{m=1}^{M-k} c_m v_{k+m} v_k \left(\mathbf{h}_{k+m}^H \mathbf{h}_{k+m} - \mathbf{h}_{k+m}^H \mathbf{h}_k \mu^m \right) \\ &= \sum_{k=1}^{M-1} \sum_{m=1}^{M-k} c_m v_{k+m} v_k \mathbf{h}_{k+m}^H \mathbf{h}_{k+m} \left(\mathbf{I} - \mathbf{\Delta}^{-m} \mu^m \right) \end{aligned} \tag{6.13}$$

we observe from (6.11) that $\mathbf{M}(\mu_l)\, \mathbf{e}_l = \mathbf{0}_{L \times 1}$. This means that the MP $\mathbf{M}(\mu)$ drops rank when the parameter μ in the above expression becomes identical to one of the true signal generators, i.e, when μ is equal to one of the values $\mu_1, \mu_2, \ldots, \mu_L$.

It follows from (2.19) and (6.6) that the (modified) generator matrix $\tilde{\mathbf{A}}$ and the signal subspace matrix $\mathbf{U}_{\mathrm{S}}$ span the same subspace. Thus, there exists an $L \times L$ full-rank mixing matrix $\mathbf{P}$ defined in (2.24), i.e., $\mathbf{U}_{\mathrm{S}} = \tilde{\mathbf{A}}\mathbf{P}$ and similarly for the rows corresponding to $v_k = 1$, we can write

$$\mathbf{u}_{\mathrm{S}}^{(k)} = v_k \mathbf{h}_k \mathbf{P} \tag{6.14}$$

where $\mathbf{u}_{\mathrm{S}}^{(k)}$ denotes the k-th row of $\mathbf{U}_{\mathrm{S}}$. Multiplying (6.13) from left and right with the full-rank matrices $\mathbf{P}^H$ and $\mathbf{P}$, respectively, and using (6.14), we obtain the MP

$$\begin{aligned} \mathbf{G}(\mu) &= \mathbf{P}^H \mathbf{M}(\mu) \mathbf{P} \\ &= \sum_{m=1}^{M-1} \sum_{m=1}^{M-k} c_m v_{k+m} v_k \left({\mathbf{u}_{\mathrm{S}}^{(k+m)}}^H \mathbf{u}_{\mathrm{S}}^{(k+m)} - {\mathbf{u}_{\mathrm{S}}^{(k+m)}}^H \mathbf{u}_{\mathrm{S}}^{(k)} \mu^m \right). \end{aligned} \tag{6.15}$$

Due to the full-rank property of the matrix $\mathbf{P}$, the MPs in (6.13) and (6.15) are equivalent in the sense that both MPs share the same set of roots, i.e., $\mathbf{G}(\mu)$ becomes singular if and only if $\mathbf{M}(\mu)$ becomes singular.

Notice that in the MP $\mathbf{G}(\mu)$ in (6.15) the estimate of the signal subspace matrix $\hat{\mathbf{U}}_{\mathrm{S}}$ is used instead of the true signal subspace matrix $\mathbf{U}_{\mathrm{S}}$. The MP $\mathbf{G}(\mu)$ will be used in Sections 6.4 and 6.5 in order to estimate the signal generators from its singularities, i.e., from its roots. For the theoretical analysis of the singularities of the MP $\mathbf{G}(\mu)$, however, the ideal (noise-free) case is considered and the signal generator matrix $\mathbf{A}$ is used instead of the signal subspace matrix $\mathbf{U}_{\mathrm{S}}$. Therefore, in the following we study the singularities of the equivalent MP $\mathbf{M}(\mu)$ defined in (6.13).

As shown in (A.4) of Appendix A in Section 6.9, the MP in (6.13) can be factorized as

$$\begin{aligned} \mathbf{M}(\mu) &= \sum_{k=1}^{M-1} \sum_{m=1}^{M-k} \sum_{n=0}^{m-1} c_m v_{k+m} v_k \mathbf{h}_{k+m}^H \mathbf{h}_{k+m-n} \mu^n \left(\mathbf{I} - \boldsymbol{\Delta}^{-1} \mu \right) \\ &= \overline{\mathbf{A}}^H \mathbf{C}(\mu) \overline{\mathbf{A}} \left(\mathbf{I} - \boldsymbol{\Delta}^{-1} \mu \right) \\ &= \mathbf{M}_{\mathrm{r}}(\mu) \mathbf{M}_{\mathrm{s}}(\mu) \end{aligned} \tag{6.16}$$

where the $(M-1) \times L$ matrix

$$\overline{\mathbf{A}} \triangleq \left[\mathbf{h}_2^T \ \mathbf{h}_3^T \ \cdots \ \mathbf{h}_M^T \right]^T \tag{6.17}$$

is formed from the last $M-1$ rows of the signal generator matrix $\mathbf{A}$ in (6.2),

$$\mathbf{C}(\mu) \triangleq \begin{bmatrix} v_2 v_1 c_1 & 0 & \cdots & 0 \\ v_3 v_1 c_2 \mu & v_3(v_1 c_2 + v_2 c_1) & \cdots & 0 \\ v_4 v_1 c_3 \mu^2 & v_4(v_1 c_3 + v_2 c_2)\mu & \cdots & 0 \\ \vdots & \vdots & \ddots & \vdots \\ v_M v_1 c_{M-1} \mu^{M-2} & v_M(\sum_{l=1}^{2} v_l c_{M-l})\mu^{M-3} & \cdots & v_M(\sum_{l=1}^{M-1} v_l c_{M-l}) \end{bmatrix}, \tag{6.18}$$

and

$$\mathbf{M}_{\mathrm{s}}(\mu) \triangleq \left(\mathbf{I} - \mathbf{\Delta}^{-1}\mu\right) \tag{6.19}$$

$$\mathbf{M}_{\mathrm{r}}(\mu) \triangleq \overline{\mathbf{A}}^{H}\mathbf{C}(\mu)\overline{\mathbf{A}} \tag{6.20}$$

are the signal and residual MPs, respectively.

From the factorization in the last row of (6.16), it can be seen that $\mathbf{M}(\mu)$ becomes singular if μ takes the value of one of the true signal generators $\mu_1, \ldots, \mu_L$. This is resulted from the fact that in this case, one of the diagonal entries of $\mathbf{M}_{\mathrm{s}}(\mu)$ becomes zero. Hence, all entries in the corresponding column of $\mathbf{M}(\mu)$ are zeros which leads to a singular MP. Thus, we conclude, that the singularity of $\mathbf{M}(\mu)$ is necessary for μ to become equal to one of the true signal generators $\mu_1, \ldots, \mu_L$. Because of the full-rank property of the mixing matrix $\mathbf{P}$, the similar statement holds true for the MP $\mathbf{G}(\mu)$ too. Next, we investigate under which conditions the singularity of $\mathbf{M}(\mu)$ and $\mathbf{G}(\mu)$ is also sufficient for μ to be equal to one of the true generators. This is a critical question since the true signal generators will be acquired from the singularities of the respective MPs later on. In this case, the sufficient conditions on $\mathbf{M}(\mu)$ and, subsequently, $\mathbf{G}(\mu)$ directly bring into view the conditions under which unique estimates can be obtained from the roots of those MPs.

In order to address this question, consider the first factor in the factorization of (6.16), i.e., the residual MP $\mathbf{M}_{\mathrm{r}}(\mu)$ defined in (6.20). Obviously, if $\mathbf{M}_{\mathrm{r}}(\mu)$ is non-singular for the values of μ inside or on the unit-circle, then the MPs $\mathbf{M}(\mu)$ and $\mathbf{G}(\mu)$ become singular if and only if μ corresponds to one of the true signal generators $\mu_1, \ldots, \mu_L$. In the next section,

we derive, for the complete sample case, simple conditions on the weighting coefficients $\{c_m\}_{m=1}^{M-1}$ for which $\mathbf{M}_{\rm r}(\mu)$ does not generate spurious roots not corresponding to the true signal generators inside or on the unit-circle. It will be shown that in this case, unique estimates can be found from the roots of $\mathbf{G}(\mu)$, or $\mathbf{M}(\mu)$, obtained inside or on the unit-circle. In Section 6.5, we study the incomplete sample case and we show that general uniqueness conditions, which are the conditions that do not depend on the data, cannot be established. To rectify this issue, we propose, besides some selection-based estimation methods, a novel estimation procedure from which unique parameter estimates can be obtained.

6.4 The Complete Sample Case

In this section, we study the case when all the data samples are available. Therefore, it is assumed $v_m = 1$ for $m = 1, \ldots, M$. Hence, the MPs in (6.13) and (6.15) reduce, respectively, to

$$\mathbf{M}_{\rm cs}(\mu) = \sum_{k=1}^{M-1} \sum_{m=1}^{M-k} c_m \mathbf{h}_{k+m}^H \mathbf{h}_{k+m} \left(\mathbf{I} - \mathbf{\Delta}^{-m} \mu^m \right) \tag{6.21}$$

and

$$\mathbf{G}_{\rm cs}(\mu) = \sum_{k=1}^{M-1} \sum_{m=1}^{M-k} c_m \left(\mathbf{u}_{\rm S}^{(k+m)^H} \mathbf{u}_{\rm S}^{(k+m)} - \mathbf{u}_{\rm S}^{(k+m)^H} \mathbf{u}_{\rm S}^{(k)} \mu^m \right) \tag{6.22}$$

where the subscript "cs" indicates the complete sample case. Then, the following theorem holds:

Theorem: Provided that $\overline{\mathbf{A}}$ in (6.17) is of full column-rank and that the weighting coefficients in (6.21) and (6.22) satisfy

$$2c_1 \geq c_2 \geq \cdots \geq c_{M-1} \geq 0; \; c_1 > 0 \tag{6.23}$$

the $L \times L$ matrices $\mathbf{M}_{\rm cs}(\mu)$ and $\mathbf{G}_{\rm cs}(\mu)$, evaluated inside and on the unit-circle, i.e., for $|\mu| \leq 1$, become singular if and only if $\mu = \mu_l$ for $l = 1, \ldots, L$.

As discussed in the previous section, we can clearly see from the factorization in (6.16), that the MP $\mathbf{M}_{\rm cs}(\mu)$ is singular if μ corresponds to a true generator. In order to prove that

with the choice of (6.23) the singularity of $\mathbf{M}_{\rm cs}(\mu)$ inside the unit-circle is also a sufficient condition for μ to be equal to a true generator, we show that the residual polynomial $\mathbf{M}_{\rm r}(\mu)$, when $v_m = 1$ for $m = 1, \ldots, M$, is always non-singular. From Sylvester's rank inequality [25] we have

$$\text{rank}\{\overline{\mathbf{A}}\} + \text{rank}\{\mathbf{C}(\mu)\} - M + 1 \leq \text{rank}\{\overline{\mathbf{A}}^H \mathbf{C}(\mu)\overline{\mathbf{A}}\} \leq \min(\text{rank}\{\mathbf{C}(\mu)\}, \text{rank}\{\mathbf{A}\}). \quad (6.24)$$

Considering that $\overline{\mathbf{A}}$ is of full column-rank L ($\leq M-1$), the matrix $\mathbf{M}_{\rm r}(\mu) = \overline{\mathbf{A}}^H \mathbf{C}(\mu)\overline{\mathbf{A}}$ is of full column- and row-rank L if $\mathbf{C}(\mu)$ is non-singular. It remains to be shown that under the conditions in (6.23), the MP $\mathbf{C}(\mu)$ does not possess any singularities inside or on the unit-circle. The proof of the latter fact is presented in Appendix B of Section 6.9.

Note that the Vandermonde matrix $\overline{\mathbf{A}}$ is of full-rank if and only if all generators $\mu_1, \ldots, \mu_L$ are distinct and also if the number of damped harmonics is less than the number of samples M [25]. Therefore, choosing the weights $\{c_m\}_{m=1}^{M-1}$ according to (6.23) in the complete sample case, the true generators $\mu_1, \ldots, \mu_L$ can be uniquely obtained from the roots of (6.22).

In practice, in order to root the MPs in (6.13) and (6.15), two different approaches can be commonly applied. In the first approach the determinant of the MP is recursively calculated using cofactor expansion and then the roots of the obtained scalar polynomial are determined. To acquire the coefficients of the determinant polynomial, the fast Fourier transform (FFT) and the inverse fast Fourier transform (IFFT) can be used where convolution in the polynomial coefficient domain is replaced by IFFT, multiplication, and FFT [25], [68]. In the second approach, the roots of the MP are calculated from the L smallest generalized eigenvalues of the corresponding block companion matrix pair [25], [30], [68].

In the finite sample case where the estimates of the rows of the signal subspace matrix $\mathbf{U}_{\rm S}$ in (6.22) are available, we propose the procedure shown in Table 6.1 to estimate the signal generators.

Algorithm HR-I

Step 1: Compute $\hat{\mathbf{R}}$ in (6.7) and find the signal subspace matrix $\hat{\mathbf{U}}_{\mathrm{S}}$ from (2.28).

Step 2: Obtain the sample version of the MP in (6.22) from

$$\hat{\mathbf{G}}_{\mathrm{cs}}(\mu) = \sum_{k=1}^{M-1} \sum_{m=1}^{M-k} c_k \left(\hat{\mathbf{u}}_{\mathrm{S}}^{(k+m)^H} \hat{\mathbf{u}}_{\mathrm{S}}^{(k+m)} - \hat{\mathbf{u}}_{\mathrm{S}}^{(k+m)^H} \hat{\mathbf{u}}_{\mathrm{S}}^{(k)} \mu^m \right). \tag{6.25}$$

Step 3: Calculate the L smallest magnitude roots $\hat{\mu}_1, \ldots, \hat{\mu}_P$ of $\hat{\mathbf{G}}_{\mathrm{cs}}(\mu)$, for instance, from the L smallest generalized eigenvalues of the block companion matrix pair associated with $\hat{\mathbf{G}}_{\mathrm{cs}}(\mu)$ [25], [30], [68].

Table 6.1: Algorithm HR-I

6.5 The Incomplete Sample Case: Methods Based on Selection

In the incomplete sample case, the general MPs $\mathbf{M}(\mu)$ and $\mathbf{G}(\mu)$ as defined in equations (6.13) and (6.15), respectively, are taken into account. Similar to the complete sample case, let us investigate the singularities of the residual MP in the factorization (6.16). However, it should be noted that the residual MP $\mathbf{M}_{\mathrm{r}}(\mu)$ in (6.20) cannot be computed analytically from the available data samples. This is due to the fact that not all the rows of complete-data (row-reduced) signal matrix $\overline{\mathbf{A}}$ in (6.20) are observable.

According to (6.16), $\mathbf{M}(\mu)$ can be written as

$$\mathbf{M}(\mu) = \overline{\mathbf{A}}^H \mathbf{C}(\mu) \overline{\mathbf{A}} \left(\mathbf{I} - \boldsymbol{\Delta}^{-1} \mu \right) \tag{6.26}$$

where $\mathbf{C}(\mu)$ is defined in (6.18). Unlike the complete sample case where simple uniqueness conditions (6.23) are derived, similar data-independent uniqueness conditions for the incomplete sample scenario cannot be obtained. Due to the unavailability of the $(m+1)$-th sample, i.e., $v_{m+1} = 0$, all entries in the m-th row of $\mathbf{C}(\mu)$ in (6.26) become equal to zero due to the masking operation in (6.18) which results in a reduced column-rank of $\mathbf{C}(\mu)$. In this case from the Sylvester's rank inequality in (6.24) we can see that the product $\overline{\mathbf{A}}^H \mathbf{C}(\mu) \overline{\mathbf{A}}$

can become rank deficient if the null-space of $\mathbf{C}(\mu)$ and the range-space of $\overline{\mathbf{A}}$ intersect. Therefore, the residual matrix polynomial can generate spurious roots at locations that depend both on the choice of the weighting coefficients $\{c_m\}_{m=1}^{M-1}$ and on the signal generator matrix $\overline{\mathbf{A}}$, i.e., on the set of the true generators themselves. Thus, in contrast to the complete sample case where $\mathbf{M}(\mu)$ is rank-deficient if and only if μ becomes equal to one of the true generators, in the incomplete sample case $\mathbf{M}(\mu)$ may show additional singularities which do not correspond to the true signal generators. In this case, data-independent uniqueness conditions cannot be obtained.

One way to deal with the appearance of the ambiguities is to develop an estimation scheme which first roots the MP $\mathbf{G}(\mu)$ in (6.15) and then separates the signal roots from the spurious roots according to some appropriate criterion. In principle, many different root-selection criteria may be applied. The best but also most complex schemes involve multi-dimensional parameter subset testing, i.e., for all possible sets of L roots taken from the set of signal and spurious roots, the set that yields the largest criterion function value is selected. One excellent criterion function is the multi-dimensional likelihood function. However, the main disadvantage of the likelihood criterion stems from the fact that for a large number of signal and spurious solutions, the computational complexity of the proposed scheme grows substantially as the number of subsets of size L increases. In the next two subsections, two of such selection-based methods are explained.

6.5.1 Selection Based on the Residual Polynomial

As it has been already mentioned in Section 6.3, all the spurious roots are resulted from $\mathbf{M}_{\mathrm{r}}(\mu)$ in (6.20). Therefore, one criterion to test whether an estimated root, say $\hat{\mu}_l$ is a residual root or not, would be to check the rank deficiency of the matrix $\mathbf{M}_{\mathrm{r}}(\hat{\mu}_l)$. If the obtained matrix is rank deficient (or close to it) then $\hat{\mu}_l$ is a residual root and should be discarded. In order to compute $\mathbf{M}_{\mathrm{r}}(\hat{\mu}_l)$, one needs to estimate the generator matrix $\overline{\mathbf{A}}$ first. However, the signal generator matrix $\overline{\mathbf{A}}$ not only depends on the generator values $\mu_1, \ldots, \mu_L$, the parameters we want to estimate, but also is defined for the complete sample

Algorithm HR-II

Step 1: Compute the MP

$$\hat{\mathbf{G}}(\mu) = \sum_{k=1}^{M-1} \sum_{m=1}^{M-k} c_m v_{k+m} v_k \left(\hat{\mathbf{u}}_{\mathrm{S}}^{(k+m)^H} \hat{\mathbf{u}}_{\mathrm{S}}^{(k+m)} - \hat{\mathbf{u}}_{\mathrm{S}}^{(k+m)^H} \hat{\mathbf{u}}_{\mathrm{S}}^{(k)} \mu^m \right) \tag{6.27}$$

from the estimated signal subspace matrix $\hat{\mathbf{U}}_{\mathrm{S}}$ in (2.28) after eigen-decomposition of $\hat{\mathbf{R}}$ in (6.7).

Step 2: Choose the roots $\hat{\mu}_1, \hat{\mu}_2, \ldots, \hat{\mu}_{L'}$ $(L' \geq L)$ of $\hat{\mathbf{G}}(\mu)$ inside the unit-circle.

Step 3: Form all the combination sets of L signal roots and $L' - L$ residual roots.

Step 4: Calculate, for each set, $\overline{\mathbf{A}}$ from the signal roots.

Step 5: Compute, for each set, $d_s \triangleq \sum_{l=1}^{L'-L} \det\{\overline{\mathbf{A}}^H \tilde{\mathbf{C}}(\hat{\mu}_l) \overline{\mathbf{A}}\}$.

Step 6: Find the set of roots with the minimum value of d_s.

Table 6.2: Algorithm HR-II

case. To overcome the mentioned difficulties, we propose to pick L roots of all the roots that has been obtained, and to treat them as the signal roots and the rest as the residual roots to form $\overline{\mathbf{A}}$ of a complete sample case. Let L' $(\geq L)$ be the total number of obtained roots inside the unit circle. Then, we should check the rank deficiency of the obtained "residual" polynomial $\mathbf{M}_{\mathrm{r}}(\hat{\mu}_l)$ by computing its determinant for all the possible combinations of L out of L' and choose the combination with the lowest determinant as the estimated signal roots.

The algorithm for selecting the signal roots is summarized in Table 6.2.

6.5.2 Selection Based on the MUSIC Criterion

The spectral MUSIC method [78] has been originally developed in the context of DOA estimation, i.e., for the undamped HR problem with $|\mu| = 1$ (see Section 3.2.1). Nevertheless, the MUSIC function of (3.3) can also be used as a one-dimensional criterion to evaluate the validity of a root in the damped harmonic case. Therefore, Algorithm HR-III in Table 6.3 can be applied to obtain the unique signal generator estimates.

Algorithm HR-III

Step 1: Compute the MP $\hat{\mathbf{G}}(\mu)$ in (6.27) from the estimated signal subspace matrix $\hat{\mathbf{U}}_{\mathrm{S}}$ in (2.28) after eigen-decomposition of $\hat{\mathbf{R}}$ in (6.7).

Step 2: Compute the roots $\hat{\mu}_1, \hat{\mu}_2, \ldots, \hat{\mu}_{L'}$ $(L' \geq L)$ of $\hat{\mathbf{G}}(\mu)$ inside the unit-circle.

Step 3: Form the Vandermonde vector $\hat{\boldsymbol{\mu}}_{l'} = [1, \hat{\mu}_{l'}, \hat{\mu}_{l'}^2, \ldots, \hat{\mu}_{l'}^{M-1}]^T$ for each root $l' = 1, \ldots, L'$.

Step 4: For each root, calculate $f_{\mathrm{HMUSIC}}(\hat{\mu}_{l'}) = \left(\hat{\boldsymbol{\mu}}_{l'}^H \hat{\boldsymbol{\mu}}_{l'}\right) / \left(\hat{\boldsymbol{\mu}}_{l'}^H \hat{\mathbf{U}}_{\mathrm{N}} \hat{\mathbf{U}}_{\mathrm{N}}^H \hat{\boldsymbol{\mu}}_{l'}\right)$.

Step 5: Find the L largest maxima of $f_{\mathrm{HMUSIC}}(\hat{\mu}_{l'})$ and their corresponding roots.

Table 6.3: Algorithm HR-III

Our computer simulations demonstrate that the selection scheme based on the MUSIC criterion in Steps 4 and 5 of Algorithm HR-III performs reasonably well and its performance achieves the performance of the ideal yet impractical selection scheme (used as the benchmark) where the estimates closest to the true generators are selected.

It should be remarked that the estimation procedure of the signal generators along with selecting the signal roots is suboptimal in the sense that due to the numerical instability of the rooting procedure, the spurious roots located closely to the signal roots may adversely affect the estimates of the signal roots, hence, resulting in a significant performance degradation at low and medium SNR values or snapshot sizes. Therefore, we introduce in the following section a more sophisticated technique based on rank-reduction criterion to uniquely obtain the signal roots without the need of further selection.

6.6 The Incomplete Sample Case: Method Based on Polynomial Intersection

From (6.26), we can observe that the signal roots of $\mathbf{M}(\mu)$ do not change for different sets of $\{c_m\}_{m=1}^{M-1}$. The reason is that the weighting coefficients affect only the MP $\mathbf{M}_{\mathrm{r}}(\mu)$. Hence, if we replace the taken set of coefficients by any different set, only the residual roots change.

Therefore, we can claim that for any two polynomials resulting from (6.26) with different sets of weighting coefficients, say $\{c_m\}_{m=1}^{M-1}$ and $\{c'_m\}_{m=1}^{M-1}$, there exist at least L common roots. Reversely, if there are exactly L common roots, then these are the signal roots.

It is well known that even small perturbations in the polynomial coefficients of MPs strongly affect the location of the roots. Different sets of weighting coefficients $\{c_m\}_{m=1}^{M-1}$ result in substantially different coefficients of the polynomials $\mathbf{M}_{\mathrm{r}}(\mu)$ and $\mathbf{M}(\mu)$ and, consequently, in different location of the roots. This has already been addressed in Section 6.4 from a slightly different perspective in the context of the residual polynomial $\mathbf{M}_{\mathrm{r}}(\mu)$ in (6.20), where it was mentioned that singularities of $\mathbf{M}_{\mathrm{r}}(\mu)$ may result from the intersection of the subspaces of $\mathbf{C}(\mu)$ and $\overline{\mathbf{A}}$, and hence depend on both the true signal generators and the weighting coefficients $\{c_m\}_{m=1}^{M-1}$. Interestingly, this only applies to the spurious roots, i.e., the roots of $\mathbf{M}_{\mathrm{r}}(\mu)$ and, therefore, to all but the signal roots in $\mathbf{M}(\mu)$, as can be observed from the factorization in (6.16). As it will be also verified by our simulations, it is very unlikely for two different random coefficient sets that the residual polynomials generate exactly identical spurious roots. In order to extract the common polynomial factor of two scalar polynomials with common roots, the properties of the Sylvester matrix will be used. Before introducing the procedure, let us present the Sylvester matrix and some of its important and useful properties.

6.6.1 Sylvester Matrix and Its Properties

Consider two scalar polynomials

$$f(\mu) = p_n\mu^n + p_{n-1}\mu^{n-1} + \cdots + p_1\mu + p_0 \tag{6.28}$$

$$g(\mu) = q_m\mu^m + q_{m-1}\mu^{m-1} + \cdots + q_1\mu + q_0 \tag{6.29}$$

of degree n and m, respectively, where $p_n \neq 0$ and $q_m \neq 0$. Then, the $(m+n) \times (m+n)$ Sylvester matrix can be defined as [23]

$$\mathbf{S}(f,g) \triangleq \begin{pmatrix} p_0 & p_1 & \cdots & p_n & 0 & 0 & \cdots & 0 \\ 0 & p_0 & p_1 & \cdots & p_n & 0 & \cdots & 0 \\ \vdots & \vdots & \vdots & \vdots & \vdots & \vdots & \vdots & \vdots \\ 0 & 0 & \cdots & p_0 & p_1 & \cdots & \cdots & p_n \\ q_0 & q_1 & \cdots & q_m & 0 & 0 & \cdots & 0 \\ 0 & q_0 & q_1 & \cdots & q_m & 0 & \cdots & 0 \\ \vdots & \vdots & \vdots & \vdots & \vdots & \vdots & \vdots & \vdots \\ 0 & 0 & \cdots & q_0 & q_1 & \cdots & \cdots & q_m \end{pmatrix}. \tag{6.30}$$

The resultant of $f(\mu)$ and $g(\mu)$ is defined as the determinant of their corresponding Sylvester matrix [23], [105], [106] and is denoted by $\text{Res}(f,g) = \det\{\mathbf{S}(f,g)\}$. We should mention that the resultant can also be expressed as $\text{Res}(f,g) = \prod_{ij}(\mu_i^{(f)} - \mu_j^{(g)})$ where $\mu_i^{(f)}$ and $\mu_j^{(g)}$ are the roots of the polynomials $f(\mu)$ and $g(\mu)$, respectively. It can be proved that the polynomials $f(\mu)$ and $g(\mu)$ have at least one common root $\breve{\mu}$ if and only if $\text{Res}(f,g) = 0$ [23], [105], [106].

Furthermore, it can be seen that if $\breve{\mu}_1, \breve{\mu}_2, \ldots, \breve{\mu}_L$ are the common roots of $f(\mu)$ and $g(\mu)$, then the Vandermonde vectors

$$\breve{\boldsymbol{\mu}}_l = [1, \breve{\mu}_l, \breve{\mu}_l^2, \ldots, \breve{\mu}_l^{m+n-1}]^T \tag{6.31}$$

for $l = 1, \ldots, L$ span the null-space of the Sylvester matrix $\mathbf{S}(f,g)$, i.e.,

$$\mathcal{N}\{\mathbf{S}(f,g)\} = \mathcal{R}\{\breve{\boldsymbol{\Upsilon}}\} \tag{6.32}$$

where $\breve{\boldsymbol{\Upsilon}}$ is the matrix containing the Vandermonde root vectors in (6.31) such that

$$\breve{\boldsymbol{\Upsilon}} = [\breve{\boldsymbol{\mu}}_1, \breve{\boldsymbol{\mu}}_2, \ldots, \breve{\boldsymbol{\mu}}_L]. \tag{6.33}$$

Let us define the unitary matrix $\mathbf{U}_0$ which consists of the eigenvectors $\mathbf{u}_{0,l}$ associated with the zero eigenvalues of $\mathbf{S}(f,g)$ such that

$$\mathbf{U}_0 = [\mathbf{u}_{0,1}, \mathbf{u}_{0,2}, \ldots, \mathbf{u}_{0,L}]. \tag{6.34}$$

The following method is proposed based on the mentioned properties.

6.6.2 The Proposed Algorithm

Consider two MPs constructed from different weighting coefficient sets of $\{c_m\}_{m=1}^{M-1}$ and $\{c'_m\}_{m=1}^{M-1}$ according to equation (6.15)

$$\mathbf{G}_1(\mu) = \sum_{k=1}^{M-1}\sum_{m=1}^{M-k} c_m v_{k+m} v_k \left(\mathbf{u}_{\mathrm{S}}^{(k+m)^H} \mathbf{u}_{\mathrm{S}}^{(k+m)} - \mathbf{u}_{\mathrm{S}}^{(k+m)^H} \mathbf{u}_{\mathrm{S}}^{(k)} \mu^m \right) \tag{6.35}$$

$$\mathbf{G}_2(\mu) = \sum_{k=1}^{M-1}\sum_{m=1}^{M-k} c'_m v_{k+m} v_k \left(\mathbf{u}_{\mathrm{S}}^{(k+m)^H} \mathbf{u}_{\mathrm{S}}^{(k+m)} - \mathbf{u}_{\mathrm{S}}^{(k+m)^H} \mathbf{u}_{\mathrm{S}}^{(k)} \mu^m \right). \tag{6.36}$$

The Sylvester matrix $\mathbf{S}(f,g)$ is assumed to be obtained from the scalar polynomials $f(\mu) = \det\{\mathbf{G}_1(\mu)\}$ and $g(\mu) = \det\{\mathbf{G}_2(\mu)\}$, each has the maximum degree of $2M-2$. Note that from (6.15) and the full-rank property of the matrix $\mathbf{P}$, one can see that the determinant roots of the above MPs are equal to those of their corresponding counterparts in (6.26). Therefore, taking into account that the common roots of $f(\mu)$ and $g(\mu)$ correspond to the true signal generators $\mu_1, \ldots, \mu_L$, we observe that the null-space of the Sylvester matrix $\mathbf{S}(f,g)$ has dimension L. Furthermore, from (6.32), for signal generators $\mu_1, \ldots, \mu_L$ the Vandermonde matrix $\breve{\mathbf{\Upsilon}}$ in (6.33) corresponding to the extended version of $\mathbf{A}$, spans the null-space of $\mathbf{S}(f,g)$. Hence, with $\mathbf{U}_0$ defined in (6.34), we have $\mathcal{R}\{\mathbf{U}_0\} = \mathcal{R}\{\breve{\mathbf{\Upsilon}}\}$. Interestingly, we have obtained the matrix $\mathbf{U}_0$ which spans the space of the $(m+n)\times L$ virtual complete data signal matrix $\breve{\mathbf{\Upsilon}}$. Because of the Vandermonde structure of $\breve{\mathbf{\Upsilon}}$, the ESPRIT approach [77] (described in Section 3.5) can be applied for estimation of $\mu_1, \ldots, \mu_P$ from $\mathbf{U}_0$. The estimation procedure for the proposed method is described in Table 6.4.

In Algorithm HR-IV shown in Table 6.4, $\hat{\mathbf{U}}_0$ is defined as the sample counterpart of the matrix $\mathbf{U}_0$ obtained from the sample versions of the respective MPs in (6.35) and (6.36), $\hat{\mathbf{G}}_1(\mu)$ and $\hat{\mathbf{G}}_2(\mu)$, where $\hat{\mathbf{U}}_0 = [\hat{\mathbf{u}}_{0,1}, \hat{\mathbf{u}}_{0,2}, \ldots, \hat{\mathbf{u}}_{0,L}]$ and $\hat{\mathbf{u}}_{0,l}$, $l = 1, \ldots, L$ are the L minor eigenvectors of the Sylvester matrix $\mathbf{S}(\hat{f}, \hat{g})$ formed from the scalar polynomials

$$\hat{f}(\mu) = \det\{\hat{\mathbf{G}}_1(\mu)\} \tag{6.37}$$

and

$$\hat{g}(\mu) = \det\{\hat{\mathbf{G}}_2(\mu)\}. \tag{6.38}$$

Algorithm HR-IV

Step 1: Compute the sample versions of the two MPs $\mathbf{G}_1(\mu)$ and $\mathbf{G}_2(\mu)$ in (6.35) and (6.36), with two different coefficient sets of $\{c_m\}_{m=1}^{M-1}$ and $\{c'_m\}_{m=1}^{M-1}$.

Step 2: Form the corresponding Sylvester matrix.

Step 3: Find the L minor eigenvectors of the Sylvester matrix, i.e., $\hat{\mathbf{u}}_{0,l}$ for $l = 1, \ldots, L$, then form $\hat{\mathbf{U}}_0$.

Step 4: Compute the eigenvalues $\hat{\mu}_l$, $l = 1, \ldots, L$ of $\mathbf{\Phi}_{\text{HR}} \triangleq \left(\overline{\hat{\mathbf{U}}}_0^H \overline{\hat{\mathbf{U}}}_0\right)^{-1} \overline{\hat{\mathbf{U}}}_0^H \underline{\hat{\mathbf{U}}}_0$ where $\overline{\hat{\mathbf{U}}}_0$ and $\underline{\hat{\mathbf{U}}}_0$ are formed from the matrix $\hat{\mathbf{U}}_0$ by removing the first and the last rows, respectively.

Table 6.4: Algorithm HR-IV

It is worth mentioning that, in the undamped case, there is a very elegant and computationally efficient scheme to construct the second polynomial. The idea is to form the coefficients of the second polynomial $\mathbf{G}_2(\mu)$ in (6.36) from the coefficients of the first polynomial, i.e., $\mathbf{G}_1(\mu)$ in (6.35), such that $c'_m = c^*_{M-m}$ for $m = 1, \ldots, M-1$. Then it can readily be verified that the roots of $\mathbf{G}_2(\mu)$ become the conjugate reciprocal of the roots of $\mathbf{G}_1(\mu)$, i.e., if μ_m is a root of $\mathbf{G}_1(\mu)$ then $1/\mu^*_m$ is a root of $\mathbf{G}_2(\mu)$. In this case any root on the unit-circle ($|\mu| = 1$) becomes a common root of both polynomials $\mathbf{G}_1(\mu)$ and $\mathbf{G}_2(\mu)$. For each root of $\mathbf{G}_1(\mu)$ outside (or inside) the unit-circle, however, there exists a corresponding root of $\mathbf{G}_2(\mu)$ inside (or outside) the unit-circle. Therefore, in general only the (signal) roots on the unit-circle are common roots of both polynomials. Hence, applying the polynomial intersection method, i.e., Algorithm HR-IV presented in Table 6.4, to these two polynomials, the signal generators can be obtained uniquely.

In the simulation section (Section 6.7), the weights $\{c_m\}_{m=1}^{M-1}$ are chosen to be either all one or all random in decreasing order. To prevent any possible performance loss, both in the threshold region and asymptotically, due to the arbitrary choice of the weights, the following iterative refinement procedure is proposed.

6.6.3 Adaptive Selection of Weighting Coefficients

The appropriate choice of the sets of weighting coefficients $\{c_m\}_{m=1}^{M-1}$ and $\{c'_m\}_{m=1}^{M-1}$ to form the two matrix polynomials $\mathbf{G}_1(\mu)$ and $\mathbf{G}_2(\mu)$ has not yet been specified. It is obvious that if some particular roots of the residual polynomials become identical, i.e., for a certain choice of $\{c_m\}_{m=1}^{M-1}$ and $\{c'_m\}_{m=1}^{M-1}$ the true signal roots are no longer the unique common roots of $f(\mu)$ and $g(\mu)$, then the rank of the null-space of $\mathbf{S}(f,g)$ has to be higher than L. In this case, Algorithm HR-IV does not yield unique solutions. However, as it has been already discussed above, the event that the residual polynomials share exactly identical roots is very unlikely for randomly generated sets of coefficients. In practice, for given sets of coefficients $\{c_m\}_{m=1}^{M-1}$ and $\{c'_m\}_{m=1}^{M-1}$, some specific roots of the corresponding residual polynomials can become close to one another. This can lead to degradation in the performance of the proposed algorithm due to the fact that these spurious roots are associated with very small eigenvalues of the $\mathbf{S}(f,g)$. This may result in the so-called subspace swap effect (explained in Section 4.1) in Step 3 of Algorithm HR-IV. Particularly, due to finite sample size, the nominal $(L+1)$-th minor eigenvalue of $\mathbf{S}(f,g)$ may become larger than the nominal L-th minor eigenvalue. This phenomenon becomes more pronounced in the case of low SNRs, where the polynomial coefficients of $f(\mu)$ and $g(\mu)$ both may deviate substantially from their ideal positions. Therefore, we propose that before constructing the matrix $\hat{\mathbf{U}}_0$, the ratio of the L-th and $(L+1)$-th smallest eigenvalues to be examined. If this ratio is close to one, then new random weighting coefficient have to be generated and the algorithm must be repeated. These iterations stop when either the eigenvalue ratio becomes larger than some pre-defined threshold or the number of iterations exceeds a specific pre-determined value.

6.6.4 Computational Complexity

The computational complexity of our proposed Algorithms I-IV is mainly determined by the polynomial rooting procedure. In general, the computational complexity required for rooting a scalar polynomial of degree M corresponds to complexity required for computing the eigenvalues of the associated companion matrix [25], [30], [68]. Therefore, the complexity

is in the order of $\mathcal{O}(M^3)$ complex operations. However, in practice, depending on the implementation the computational complexity can be much lower than the nominal order. This is because of the highly-sparse structure of the companion matrix and considering the fact that only the L minor eigenvalues are required to be computed. Assuming that a largest shift of M_0 ($\leq M-1$) is used in our algorithms, the degree of the polynomials in (6.37) and (6.38) becomes equal to LM_0. Therefore, ignoring potential computational savings due to sparsity, for Algorithms I-III (Tables 6.1-6.3), since only one of these polynomials is used the complexity is in the order of $\mathcal{O}(L^3M_0^3)$ operations. For Algorithm IV (Table 6.4), however, the complexity is in the order of $\mathcal{O}(8L^3M_0^3)$ operations due to the eigendecomposition of the $2LM_0 \times 2LM_0$ sparse Sylvester matrix.

6.7 Simulations

In this section, we compare numerically the performance of the proposed methods in different simulation setups. In the case of undamped harmonics, the MIAA method of [89] is also included in the figures. Originally, in the MIAA method the frequencies are estimated from a single snapshot. However, MIAA allows a modification to the case of multiple snapshots (similar to the IAA method of [107]) which we have used in this thesis to have a fair comparison. In this modification, as we explained in Section 3.7 and Table 3.1, the estimated power at each frequency grid point is computed from each snapshot and then averaged.

The notation for various methods used in the figures are presented in the following:

HR-I denotes Algorithm HR-I (Table 6.1) for the complete sample case described in Section 6.4.

HR-II denotes the selection Algorithm HR-II (Table 6.2) using the residual MP in (6.20) for the incomplete sample case introduced in Section 6.5.1.

HR-III denotes the selection Algorithm HR-III (Table 6.3) using the MUSIC function for the incomplete sample case presented in Section 6.5.2.

HR-IV denotes Algorithm HR-IV (Table 6.4) based on the polynomial intersection for the incomplete sample case introduced in Section 6.6.2.

HR-IV-CB denotes Algorithm HR-IV based on the polynomial intersection for the incomplete sample case using the conjugate and backward re-ordering of the coefficients of the first polynomial as the coefficients of the second polynomial introduced in Subsection 6.6.2.

ideal selection denotes the idealistic selection scheme based on the knowledge of the true generators.

root-MUSIC denotes the root-MUSIC technique described in [7] and briefly in Section 3.2.3.

MIAA denotes the modified method of MIAA presented in [89] and briefly in Section 3.7 and Table 3.1.

In the first example, the complete sample case is addressed. Four cases of choosing the weighting coefficients are considered: the case where $c_1 = 1$ and the remaining coefficients are zero (in this case, our algorithm reduces to the conventional ESPRIT algorithm), the case of uniform weighting coefficients where $c_m = 1$ for $m = 1, \ldots, M-1$, the case of linearly decreasing weighting coefficients, and the case where new decreasing random set of weights in each Monte-Carlo run is used. The sample support is $M = 8$ and the number of snapshots is $N = 50$. We consider $L = 2$ damped harmonics with $\mu_1 = 0.6777 - 0.4464j$, $\mu_2 = 0.8442 + 0.4508j$. In all simulations, we estimate the harmonics parameters and display the RMSE of the estimates $\hat{\mu}_1, \hat{\mu}_2$ for different values of the SNRs. Here, the SNR is defined as

$$\text{SNR} \triangleq 10 \log \left[\frac{\text{Tr}(\mathbf{A}\mathbf{R}_s\mathbf{A}^H)}{\sigma^2 ML} \right]. \tag{6.39}$$

This definition is consistent with the definition of the SNR in the undamped harmonic case used in the DOA estimation problems of previous chapters. For each of the SNR values, $J_r = 500$ Monte-Carlo runs were performed.

The RMSE performance of the harmonic estimation obtained from the proposed methods for different weighting coefficients is displayed in Fig. 6.1. These results are compared to the stochastic Cramér-Rao bound (CRB) that is derived in Appendix C of Section 6.9. We observe a gain of about 2dB in the case of linearly decreasing or uniform weighting coefficients (where all the available shifts are used) as compared to the case of conventional ESPRIT with the single non-zero weight. We observe that the performance of our proposed Algorithm I is robust with respect to the choice of the coefficients. This robustness can further be observed from Fig. 6.2 where the histogram of the RMSE for 10000 sets of randomly selected weighting coefficients for the mentioned scenario at the SNR= -1dB and averaged over $J_r = 500$ Monte-Carlo runs for each set is displayed. The SNR in this figure is deliberately chosen to lie in the sensitive region between the threshold and the asymptotic regions (see Fig. 6.1). It can be seen that RMSE of the estimates only varies slightly with the choice of the weighting coefficients.

As the second simulation example, we consider the undamped HR in the complete sample case. In Fig. 6.3, we compare the RMSE of Algorithm I with different sets of coefficients and the MIAA method shown in Table 3.1 for the undamped case versus the SNR. It has been observed that in the case of small sample size K or when the parameters (i.e., the frequencies) are closely-separated the MIAA is incapable to resolve the parameters even at high SNRs. Therefore, in order to obtain a meaningful comparison where all sources are resolved the MIAA requires a sufficiently large sample size. Our methods, on the other hand, offer high resolution estimation performance. In this example we assume $M = 30$, $N = 20$, two undamped signals with $\mu_1 = 0.8660 + 0.5000j$ and $\mu_2 = 0.8118 + 0.5840j$, and 100 Monte-Carlo runs at each SNR. For the MIAA, the search over the radial frequency $\omega_\mu = \measuredangle(\mu) \in (0, 2\pi]$ is performed over $N_g = 300$ grid points and at most ten iterations are used. Our proposed method shows significantly better performance than the MIAA in this scenario and runs approximately 200 times faster than the MIAA. In our simulations, we observe that the performance of the MIAA improves significantly when we increase M to 100 or more at the cost of substantially increased amount of computational time. Another drawback of the MIAA is its limited accuracy as the resolution capability of the MIAA is

very much dependent on the number of search gird points. This means that in order to stay close to the CRB, the MIAA requires not only a large amount of samples but also more grid points which increases its computational complexity even further.

In the third simulation setup, the incomplete sample case is considered. We assume three damped harmonics with $\mu_1 = 0.8636 + 0.4677j$, $\mu_2 = 0.6799 + 0.5932j$ and $\mu_3 = 0.6678 - 0.4511j$. The sample support is $M = 10$ and only 5 effective samples are available, i.e., $v_m = 1$ for $m = 1, 3, 4, 6, 10$ and $v_m = 0$ for $m = 2, 5, 7, 8, 9$. The number of snapshots is $N = 20$ and the number of simulation runs is equal to $J_r = 1000$. In all simulation results, the weighting coefficients c_m of the first set, $\{c_m\}_{m=1}^{M-1}$, are all chosen to be equal to one. In this case, as also confirmed by simulations, the generator can no longer be determined uniquely from Algorithm HR-I. Thus, Algorithms HR-II, HR-III, or HR-IV must be applied to obtain unique estimates of the signal generator parameters. Therefore, the second set of weighting coefficients $\{c'_m\}_{m=1}^{M-1}$ is chosen from a uniform random distribution on the interval $[0, 2)$. In Fig. 6.4, the performance of the different methods is displayed and compared to the corresponding CRB. From Fig. 6.4, it can be seen that in this scenario, Algorithms HR-II, HR-III, and HR-IV can successfully distinguish between the true signal roots and the spurious signal roots. Moreover, our proposed methods based on selection, i.e., HR-II and HR-III, perform as good as the idealistic clairvoyant selection scheme based on the knowledge of the true generators. Despite this, the polynomial intersection method of Algorithm HR-IV still outperforms the selection-based method.

In Fig. 6.5, the resolution probability of the two estimated signals with the closest signal generators, which in our scenario are given by μ_1 and μ_2 is shown. Similar to the criterion defined in (5.104) for the DOA estimation problem, we assume that the two signal generators are resolved when

$$\sum_{l=1}^{2} |\hat{\mu}_l - \mu_l| \;\leq\; |\mu_1 - \mu_2|. \tag{6.40}$$

To demonstrate the effect of the adaptive selection of the weighting coefficients in Algorithm HR-IV presented in Table 6.4, the performance for different number of iterations in the same scenario is displayed in Fig. 6.6. It can be observed that, after approximately

10-20 iterations, no substantial performance improvement occurs. From Fig. 6.6 we can see that the choice of the weighting coefficients can improve the threshold performance, however, the choice has little effect on the asymptotic performance of the algorithm.

In the fourth example, in Fig. 6.7, we consider the undamped case ($|\mu| = 1$) where $\mu_1 = 0.5582 - 0.8297j$ and $\mu_2 = 0.4475 - 0.8943j$. This case corresponds to the DOA estimation problem where a uniform linear array of ten sensors is assumed with two sources at the angles $\theta_1 = 18.15^\circ$ and $\theta_2 = 20.63^\circ$ relative to the broadside of the array. Therefore, our results are also compared to the results obtained from the root-MUSIC algorithm (explained in Section 3.2.3) for the case where the corresponding sensors are missing. As before, let $v_m = 1$ for $m = 1, 3, 4, 6, 10$ and $N = 50$, and the number of simulation runs be $J_r = 1000$. As illustrated by the figure, the eigenvector method based on polynomial intersection demonstrates better performance than the selection scheme and the root-MUSIC technique. Moreover, it can be observed from Fig. 6.8 that the proposed method outperforms the selection scheme and the root-MUSIC method in terms of source resolution probability. It should be noted that also the MIAA is unable to resolve the signal generators in this scenario.

In the fifth example, in Fig. 6.9, we assume two undamped signals with the generators $\mu_1 = 0.5143 - 0.8576j$ and $\mu_2 = 0.2103 - 0.9776j$. The number of samples is increased to $M = 20$, the number of snapshots is $N = 30$, and $v_m = 1$ for $m = 1, 4, 8, 9, 10, 12, 17, 19, 20$ and $v_m = 0$ otherwise. As mentioned in the second example, the number of samples is increased so that the sources can be resolved using the MIAA. For such a large sample size M the degree of the polynomials in (6.37) and (6.38) becomes very large, leading to large computational complexity. However, in this case we can reduce the degree of the polynomials in (6.37) and (6.38) by limiting the maximum shift, i.e., confining the index m in (6.35) and (6.36) to a value M_0 smaller than $M - 1$. In other words, $c_m = 0$ for $m = M_0 + 1, \ldots, M - 1$. In this example, we assume $M_0 = 9$. For the MIAA, the frequency search is performed over $N_g = 200$ grid points and at most ten iterations are used. The simulations revealed that our method performs more than 90 times faster than the MIAA. The limited RMSE accuracy of the MIAA is apparent in this figure and can be explained

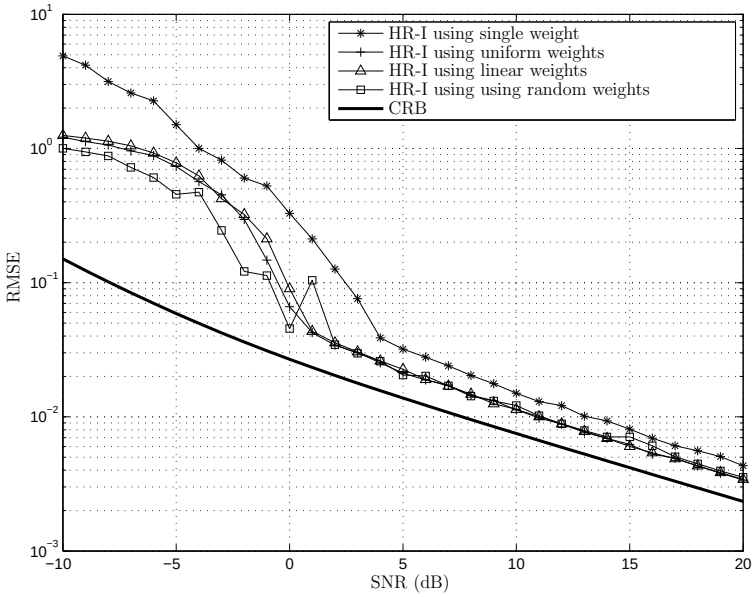

Figure 6.1: Performance comparison of different weighting coefficients for the damped HR complete sample case ($|\mu| < 1$).

by the limited search grid resolution. In this figure, we also display the performance of our proposed method using the conjugate and backward re-ordering of the first polynomial coefficients which has been explained at the end of Section 6.6.2. In Fig. 6.10, the resolution capability of these methods are compared.

6.8 Chapter Summary

An approach for estimating the damped harmonics has been presented along with the derivation of the uniqueness conditions. The weighted summation of the invariance matrices of the different shifts are used to form a matrix whose roots provide us with the harmonic parameters. Two cases of the complete sample case and the incomplete sample case were taken into account. In the first case, the uniqueness conditions for the estimates were derived and the method is shown to provide approximately 2dB gain compared to the ESPRIT method. For the incomplete sample case, the uniqueness of the estimates can not be guaranteed, therefore, different novel algorithms have been proposed to deal with

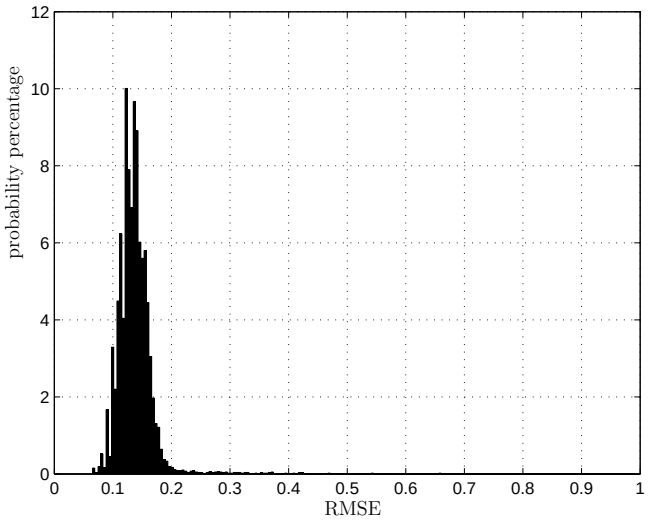

Figure 6.2: Histogram of the RMSE distribution for 10000 random sets of weighting coefficients and SNR= -1dB

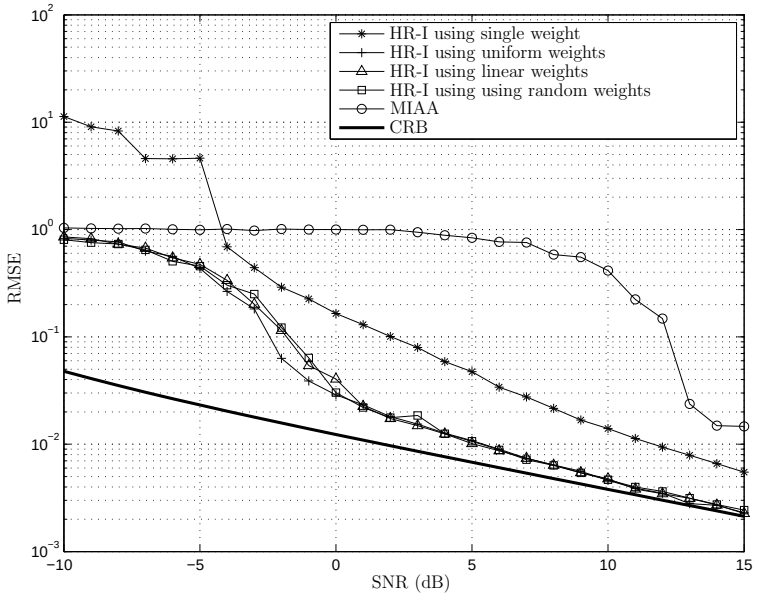

Figure 6.3: Performance comparison of different weighting coefficients and MIAA for the undamped HR complete sample case ($|\mu| = 1$).

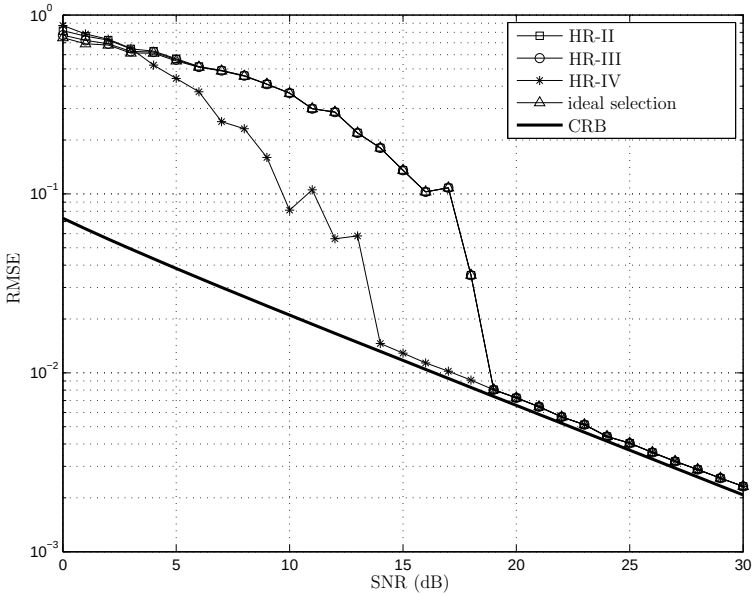

Figure 6.4: Performance comparison of different methods for the damped HR incomplete sample case ($|\mu| < 1$).

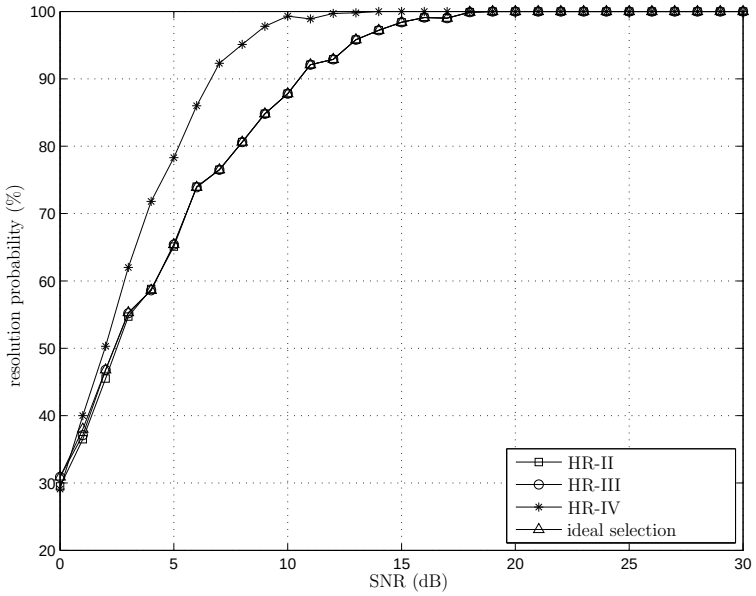

Figure 6.5: Resolution probability vs. SNR for different methods in the damped HR incomplete sample case ($|\mu| < 1$).

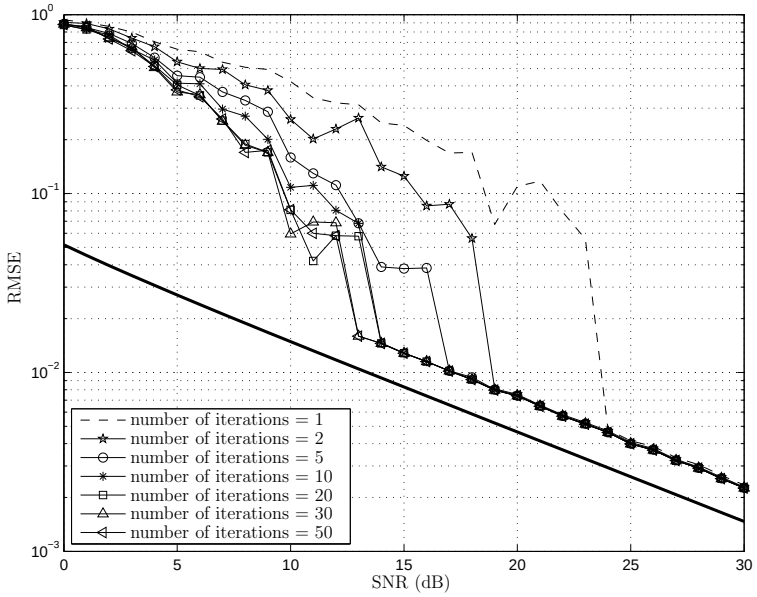

Figure 6.6: The effect of iteration in the selection of the weighting coefficients on the performance of the proposed method for the damped HR incomplete sample case

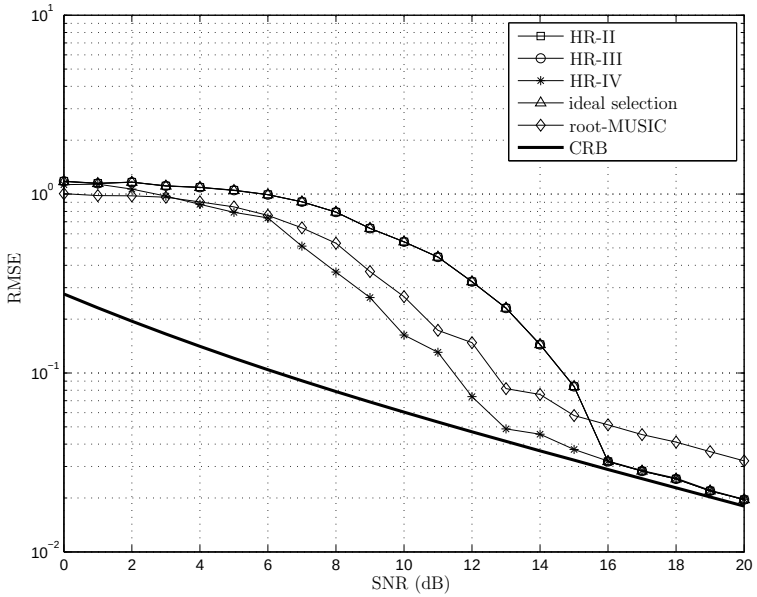

Figure 6.7: Performance comparison of different methods for the undamped HR incomplete sample case ($|\mu| = 1$).

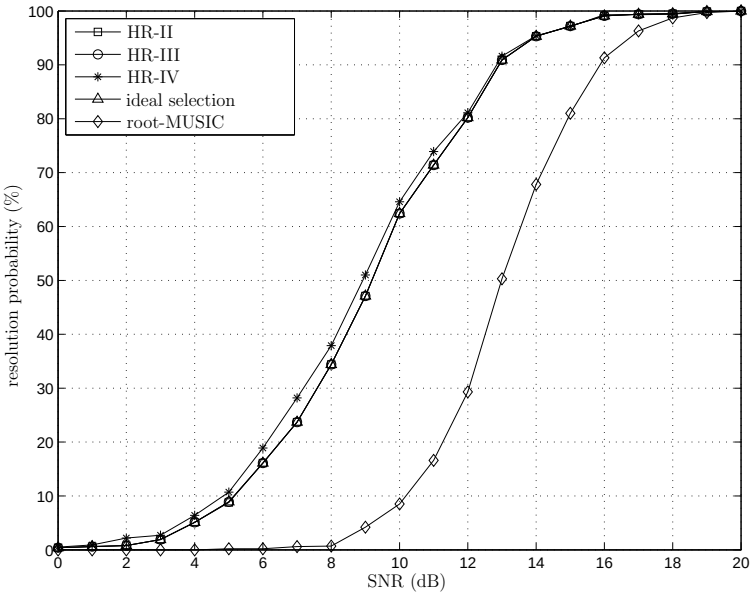

Figure 6.8: Resolution probability vs. SNR for different methods in the undamped HR incomplete sample case ($|\mu| = 1$).

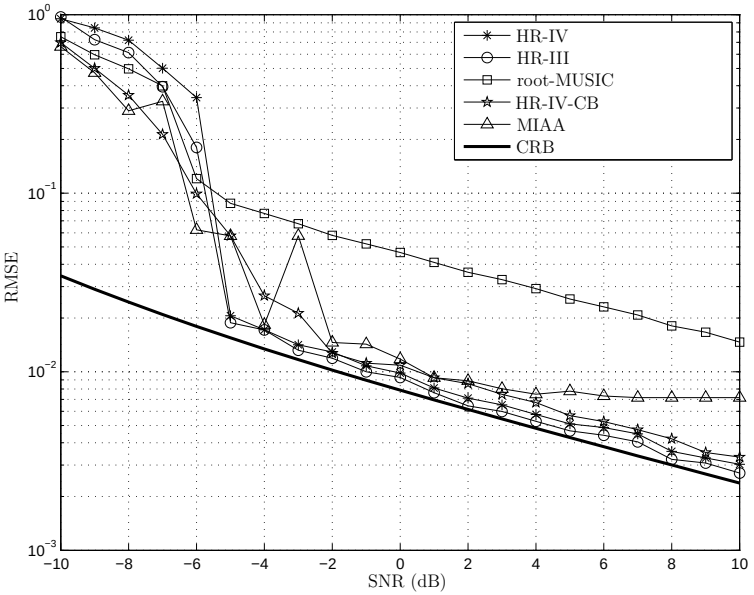

Figure 6.9: Performance comparison of different methods for the undamped HR incomplete sample case ($|\mu| = 1$).

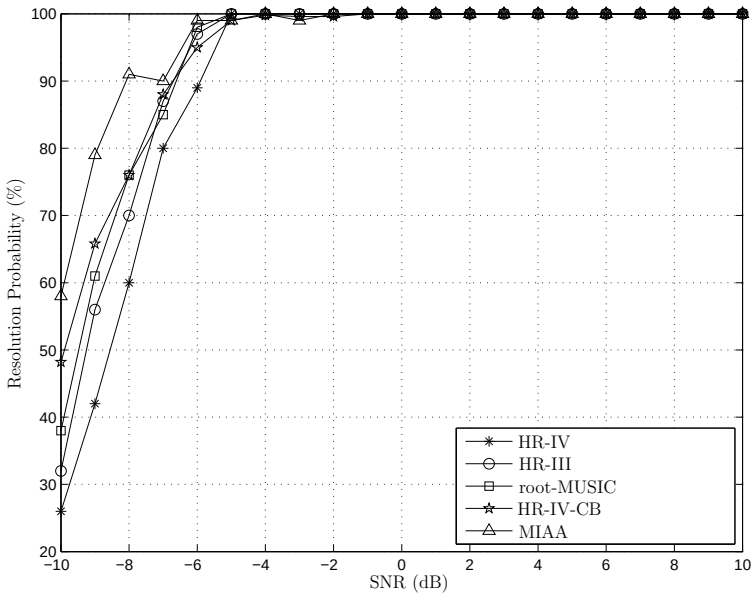

Figure 6.10: Resolution probability vs. SNR for different methods in the undamped HR incomplete sample case ($|\mu| = 1$).

the intrinsic non-uniqueness of the scenarios. Some of these techniques were based on selecting the proper estimates from all of the obtained estimates. To this end, different ideas for selection criteria were presented and successfully implemented. To avoid the selection procedure and its deficiencies, a more sophisticated yet elegant technique based on the properties of the Sylvester matrix and polynomial intersection were proposed. All of the methods, as observed from the simulations, have been successful in reducing the effect of non-uniqueness where some samples are missing. However, the algorithms based on the polynomial intersection appears to be more promising.

6.9 Appendices

Appendix A: Proof of Equation (6.16)

According to Section 6.3, we can obtain the following multiple-shift equation (6.13):

$$\mathbf{M}(\mu) \;=\; \sum_{k=1}^{M-1}\sum_{m=1}^{M-k} c_m v_{k+m} v_k \mathbf{h}_{k+m}^H \mathbf{h}_{k+m} \left(\mathbf{I} - \boldsymbol{\Delta}^{-m}\mu^k\right) = \mathbf{0}_{L\times 1} \tag{A.1}$$

for $\mu = \mu_l$ and $c_m \in \mathbb{R}^+$, respectively. It can be readily verified that $\mathbf{M}(\mu)$ in equation (A.1) can be factorized as

$$\begin{aligned}
\mathbf{M}(\mu) &= \sum_{k=1}^{M-1}\sum_{m=1}^{M-k} c_m v_{k+m} v_k \mathbf{h}_{k+m}^H \mathbf{h}_{k+m} \left(\mathbf{I} + \boldsymbol{\Delta}^{-1}\mu + \cdots + \boldsymbol{\Delta}^{-m+1}\mu^{m-1}\right)\left(\mathbf{I} - \boldsymbol{\Delta}^{-1}\mu\right) \\
&= \sum_{k=1}^{M-1}\sum_{m=1}^{M-k}\sum_{n=0}^{m-1} c_m v_{k+m} v_k \mathbf{h}_{k+m}^H \mathbf{h}_{k+m} \boldsymbol{\Delta}^{-n}\mu^n \left(\mathbf{I} - \boldsymbol{\Delta}^{-1}\mu\right) \\
&= \sum_{k=1}^{M-1}\sum_{m=1}^{M-k}\sum_{n=0}^{m-1} c_m v_{k+m} v_k \mathbf{h}_{k+m}^H \mathbf{h}_{k+m-n} \mu^n \left(\mathbf{I} - \boldsymbol{\Delta}^{-1}\mu\right).
\end{aligned} \tag{A.2}$$

Furthermore,

$$\mathbf{h}_m^H \;=\; \mathbf{A}^H \mathbf{e}_m = \overline{\mathbf{A}}^H \mathbf{e}_{m-1} \tag{A.3}$$

where the $(M-1)\times L$ matrix $\overline{\mathbf{A}}$ is the matrix $\mathbf{A}$ with the dropped first row. Then, equation (A.2) translates to

$$\begin{aligned}
\mathbf{M}(\mu) &= \sum_{k=1}^{M-1}\sum_{m=1}^{M-k}\sum_{n=0}^{m-1} c_m v_{k+m} v_k \overline{\mathbf{A}}^H \mathbf{e}_{k+m-1}\mathbf{e}_{k+m-n-1}\overline{\mathbf{A}}\mu^n \left(\mathbf{I} - \boldsymbol{\Delta}^{-1}\mu\right) \\
&= \sum_{k=1}^{M-1}\sum_{m=1}^{M-k}\sum_{n=0}^{m-1} c_m v_{k+m} v_k \overline{\mathbf{A}}^H \mathbf{E}_{k+m-1,k+m-n-1}\overline{\mathbf{A}}\mu^n \left(\mathbf{I} - \boldsymbol{\Delta}^{-1}\mu\right) \\
&= \overline{\mathbf{A}}^H \left(\sum_{k=1}^{M-1}\sum_{m=1}^{M-k}\sum_{n=0}^{m-1} c_m v_{k+m} v_k \mathbf{E}_{k+m-1,k+m-n-1}\mu^n\right)\overline{\mathbf{A}}\left(\mathbf{I} - \boldsymbol{\Delta}^{-1}\mu\right) \\
&= \overline{\mathbf{A}}^H \left(\sum_{k=1}^{M-1} \mathbf{C}_k(\mu)\right)\overline{\mathbf{A}}\left(\mathbf{I} - \boldsymbol{\Delta}^{-1}\mu\right) \\
&= \overline{\mathbf{A}}^H \mathbf{C}(\mu)\overline{\mathbf{A}}\left(\mathbf{I} - \boldsymbol{\Delta}^{-1}\mu\right)
\end{aligned} \tag{A.4}$$

where $\mathbf{E}_{k,l}$ denotes the $(M-1)\times(M-1)$ matrix containing a one in the (k,l) entry and zeros elsewhere, and

$$\mathbf{C}(\mu)=\sum_{k=1}^{M-1}\mathbf{C}_k(\mu). \tag{A.5}$$

Here, $\mathbf{C}_k(\mu)$ is defined as

$$\mathbf{C}_k(\mu)=v_k\sum_{m=1}^{M-k}c_m v_{k+m}\sum_{n=0}^{m-1}\mathbf{E}_{k+m-1,k+m-n-1}\mu^n \tag{A.6}$$

for $k=1,\ldots,M-1$. Hence, the matrix $\mathbf{C}(\mu)$ can be represented more explicitly using (6.18).

Appendix B: Proof of Uniqueness Conditions For the Complete Sample Case

In Appendix A, it has been demonstrated that for the complete sample case, the MP $\mathbf{M}(\mu)$ in (6.21) can be factorized as

$$\mathbf{M}(\mu)=\overline{\mathbf{A}}^H\mathbf{C}(\mu)|_{\mathbf{V}=\mathbf{I}}\overline{\mathbf{A}}\left(\mathbf{I}-\boldsymbol{\Delta}^{-1}\mu\right) \tag{B.1}$$

where the matrix $\mathbf{C}(\mu)$ in (6.18) transforms to

$$\mathbf{C}(\mu)|_{\mathbf{V}=\mathbf{I}}=\begin{bmatrix} c_1 & 0 & 0 & \cdots & 0\\ c_2\mu & c_2+c_1 & 0 & \cdots & 0\\ c_3\mu^2 & (c_3+c_2)\mu & c_3+c_2+c_1 & \cdots & 0\\ \vdots & \vdots & \vdots & \ddots & \vdots\\ c_{M-1}\mu^{M-2} & (\sum_{l=1}^{2}c_{M-l})\mu^{M-3} & (\sum_{l=1}^{3}c_{M-l})\mu^{M-4} & \cdots & (\sum_{l=1}^{M-1}c_{M-l}) \end{bmatrix}. \tag{B.2}$$

The fourth term in the right-hand side of (B.1), i.e., $\left(\mathbf{I}-\boldsymbol{\Delta}^{-1}\mu\right)$, becomes singular if and only if μ is equal to one of the true generators $\mu_1,\ldots,\mu_L$. From the definition in (6.20), we conclude that for the complete sample case

$$\mathbf{M}_{\mathrm{r}}(\mu)=\overline{\mathbf{A}}^H\mathbf{C}(\mu)|_{\mathbf{V}=\mathbf{I}}\overline{\mathbf{A}}. \tag{B.3}$$

Recall that, in order to prove that under condition (6.23) all singularities of $\mathbf{M}(\mu)$ inside the unit-circle correspond to true signal generators, it is sufficient to show that $\mathbf{M}_{\mathrm{r}}(\mu)$ is

positive definite and, hence, non-singular for $|\mu| \leq 1$. The non-Hermitian matrix $\mathbf{M}_{\rm r}(\mu)$ is referred to as positive definite if its Hermitian part is positive definite, i.e., if

$$\begin{aligned} \mathbf{x}^H \left(\mathbf{M}_{\rm r}(\mu) + \mathbf{M}_{\rm r}^H(\mu)\right) \mathbf{x} &= \\ \mathbf{x}^H \overline{\mathbf{A}}^H \left(\mathbf{C}(\mu)|_{\mathbf{V}=\mathbf{I}} + \mathbf{C}^H(\mu)|_{\mathbf{V}=\mathbf{I}}\right) \overline{\mathbf{A}}\mathbf{x} &= \\ \tilde{\mathbf{x}}^H \left(\mathbf{C}(\mu)|_{\mathbf{V}=\mathbf{I}} + \mathbf{C}^H(\mu)|_{\mathbf{V}=\mathbf{I}}\right) \tilde{\mathbf{x}} &> 0 \end{aligned} \tag{B.4}$$

for any $\mathbf{x} \neq \mathbf{0} \in \mathbb{C}^{L\times 1}$ and $\tilde{\mathbf{x}} = \overline{\mathbf{A}}\mathbf{x}$. In the above equation, we assume that $\overline{\mathbf{A}}$ has full column-rank. Hence, we can conclude that the Hermitian part of $\mathbf{M}_{\rm r}(\mu)$ is positive definite if the Hermitian matrix $\bar{\mathbf{C}}(\mu) = \mathbf{C}(\mu)|_{\mathbf{V}=\mathbf{I}} + \mathbf{C}^H(\mu)|_{\mathbf{V}=\mathbf{I}}$ is positive definite. Therefore, it suffices to derive the conditions under which $\bar{\mathbf{C}}(\mu)$ is positive definite. We write $\bar{\mathbf{C}}(\mu)$ as

$$\bar{\mathbf{C}}(\mu) = \begin{bmatrix} 2c_1 & c_2\mu^* & c_3(\mu^*)^2 & \cdots & c_{M-1}(\mu^*)^{M-2} \\ c_2\mu & 2(c_1+c_2) & (c_2+c_3)\mu^* & \cdots & (c_{M-2}+c_{M-1})(\mu^*)^{M-3} \\ c_3\mu^2 & (c_2+c_3)\mu & 2(c_1+c_2+c_3) & \cdots & (\sum_{m=M-3}^{M-1} c_k)(\mu^*)^{M-4} \\ \vdots & \vdots & \vdots & \ddots & \vdots \\ c_{M-1}\mu^{M-2} & (c_{M-2}+c_{M-1})\mu^{M-3} & (\sum_{m=M-3}^{M-1} c_m)\mu^{M-4} & \cdots & 2(\sum_{m=1}^{M-1} c_m) \end{bmatrix} \tag{B.5}$$

which can be viewed as a matrix composed of $(M-1)$ similar nested matrices, denoted by $\bar{\mathbf{C}}^{(m)}(\mu)$, for $m = 1, \ldots, M-1$. The matrix $\bar{\mathbf{C}}^{(m)}(\mu)$ is obtained from $\bar{\mathbf{C}}^{(m-1)}(\mu)$ by removing the last row and the last column and appending one column and one row of zeros from the left and the top, so that the dimension $(M-1)\times(M-1)$ of the matrix remains unchanged. Thus $\bar{\mathbf{C}}(\mu)$ can be expressed as

$$\bar{\mathbf{C}}(\mu) = \bar{\mathbf{C}}^{(1)}(\mu) + \bar{\mathbf{C}}^{(2)}(\mu) + \cdots + \bar{\mathbf{C}}^{(M-1)}(\mu) \tag{B.6}$$

where

$$\bar{\mathbf{C}}^{(m)}(\mu) \triangleq \mathbf{J}_{m-1}\bar{\mathbf{C}}^{(1)}(\mu)\mathbf{J}_{m-1}^T, \tag{B.7}$$

$$\mathbf{J}_m = \begin{bmatrix} \mathbf{0}_{m,M-1-m} & \mathbf{0}_{m,m} \\ \mathbf{I}_{M-1-m} & \mathbf{0}_{M-1-m,m} \end{bmatrix}, \tag{B.8}$$

and

$$\bar{\mathbf{C}}^{(1)}(\mu) \triangleq \begin{bmatrix} 2c_1 & c_2\mu^* & c_3(\mu^*)^2 & \cdots & c_{M-1}(\mu^*)^{M-2} \\ c_2\mu & 2c_2 & c_3\mu^* & \cdots & c_{M-1}(\mu^*)^{M-3} \\ c_3\mu^2 & c_3\mu & 2c_3 & \cdots & c_{M-1}(\mu^*)^{M-4} \\ \vdots & \vdots & \vdots & \ddots & \vdots \\ c_{M-1}\mu^{M-2} & c_{M-1}\mu^{M-3} & c_{M-1}\mu^{M-4} & \cdots & 2c_{M-1} \end{bmatrix}. \tag{B.9}$$

In order to obtain the conditions for which $\bar{\mathbf{C}}(\mu)$ is positive definite, due to the nested structure of $\bar{\mathbf{C}}(\mu)$ in (B.6) and (B.7), it is sufficient to show that $\bar{\mathbf{C}}^{(1)}(\mu)$ is positive definite, as in this case the matrices $\bar{\mathbf{C}}^{(m)}(\mu)$ are non-negative definite for $m = 1, \ldots, M-1$. Applying the elementary matrix operations of adding the $(m+1)$-th column multiplied by $-\mu$ to the m-th column, and then adding the $(m+1)$-th row multiplied by $-\mu^*$ to the m-th row, for $m = 1, \ldots, M-1$ we obtain

$$\tilde{\mathbf{C}}^{(1)}(\mu) = \bar{\mathbf{W}}^H(\mu)\bar{\mathbf{C}}^{(1)}(\mu)\bar{\mathbf{W}}(\mu) \tag{B.10}$$

where $\bar{\mathbf{W}}(\mu)$ is a $(M-1) \times (M-1)$ full-rank square matrix defined as

$$\bar{\mathbf{W}}(\mu) = \begin{bmatrix} 1 & 0 & 0 & \cdots & 0 \\ -\mu & 1 & 0 & \cdots & 0 \\ 0 & -\mu & 1 & \cdots & 0 \\ \vdots & \vdots & \ddots & \ddots & \vdots \\ 0 & 0 & \cdots & -\mu & 1 \end{bmatrix}. \tag{B.11}$$

It can readily be verified that according to (B.10), we obtain

$$\tilde{\mathbf{C}}^{(1)}(\mu) = \begin{bmatrix} 2c_1 & -c_2\mu^* & 0 & 0 & \cdots & 0 \\ -c_2\mu & 2c_2 & -c_3\mu^* & 0 & \cdots & 0 \\ 0 & -c_3\mu & 2c_3 & -c_4\mu^* & \cdots & 0 \\ \vdots & \vdots & \vdots & \vdots & \ddots & \vdots \\ 0 & 0 & 0 & \vdots & \ddots & -c_{M-1}\mu^* \\ 0 & 0 & 0 & \cdots & -c_{M-1}\mu & 2c_{M-1} \end{bmatrix}. \tag{B.12}$$

Next we derive conditions on the coefficients c_m, for $m = 1, \ldots, M-1$, for which $\tilde{\mathbf{C}}^{(1)}(\mu)$ is positive definite, as this then implies the positive definiteness property of $\bar{\mathbf{C}}(\mu)$. Applying

the Gershgorin circle theorem [21] to the rows of the above matrix yields

$$|\lambda_1 - 2c_1| \leq |-c_2\mu^*| \tag{B.13}$$

$$|\lambda_{K-1} - 2c_{M-1}| \leq |-c_{M-1}\mu^*| \tag{B.14}$$

$$|\lambda_i - 2c_i| \leq |c_i\mu| + |-c_{i+1}\mu^*| \tag{B.15}$$

for $i = 2, \ldots, M-2$, where λ_i is the i-th eigenvalue of the Hermitian matrix $\tilde{\mathbf{C}}^{(1)}(\mu)$ and, hence, λ_i is real-valued. Expanding the above inequalities and taking into account that c_i is a real positive scalar, we obtain

$$2c_1 - c_2|\mu| \leq \lambda_1 \leq 2c_1 + c_2|\mu| \tag{B.16}$$

$$2c_{M-1} - c_{M-1}|\mu| \leq \lambda_{M-1} \leq 2c_{M-1} + c_{M-1}|\mu| \tag{B.17}$$

$$c_i(2 - |\mu|) - c_{i+1} \leq \lambda_i \leq c_i(2 + |\mu|) + c_{i+1}. \tag{B.18}$$

To guarantee that $\tilde{\mathbf{C}}^{(1)}(\mu)$ is positive definite, λ_i must be positive. Hence, the values $2c_1 - c_2|\mu|$ and $c_i(2-|\mu|) - c_{i+1}$ need to be positive. Assuming $|\mu| \leq 1$, we can remark that if $c_i \geq c_{i+1}$ and $2c_1 \geq c_2$, then $c_i(2 - |\mu|) - c_{i+1}$ is positive and, hence, λ_i will always be positive. Therefore, for $|\mu| \leq 1$, and provided that $2c_1 \geq c_2 \geq \cdots \geq c_{M-1} \geq 0$, the matrix $\tilde{\mathbf{C}}^{(1)}(\mu)$ is positive definite. This completes our proof.

Appendix C: CRB Derivation

Our derivation of the CRB for the harmonic retrieval problem in the incomplete sample case is based on [49]. Using the model in (2.6), i.e., $\mathbf{z}(t) = \sum_{l=1}^{L} \boldsymbol{\mu}_l s_l(t) + \mathbf{n}(t)$, and considering the stochastic signal case, $\mathbf{z}(t)$ has a zero-mean Gaussian distribution with the covariance matrix $\mathbf{R}$. We define the vector $\boldsymbol{\omega}$

$$\boldsymbol{\omega} = [\mathrm{Re}\{\mu_1\}, \ldots, \mathrm{Re}\{\mu_L\}, \mathrm{Im}\{\mu_1\}, \ldots, \mathrm{Im}\{\mu_L\}]\,. \tag{C.1}$$

In our model, we assumed that the noise power σ^2, the signal covariance matrix $\mathbf{R}_s$ and the vector $\boldsymbol{\omega}$ are unknown.

Defining $\mathbf{V}$ as in (6.5), it can be shown from [49] that the compact form of the CRB matrix for the unknown vector $\boldsymbol{\omega}$ can be expressed as

$$\mathrm{CRB}(\boldsymbol{\omega}) = \frac{\sigma^2}{N}\left[\mathrm{Re}\{(\underline{\mathbf{1}} \otimes \mathbf{U}_{\mathrm{C}}) \odot (\boldsymbol{\Omega}^H \boldsymbol{\Pi}^{\perp}_{\tilde{\mathbf{A}}} \boldsymbol{\Omega})\}\right]^{-1} \tag{C.2}$$

where $\underline{\mathbf{1}}$ denotes the 2×2 matrix containing ones in all entries, the modified signal generator matrix is defined as $\tilde{\mathbf{A}} \triangleq \mathbf{V}\mathbf{A}$,

$$\mathbf{U}_{\mathrm{C}} = \mathbf{R}_s(\tilde{\mathbf{A}}^H \tilde{\mathbf{A}} \mathbf{R}_s + \sigma^2 \mathbf{I})^{-1} \tilde{\mathbf{A}}^H \tilde{\mathbf{A}} \mathbf{R}_s \tag{C.3}$$

and

$$\boldsymbol{\Pi}^{\perp}_{\tilde{\mathbf{A}}} = \mathbf{I} - \tilde{\mathbf{A}}(\tilde{\mathbf{A}}^H \tilde{\mathbf{A}})^{-1} \tilde{\mathbf{A}}^{-1}. \tag{C.4}$$

The $2L \times M$ matrix $\boldsymbol{\Omega}$ indicates the first partial derivative of the columns of $\tilde{\mathbf{A}}$ with respect to the corresponding unknown parameters of vector $\boldsymbol{\omega}$

$$\boldsymbol{\Omega} = \left[\frac{\partial \tilde{\boldsymbol{\mu}}_1}{\partial \mathrm{Re}\{\mu_1\}}, \ldots, \frac{\partial \tilde{\boldsymbol{\mu}}_L}{\partial \mathrm{Re}\{\mu_L\}}, \frac{\partial \tilde{\boldsymbol{\mu}}_1}{\partial \mathrm{Im}\{\mu_1\}}, \ldots, \frac{\partial \tilde{\boldsymbol{\mu}}_L}{\partial \mathrm{Im}\{\mu_L\}}\right] \tag{C.5}$$

where $\tilde{\boldsymbol{\mu}}_l$ is the l-th column of $\tilde{\mathbf{A}}$ given as

$$\tilde{\boldsymbol{\mu}}_l \triangleq \mathbf{V}\left[1, \mu_l, \mu_l^2, \ldots, \mu_l^{M-1}\right]^T. \tag{C.6}$$

From (C.5), the matrix $\boldsymbol{\Omega}$ can be written as

$$\boldsymbol{\Omega} = \left[\mathbf{Q}\tilde{\mathbf{A}}, j\mathbf{Q}\tilde{\mathbf{A}}\right] \tag{C.7}$$

where

$$\mathbf{Q} \triangleq \mathrm{diag}\{0, 1, 2, \ldots, M-1\}. \tag{C.8}$$

Then, we can compute the required $2L \times 2L$ matrix $\mathrm{CRB}(\boldsymbol{\omega})$ from (C.2).

Chapter 7

Conclusions and Future Works

In this thesis, we studied and devised some novel techniques for estimating the signal DOAs and harmonics (with or without the damped factor) in harsh environments and difficult and non-ideal conditions. In the case of array geometry uncertainties, our methods were able to fully-calibrate the partly-calibrated arrays as well.

After the introductory notes in Chapter 1, we introduced the general signal model in Chapter 2. In Chapter 3, we presented the previous works and the state-of-the-art DOA estimation techniques. The proposed methods of this thesis were compared to the methods presented in Chapter 3. Next, an approach to increase the resolution capability of subspace-based DOA estimation methods and to mitigate the effects of difficult and non-ideal conditions (low SNR, small number of snapshots, and very closely-spaced sources) were proposed in Chapter 4. The high resolution was achieved by combining the estimator bank idea and the technique of quality assessment of the estimates and the identification and cure of the outliers in the estimates. For the latter technique, which is based on hypothesis testing, a new method along with the already-known GLRT and also with the LMPT was proposed and successfully implemented. Moreover, to overcome the problem of estimating the final set of DOA estimates from all the proper ones, two techniques were introduced. The simulation results show substantial improvement in DOA estimation performance for very closely-spaced sources in low SNR or small number of snapshots regions.

In Chapter 5, the uncertainties in the array manifold matrix, which can be created by many factors, were taken into account. Various cases of partly-calibrated arrays were considered and novel DOA estimation/calibration techniques were presented. These techniques exploit the uncertain or unknown part of the manifold as well as its structure in the process of DOA estimation. For the arbitrary partly-calibrated array, an approach based on the linear combination of subspace mismatch functions is proposed. Basically, these functions can be transformed into multivariate ones dependent only on the DOAs by estimating (from two proposed techniques) the other unknown parts of the array manifold. To facilitate the estimation of the DOAs, these functions can be turned into univariate ones. With the help of two other new methods and benefiting from random coefficients, we were able to achieve a significant improvement in the performance avoiding the iterative and computationally costly methods for DOA estimation in multivariate functions. In this chapter, two special cases of partly-calibrated arrays are also considered: one with identical subarrays, and one with pairwise calibrated sensors (which is equivalent to multiple different subarrays consisting of two sensors each). The joint DOA estimation and calibration methods proposed for these sorts of arrays also incorporate the unknown part of the array manifold and its structure into the search-based DOA estimation process. Moreover, the estimation of the unknown part of the array manifold based on convex optimization technique was proposed which, although suboptimal and costly, can provide a benchmark for the performance of the proposed simple technique without convex optimization. These methods outperform the existing competing methods (concisely described in Sections 3.3, 3.4, and 3.6).

The one-dimensional harmonic retrieval problem, where specific spatial and temporal samples are not available, was considered in Chapter 6. After introducing the general search-free technique of WMI for estimating the harmonics, either with or without the damped factors, the scenario-independent conditions under which the estimates can be obtained uniquely were derived for the complete sample case. For the incomplete sample case, we have shown that such scenario-independent uniqueness conditions (similar to the complete sample case) do not generally exist. To overcome this drawback, some selection techniques were presented which choose the proper signal harmonics among the estimates (possibly

more than the existing signals due to the non-uniqueness) obtained from WMI technique based on some criteria. A more sophisticated novel method was also proposed which relies on the polynomial intersection and Sylvester matrix properties. All these techniques proved to be very successful to deal with the non-uniqueness of the estimates and outperform the state-of-the-art method of MIAA presented in Section 3.7.

There can be numerous extensions to the works presented in this thesis. For improving the performance in difficult conditions discussed in Chapter 4, one can always look into the other hypothesis testings which can yield better performance. Furthermore, test statistics other than the two presented here (the GLRT and the LMPT) could be found that could improve the overall performance. Developing other combining methods for obtaining the final set of estimates, that could improve the performance threshold, would also be another interesting future work.

The ideas presented for the partly-calibrated arrays in Chapter 5 are the most promising. As it has been shown, the methods proposed in Chapter 5 are mainly based on the subspace mismatches and estimating the unknown part of the array manifold matrix. The identification and uniqueness conditions are among the problems that remained to be solved for all the proposed techniques in Chapter 5. Moreover, the methods that we described in this chapter demand some performance analysis. This can help in predicting the asymptotic and non-asymptotic behavior of these methods as well as in finding suitable conditions (probably optimum) to arrange the mismatch functions and their weights. Similar to the counterpart methods of GESPRIT in [16], RARE in [66], and MI-MUSIC in [92], the problem of looking for faster, search-free techniques for the proposed methods are desirable and this may be achieved by considering the types of arrays with specific (most likely linear) geometry. Hence, the superiority of our proposed methods can be combined with the reduction in the computational costs. The appearance of pseudo-inverse in algorithms proposed for the APCA model (e.g., Algorithm APCA-I presented in Table 5.2) adversely affects the accuracy of the estimates. It might be possible to avoid the pseudo-inverse in a similar way as in Algorithm PCAMIS-I. The methods for APCA seem to have many applications

in sensor networks due to their sparsity and the unknown parts in the array manifold matrix, i.e., their partly-calibrated model. Therefore, studying these methods and devising new ones for the case of near-field sources helps in sensor network applications where the sources are no longer far-field. These types of arrays (PCAs) can also be used for acoustic applications where the sources are wide-band. Hence, modifying the proposed techniques for wideband sources would also be beneficial.

For the harmonic retrieval problem in Chapter 6, there are still some open problems. For instance, the one dimensional sampling was considered in our model but one can also look at the more general two dimensional case and develop fast methods where some samples are missing in that case too. Moreover, non-uniform sampling schemes in the incomplete sample case can also be studied. Another extension would be developing a technique for obtaining the optimum weighting coefficients in the WMI algorithm both for the complete and the incomplete sample case so that the estimation performance improves even further. Finally, the performance analysis of the new methods introduced in this thesis for HR problem, although very challenging, would help to acquire better understanding of the behavior of these methods.

Bibliography

[1] Y. I. Abramovich, N. K. Spencer, and A. Y. Gorokhov, "Bounds on maximum likelihood ratio — Part I: Application to antenna array detection-estimation with perfect wavefront coherence," *IEEE Trans. Signal Processing,* pp. 1524-1536, Dec. 2004.

[2] Y. I. Abramovich and N. K. Spencer, "Performance breakdown of subspace-based methods in arbitrary antenna arrays: GLRT-based prediction and cure," *ICASSP'04*, Montreal, Canada, vol. 2, pp. 233-236, May 2004.

[3] Y. I. Abramovich, D. A. Gray, A. Y. Gorokhov, and N. K. Spencer, "Positive-definite Toeplitz completion in DOA estimation for nonuniform linear antenna arrays — Part I: Fully augmentable arrays," *IEEE Trans. Signal Processing*, vol. 46, pp. 2458-2471, Sep. 1998.

[4] F. Athley and C. Engdahl, "Direction-of-arrival estimation using separated subarrays," in *in Proc. 34th Asilomar Conference on Signals, Systems, and Computers*, Pacific Groove, CA, vol. 1, pp. 585-589, Nov. 2000.

[5] R. Badeau, B. David, and G. Richard, "High-resolution spectral analysis of mixtures of complex exponentials modulated by polynomials," *IEEE Trans. Signal Processing*, vol. 54, pp. 1341-1350, Apr. 2006.

[6] R. Badeau, B. David, and G. Richard, "Selecting the modeling order for ESPRIT high resolution method: An alternative approach," *IEEE ICASSP'04*, Montreal, Canada, vol. 2, pp. 1025-1028, May 2004.

[7] A. J. Barabell, "Improving the resolution performance of eigenstructure-based direction-finding algorithms," *IEEE ICASSP 83*, Boston, MA, USA, pp. 336-339, Apr. 1983.

[8] A. Bax, "A simple description of two-dimensional NMR spectroscopy," *Bulletin of Magnetic Resonance*, vol. 7, pp. 167-183, 1985.

[9] J. F. Bohme, "Source-parameters estimation by approximate maximum likelihood and nonlinear regression," *IEEE Journal of Oceanic Engineering*, vol. 10, Issue 3, pp. 206-212, July 1985.

[10] S. Boyd and L. Vandenberghe, *Convex Optimization*, Cambridge University Press, 2004.

[11] Y. Bresler and A. Macovski, "Exact maximum likelihood parameter estimation of superimposed exponential signals in noise," *IEEE Trans. Acoustics, Speech, and Signal Processing*, vol. 34, pp. 1081-1089, Oct. 1986.

[12] F. K. W. Chan, H. C. So, W. H. Lau, and C. F. Chan, "Efficient approach for sinusoidal frequency estimation of gapped data," *IEEE Signal Processing Letters*, vol. 17, pp. 611-614, June 2010.

[13] M. H. DeGroot and M. J. Schervish, *Probability and Statistics*, Addison-Wesley, 2002

[14] B. Friedlander, "A sensitivity analysis of MUSIC algorithm," *IEEE Trans. Antennas and Propagation*, vol. 38, pp. 1740-1751, Oct. 1990.

[15] B. Friedlander and A. J. Weiss, "Direction finding using spatial smoothing with interpolated arrays," *IEEE Trans. Aerospace and Electronic Systems*, vol. 28, pp. 574-587, Apr. 1992.

[16] F. Gao and A. B. Gershman, "A generalized ESPRIT approach to direction-of-arrival estimation," *IEEE Signal Processing Letters*, vol. 10, no. 3, pp. 254-257, Mar. 2005.

[17] A. B. Gershman, "Pseudo-randomly generated estimator banks: A new tool for improving the threshold performance of direction finding," *IEEE Trans. Signal Processing*, vol. 46, pp. 1351-1364, May 1998.

[18] A. B. Gershman, "Direction finding using beamspace root estimator banks," *IEEE Trans. Signal Processing,* vol. 46, pp. 3131-3135, Nov. 1998.

[19] A. B. Gershman and P. Stoica, "New MODE-based techniques for direction finding with an improved threshold performance," *Signal Processing*, vol. 76, 221-235, no. 3, Aug. 1999.

[20] A. B. Gershman, J. F. Bohme, "Improved DOA estimation via pseudorandom resampling of spatial spectrum," *IEEE Signal Processing Letters,* vol. 4, pp. 54-57, Feb. 1997.

[21] G. H. Golub and C. F. Van Loan, *Matrix Computations,* Baltimore, Johns Hopkins University Press, 1984.

[22] M. Haardt and J. A. Nossek, "Simultaneous Schur decomposition of several nonsymmetric matrices to achieve automatic pairing in multidimensional harmonic retrieval," *IEEE Trans. Signal Processing*, vol. 46, pp. 161-169, Jan. 1998.

[23] G. Hatke and K. W. Forsythe, "A class of polynomial rooting algorithms for joint azimuth/elevation estimation using multidimensional arrays," *Proc. 30th Asilomar on Signals, Systems, and Computers*, Pacific Grove, CA, vol. 1, pp. 694-699, Nov. 1996.

[24] M. Hawkes, A. Nehorai, and P. Stoica, "Performance breakdown of subspace-based methods: Prediction and cure," *ICASSP'01*, Salt Lake City, USA, vol. 6, pp. 4005-4008, May 2001.

[25] R. A. Horn and C. R. Johnson, *Matrix Analysis*, Cambridge University Press, New York, NY, USA, 1985.

[26] L. Huang, T. Long, and S. Wu, "Source enumeration for high-resolution array processing using improved Gerschgorin radii without eigendecomposition," *IEEE Trans. Signal Processing*, vol. 56, pp. 5916-5925, Dec. 2008.

[27] S. John, "Some optimal multivariate test," *Biometrika*, **38**, pp. 123-127, 1971.

[28] S. John, "The distribution of a statistics used for testing sphericity of normal distributions," *Biometrika*, **59**, pp. 169-173, 1972.

[29] B. A. Johnson, Y. I. Abramovich, and X. Mestre, "MUSIC, G-MUSIC and maximum-likelihood performance breakdown" *IEEE Trans. Signal Processing*, vol. 56, no. 8, pp. 3944-3958, Aug. 2008.

[30] T. Kailath, *Linear Systems*. Prentice-Hall Inc., Upper Saddle River, N.J., 1980

[31] M. Kaveh and A. J. Barabell, "The statistical performance of the MUSIC and minimum-norm algorithms in resolving plane waves in noise," *IEEE Trans. Acoustics, Speech, and Signal Processing*, vol. 34, pp. 331-341, Feb. 1986.

[32] H. Krim, P. Forster, and J. G. Proakis, "Operator approach to performance analysis of root-MUSIC and root Min-Norm," *IEEE Trans. Acoustics, Speech, and Signal Processing*, vol. 40, pp. 1687-1688, July 1992.

[33] H. Krim and M. Viberg, "Two decades of array signal processing research," *IEEE Signal Processsing Magazine*, pp. 67-93, July 1996.

[34] R. Kumaresan and D. W. Tufts, "Estimating the parameters of exponentially damped sinusoids and pole-zero modeling in noise," *IEEE Trans. Acoustics, Speech, and Signal Processing*, vol. 30, pp. 833-840, Dec. 1982.

[35] R. Kumaresan and D. W. Tufts, "Estimating the angles of arrival of multiple plane waves," *IEEE Trans. Aerospace and Electronic Systems*, vol. 19, pp. 134-139, Jan. 1983.

[36] S. Y. Kung, K. S. Arun, and D. V. Bhaskar Rao, "State-space and singular-value decomposition-based approximation methods for the harmonic retrieval problem," *J. Opt. Soc. Amer.*, vol. 73, no. 12, pp. 1799-1811, Dec. 1983.

[37] J. Li, P. Stoica and D. Zheng, "An efficient algorithm for two-dimensional frequency estimation," *Multidimensional Systems and Signal Processing*, vol. 7, pp. 151-178, Apr. 1996.

[38] Y. Li, J. Razavilar, and K. J. R. Liu, "A high-resolution technique for multidimensional NMR spectroscopy," *IEEE Trans. Biomedical Engineering*, vol. 45, pp. 78-86, Jan. 1998.

[39] J. Li and P. Stoica, "An adaptive filtering approach to spectral estimation and SAR imaging," *IEEE Trans. Signal Processing*, vol. 44, pp. 1469-1484, June 1996.

[40] J. Li, Y. Wang, P. Stoica, and T. L. Marzetta, "Nonparametric spectral analysis with missing data via the EM algorithm," *IEEE Proc. 38th Asilomar Conference on Signals, Systems, and Computers*, vol. 1, Pacific Grove, CA, pp. 8-12, Nov. 2004.

[41] D. A. Linebarger, R. D. DeGroat, and E. M. Dowling, "Efficient direction-finding methods employing forward-backward averaging" *IEEE Trans. Signal Processing*, vol. 42, pp. 425-432, Aug. 1994.

[42] X. Liu and N. D. Sidiropoulos, "On constant modulus multidimensional harmonic retrieval," *IEEE ICASSP'02*, Orlando, FL, USA, pp. 2977-2980, May 2002.

[43] J. T. H. Lo and S. L. Marple, "Eigenstructure methods for array sensor localization," *IEEE ICASSP '87*, vol. 12, pp. 2260-2263, Dallas, Texas, Apr. 1987.

[44] J. T. H. Lo and S. L. Marple, "Observability conditions for multiple signal direction finding and array sensor localization," *IEEE Trans. Signal Processing*, vol. 40, pp. 2641-2650, Nov. 1992.

[45] C. P. Mathews and M. D. Zoltowski, "Eigenstructure techniques for 2-D angle estimation with uniform circular arrays," *IEEE Trans. Signal Processing*, vol. 42, pp. 2395-2407, Sep. 1994.

[46] X. Mestre and F. Rubio, "An improved subspace-based algorithm in the small sample size regime," *IEEE ICASSP'06*, Toulouse, France, vol. 4, pp. 1073-1706, May 2006.

[47] K. N. Mokios, N. D. Sidiropoulos, M. Pesavento, and C. F. Mecklenbräuker, "On 3D harmonic retrieval for wireless channel sounding," *IEEE ICASSP'04*, Montreal, Canada, pp. 89-92, May 2004.

[48] R. J. Muirhead, *Aspects of Multivariate Statistical Theory*, Wiley, 1982.

[49] A. Nehorai and E. Paldi, "Vector-sensor array processing for electromagnetic source localization," *IEEE Trans. Signal Processing*, vol. 42, pp. 376-398, Feb. 1992.

[50] B. C. Ng and A. Nehorai, "Optimum active array shape calibration," *IEEE Proc. 25th Asilomar Conference on Signals, Systems, and Computers*, pp. 893-897, Nov. 1991.

[51] B. C. Ng and W. Ser, "Array shape calibration using sources in known locations," *IEEE ICCS/ISITA '92 Communications on the Move*, Singapore, pp. 836-840, 1992.

[52] S. K. Oh and C. K. Un, "A sequential estimation approach for performance improvement of eigenstructure-based methods in array processing," *IEEE Trans. Signal Processing* vol. 41, pp. 457-463, Jan. 1993.

[53] B. Ottersten, M. Viberg, P. Stoica, and A. Nehorai, *"Exact and large sample maximum likelihood techniques for parameter estimation and detection in array processing,"* in Radar Array Processing, S. Haykin, J. Litva, and T. J. Shepherd, Eds., pp. 99-151. Springer-Verlag, Berlin, 1993, chapter 4, Springer Series in Information Sciences, vol 25.

[54] B. Ottersten, M. Viberg, and T. Kailath, "Analysis of subspace fitting and ML techniques for parameter estimation from sensor array data," *IEEE Trans. Signal Processing*, vol. 40, pp. 590-600, Mar. 1992.

[55] A. J. Park, C. Lee, H. Kang, and B. Youn, "Generalization of the subspace-based array shape estimations," *IEEE Trans. Oceanic Engineering*, vol. 29, pp. 847-856, July 2004.

[56] P. Parvazi, A. B. Gershman, and Y. I. Abramovich, "Detecting Outliers in the Estimator Bank-Based Direction Finding Techniques using the Likelihood Ratio Quality Assessment," *IEEE ICASSP'07*, Honolulu, USA, vol. 2, pp. 1065-1068, Apr. 2007.

[57] P. Parvazi, A. B. Gershman, and Y. I. Abramovich, "Improving the threshold performance of the estimator bank direction finding techniques using outlier identification and cure", *Proceedings of the IEEE International Symposium on Wireless Pervasive Computing*, Santorini, Greece, pp. 270 - 273, May 2008.

[58] P. Parvazi and A. B. Gershman, "Direction-of-arrival and spatial signature estimation in antenna arrays with pairwise sensor calibration," *IEEE ICASSP'10*, Dallas, TX, USA, pp. 2618-2621, Mar. 2010.

[59] P. Parvazi, M. Pesavento, and A. B. Gershman, "Direction-of-arrival estimation and array calibration for partly-calibrated arrays," *IEEE ICASSP'11*, Prague, Czech Republic, pp. 2552-2555, May 2011.

[60] P. Parvazi, M. Pesavento, and A. B. Gershman, "Exploiting multiple shift-invariances in harmonic retrieval: the incomplete data case," *IEEE SSP'11*, Nice, France, pp. 729-732, June 2011.

[61] P. Parvazi, M. Pesavento, and A. B. Gershman, "Rooting-based harmonic retrieval using multiple shift-invariances: the complete and the incomplete sample cases," *IEEE Trans. Signal Processing*, 2011, accepted.

[62] P. Parvazi and M. Pesavento, "A new direction-of-arrival estimation and calibration method for arrays composed of multiple identical subarrays," *IEEE SPAWC'11*, San Francisco, CA, USA, pp. 166-170, June 2011.

[63] A. Paulraj and T. Kailath, "Direction of arrival estimation by eigenstructure methods with unknown sensor gain and phase," *IEEE ICASSP'85*, Tampa, Florida, USA, pp. 640-643, Mar. 1985.

[64] M. Pesavento, S. Shahbazpanahi, J. F. Böhme, and A. B. Gershman, "Exploiting multiple shift invariances in multidimensional harmonic retrieval of damped exponentials," *IEEE ICASSP'05*, Philadelphia, PA, USA, pp. 1017-1020, Mar. 2005.

[65] M. Pesavento, C. F. Mecklenbräuker, and J. F. Böhme, "Multidimensional rank-reduction estimator for parametric MIMO channel models," *EURASIP Journal of Appl. Signal Processing*, special issue on Advances in Smart Antennas, pp. 1354-1363, Aug. 2004.

[66] M. Pesavento, A. B. Gershman, and K. M. Wong, "Direction finding in partly calibrated sensor arrays composed of multiple subarrays," *IEEE Trans. Signal Processing*, vol. 50, pp. 2103-2115, Sep. 2002.

[67] M. Pesavento and J. F. Böhme, "Rooting versus joint diagonalization in 2-D harmonic retrieval," *IEEE Sensor Array and Multichannel Signal Processing Workshop*, Sitges, Barcelona, Spain, pp. 303-307, July 2004.

[68] M. Pesavento, *Fast Algorithms for Multidimensional Harmonic Retrieval*, Ph.D thesis, Ruhr-University Bochum, 2005.

[69] M. Pesavento, "Exploiting Multiple Shift Invariances In Harmonic Retrieval," *IEEE ICASSP'09*, Taipei, Taiwan, pp. 2101-2104, Apr. 2009.

[70] V. F. Pisarenko, "The retrieval of harmonics from a covariance function," *Geophysical Journal of the Royal Astronomical Society*, vol. 33, pp. 347-366, Sep. 1973.

[71] C. Proukakis and A. Manikas, "Study of ambiguities of linear arrays," *ICASSP'94*, Adelaide, South Australia, Australia, pp. 549-552, Apr. 1994.

[72] L. Qiong, G. Long, and Y. Zhongfu, "An overview of self-calibration in sensor array processing," *IEEE International Symposium on Antennas, Propagation and EM Theory*, Beijing, China, pp. 279-282, Oct.-Nov. 2003.

[73] B. D. Rao, "Lowering the threshold SNR of singular value decomposition based methods," *ICASSP 1988*, New York, USA, pp. 2472-2475, Apr. 1988.

[74] S. S. Reddi, "Multiple source location - a digital approach," *IEEE Trans. Aerospace and Electronic Systems*, vol. AES-15, pp. 95-105, Jan. 1979.

[75] L. Rippert, "Optical Fiber for Damage Monitoring in Carbon Fiber Reinforced Plastic Composite Materials," Ph.D. dissertation, Katholieke Universiteit Leuven, Belgium, 2003.

[76] Y. Rockah and P. M. Schultheiss, "Array shape calibration using sources in unknown locations - Part 1: Far-field sources," *IEEE Trans. Acoustics, Speech, and Signal Processing*, vol. 35, pp. 286-299, Mar. 1987.

[77] R. Roy and T. Kailath, "ESPRIT - Estimation of signal parameters via rotational invariance techniques," *IEEE Trans. Acoustics, Speech, and Signal Processing*, vol. 37, pp. 984-995, July 1989.

[78] R. O. Schmidt, "Multiple emitter location and signal parameter estimation," *IEEE Trans. Antennas and Propagation*, vol. 34, pp. 276-280, Mar. 1986.

[79] C. M. S. See, "Method for array calibration in high-resolution sensor array processing," *IEE Proc. Radar, Sonar Navigation*, vol. 142, pp. 93-96, Jun. 1995.

[80] C. M. S. See and A. B. Gershman, "Direction-of-arrival estimation in partly calibrated subarray-based sensor arrays," *IEEE Trans. Signal Processing*, vol. 52, pp. 329-328, Feb. 2004.

[81] L. P. H. K. Seymour, C. F. N. Cowan, and P. M. Grant, "The effects of sensor positioning errors on bearing estimation," *IEE Colloquium on Passive Direction Finding*, pp. 9/1-9/8, 31 Jan. 1989.

[82] T. Shan, M. Wax, and T. Kailath, "On spatial smoothing for direction-of-arrival estimation of coherent signals,", *IEEE Trans. Acoustics, Speech, and Signal Processing*, vol. 33, pp. 806-811, Aug. 1985.

[83] N. D. Sidiropoulos, T. N. Davidson, and T. Luo, "Transmit beamforming for physical-layer multicasting," *IEEE Trans. Signal Processing*, vol. 54, pp. 2239-2251, June 2006.

[84] N. K. Spencer and Y. I. Abramovich, "Performance Analysis of DOA Estimation Using Uniform Circular Antenna Arrays in the Threshold Region," *IEEE ICASSP'04*, Montreal, Canada, pp. 233-236, May 2004.

[85] P. Stoica and A. Nehorai, "MUSIC, maximum likelihood and Cramer-Rao Bound," *IEEE Trans. Acoustics, Speech, and Signal Processing*, vol. 37, pp. 720-741, May 1989.

[86] P. Stoica and A. Nehorai, "MUSIC, maximum likelihood and Cramer-Rao Bound: Further results and comparisons," *IEEE Trans. Acoustics, Speech, and Signal Processing*, vol. 38, pp. 2140-2150, Dec. 1990.

[87] P. Stoica and A. B. Gershman, "Maximum likelihood DOA estimation by data-supported grid search," *IEEE Signal Processing Letters*, vol. 6, pp. 273-275, Oct. 1999.

[88] P. Stoica and K. C. Sharman, "Maximum likelihood methods for direction-of-arrival estimation," *IEEE Trans. Acoustics, Speech, and Signal Processing*, vol. 38, pp. 1132-1143, July 1990.

[89] P. Stoica, J. Li, and J. Ling, "Missing data recovery via a nonparametric iterative adaptive approach," *IEEE Signal Processing Letters*, vol. 16, pp. 241-244, Apr. 2009.

[90] A. L. Swindlehurst, B. Otterstein, and T. Kailath, "An analysis of MUSIC and Root-MUSIC in the presence of sensor perturbations," in *in Proc. 23rd Asilomar Conference on Signals, Systems, and Computers*, pp. 930-934, Nov. 1989.

[91] A. L. Swindlehurst, B. Ottersten, R. Roy, and T. Kailath, "Multiple invariance ESPRIT," *IEEE Trans. Signal Processing*, vol. 40, pp. 867-881, Apr. 1992.

[92] A. L. Swindlehurst, P. Stoica, and M. Jansson, "Exploiting arrays with multiple-invariances using MUSIC and MODE," *IEEE Trans. Signal Processing*, vol. 49, pp. 2511-2521, Nov. 2001.

[93] A. L. Swindlehurst, "Optimal direction finding with partially calibrated arrays," *IEEE ICASSP'95*, Detroit, Michigan, USA, vol. 3, pp. 1880-1883, May 1995.

[94] J. K. Thomas, L. L. Scharf, and D. E. Tufts, "The probability of a subspace swap in the SVD," *IEEE Trans. Signal Processing*, vol. 43, pp. 730-734, Mar. 1995.

[95] D. W. Tufts, A.C. Kot, and R. J. Vaccaro, "The threshold analysis of SVD-based algorithms," *IEEE ICASSP'88*, New York, USA, pp. 2416-2419, Apr. 1998.

[96] E. Tuncer and B. Friedlander, *Classical and Modern Direction-of-Arrival Estimation*, Academic Press, Elsevier Inc., USA, 2009.

[97] F. Vanpoucke, M. Moonen, and Y. Berthoumieu, "An efficient subspace algorithm for 2-D harmonic retrieval," *IEEE ICASSP'94*, Adelaide, South Australia, Australia, pp. 461-464, Apr. 1994.

[98] H. L. Van Trees, *Detection, Estimation and Modulation Theory - Part IV: Optimum Array Processing*, Wiley-Interscience, 2002.

[99] W. Verhelst, K. Hermus, P. Lemmerling, P. Wambacq, and S. Van Huffel, "Modeling audio with damped sinusoids using total least squares algorithms," in *Total Least Squares and Errors-in-Variables Modeling: Analysis, Algorithms and Applications*, S. Van Huffel and P. Lemmerling, Eds. Dordrecht, The Netherlands: Kluwer, 2002, pp. 331-340.

[100] M. Viberg, B. Ottersten, and T. Kailath, "Detection and estimation in sensor arrays using weighted subspace fitting," *IEEE Trans. Signal Processing*, vol. 39, pp. 2436-2449, Nov. 1991.

[101] M. Wax and T. Kailath, "Detection of signals by information theoretic criteria," *IEEE Trans. Acoustics, Speech, and Signal Processing*, vol. 2, pp. 387-392, Apr. 1985.

[102] M. Wax and I. Ziskind, "Detection of the number of coherent signals by the MDL principle," *IEEE Trans. Acoustics, Speech, and Signal Processing*, vol. 37, pp. 1190-1196, Aug. 1989.

[103] A. J. Weiss and B. Friedlander, "Array shape calibration using sources in unknown locations: a maximum likelihood approach," *IEEE Trans. Acoustics, Speech, and Signal Processing*, vol. 37, pp. 1958-1966, Dec. 1989.

[104] A. Weiss and B. Friedlander, "DOA and steering vector estimation using a partially calibrated array," *IEEE Trans. Aerospace and Electronic Systems*, vol. 32, pp. 1047-1057, July 1996.

[105] E. W. Weisstein "Resultant." From MathWorld – A Wolfram Web Resource. http://mathworld.wolfram.com/Resultant.html

[106] E. W. Weisstein "Sylvester Matrix." From MathWorld – A Wolfram Web Resource. http://mathworld.wolfram.com/SylvesterMatrix.html

[107] T. Yardibi, J. Li, P. Stoica, M. Xue, and A. B. Baggeroer, "Source localization and sensing: A nonparametric iterative adaptive approach based on weighted least square," *IEEE Trans. Aerospace and Electronic Systems*, vol. 46, pp. 425-436, Jan. 2010.

[108] I. Ziskind and M. Wax, "Maximum likelihood localization of multiple sources by alternating projection," *IEEE Trans. Acoust., Speech, Signal Processing*, vol. 36, no. 10, pp. 1553-1560, Oct. 1988.

[109] M. D. Zoltowski, J. M. Kautz, and S. D. Silverstein, "Beamspace Root-MUSIC," *IEEE Trans. Signal Processing*, vol. 41, pp. 344-364, Feb. 1996.

[110] M. D. Zoltowski, M. Haardt, and C. P. Mathews, "Closed-form 2-D angle estimation with rectangular arrays in element space or beamspace via unitary ESPRIT," *IEEE Trans. Signal Processing*, vol. 44, pp. 316-328, Jan. 1993.

Curriculum Vitae

Address: S3/06-203, Merckstr. 25, 64283, Darmstadt, Germany

Email: pouyan.parvazi@nt.tu-darmstadt.de **Phone:** +49-6151-164476

Country of Citizenship (residence): Iran (Germany)

Education

- **Ph.D. (2011) Electrical Engineering Communications, TU Darmstadt, Germany**

  Advisors: Prof. Alex B. Gershman and Prof. Marius Pesavento

  Thesis title: *"Sensor Array Processing in Difficult and Non-idealistic Conditions"*

- **M.Sc. (2000) Electrical Engineering Communications, University of Tehran, Iran**

  Advisor: Prof. H. Jamali

  Thesis title: *"Improving the Performance of GSM Systems Using Turbo Equalization"*

  Top M.Sc. student in Communication System Track M.Sc. (GPA: 17.73/20.00)

- **B.Sc. (1997) Electrical Engineering, University of Tehran, Iran**

  Advisor: Prof. R. Faraji-Dana

  Thesis title: *"Design of User Interface for Harmonic Balance Method in Nonlinear Circuits"*

  Second best M.Sc. student in Communication Systems Track (GPA: 16.45/20.00)

- **Diploma in Mathematics & Physics (1993)**

  Exceptional Talents Secondary and High school, Tehran, Iran (GPA: 19.36/20.00)

Research Background/Interest

- robust array signal processing: DOA estimation in partly-calibrated arrays, shift-invariance arrays, threshold performance improvement, subspace-based methods,

calibration techniques

- parametric signal estimation (harmonic retrieval)
- convex optimization for robust distributive beamforming and cognitive radio
- space-time codes and multi-user communications systems
- channel coding

Experiences

- Graduate Research Assistant, "Wissentschaflicher Mitarbeiter", TU Darmstadt, 2005-2011
- Graduate Teaching Assistant and Project Advisor, "Advanced Algorithms for Smart Antenna Systems", TU Darmstadt, 2007-2011
- Graduate Teaching Assistant, "Information Theory", TU Darmstadt, 2011
- Research Engineer, Communications Dept., Ministry of Science, Research and Technology's Research Institute, Iran, 2001-2005
- Graduate Teaching Assistant, "Synchronization Techniques", University of Tehran, 1999-2000
- Graduate Teaching Assistant, "Advanced Communication Theory", University of Tehran, 1999-2000
- Undergraduate Teaching Assistant, "Electromagnetics", University of Tehran, 1999
- Summer intern, Antenna Systems Lab, Department of Electrical and Computer Engineering, University of Tehran, 1996
- Reviewer, IEEE Transactions for Signal Processing, IEEE Signal Processing Letters, IEEE International Conference on Acoustics, Speech, and Signal Processing (ICASSP), IET Signal Processing, European Association for Signal Processing (EURASIP), European Signal Processing Conference (EUSIPCO), International ITG Workshop on Smart Antennas (WSA)

Erklärung laut §9 der Promotionsordnung

Ich versichere hiermit, dass ich die vorliegende Dissertation allein und nur unter Verwendung der angegebenen Literatur verfasst habe. Die Arbeit hat bisher noch nicht zu Prüfungszwecken gedient.

Darmstadt, 8. Dezember 2011,